Understanding the Dark Matter Halos of the Andromeda Satellites

---

Emily Jane Elizabeth Charles

Supervisor: Dr Michelle L. M. Collins
Co-Supervisor: Professor Justin I. Read

Internal Examiner: Dr Denis Erkal
External Examiner: Dr Azadeh Fattahi

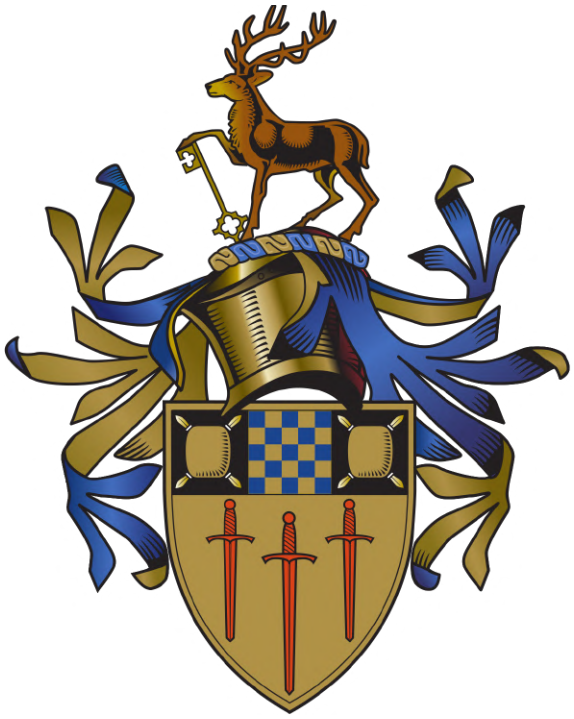

Astrophysics PhD
University of Surrey
December 21, 2023

Dedication

To my ever-patient and ever-loving fiancé, David.
You are the stars to my dark matter.
Our love could survive even the strongest tidal stripping.

Abstract

In the current cosmological model, the Lamda Cold Dark Matter model (ΛCDM), dark matter is thought to make up the vast majority ($\sim 85\%$) of the matter in the Universe, and it forms the backbone of structure formation. Yet, due to the elusive properties of dark matter, we still know very little about it. The particle nature of dark matter is one of the most pressing, unanswered questions in astrophysics.

Despite the considerable success of the ΛCDM model at explaining large-scale structure formation in the Universe, there are a number of outstanding tensions between the model and observations at small (dwarf galaxy) scales. Understanding these tensions is key to our understanding of dark matter, making dwarf galaxies ideal probes. Fortunately, within the observable region that we reside in, known as the Local Group, there is an abundance of dwarf galaxies covering a broad range of properties. In this thesis, I primarily focus on investigating the dark matter content of the dwarf galaxy satellites of our galactic neighbour, the Andromeda galaxy (M31).

First, I present results from the dynamical mass modelling analysis of Andromeda (And) XXV. Intriguingly, I find And XXV has an unusually low central dark matter density when compared to other dwarfs of a similar mass. In a follow-up study, I then investigate possible causes of the low central densities observed in both And XXV and And XXI (identified to have a similarly low central density in a previous study). I test the effects of stellar feedback, tidal stripping and halo concentrations, as well as a range of different dark matter models. I find that in both cold and warm dark matter, stellar feedback alone cannot explain the densities. Instead, And XXV requires a combination of stellar feedback and extreme tidal stripping, whereas And XXI favours stellar feedback and an extremely low halo concentration. Finally, I detail the discovery of two ultra-faint dwarf galaxies around M31 and Triangulum (M33). Both of these dwarfs have tantalising features, which could have potential ramifications for our understanding of dwarf galaxy evolution.

The work I present in this thesis lays the groundwork for analysing the remaining M31 dwarf galaxies. When combined with the upcoming mass modelling of the entire M31 system, as well as the wealth of dwarfs posited to be discovered by upcoming astronomical surveys, the methods presented in this thesis will provide robust constraints on both the nature of dark matter and galaxy formation and evolution pathways.

Declaration

This thesis and the work to which it refers are the results of my own efforts. Any ideas, data, images or text resulting from the work of others (whether published or unpublished) are fully identified as such within the work and attributed to their originator in the text, bibliography or in footnotes. This thesis has not been submitted in whole or in part for any other academic degree or professional qualification. I agree that the University has the right to submit my work to the plagiarism detection service Turnitin®UK for originality checks. Whether or not drafts have been so assessed, the University reserves the right to require an electronic version of the final document (as submitted) for assessment as above.[1]

Aspects of this work have appeared in the following publications:

- **Chapter 2:**
  Charles, Emily J. E., Collins, Michelle L. M., Rich, R. Michael, Read, Justin I., Kim, Stacy Y., Ibata, Rodrigo A., Martin, Nicolas F., Chapman, Scott C., Balbinot, Eduardo, Weisz, Daniel R., 2023, MNRAS, 521, 3527, *Andromeda XXV - a dwarf galaxy with a low central dark matter density* - Charles et al. (2023)

- **Chapter 4:**
  Martínez-Delgado, David, Karim, Noushin, Charles, Emily J. E., Boschin, Walter, Monelli, Matteo, Collins, Michelle L. M., Donatiello, Giuseppe, Alfaro, Emilio J., 2022, MNRAS, 509, 16, *Pisces VII: discovery of a possible satellite of Messier 33 in the DESI legacy imaging surveys* - Martínez-Delgado et al. (2022)

  Collins, Michelle L. M., Charles, Emily J. E., Martínez-Delgado, David, Monelli, Matteo, Karim, Noushin, Donatiello, Giuseppe, Tollerud, Erik J., Boschin, Walter, 2022, MNRAS, 515, L72, *Pegasus V/Andromeda XXXIV-a newly discovered ultrafaint dwarf galaxy on the outskirts of Andromeda* - Collins et al. (2022a)

[1] This declaration is not in my own words but was downloaded from https://surrey-content.surrey.ac.uk/sites/default/files/2023-04/Handbook$%$202022-23$%$20Final$%$20v3.pdf

Aspects of this work are in preparation and will shortly appear in the following publication:

- **Chapter 3:**
  Charles, Emily J. E., Kim, Stacy Y., Collins, Michelle L. M., Read, Justin I., et al., in prep, MNRAS, *Investigating the unusually low central dark matter densities of Andromeda XXI and Andromeda XXV*

Acknowledgements

I would like to thank the following individuals and organisations, without whom this thesis would not have been possible:

- My amazing supervisors, Michelle Collins and Justin Read, for providing me with this wonderful opportunity, for sharing their wealth of scientific knowledge with me and for their continued patient support and understanding which has helped me grow as both an individual and a researcher. Michelle introduced me to the wonderful world of the Andromeda dwarf galaxies during my undergraduate final-year project and I have not looked back since.

- My wonderful fiancé, David, for your love, support and encouragement. Thank you for providing me with a safe and comfortable space to navigate the ups and downs of PhD life and for always believing in me and encouraging me, even when I could not always see the stars shining in the galaxies. You are my best friend – my forever and always. I love you to the edge of the Universe and back!

- My Mum for always encouraging me to reach for the stars and beyond.

- All of the female astrophysics pioneers who have paved the way and laid the groundwork that has allowed me to be writing this thesis today. Your hard work, determination and battles for recognition must be forever remembered and appreciated.

- David Martínez-Delgado for inviting me to join the exciting collaboration searching for satellites in the Andromeda/Triangulum system.

- The University of Surrey Doctoral College for providing the funding that made the research presented in this thesis possible.

- I also have to specifically thank Emma Francis from the Doctoral College for all of her helpful career advice that gave me the confidence and resources to take a leap of faith to follow an alternative career path.

- The University of Surrey Astrophysics Group for being such a welcoming and understanding group of awesome people. Within the group, I especially have to thank Sophia Lilleengen for the extremely helpful coding advice, plot styling tips, typo-finding, but most of all for being a selfless and compassionate confidant on all things PhD related; and Stacy Kim for all of the wonderful advice, bug fixing, mathematical error locating and the many rejuvenating board game nights topped off with additional kitty cuddles.

- My wonderful co-authors and collaborators for all of your insightful comments and feedback on numerous manuscripts that have gone a long way to improving the quality of the work presented in this thesis.
- My examiners, Azadeh Fattahi and Denis Erkal, for your time reading my thesis and conducting my viva voce examination.
- Finally, to my two adorable cats, Luna and Helix. Thank you for the numerous much-needed, re-energising and motivating cuddles. Even if you would frequently block the computer screen, delete code and send cryptic Slack messages, your floofy love and affection will forever be invaluable.

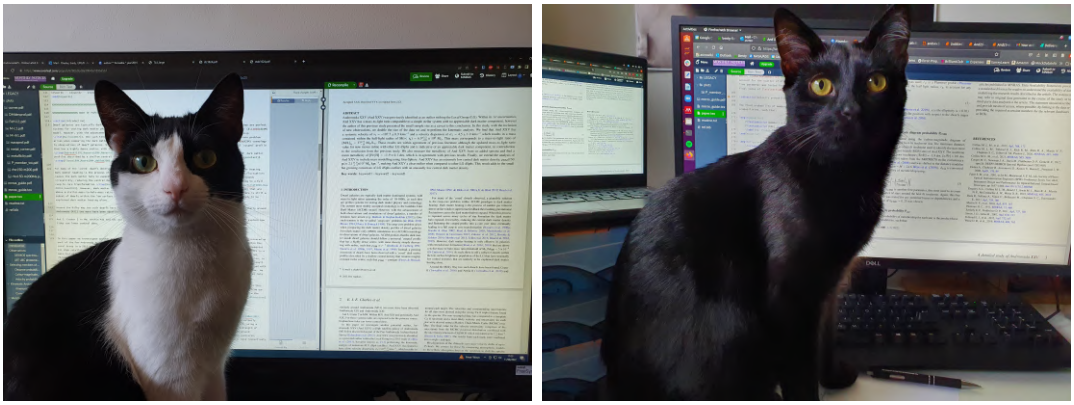

Figure 1: To my forever loving *(and forever computer-screen-blocking)* cats, Luna and Helix. Thank you for your endless, invaluable kitty love.

Furthermore, I have had the privilege of working with data from a range of observatories:

- The photometric observations presented in this thesis are obtained primarily from the Large Binocular Telescope (LBT). The LBT is an international collaboration among institutions in the United States, Italy and Germany. LBT Corporation partners are: The University of Arizona on behalf of the Arizona university system; Istituto Nazionale di Astrofisica, Italy; LBT Beteiligungsgesellschaft, Germany, representing the Max-Planck Society, the Astrophysical Institute Potsdam, and Heidelberg University; The Ohio State University, and The Research Corporation, on behalf of The University of Notre Dame, University of Minnesota and University of Virginia.
- The photometry for the two Andromeda/Triangulum satellites were based in part on observations at Kitt Peak National Observatory at NSF's NOIRLab, which is managed by the Association of Universities for Research in Astronomy (AURA) under a cooperative agreement with the National Science Foundation. We are honored to be permitted to conduct astronomical research on Iolkam Du'ag (Kitt Peak), a mountain with particular significance to the Tohono O'odham.

- A significant proportion of the kinematic data presented in this thesis was obtained at the W.M. Keck Observatory, which is operated as a scientific partnership among the California Institute of Technology, the University of California and the National Aeronautics and Space Administration. The Observatory was made possible by the generous financial support of the W.M. Keck Foundation. Data were also used from observations obtained with MegaPrime/MegaCam, a joint project of CFHT and CEA/DAPNIA, at the Canada-France-Hawaii Telescope which is operated by the National Research Council of Canada, the Institut National des Sciences de l'Univers of the Centre National de la Recherche Scientifique of France, and the University of Hawaii. I wish to recognise and acknowledge the very significant cultural role and reverence that the summit of Mauna Kea has always had within the indigenous Hawaiian community.

Finally, I have used many software packages throughout my research. The availability of high-quality publicly available software made by astronomers for astronomers is a wonderful reflection of the astronomy community and what we can achieve when we work together. Within this thesis, I have used the following software packages:

- astropy (Astropy Collaboration et al., 2013, 2018, 2022)
- corner (Foreman-Mackey, 2016)
- colossus (Diemer, 2018)
- dis (Kim & Peter, 2021)
- DRAGONS (Labrie et al., 2019)
- emcee (Foreman-Mackey et al., 2013)
- GravSphere (Read & Steger, 2017; Read et al., 2018, 2021; Genina et al., 2020a; Collins et al., 2021)
- matplotlib (Hunter, 2007)
- numpy (Harris et al., 2020)
- scipy (Virtanen et al., 2020)

Contents

List of Figures

List of Tables

Introduction

1.1 Dark Matter

We currently only understand approximately 5% of the Universe. The most successful cosmological model to date is the Lambda Cold Dark Matter Model (ΛCDM, Blumenthal et al., 1984). In ΛCDM, only 5% of the mass–energy budget of the Universe is the baryonic matter that we observe as stars, gas and dust. The remaining mass–energy budget of the Universe is dominated by two 'dark' components, dark energy (68%) and dark matter (27%) (Planck Collaboration et al., 2016, 2020). A significant field of study within astrophysics, and this thesis, is focused on trying to understand the latter.

1.1.1 What is Dark Matter?

Dark matter is a theoretical form of matter thought to make up $\sim 85\%$ of the matter quota of the Universe and forms the scaffolding necessary for structure formation. Yet we still know very little about its nature. We believe that it is non-baryonic (i.e. not protons or neutrons), it is cold (i.e. the particle velocities were non–relativistic at the epoch of radiation–matter equality) and that it is collisionless (i.e. the particles only interact via gravity) (e.g. Peebles, 1982; Flynn et al., 1996; Kalberla et al., 1999; Read & Trentham, 2005; Tisserand et al., 2007). This combination of factors makes dark matter an extremely elusive substance; as such, its particle nature is unknown.

The first, most widely considered, dark matter particle candidate were weakly interacting massive particles (WIMP Lee & Weinberg, 1977; Steigman & Turner, 1985; Kolb & Turner, 1990; Jungman et al., 1996). This class of particles have masses of $\sim$ 100 GeV, interact over small–scales comparable to the weak force and were thermally created in the early Universe. Predictions from particle physics suggest a new particle with these properties should exist. Furthermore, the current–day abundance of dark matter, if produced thermally, requires a self–annihilation cross–section in line with that predicted for WIMPs. This combination of coincidences became known as the WIMP Miracle (Feng & Kumar, 2008) and painted WIMPs as an exciting dark matter candidate. However, after decades of null detections, confidence in WIMPs is beginning to wane (e.g. Bertone & Tait, 2018; Arcadi et al., 2018). Now other alternative particle candidates are gaining traction, for example, axions. Axions are theoretical particles that were first postulated as a solution to the strong charge–parity problem in quantum chromodynamics (Peccei & Quinn, 1977; Preskill et al., 1983). They are thought to weakly interact with standard model particles, they would be non–relativistic (cold) and, within the mass range of $10^{-5} - 10^{-2}$ eV, would able to constitute some or all of the CDM density required. These properties mean that axions are quickly gaining the interest of cosmologists

as interesting dark matter candidates (e.g. Buckley & Peter, 2018). Beyond WIMPs and axions, many other dark matter particles have been hypothesised, for a detailed overview of the different candidates, see Kolb & Turner (1990); Hooper & Profumo (2007); Feng (2010).

A plethora of particle physics experiments have searched for direct or indirect detection of a dark matter particle (e.g. Bertone et al., 2005; Raby et al., 2008; Bernabei et al., 2010; Aprile et al., 2011; Aalseth et al., 2011; Behnke et al., 2011; Angloher et al., 2012; Cherwinka et al., 2012; Akerib et al., 2017). However, many of these experiments are particle specific. As we are still unsure of the particle nature of dark matter, these experiments are comparable to looking for a needle in a cosmological haystack. To date, we have not had a confirmed direct detection of a dark matter particle (Bertone & Tait, 2018). Instead, we turn to the 15% of the matter within the Universe we *can* observe and measure the effect of the invisible dark matter on this visible, baryonic matter. These observations will help us constrain the possible properties of dark matter, which will, in turn, narrow down the particle physics search (e.g. Peter, 2012; Buckley & Peter, 2018)

1.1.2 The Discovery and Evidence of Dark Matter

References to the concept of a missing mass in the form of a 'dark matter' exist as far back as Barnard & Ranyard (1894), who questioned whether dark regions on the sky were because of a paucity of stars, or due the existence of absorbing matter along the line-of-sight. Poincare (1906), Öpik (1915), Kapteyn (1922) and Oort (1932) all discussed the existence of a possible non-luminous matter but concluded that it would contribute less than, or equal to the amount of visible matter.

Instead, the coining of the term 'dark matter' is typically associated to Zwicky (1933) (translated to English in Andernach & Zwicky, 2017) and subsequent follow–up work (Zwicky, 1937). Zwicky investigated eight galaxies within the Coma cluster, assuming virial equilibrium, and found that their observed velocity dispersions were $\mathcal{O}(1000)$ kms^{-1}, significantly higher than the theoretically predicted $\sim$ 80 kms^{-1}. These high velocity dispersions demonstrated that the Coma cluster needed to be at least 400 times more massive than the observed mass. Zwicky hypothesised that this discrepancy could be explained by missing non–luminous mass, dark matter. This result was supported by a similar and concurrent study of the Virgo cluster by Smith (1936).

However, dark matter was not seriously considered within the astronomical community until the 1970s, when galaxy rotation curve studies pioneered by Vera Rubin presented strong evidence for missing mass within galaxies. Aided by improvements in spectroscopy technology, Rubin was able to perform detailed spectroscopic observations of the Andromeda Galaxy (M31) using the 21cm hydrogen emission line (Rubin & Ford, 1970). This work was followed by many other spectroscopic observations of galaxies (e.g. Freeman, 1970; Rubin et al., 1978, 1980, 1982; Rubin, 1983; Rogstad & Shostak, 1972; Roberts & Rots, 1973; Bosma, 1978; van Albada et al., 1985). The rotation curves from many of these observations revealed an unexpected flattening corresponding to a constant circular velocity at large radii instead of the expected decreasing circular velocity described by the Keplarian model. This again

demonstrated the need for missing mass, showing that galaxies reside inside dark matter halos extending well beyond the galaxy's visible component, helping to cement the idea of dark matter being abundant throughout the Universe rather than an issue isolated only to galaxy clusters.

Since its discovery, additional evidence for the existence of dark matter has come to fruition. For example, the effect of gravitational lensing provided further evidence that highlights the need for missing mass within different structures in the Universe. Gravitational lensing occurs when a foreground object has a sufficient mass that it can distort the light rays originating from a background object (Einstein, 1917, 1936). By analysing the lensed object, we can determine the mass content and distribution of the foreground object. Lensing observations can be used to provide evidence and constraints for dark matter; an exquisite example is the collision of two galaxy clusters known as the Bullet Cluster, shown in Figure 1.1. The pink region highlights the distribution of the hot gas (baryonic matter) observed with X–ray telescopes (Markevitch et al., 2002; Barrena et al., 2002) and the blue region is the dark matter distribution which was determined from weak lensing observations (Clowe et al., 2004, 2006) and was found to trace the stellar component. There is a distinct separation between the two regions because the gaseous components interacted and thus slowed down during the interaction, whereas the dark matter did not interact, allowing it to continue, highlighting its collisionless nature. This result has been supported by similar studies of other galaxy cluster collisions (e.g. Bradač et al., 2008; Harvey et al., 2015).

We have also found evidence for dark matter on larger scales and/or beyond the need for missing mass within astronomical systems. Some of the strongest dark matter constraints have come from cosmic abundance calculations from the Cosmic Microwave Background (CMB) observations. The CMB is the remnants of radiation from the very early Universe, which has since cooled with the expansion of the Universe to ~ 2.7 K. Since its serendipitous discovery (Dicke, 1946; Penzias & Wilson, 1965), the CMB has been mapped in detail (e.g. Cosmic Background Explorer, COBE: Mather et al., 1990; Smoot et al., 1992; Efstathiou et al., 1992 and Wilkinson Microwave Anisotropy Probe, WMAP: Bennett et al., 2003; Komatsu et al., 2009). Planck is the most recent probe to map the CMB providing the highest resolution results to date (Planck Collaboration et al., 2016, 2020). These studies show that within the CMB there are small temperature fluctuations corresponding to density anisotropies in the early universe. These density anisotropies became the seeds for structure formation. By mapping the amplitude of the temperature fluctuations at different angular sizes (Figure 1.2), we can probe the cosmological makeup of the Universe, including the dark matter content of the Universe. The results from these observations broadly matched with predictions from ΛCDM (Planck Collaboration et al., 2016, 2020). Moreover, constraints can be derived from combining the CMB observations with detailed studies of the abundance and clustering of galaxies (e.g. Tegmark et al., 2006; Percival et al., 2007; Aubourg et al., 2015)

Further cosmic abundance evidence comes in the form of primordial nucleosynthesis. Predictions for the abundances of the first elements to form (deuterium, helium and lithium) are tightly correlated with the proportion of baryonic matter in the Universe. The observed primordial abundances match exactly with predictions

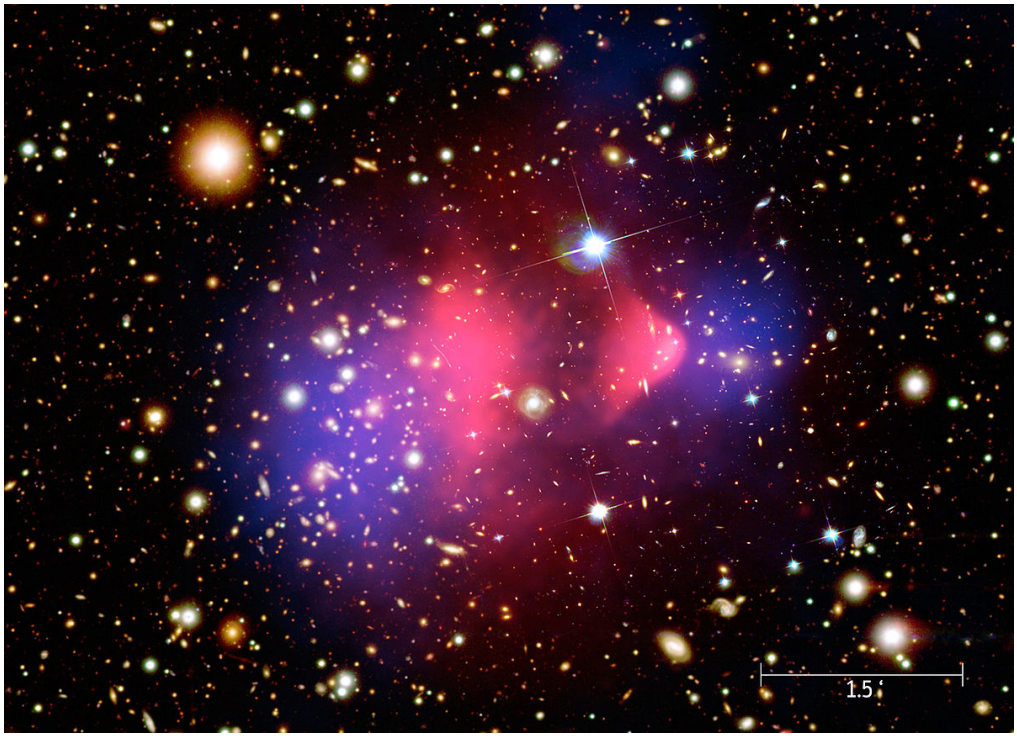

Figure 1.1: A composite image of the Bullet Cluster, showing the collision of two galaxy clusters. The distinct separation between the hot gaseous component (pink) and dark matter component (blue) illustrates the collisionless nature of dark matter. *Image Credit: X–ray: NASA/CXC/CfA/M.Markevitch et al.; Optical: NASA/STScI; Magellan/U.Arizona/D.Clowe et al.; Lensing Map: NASA/STScI; ESO WFI; Magellan/U.Arizona/D.Clowe et al.*

from ΛCDM, assuming that baryonic matter makes up only 5% of the Universe (e.g. Walker et al., 1991; Smith et al., 1993; Burles et al., 1999; Cyburt, 2004; Steigman, 2007; Fields, 2011).

1.1.3 Dark Matter and Structure Formation

Dark matter is thought to provide the backbone of structure formation in the Universe. It is distributed throughout the Universe in a complex cosmological web. At large scales, this web appears isotropic and homogeneous. However, as we begin to zoom in, systems of voids, nodes and filaments begin to appear (e.g. Springel et al., 2005). Within the nodes are regions of high dark matter density, called dark matter halos. The largest halos contain galaxy clusters, $M \sim 10^{15}$ $M_\odot$ comprised of thousands of galaxies gravitationally bound together and continuing down the mass scale to the smallest subhalos hosting a luminous component $M \sim 10^{9}$ $M_\odot$ corresponding to dwarf galaxies, or even galaxy-less subhalos at lower mass scales (e.g. Benson et al., 2002; Okamoto et al., 2008; Benitez-Llambay & Frenk, 2020; Nadler et al., 2020c).

Dark matter halos form hierarchically in a ΛCDM cosmology. Smaller halos form first and then grow in size through a combination of accretion and mergers (White & Rees, 1978; Fall & Efstathiou, 1980). The baryonic gas traces the gravitational

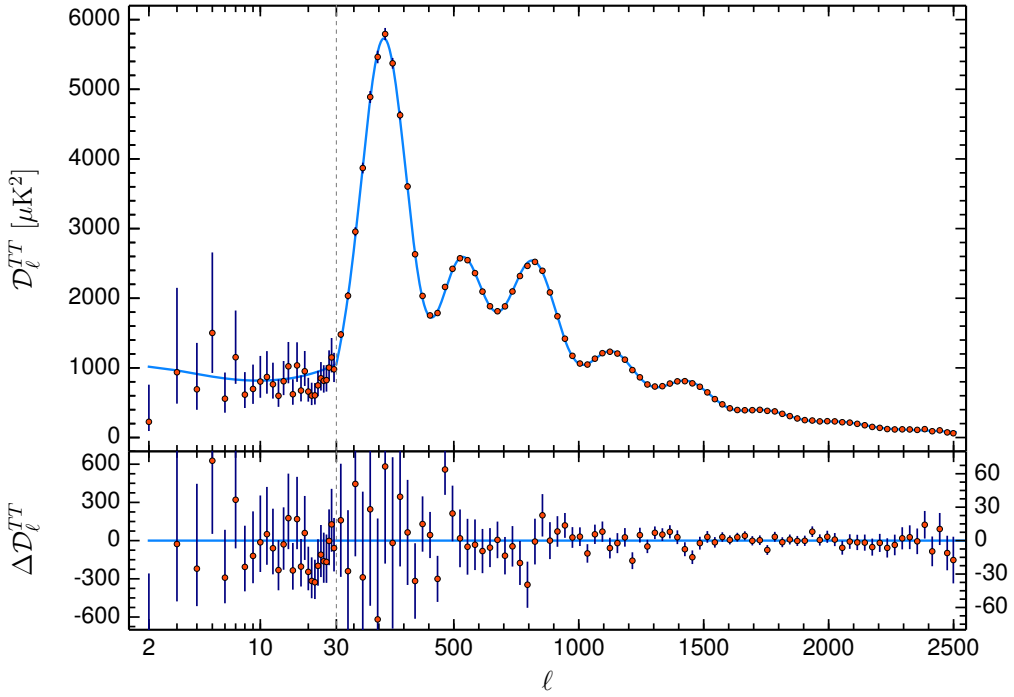

Figure 1.2: The power spectrum of the CMB temperature fluctuations at different angular sizes as observed by Planck. We can see that the observational data (red data points) matches with the theoretical ΛCDM predictions (light blue curve). *Image Credit: Planck Collaboration et al. (2020)*

potential of the dark matter halos. It falls into the centre of the potential well, losing energy through cooling, and starts forming stars. The resulting galaxies (or dwarf galaxies) are, therefore deeply embedded inside the dark matter halo. The dark matter halo extends well beyond the visible component of the galaxy, with the stellar component typically $\sim 1.5\%$ the size of the dark matter halo (Kravtsov, 2013).

Defining the edge of a dark matter halo is challenging. Instead, we often discuss halo sizes in terms of the virial radius, r_{200}. The virial radius is conventionally defined as the radius at which the enclosed density is 200 times the critical density of the Universe at a redshift of $z = 0$. Throughout this thesis we used $\rho_{\rm crit} = 135.05\ {\rm M}_\odot{\rm kpc}^{-3}$, derived from the cosmological parameters from Planck Collaboration et al. (2020). The virial mass, M_{200}, is therefore the mass enclosed within a sphere of radius r_{200} and is defined by:

$$M_{200} = \frac{4}{3}\pi 200 \rho_{\rm crit} r_{200}^3 \tag{1.1}$$

The virial mass is also related to the concentration of the dark matter halo, c_{200}, within a relatively tight scatter through the mass-concentration relation (e.g. Neto et al., 2007; Dutton & Macciò, 2014; Ludlow et al., 2014).

The internal structure of a dark matter halo can be characterised by its density profile, $\rho(r)$. Dubinski & Carlberg (1991) showed that dark matter halo density profiles from N-body simulations can be reasonably well described as a broken power

law, known as a Hernquist profile (Hernquist, 1990):

$$\rho(r) = \rho_0 \left(\frac{r}{r_s}\right)^{-\gamma} \left(1 + \frac{r}{r_s}\right)^{\gamma-\beta} \tag{1.2}$$

where γ describes the slope of the inner radial density profile ($\gamma = 1$) and β describes the slope out the outskirts of the profile ($\beta = 4$).

Navarro et al. (1996b, 1997) went on to show that this profile appeared to be universal for halos of different mass, albeit with a slightly lower value for the slope at the outskirts ($\beta = 3$), giving the now commonly used Navarro, Frenk and White (NFW) profile:

$$\rho(r) = \rho_0 \left(\frac{r}{r_s}\right)^{-1} \left(1 + \frac{r}{r_s}\right)^{-2} \tag{1.3}$$

More recent simulations, driven by higher resolutions, have found that this profile is not universal and that γ can evolve smoothly as a function of radius (Merritt et al., 2006; Stadel et al., 2009; Navarro et al., 2010; Bullock & Boylan-Kolchin, 2017). An alternative is the three parameter Einasto profile (Einasto, 1965) and has been shown to be a better fit to simulations (e.g. Merritt et al., 2006). However, the NFW profile is still an adequate description for small halos (i.e. dwarf galaxies), and is typically implemented due to its simpler form (e.g. Dutton & Macciò, 2014).

1.2 Dwarf Galaxies of the Andromeda Galaxy

Other than the Large and Small Magellanic Clouds, which are visible to the naked eye, the first dwarf galaxies were not discovered until 1938, when Shapley (1938) observed the Milky Way dwarfs, Sculptor and Fornax. More dwarfs were discovered at a steady rate after Sculptor and Fornax through photographic surveys (e.g. Harrington & Wilson, 1950; Wilson, 1955; van den Bergh, 1972; Cannon et al., 1977; Canterna & Flower, 1977; Irwin et al., 1990; Ibata et al., 1994; Armandroff et al., 1998; Whiting et al., 1999; Martin et al., 2004). However, over the past few decades, the dwarf population has exploded, aided by the advent of digital surveys such as the Sloan Digital Sky Survey (SDSS, Gunn & Knapp, 1993; York et al., 2000), Pan–Andromeda Archaeological Survey (PAndAS, Martin et al., 2006; Ibata et al., 2007; McConnachie et al., 2009), Dark Energy Survey (DES, Bechtol et al., 2015; Abbott et al., 2018), Panoramic Survey Telescope and Rapid Response System (Pan–STARRS, Chambers et al., 2016) and the DECam Local Volume Exploration Survey (DELVE, Drlica-Wagner et al., 2021). A summary of Milky Way dwarf discovery through the ages is shown in Figure 1.3.

1.2.1 What are Dwarf Galaxies?

Pinpointing a standard definition for what constitutes a dwarf galaxy within the astronomy community is challenging. Moreover, the parameter space considered a dwarf galaxy often needs to be updated as new surveys push the boundaries of dwarf discovery, uncovering systems of ever–increasing extremity. For example, the

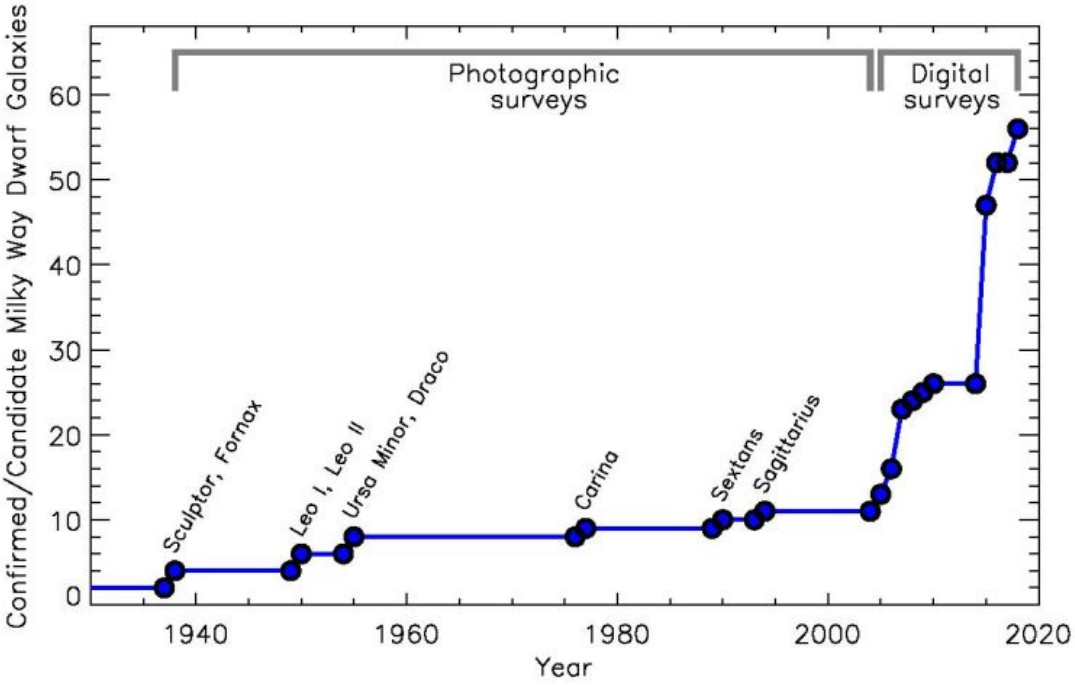

Figure 1.3: The Milky Way dwarf galaxy satellite census as a function of time. The rate of discovery remains relatively steady between 1938 and 2004. However, the majority of discoveries came after 2005 as a result of digital surveys such as SDSS, DES and Pan–STARRS. Each survey approximately doubled the satellite population. *Image Credit: Simon (2019)*

once relatively solid distinction between globular clusters and dwarf galaxies has now begun to blur with the discovery of smaller, fainter dwarfs and brighter, larger globular clusters (e.g. Da Costa et al., 1982; Côté et al., 2002; Gilmore et al., 2007; Kirby et al., 2013a; Martin et al., 2016a; Simon et al., 2017; Fritz et al., 2019; Longeard et al., 2018, 2021; Cerny et al., 2023, Taylor et al., in prep) or even the discovery of the purported dark–matter deficient systems (van Dokkum et al., 2018, 2019; Guo et al., 2020). In an early review, dwarfs were defined as having a *'small intrinsic size, small absolute luminosity and low surface brightness'* (Hodge, 1971), a definition which still holds up relatively well today. Dwarf galaxies are typically comprised of tens–of–thousands to billions of stars, with half–light radii ranging from $10 - 1000$s parsecs, stellar masses of approximately $10^3 - 10^9$ $M_\odot$ and absolute magnitudes in the region of $-1.5 \lesssim M_V \lesssim -18$ (e.g. McConnachie, 2012). The term dwarf galaxy encompasses a wide spectrum of morphologies, luminosities, sizes and masses, as demonstrated in Figure 1.4.

Beyond the visible portion of the dwarf, there is a large dark matter halo that extends well beyond the stellar component of the dwarf. Dwarf galaxies are deeply embedded in the dark matter halo they reside in and are some of the most dark matter dominated systems in the Universe (e.g. Mateo, 1998; Simon & Geha, 2007; Gilmore et al., 2007).

Dwarf galaxies are typically observed part of a group of satellites orbiting a larger

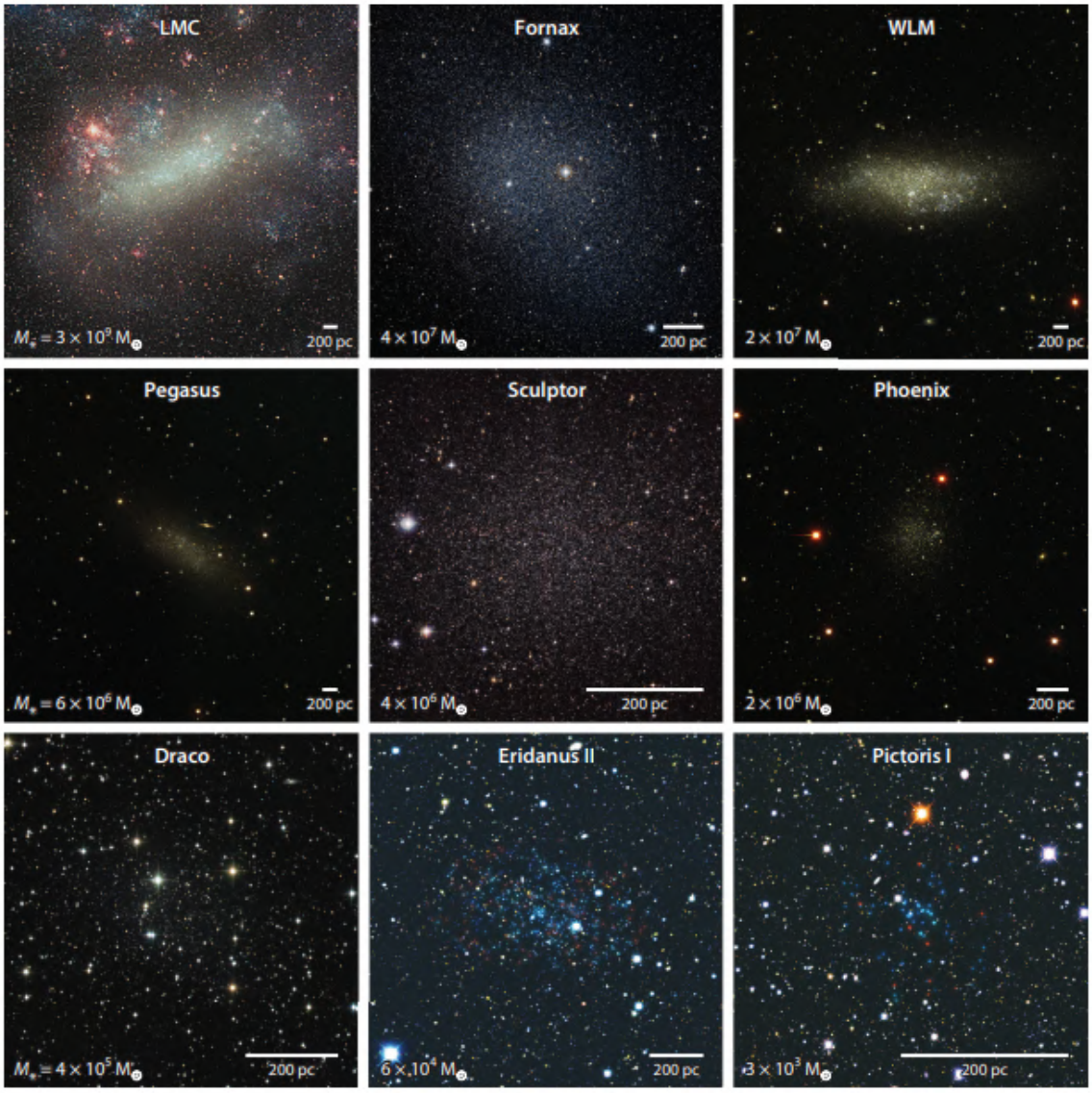

Figure 1.4: An image illustrating the diversity of size, luminosity, mass and morphology covered by the term 'dwarf galaxy'. Shown are nine dwarf galaxies spanning six orders of magnitude in stellar mass. In each panel, the stellar mass is listed in the lower—left corner, and a scale bar demonstrating 200 pc is shown in the lower–right corner. The LMC, WLM, and Pegasus are dIrrs, with a rich gas reservoir fueling ongoing star formation. The remaining six are dSph galaxies that are currently quiescent with no gas content. *Image Credit: Bullock & Boylan-Kolchin (2017)*

host galaxy. The Milky Way has more than 60 known satellites (Drlica-Wagner et al., 2020, and references within) and M31 $\sim$ 35 satellites (e.g. McConnachie, 2012; Martin et al., 2016c). Although, dwarf galaxies have also been found to exist as isolated systems in the field (e.g. Monelli et al., 2010a,b; Higgs et al., 2016; Higgs & McConnachie, 2021; Sand et al., 2022).

Dwarf Spheroidals v.s. Dwarf Irregulars

Dwarf galaxies can be broadly categorised into two main types based on their morphology, dwarf irregulars (dIrrs) and dwarf spheroidal (dSphs).

dIrr galaxies are gas–rich systems, mostly comprised of neutral hydrogen (HI) and ionised atomic hydrogen (HII) (e.g. Mo et al., 2010). Observations of the HI spectral line ($\lambda = 21$ cm) show that the HI content is distributed smoothly throughout the dwarf and often very extended many times larger than the visible matter in the galaxy (e.g. Fisher & Tully, 1975, 1981; Thuan & Seitzer, 1979a,b; Thuan & Martin, 1981; Hoffman et al., 1987). In contrast, the HII gas distribution is clumpy, resulting in an irregular morphology referred to in the name dIrr. The HII clouds correlate to regions of ongoing star formation as they are produced when young massive stars produce high–energy ultraviolet radiation that is able to ionise the HI gas in the interstellar medium (e.g. Tully et al., 1981; Tielens & Hollenbach, 1985; Israel & Koornneef, 1988; van Zee et al., 1998).

dSphs, on the other hand, are gas–poor systems with little to no gas reservoir. They are characterised as low surface brightness objects with a fairly regular structure. They typically host simple old stellar populations with no active or recent star formation (e.g. Dolphin, 2002; Weisz et al., 2011; de Jong et al., 2008; Brown et al., 2012, 2014; Belokurov, 2013; Weisz et al., 2014; Gallart et al., 2015; Skillman et al., 2017; Weisz et al., 2019b; Savino et al., 2023) and often have high mass–to–light ratios ($\sim 10 - 1000$ $M_\odot/L_\odot$) corresponding to a large dark matter component (e.g. Mateo, 1998; Simon & Geha, 2007; Gilmore et al., 2007). The large dark matter component, in combination with the lack of gas makes dSphs pristine systems for testing dark matter physics (e.g. Tolstoy et al., 2009; Buckley & Peter, 2018; Simon, 2019; Sales et al., 2022; Battaglia & Nipoti, 2022). For this reason, we chose to focus on dSphs for this thesis.

Ultra Faint Dwarfs

Dwarf galaxies can also be split into a number of subcategories based on certain defining characteristics that distinguish them from 'normal' dwarf galaxies. One specific subcategory that we consider in this thesis is ultra–faint dwarfs (UFDs).

After the discovery of Sextans in 1990 (Irwin et al., 1990), the search for dwarf galaxies with lower luminosities came to a halt. Hampered by technological constraints, dwarfs with lower luminosities were not observed despite theoretical predictions indicating that dwarfs with significantly lower luminosities should exist (e.g. Benson et al., 2002). Therefore, dwarf galaxies were considered to have absolute magnitudes of $M_V < -8.7$, resulting in a luminosity lower bound of $L > 2.5 \times 10^5$ $L_\odot$ (Simon, 2019). However, the first results from SDSS showed that these predictions were true (Zucker et al., 2004) and with the subsequent discoveries from SDSS and other surveys, even fainter satellite objects were discovered (e.g. Willman et al., 2005a,b; Zucker et al., 2006). The nature of these new faint objects was uncertain, and only with follow–up spectroscopy were they confirmed to be very faint dwarf galaxies rather than globular clusters (Simon & Geha, 2007; Martin et al., 2007). At this point, the term UFD came into fruition.

The term UFD still has some variability in definition, although the standard

consensus is that UFDs are faint dwarf galaxies with an absolute magnitude lower than $M_V = -7.7$ corresponding to a luminosity lower bound of $L = 10^5$ $L_\odot$ (Simon, 2019). They are thought to host old metal–poor stellar populations, having formed the majority of their stars before the end of the epoch of reionisation ($z \sim 6$). Reionisation is thought to have quenched star formation in UFDs, resulting in little to no chemical enrichment thereafter (Bullock et al., 2000; Somerville, 2002; Benson et al., 2002; Brown et al., 2014; Simon, 2019). As such, UFDs are often considered 'pristine fossils' providing insight into the conditions present during the reionisation epoch (e.g. Bovill & Ricotti, 2009, 2011a,b; Salvadori & Ferrara, 2009). However, recent discoveries of UFDs with potential overdensities of young blue stars (< 1 Gyr) could call into question the effectiveness of reionisation at quenching star formation in UFDs (Oñorbe et al., 2015; McQuinn et al., 2023; Collins et al., 2023; Savino et al., 2023).

1.2.2 The Andromeda Satellite System

The first dwarf galaxies were identified around the Milky Way, but we are fortunate to have another galaxy system, the Andromeda Galaxy, which is rich with dwarf galaxies on our cosmological doorstep. The Andromeda Galaxy was first described as a 'nebulous smear' or 'small cloud' by astronomer Abd al–Rahman al–Sufi in 964. Andromeda was first assigned the identifier M31 in Messier (1774). Around the same time, satellites M32, M110, NGC185 and NGC147 were discovered (Messier, 1781; Herschel, 1786, 1833, 1864). As the concept of extra–galactic systems was not yet understood, these objects (including M31) were categorised as 'faint nebulae'. It was not until the discovery of Cepheid variable stars (Leavitt & Pickering, 1912), which allowed for the subsequent application of the Cepheid distance scale (Hubble, 1926) that these systems were eventually identified to be extra–galactic in nature, which paved the way for future dwarf galaxy discovery.

The first dwarf galaxies of M31, Andromeda (And) I, And II and And III were discovered by van den Bergh (1972). More M31 satellites were discovered in the decades following, with a handful of known satellites around the end of the century (Armandroff et al., 1998, 1999; Morrison et al., 2003). The majority of the M31 satellites were discovered as part of large–scale dedicated discovery surveys. The PAndAS survey found 17 satellites (Martin et al., 2006, 2009, 2016c; Ibata et al., 2007; Irwin et al., 2008; McConnachie et al., 2008; Richardson et al., 2011), with the remaining 8 satellites split between SDSS and PanSTARS (Zucker et al., 2004, 2007; Majewski et al., 2007; Slater et al., 2011; Bell et al., 2011; Martin et al., 2013a,b), and a few other dwarfs have been discovered since. The dSphs of M31 have also undergone spectroscopic analysis (e.g. Kalirai et al., 2010; Tollerud et al., 2012; Collins et al., 2013) to resolve the kinematics and chemical composition of many of the M31 dwarfs.

1.2.3 Observing M31 Dwarfs

Due to their relatively close proximity, the individual stars inside the M31 satellites can be resolved to provide a wealth of observational data. There are two main ways

in which we can observe M31 dwarf galaxies, photometry and spectroscopy.

Photometry

Photometry is an observational technique that involves measuring the amount of flux radiated by an astronomical object. Photometric techniques have evolved over time, starting with hand–drawn images of observations, to photographic plates, to digital charge–coupled device imaging. From photometric observations, we can gain the spatial positions of the stars as well as the magnitude and colour (if imaged in more than one band). Using these observations, we can gain insight into the structural properties and distance of the dwarf. We can also begin to place some limits on the chemical makeup and star formation. Below, I will briefly outline some of the common photometric analysis techniques we used in this thesis. The majority of these methods use key features on a colour magnitude diagram (CMD). These features are illustrated in Figure 1.5.

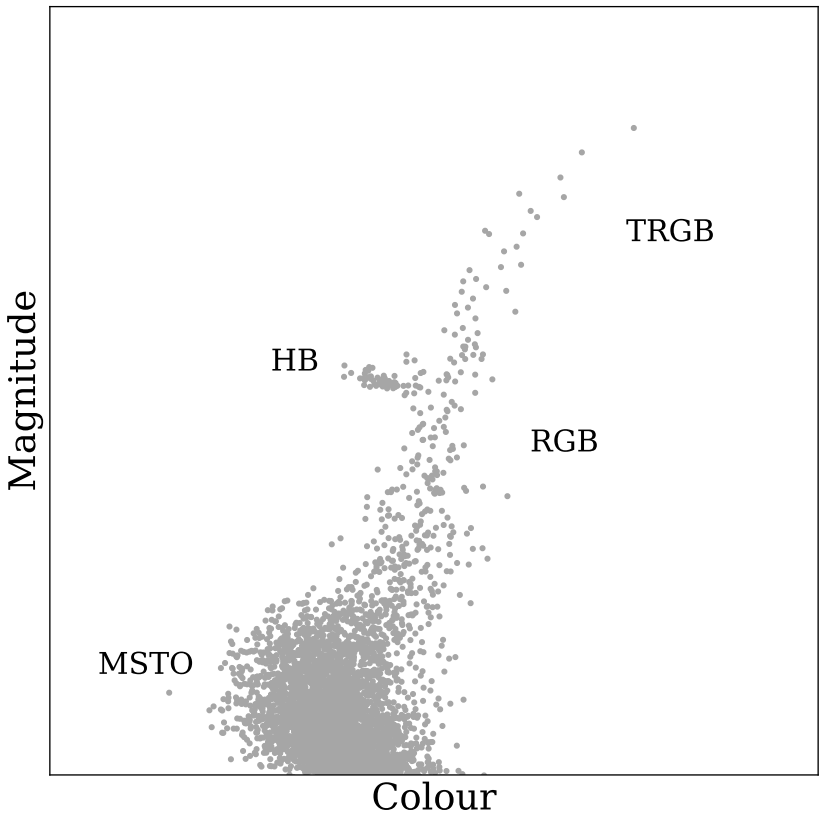

Figure 1.5: A simulated colour magnitude diagram of a dwarf galaxy, with the structures commonly used for analysis labelled: the tip of the red giant branch (TRGB), the red giant branch stars (RGB), the horizontal branch stars (HB) and the main sequence turn–off stars (MSTO).

Before most other analyses can occur, an accurate distance estimate of a system

is often required. Stars populating the tip of the red giant branch (TRGB) are the brightest stars in the system, making them easier to observe. The TRGB can be used to determine a distance estimate by isolating the TRGB. This can be done using Sobel edge detection (e.g. Lee et al., 1993) or more rigorously using Bayesian inference techniques (e.g. Conn et al., 2012; Tollerud et al., 2016). The TRGB has a known absolute luminosity in each band, for example, $M_{r,\mathrm{TRGB}} = -3.01 \pm 0.1$ (Sand et al., 2014). This value can be compared to the apparent magnitude of the TRGB and then converted into a distance. The TRGB was used to measure the distances to 27 of the M31 satellites in Conn et al. (2012).

The TRGB of the M31 satellites is often sparse and suffers from contamination effects, so if the photometry allows, the horizontal branch (HB) is often used instead. Again this feature has a known absolute magnitude that can be compared to the apparent magnitude and converted into a distance. The HB has long been known to be a reliable distance estimator (e.g. Vandenberg et al., 1990; Carretta et al., 2000), although deeper photometry is required to reach this feature, which is often difficult to impossible from the ground for the M31 satellites. Instead, HB observations often require space–based imaging (Weisz et al., 2014, 2019a). Furthermore, with multi–epoch spaced–based observations, variable stars, such as RR Lyrae stars, can further constrain HB–determined distances, which is especially useful for UFD systems with sparse HBs (e.g. Savino et al., 2022).

With a distance estimate, it is then possible to constrain the structural properties of the dwarf. The key properties are the central coordinates, the half–light radius, the ellipticity and the position angle. The structural properties can be measured using an algorithm that assumes a likelihood function consisting of an exponential radial density profile for the overdensity (dwarf) and constant background contamination. Using Bayesian inference tools such as Markov Chain Monte Carlo (e.g. Foreman-Mackey et al., 2013), the algorithm can be applied simultaneously to the overdensity and the background to determine the structural properties and corresponding uncertainties. A typical example of such a method is described Martin et al. (2016b). This algorithm also determines the number of stars observable above a certain magnitude limit. This value can be used in combination with simulated stellar populations to determine the luminosity of the dwarf.

An isochrone is a curve on a CMD representing a stellar population of the same age but with different luminosities. There are multiple online open access isochrone databases (e.g. Dartmouth Dotter et al., 2008, Padova Girardi et al., 2010a, Parsec Bressan et al., 2012, MIST Choi et al., 2016, BASTI Hidalgo et al., 2018). By fitting isochrones to the RGB, either by eye or with a fitting algorithm, it is possible to place some basic constraints on the metallicity[1] and age of a dwarf galaxy. With the HB basic star formation histories, such as quenching times, can be obtained (Weisz et al., 2019b). However, the main sequence turn off (MSTO) is required to derive precise measurements of the star formation history due to the age–metallicity degeneracy. Galaxies shift in colour, becoming redder as the galaxy ages since more stars move to the RGB. Galaxies can also appear red for systems with higher metallicity. The observed effect of increased age can be counteracted by decreased metallicity (Worthey, 1994; Ferreras et al., 1999). The MSTO contains spectral features in the

[1] In astronomy, any element other than hydrogen and helium are considered metals.

ultraviolet and infrared that are non–linear with temperature and thus can break this age–metallicity degeneracy (e.g. Worthey, 1999). For the M31 dwarfs multi–orbit, $\mathcal{O}(10)$, space–based observations are required to reach the MSTO. As such, detailed SFHs for the M31 dwarfs have only recently become available (e.g. Skillman et al., 2017; Collins et al., 2022b; Savino et al., 2023). For accurate chemical composition measurements, we often turn to spectroscopy.

Spectroscopy

Spectroscopy is the method of splitting electromagnetic radiation into a spectrum of constituent wavelengths to measure the absorption or emission of radiation by matter. As photons produced inside the star pass through the stellar material, some of the light will be absorbed, resulting in regions of reduced flux known as absorption lines. The properties of these absorption lines can be used to determine the chemical composition and kinematics of a dwarf galaxy. It is possible to resolve individual stars at the distance of M31. As such, the majority of spectroscopic observations of M31 use slit masks in combination with a diffraction grating to obtain spectra for each individual star. However, only the brightest RGB stars can be observed spectroscopically (e.g. Kalirai et al., 2010; Tollerud et al., 2012; Collins et al., 2013).

We often define the chemical composition of a dwarf galaxy in terms of its metallicity or iron abundance [Fe/H]. Metallicity values are relative to the Sun. An object with [Fe/H]$= +1$ has a metallicity ten times that of the Sun. Conversely, an object with [Fe/H]$= -1$ has a metallicity that is one-tenth of the Sun, and so on. However, due to the relatively low signal–to–noise ratio of spectra for objects at the distance of M31, it is not possible to determine the metallicity directly from the iron absorption lines. Instead, the broad calcium II triplet (CaT) lines found at $\lambda = 8498$Å, 8544Å and 8662Å are easily observable, even for M31 dwarfs, and are known to be a good proxy for iron abundance (e.g. Rutledge et al., 1997a,b; Armandroff et al., 1998; Olszewski et al., 1991; Armandroff & Da Costa, 1991). The equivalent widths (EWs) of the CaT absorption lines can be measured from the spectroscopic observations and converted into a metallicity using an empirical conversion (Armandroff & Da Costa, 1991; Battaglia et al., 2008). Although a study by Starkenburg et al. (2010) found that the standard EWs conversions were biased at low metallicities, which was an issue for dwarf galaxies which are typically very metal–poor systems ($-1.0 \lesssim$ [Fe/H] $\lesssim -2.5$ dex). The same paper presented a modification to the empirical relation, which amends this bias at low metallicities, and is now the standard method of measuring the metallicity from the CaT lines (e.g. Ho et al., 2012; Collins et al., 2013, 2021; Martin et al., 2014; Longeard et al., 2018; Preston et al., 2019; Gregory et al., 2019, 2020; Charles et al., 2023).

Kinematics is the study of motion within a system. In the context of dwarf galaxies, we measure the movement of the individual stars inside the dwarf. For the M31 dwarfs, the velocity of the individual stars is typically measured using the same spectroscopic observations of the CaT lines. Stars inside galaxies are typically orbiting with individual velocities in the order of ~ 100s km s^{-1}. As such, the wavelength of the absorption line will be shifted from the rest frame wavelength. The velocity of the star can be determined by measuring this shift (Doppler, 1846; Eddington, 1923; Huggins, 1868; Hubble, 1929). The systemic velocity of each star does not

contain much information about the dwarf. Instead, we study the distribution of velocities, the velocity dispersion. Dwarf galaxies typically have velocity dispersions of $\sim$10 km s^{-1} (e.g. Koposov et al., 2009). Assuming a flat dispersion profile, the mass contained within the half–light radius of the dwarf can then be calculated from the velocity dispersion (e.g. Walker et al., 2009; Wolf et al., 2010). Armed with this mass value (and the luminosity from photometry), we can calculate the mass–to–light ratio, which begins to provide information about the dark matter content of dwarf galaxies.

1.3 Dwarf Galaxies and Dark Matter – Making the Invisible Visible

Dwarf galaxies typically have mass–to–light ratios of $\sim 10 - 1000$s, making them some of the most dark matter dominated systems in the Universe. Over the past few decades, the explosion in dwarf discovery, alongside rapid developments in simulation techniques, has allowed us to push our understanding of dark matter to smaller and more extreme scales.

1.3.1 Challenges for Dark Matter in a ΛCDM Universe

Theoretical predictions from ΛCDM match our observations and simulations of the Universe at large scales remarkably well. However, on small scales (e.g. galactic), a number of tensions arise (e.g. Bullock & Boylan-Kolchin, 2017; Sales et al., 2022). The tensions are summarised in Figure 1.6. Many of these tensions originated from comparisons of dark matter only simulations and Local Group dwarf galaxy observations. Over time these tensions have evolved, especially with the advancements in simulation capabilities allowing for higher resolution and the inclusion of the complex baryonic physics that was missing in the first dark matter only simulations. In this thesis, we will discuss two tensions, the missing satellite problem and the central density problem. However, we refer the interested reader to Sales et al. (2022) for a comprehensive review of the current state of ΛCDM tensions.

Missing Satellite Problem

The first simulations of Milky Way–like halos produced hundreds of subhalos which was in stark contrast to the (then observed) ~ 10 satellites around the Milky Way; this tension became known as the missing satellite problem (MSP, Moore et al., 1999; Klypin et al., 1999. Since the advent of the MSP, simulation resolution has improved, increasing the number of expected satellites to the order of thousands (e.g. Springel et al., 2008). This discrepancy would still present a significant tension even when accounting for the current satellite population consensus (Milky Way: ~ 60, M31: ~ 35).

With dwarfs being discovered at a rapid rate and with dedicated surveys pushing deeper magnitude limits uncovering fainter systems, a natural solution appeared to present itself; perhaps we simply had not found all of the Milky and M31 dwarfs.

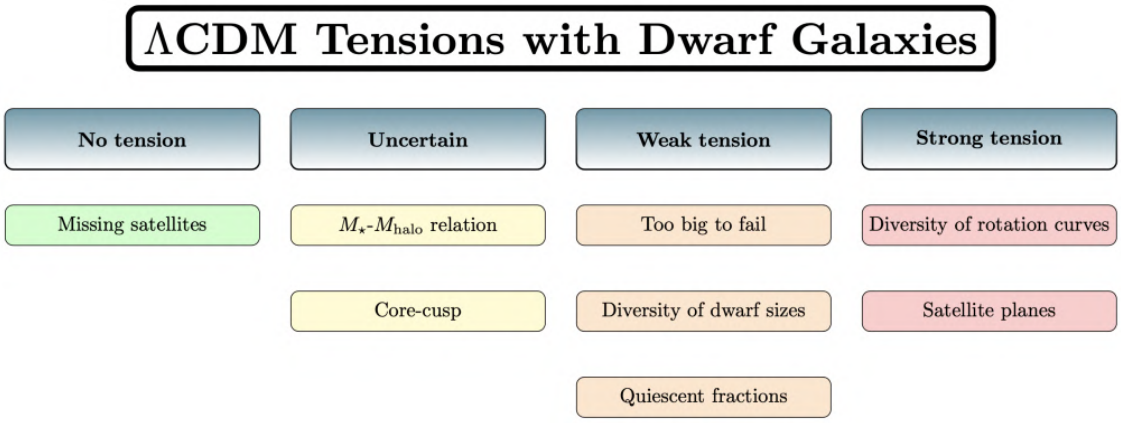

Figure 1.6: A summary of the current tensions between ΛCDM predictions and Local Group dwarf galaxy observations. The severity of the tension is indicated by the colour and position, moving from no tension (green, left) to strong tension (red, right). In this thesis, I primarily focus on the missing satellites, core–cusp and diversity of rotation curves problems. *Image Credit: Sales et al. (2022)*

A number of studies investigated the Local Group satellite population applying a combination of halo occupancy fractions and completeness corrections found that the number of expected subhalos came in line with simulations (e.g. Tollerud et al., 2008; Hargis et al., 2014; Kim et al., 2018; Newton et al., 2018). Furthermore, internal and external feedback processes (discussed in § 1.3.2) have been shown to affect the formation and growth of dwarf galaxies in dark matter subhalos (e.g. Bullock et al., 2000; Benson et al., 2003; Brown et al., 2014; Wheeler et al., 2014; Shen et al., 2014; Wetzel et al., 2016; Sawala et al., 2016; Read et al., 2016, 2018; Simpson et al., 2018; Buck et al., 2019; Garrison-Kimmel et al., 2019; Engler et al., 2021; Munshi et al., 2021). Results from studies considering the effects of completeness corrections and feedback provide the evidence to conclude there is no MSP for the Milky Way and M31.

While the MSP is considered solved for the Milky Way and M31, M33 still presents a potential dearth of satellites, providing another interesting test case for MSP solutions. Cosmological simulations predict that M33 should have ~ 10 satellites with a luminosity of $L > 10^4$ $L_\odot$ (Dooley et al., 2017; Patel et al., 2018b). Yet, to date M33 has only two (potential) satellites, And XXII (Martin et al., 2009; Chapman et al., 2013) and Pisces VII (Collins et al., 2022a, 2023), as illustrated in Figure 1.7. Completeness corrections may also be able to explain the potential MSP in M33. Firstly, the PAndAS survey only probed a region of radius 50 kpc around M33, which accounts for only a third of its virial radius (Patel et al., 2018a). Secondly, the survey was only able to detect dwarfs down to a limiting luminosity of $L \gtrsim 2 \times 10^4$ $L_\odot$ (Doliva-Dolinsky et al., 2022, 2023). Considering the UFD nature of And XXII ($L = 3.1 \times 10^4$ $L_\odot$ Savino et al., 2022) and Pisces VII ($L = 1.6 \times 10^4$ $L_\odot$ Collins et al., 2023) it is likely that M33 has a rich satellite population waiting to be discovered by future surveys that cover a wider footprint and are able to probe fainter luminosities. However, if future surveys fail to identify these dwarfs, this would reopen an interesting discussion around the MSP and the history of M33.

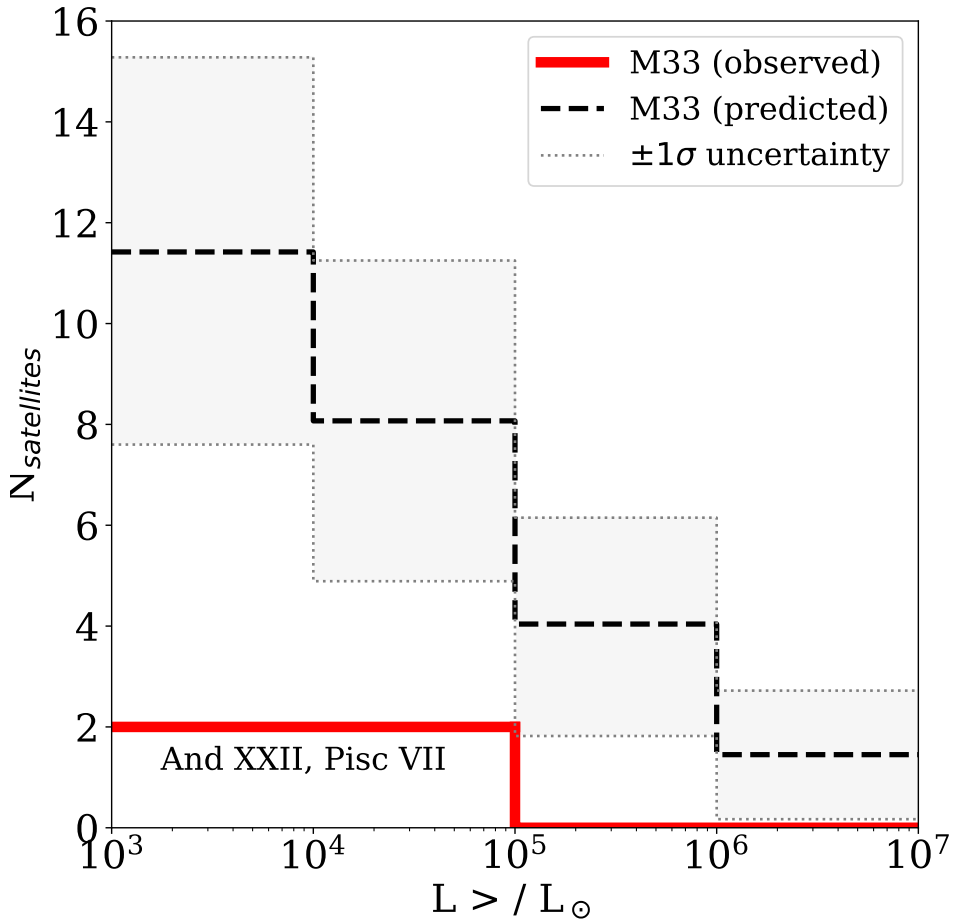

Figure 1.7: Luminosity function for M33. The number of predicted satellites (obtained from Patel et al., 2018b) is shown by the black dashed line, the light grey shaded region is the corresponding 1σ uncertainty. And XXII and Pisces VII, the two (possible) known M33 satellites are shown by the red line. There is a clear dearth of satellites at all luminosities but especially at the lower end.

Central Density Problems

Another small–scale challenge relates to the distribution of dark matter within the inner regions of dwarf galaxies. The radial dark matter density profile of dwarf galaxies can be described by the functional form $\rho(r)_{\rm DM} \propto r^{-\gamma}$, where γ controls the gradient of the inner slope. ΛCDM predicts that the radial profile of dark matter subhalos should follow a universal cuspy profile, known as a Navarro–Frenk–White (NFW) profile (Dubinski & Carlberg, 1991; Navarro et al., 1996b, 1997; Moore et al., 1999). The NFW profile is characterised by a high central density that steeply decreases with increasing radius ($\gamma = 1$), such that $\rho(r)_{\rm DM} \propto r^{-1}$. Many of the Local Group dwarf galaxies fall into this cuspy regime (e.g. Read et al., 2018, 2019; Zoutendijk et al., 2021). However, a significant (and growing) number of dwarfs have instead been observed to have cored dark matter density profiles (e.g. Flores & Primack, 1994; Moore, 1994; de Blok et al., 2001; de Blok, 2010; Marchesini et al.,

2002; Simon et al., 2005; Battaglia et al., 2008; Walker et al., 2010; Kuzio de Naray & Kaufmann, 2011; Agnello & Evans, 2012; Amorisco & Evans, 2012; Newman et al., 2013; Read et al., 2017, 2019; Relatores et al., 2019; Collins et al., 2021; Charles et al., 2023). Cored profiles are characterised by a (typically) lower central density that remains approximately constant in the centre, shallowly decreasing with radius ($\gamma = 0$), such that $\rho(r)_{\rm DM} \sim$ constant. This became known as the cusp–core problem.

While measuring the slope of the central density is trivial in simulations it is substantially more difficult observational. Cores have been observed in the rotation curves of gas–rich dIrrs (e.g. Flores & Primack, 1994; Moore, 1994; McGaugh et al., 2001; Marchesini et al., 2002; Simon et al., 2005; de Blok et al., 2008; de Blok, 2010; Kuzio de Naray et al., 2008; Read et al., 2017; Iorio et al., 2017). However, precisely confining the inner slope in dSphs is often harder due to their lack of gas. Typically, the dark matter content of dSphs is derived from the velocity dispersion profile of the stellar contribution, see § 1.3.3. Instead, due to the difficulty constraining the inner slope, the cusp–core problem is often reframed as a central density problem; CDM predicts the inner regions of some dwarfs should contain more dark matter than inferred from observations (Oman et al., 2015; Weinberg et al., 2015; Read et al., 2018). When approached from this slightly alternative angle, the focus is on measuring the central density rather than defining the central slope of the radial dark matter density profile.

1.3.2 Proposed Solutions to the Central Density Problems

Internal and External Feedback Mechanisms

The central density problem originated from comparing dark matter only simulations to observations. These simulations ignored the effects of the baryonic matter inside dwarf galaxies (stars and gas), only considering structure formation driven by the gravitational force of the dark matter component (e.g. White, 1976; Davis et al., 1985; Moore et al., 1999). Dwarf galaxies are dark matter dominated, with the dark matter component contributing tens to thousands of times more mass than the baryonic matter. Hence this assumption was a suitable compromise, especially as dark matter only simulations are much more computationally simple. Baryonic feedback processes were proposed as a potential solution to the central density challenges by providing a formation channel for the cores observed in dwarf galaxies (e.g. Navarro et al., 1996a; Read & Gilmore, 2005; Mashchenko et al., 2008; Pontzen & Governato, 2012; Zolotov et al., 2012; Pontzen & Governato, 2014; Brooks & Zolotov, 2014; Madau et al., 2014; Chan et al., 2015; Oñorbe et al., 2015; Wetzel et al., 2016; Tollet et al., 2016; Read et al., 2016, 2019). However, it was not until recently, with advancements in simulation techniques and computing technology, that we were able we were able to put the missing baryonic physics into these simulations to test these scenarios (e.g. Bullock et al., 2000; Benson et al., 2003; Brown et al., 2014; Wheeler et al., 2014; Shen et al., 2014; Wetzel et al., 2016; Sawala et al., 2016; Read et al., 2016, 2018; Simpson et al., 2018; Buck et al., 2019; Garrison-Kimmel et al., 2019; Engler et al., 2021; Munshi et al., 2021).

Fluctuations in the gravitational potential in the centre of dark matter halos

can cause the dark matter to migrate from the centre of the subhalo towards the outskirts in a process known as dark matter heating (Navarro et al., 1996a; Read & Gilmore, 2005; Pontzen & Governato, 2012; Oñorbe et al., 2015; Read et al., 2016). The baryonic matter (stars) inside dwarf galaxies are potential sources of these gravitational fluctuations. Supernovae and stellar feedback produce gas outflow, rapidly redistributing mass within the halo. Over time, cooling allows the gas to inflow, again redistributing the mass. This shifting of mass within the halo results in variability in the gravitational potential. The effect has been shown to be small for individual feedback events (Gnedin & Zhao, 2002). However, Read & Gilmore (2005) show that cores can be formed if this dark matter heating effect occurs over multiple bursts of star formation. The level of coring due to baryonic feedback seen in the simulations was specific to the stellar prescription implemented, but the general consensus shows that dark matter heating is most effective in dwarfs with a moderate stellar component $M_* > \times 10^6$ $M_\odot$ (Zolotov et al., 2012; Di Cintio et al., 2014; Madau et al., 2014; Brooks & Zolotov, 2014; Chan et al., 2015) and extended star formation (Read & Gilmore, 2005; Read et al., 2016).

A range of environmental effects can also alter the shape of the inner slope of the dark matter density profile of dwarf galaxies (e.g. Mayer et al., 2001; Johnston et al., 2002; Hayashi et al., 2003; Kravtsov et al., 2004; D'Onghia et al., 2009; Peñarrubia et al., 2008, 2009, 2010; Kazantzidis et al., 2011; Tomozeiu et al., 2016; Frings et al., 2017; Garrison-Kimmel et al., 2017; Fattahi et al., 2018; van den Bosch & Ogiya, 2018; Errani et al., 2018; Errani & Peñarrubia, 2020; Errani & Navarro, 2021). Satellites within the virial radius of their host can undergo host–satellite interactions. For example, tidal stripping is the process of mass loss due to the gravitational influence of the host, causing matter within the satellite to become unbound. Furthermore, dwarfs can experience ram pressure stripping. Ram pressuring stripping is strongest on highly elliptical orbits, although the process can still occur for circular orbits. The eccentricity of the orbit causes the dwarf to rapidly move in and out of the host halo. This causes fluctuations in the gravitational potential of the subhalo, dynamically heating the dark matter and redistributing the dark matter away from the centre of the dwarf, thus decreasing the central density. The stellar component is deeply embedded inside the dark matter subhalo and both tidal mechanisms are most effective from at extreme edges of the subhalo working inwards (Peñarrubia et al., 2008, 2010). As such, the dark matter is preferentially removed, with the stellar component only affected after significant tidal interactions. Furthermore, dwarfs with cusped dark matter profiles are very effective at protecting the inner dark matter distribution. For the central density to demonstrate cusp-core transformations extreme tidal mass loss is required (Peñarrubia et al., 2008, 2010; Fattahi et al., 2018; van den Bosch & Ogiya, 2018; Errani et al., 2018; Errani & Peñarrubia, 2020; Errani & Navarro, 2021).

Alternatives to ΛCDM

Alternative dark matter models exist beyond CDM. The models alter the mass and/or collisionality of the dark matter particle. It is possible that these alternative models may provide solutions to some of the small–scale challenges. In this thesis, I focus on warm dark matter (WDM) and self–interacting dark matter (SIDM) as two

alternate dark matter models, which I briefly introduce below. However, there are many more models proposed in the literature, and we refer the interested reader to these reviews for an in–depth discussion on dark matter models (Peter, 2012; Feng, 2010; Buckley & Peter, 2018; Arbey & Mahmoudi, 2021).

WDM (Bond et al., 1982; Bardeen et al., 1986; Bode et al., 2001) particles have a higher relative velocity and lower masses than CDM because the particles were still relativistic when they decoupled from normal matter. Due to the higher velocities, WDM can escape overdense regions which are smaller than the 'free–streaming' length. For WDM particles with masses $\mathcal{O}(1)$ keV, the free–streaming length is comparable to galactic scales. On large scales ($>$ 10 Mpc), WDM is virtually indistinguishable from CDM, however, below the free-streaming length, the subhalo mass function is greatly reduced, resulting in the suppression of small-scale structure formation. WDM has been proposed as a potential solution to the central density problem as the resulting halos on dwarf galaxy scales appear fluffier, less cuspy and significantly less dense than CDM halos (e.g. Hogan & Dalcanton, 2000; Bode et al., 2001; Avila-Reese et al., 2001; Wang & White, 2007; Schneider et al., 2012; Lovell et al., 2014, 2017).

SIDM (Spergel & Steinhardt, 2000) introduces an additional force which allows the dark matter particles to undergo interactions with one another, in contrast to CDM where the only relevant dark matter interaction is gravitational. These 'self–interactions' allow for the exchange of energy between dark matter particles. The rate of interaction is governed by a cross–section $\sigma_{\rm m}$. In the early Universe, there is negligible difference between CDM and SIDM halo densities as the low density means that the probability of a collision between particles is low. However, as the halos coalesce more matter and thus grow in density, the probability of collisions increases in the highly–dense central regions. Over time, an equilibrium will be reached between the gravitational acquisition of more matter and the energy transfer of self–interactions forming a large central core in the dark matter density profile, thus providing a potential solution to the central density problem (e.g. Vogelsberger et al., 2012; Walker & Peñarrubia, 2011; Rocha et al., 2013; Fry et al., 2015; Elbert et al., 2015; Kaplinghat et al., 2016; Robles et al., 2017; Schneider et al., 2017; Sameie et al., 2021).

Both CDM and these alternative dark matter models invoke the same need for an exotic, currently undetected form of matter. However, there is an alternative theory that does not require a new 'dark' type of matter, instead altering the behaviour of gravity on galactic scales, known as Modified Newtonian Gravity (MOND, Milgrom, 1983a,b,c). This model states that at large accelerations, gravity acts as prescribed by Newtonian dynamics with the gravitational force inversely proportional to the square of the radial distance, but at smaller accelerations, the laws of gravity increasingly deviate from Newtonian dynamics, instead becoming inversely proportional with radial distance. MOND was initially proposed as a solution to the flat rotation curves observed, and indeed it has been shown that it can explain a variety of rotation curves (e.g. Begeman et al., 1991; Sanders, 1996; Sanders & Verheijen, 1998; Sanders & Noordermeer, 2007; McGaugh et al., 2016). Furthermore, MOND could possibly explain a handful of the small–scale tensions for CDM (e.g. McGaugh, 2012; Kroupa et al., 2012; Famaey & McGaugh, 2012; McGaugh et al.,

2016). However, it fails to explain many other observations that point to the existence of dark matter (e.g. Aguirre et al., 2001; Clowe et al., 2004, 2006; Natarajan & Zhao, 2008; Dodelson, 2011; Safarzadeh & Loeb, 2021). For this reason, we have not considered MOND for further study in this thesis.

1.3.3 Measuring the Dark Matter Inside Dwarf Galaxies

The small–scale challenges still present a significant area of study. Simulations are beginning to provide possible solutions to the central density problems, but it is imperative that these solutions can be observed and tested in real–world systems. Dwarf galaxies are the perfect systems to test proposed solutions to these. We are fortunate to have so many dwarf galaxy dark matter laboratories on our galactic doorstep, but how do we go about measuring the invisible dark matter inside dwarf galaxies?

With the mass–to–light ratio of the dwarf, we can begin to understand the dark matter content of the dwarf. Is it dark matter dominated or not? However, to test proposed solutions to the small–scale challenges, such as dark matter heating, we need to know the distribution of the dark matter inside the dwarf. For dIrrs with a significant gas content, this can be achieved relatively easily with gas rotation curves. However, for dSphs, we must instead turn to the stars to trace the dark matter in a process known as dynamical mass modelling.

Dynamical Mass Modelling

The history of dynamical mass modelling goes back to work by Eddington (1915a,b) modelling star clusters and the seminal model of the Milky Way (Kapteyn, 1922). Subsequently, mass modelling techniques have been applied to a range of different scenarios (e.g. Zwicky, 1937; Meylan, 1987; Kleyna et al., 2001; Łokas & Mamon, 2003; Watkins et al., 2013; Read et al., 2018; Gregory et al., 2019; Collins et al., 2021; Charles et al., 2023). In this thesis, I use the mass modelling tool `GravSphere` (Read et al., 2017, 2018; Genina et al., 2020b; Collins et al., 2021) to derive the dark matter mass and density profiles of M31 dwarfs. Below, I briefly outline the underpinning physics, but for a more detailed discussion of the specifics of `GravSphere`, I refer the reader to Read et al. (2017); Genina et al. (2020b); Collins et al. (2021) and for detailed derivations of the physics discussed Binney & Tremaine (2008); Binney (1980); Binney & Mamon (1982).

The stars of dwarf galaxies can be considered collisionless tracers of the matter inside the dwarf. As such, they can be assumed to follow the collisionless Boltzmann equation (CBE). Given the positions and velocities of the stars in the system, it is possible to solve the CBE to determine the mass distribution. However, solving the CBE in practice for dwarf galaxies is often difficult. To combat this, `GravSphere` integrates the CBE equation over each velocity component, creating a set of three velocity moment equations, an approach first suggested by Jeans (1922) known as the Jeans equations. Following the assumption that dwarf galaxies are non–rotating spherical systems, only the radial velocity component is relevant, arriving at the Spherical Jean equations (Binney, 1980). Furthermore, for M31 dwarfs, we are only

able to measure the line–of–sight velocity dispersion, meaning the Spherical Jeans equations are projected along the line of sight (Binney & Mamon, 1982).

One important advantage of this method is that the required data inputs are simply a velocity dispersion profile and a surface brightness profile, both of which are easily observationally obtained for the M31 dwarfs. Furthermore, the Jeans equations are not computationally expensive and thus can be solved relatively rapidly. However, there is a well–known and significant disadvantage to this method, known as the mass–velocity anisotropy degeneracy (e.g. Merrifield & Kent, 1990; Wilkinson et al., 2002; Łokas & Mamon, 2003; de Lorenzi et al., 2009). Proper motions can be used to measure the velocity anisotropy and have been proposed as a possible method to break this degeneracy (e.g. Strigari et al., 2007; van der Marel & Anderson, 2010; Watkins et al., 2013); however, proper motions are not available for M31 dwarfs. Instead, `GravSphere` uses fourth-order moments of the velocity known as virial shape parameters (VSPs) (Merrifield & Kent, 1990; Richardson & Fairbairn, 2014). The VSPs produce two scalar quantities that rely only on the velocity anisotropy, allowing constraints to be placed on this property, thus breaking the mass–velocity anisotropy degeneracy.

Armed with only the line of sight velocities obtained from spectroscopic measurements and the light profile obtained from photometry, `GravSphere` is able to produce dark matter mass and density profiles for dwarf galaxies, even for the relatively small kinematic sample sizes present for M31 dwarfs.

1.4 Thesis Overview

Dark matter is thought to be the dominant source of matter in the Universe, and yet we still know little about its nature. Dwarf galaxies are dark matter dominated systems that are perfect for testing our understanding of dark matter. A number of potential solutions have been proposed to solve a number of the small–scale challenges faced by dark matter. Simulations have shown many of these solutions work theoretically, and now they need to be tested on observations of dwarf galaxies. In this thesis, the primary focus is on investigating the dark matter content of the dSph satellite population of M31 to better understand ΛCDM and dark matter. Alongside this work, I was also part of a collaboration seeking to discover more dwarf galaxies in the M31/M33 system, adding the dwarf galaxy consensus and providing more test beds for dark matter physics.

In Chapter 2, I perform the kinematic analysis of Andromeda XXV, a dSph satellite of M31 which was previously identified as a dwarf with little–to–know dark matter. I extend this analysis to include dynamical mass modelling to derive the dark matter density profile, allowing us to gain a better insight into the dark matter content of this unusual dwarf.

In Chapter 3, I investigate the unusually low central dark matter densities of two M31 satellites, Andromeda XXV, found in Chapter 2, as well as Andromeda XXI identified in a previous study. We investigate the effects of dark matter heating, tidal stripping and unusual halo concentrations in a range of cosmologies in an attempt to reconcile the low central densities of both dwarfs.

In Chapter 4, I present work detailing the discovery of two UFD dwarf galaxies in the M31/M33 system, Pisces VII and Pegasus V. We discuss the unusual features of these UFDs and their potential impacts on our understanding of dark matter and galaxy formation.

Finally, in Chapter 5, I present a short summary of the work covered in this thesis and outline future prospects for this research.

Andromeda XXV – a dwarf galaxy with a low central dark matter density

Manuscripts

The work presented in this chapter is taken from the following manuscript accepted for publication in the Monthly Notices of the Royal Astronomical Society:

- Andromeda XXV – a dwarf galaxy with a low central dark matter density – Charles et al. (2023) *First author*

Statement of contribution

I led the analysis for this work with the following coauthor contributions. Michael Rich was the PI for the initial kinematic observations taken in 2010 used in this study. Michelle Collins was PI for the follow–up kinematic observations obtained in 2018, with Eduardo Balbinot visiting the observatory at Keck to support with this observing run. Rodrigo Ibata designed the pipeline and performed the reduction of the kinematic data, discussed in §2.2.1. Nicolas Martin was the PI for the LBT photometry, mentioned in §2.2.2. Finally, Justin Read designed the `GravSphere` code described in §2.6.

I also led the writing of the manuscript. However, I received feedback predominately from my supervisory team (Michelle Collins and Justin Read), but also the wider coauthor list and anonymous reviewer, which helped significantly improve the quality of the manuscript.

Summary

Andromeda (And) XXV has previously been reported as a dwarf spheroidal galaxy (dSph) with little–to–no dark matter. However, the uncertainties on this result were significant. In this study, we nearly double the number of member stars and re–derive the kinematics and mass of And XXV. We find that And XXV has a systemic velocity of $\nu_{\rm r} = -107.7 \pm 1.0$ kms^{-1} and a velocity dispersion of $\sigma_{\nu} = 3.7^{+1.2}_{-1.1}$ kms^{-1}. With this updated velocity dispersion and a new literature measurement of the radial surface brightness profile, we derive a mass contained within the half–light radius of M(r$<$ r$_{\rm h}$) $= 4.7^{+3.0}_{-2.9} \times 10^6$ M$_{\odot}$. This mass corresponds to a mass–to–light ratio of $[M/L]_{\rm r_h} = 25^{+17}_{-16}$ M$_{\odot}$/L$_{\odot}$, demonstrating that And XXV is most–likely dark

matter dominated. We also measure the metallicity of And XXV to be [Fe/H] = -1.9 ± 0.1 dex, which is in agreement with previous results. Finally, we extend the analysis of And XXV to include mass modelling using `GravSphere`. We find that And XXV has a low central dark matter density, $\rho_{\rm DM}(150 \text{ pc}) = 2.3^{+1.4}_{-1.1} \times 10^7$ $M_\odot$ kpc^{-3}, which makes And XXV a clear outlier when compared to other Local Group dSphs of the similar stellar mass. In a companion paper, we will explore whether some combination of dark matter cusp–core transformations and/or tides can explain And XXV's low density.

2.1 Introduction

Dwarf galaxies are typically dark matter dominated systems, with mass–to–light ratios in the range 10–1000s, making them ideal systems for testing dark matter physics and cosmology (e.g. Mateo, 1998; Tolstoy et al., 2009; Simon, 2019). The most successful cosmological model to date is Lambda Cold Dark Matter (ΛCDM), which explains the cosmic microwave background radiation (e.g. Peebles, 1982; Komatsu et al., 2009; Aubourg et al., 2015; Planck Collaboration et al., 2016, 2020), nucleosynthesis (e.g. Walker et al., 1991; Smith et al., 1993; Burles et al., 1999; Cyburt, 2004; Steigman, 2007; Fields, 2011) and structure formation on large scales (e.g. Bond et al., 1996; Springel et al., 2005; Gao et al., 2005a,b; Tegmark et al., 2006; Springel et al., 2006), albeit by invoking three mysterious components – dark matter, dark energy and inflation (Planck Collaboration et al., 2016, 2020). However, on galactic scales, particularly dwarf galaxies, there have been a number of long–standing tensions between ΛCDM predictions and observations (e.g. Bullock & Boylan-Kolchin, 2017; Buckley & Peter, 2018; Sales et al., 2022). One such tension is the so–called 'cusp–core' problem (Moore, 1994; Flores & Primack, 1994; de Blok, 2010; Navarro et al., 2010; Walker & Peñarrubia, 2011; Read et al., 2017; Genina et al., 2018; Read et al., 2019), which arises when comparing the dark matter density profiles of dwarf galaxies from dark matter only simulations in a ΛCDM cosmology to observations of dwarf galaxies. ΛCDM predicts that the dark matter inside dwarf galaxies should follow a universal 'cusped' profile that has a highly dense centre that steeply decreases with radius, such that $\rho_{\rm DM} \propto r^{-1}$ (Dubinski & Carlberg, 1991; Navarro et al., 1996b, 1997; Moore et al., 1999). Instead, a growing number of dwarfs have been observed with 'cored' dark matter profiles described by a shallow central density that remains roughly constant in the centre, such that $\rho_{\rm DM} \sim$ constant (Flores & Primack, 1994; Moore, 1994; de Blok et al., 2001; de Blok, 2010; Marchesini et al., 2002; Simon et al., 2005; Battaglia et al., 2008; Walker et al., 2010; Agnello & Evans, 2012; Amorisco & Evans, 2012; Newman et al., 2013; Read et al., 2017, 2019).

For many of the cored dwarfs observed, a plausible solution to the cusp–core problem within the ΛCDM paradigm is dark matter heating. This is the process of sudden gas removal due to stellar winds, dynamical friction or supernovae feedback which results in gravitational fluctuations, causing the dark matter halo to expand. When this process is repeated across many cycles of star formation the dark matter halo expands irreversibly, reducing the central dark matter density and flattening the cusped profile into a core over time (Navarro et al., 1996a; Gnedin & Zhao, 2002; Read & Gilmore, 2005; Mashchenko et al., 2008; Pontzen & Governato, 2012; Zolotov et al., 2012; Brooks & Zolotov, 2014; Oñorbe et al., 2015; Tollet et al., 2016; Read et al., 2016, 2019). However, dark matter heating is only proposed to be effective in galaxies with extended star formation (Read et al., 2016, 2019) that are above a stellar–mass–to–halo–mass ratio threshold of $M_*/M_{200} \sim 5 \times 10^{-4}$ (Di Cintio et al., 2014, but see Orkney et al. (2021)).

Puzzlingly, there is a subset of dwarfs within the low surface brightness population of the Local Group (LG) with M_*/M_{200} below this threshold with unusually low central densities that are unlikely to be explained by dark matter heating alone.

Around the Milky Way (MW) two such dwarfs have been found, Crater II (Torrealba et al., 2016) and Antlia II (Torrealba et al., 2019). Similarly around Andromeda (M31) two more have been observed, Andromeda XIX (McConnachie et al., 2008; Collins et al., 2020) and Andromeda XXI (Martin et al., 2009; Collins et al., 2021). These systems have a diffuse nature, described by a large half–light radius and very low surface brightness. Furthermore, the mass contained within the half–light radius for these systems, determined from velocity dispersions measurements, are less massive than other galaxies with similar size and brightness (Caldwell et al., 2017; Fu et al., 2019; Torrealba et al., 2019; Collins et al., 2020, 2021), meaning that it is likely that these systems reside in low mass and low density dark matter halos. While detailed star formation histories for these systems are not currently available to completely rule out dark matter heating as the cause, even under the (unlikely) assumption of highly efficient dark matter heating, their low densities cannot be reproduced (Torrealba et al., 2019; Collins et al., 2021). Instead, tidal interactions with the host (MW or M31) are the suspected culprit causing the low density dark matter halos of these systems (Torrealba et al., 2019; Fu et al., 2019; Collins et al., 2021).

In this paper, we investigate another potential outlier, Andromeda (And) XXV, a dSph satellite galaxy of M31 first discovered as part of the Pan–Andromeda Archaeological Survey (Richardson et al., 2011). And XXV was previously identified as a potential outlier within the LG in a 2013 study (Collins et al. (2013), hereafter known as C13) that performed a kinematic analysis of numerous M31 dSph satellites. And XXV was found to have a low velocity dispersion, $\sigma_{\rm v}$=3.0$^{+1.2}_{-1.0}$ kms^{-1}, which results in a mass-to-light ratio of $[{\rm M/L}]_{\rm r_h}$=10.3$^{+7.0}_{-6.7}$ ${\rm M}_{\odot}/{\rm L}_{\odot}$. This is consistent with a dark matter dominated sytstem. However, due to the small number of member stars (26) with stellar kinematics in their sample, the uncertianity on this value is significant. As such, within the uncertainties the presence of dark matter is not required and And XXV could be described by a simple stellar system with no appreciable dark matter component. C13 point out, more stellar velocities are needed to confirm or rule out the presence of dark matter in this system. We present a revised kinematic analysis, using the spectroscopic data set outlined in C13 combined with new observations to provide a larger sample size, nearly double that used in C13, allowing us to critically reassess if And XXV really is a dSph with no appreciable dark matter. We will also extend the analysis to investigate the metallicity of And XXV. Finally, we use the dynamical mass modelling tool `BINULATOR + GravSphere` (Read & Steger, 2017; Read et al., 2018, 2019; Gregory et al., 2019; Genina et al., 2020b; Collins et al., 2021; Read et al., 2021), to gain an insight into the dark matter content of And XXV.

The outline of the paper is as follows: in §2.2 we detail the photometric and spectroscopic observations used in this study. We detail the contaminant removal procedure used to remove MW and M31 contaminant stars from our sample in §2.3 and discuss our kinematic analysis of And XXV in §2.4. In §2.5 we investigate the metallicity of And XXV. Next, we outline the dynamical mass modelling results for And XXV §2.6. In §2.7 we discuss our results and finally we conclude in §2.8.

2.2 Observations

2.2.1 DEIMOS Spectroscopy

The spectroscopic data for And XXV were obtained using the Deep Extragalactic Imaging Multi–Object Spectrograph (DEIMOS) Faber et al. (2003); Cooper et al. (2012) mounted on the Keck II telescope. The observations are comprised of two masks. The first was taken in September 2010 (previously presented in C13), and the second mask was observed on 18th August 2018. The instrumental setup was the same for both masks, using a 1200 line mm^{-1} grating with a resolution of 1.3 Å. To determine the velocity and metallicity of each member star, we use the calcium triplet (Ca(II)) lines. The Ca(II) lines are present in the region around ∼8500 Å. As such our observations targeted the wavelength range of $\sim 5600 - 9800$ Å with a central wavelength of 7800 Å to resolve the Ca(II) lines. Each mask was split into 3×20 minute exposures, combining to give a total exposure time of 3600 seconds per mask. The average seeing was $\sim 0.8''$ for both masks, which resulted in an average signal–to–noise ratio (S/N) of ∼5 per pixel ($M_V < 21$: S/N∼16, $21 \leq M_V < 24$: S/N∼6, $M_V > 24$: S/N∼2).

The data were reduced using a custom pipeline, described in detail in Ibata et al. (2011) and C13. In short, the pipeline detects and removes cosmic rays, then corrects for scattered light, slit function, illumination and fringing. To account for pixel–to–pixel variations flat–fielding was performed. Next wavelength calibrations of each pixel were conducted using arc–lamp exposures. Then, the sky was subtracted from the 2-dimensional spectra. Finally, each spectrum was extracted (without resampling) from a small spatial region around each target. The velocities and corresponding uncertainties for all stars were derived using the strong Ca(II) triplet feature found in the spectra of the non–resampled data. A Markov Chain Monte Carlo (MCMC) routine fit a Gaussian to the three Ca(II) triplet lines and determined the offset of the line compared to the known rest–frame wavelengths. This shift was converted into a velocity. The final value for the velocity uncertainty comprises of the uncertainty from the MCMC posterior distribution combined with the uncertainty inherent to DEIMOS and the reduction pipeline which was taken to be 3.2 kms^{-1} (Collins et al., 2020). This is similar to the uncertainty of 3.4 kms^{-1} found in Martin et al. (2014) for the same type of targets. The results from each mask were combined into a single catalogue.

Misalignments of the slitmasks can cause velocity shifts of up to 15 kms^{-1}. We correct for these by comparing atmospheric models to the telluric absorption lines in the spectrum to shift the spectra to the correct frame as described in C13. To further confirm if any significant misalignment had occurred we check for a velocity error gradient across the mask. None were found in either mask. Finally, there were a few stars present both masks which were compared to ensure the velocity uncertainties were well measured.

2.2.2 LBT LBC Photometry

The photometric data for And XXV were obtained using the Large Binocular Cameras (LBC) mounted on the Large Binocular Telescope (LBT) in the $V_{\rm Bessell}$– and $i_{\rm SLOAN}$–bands. Observations were conducted on the nights of 28th October and 8th November, 2011 with a seeing that was ranging from 0.7" to 1.2". With its 4i say ChargeCCDs, the cameras both cover an area of about 23×25 arcmin^2. In total, 29 exposures of 360 s were taken with each filter, for a total exposure time of 2.9 h per band.

The raw photometry was reduced using the CASU pipeline where the images are debiased, flat-fielded, trimmed, and gain–corrected (Irwin & Lewis, 2001). The reduced photometric data was made into a catalogue. Each datum was then morphologically categorised to distinguish between stellar, non–stellar (e.g. background galaxies) or noise-like objects. Only stellar objects were considered for further analysis. Finally, the data were extinction corrected using the dust maps from Schlafly & Finkbeiner (2011), using $A_{\rm V} = 0.270$ mag and $A_{\rm i} = 0.171$ mag.

The photometric and spectroscopic observations were combined by cross-matching the on-sky position of each star within an allowed tolerance of ± 1 arcsecond.

2.3 Selecting members of Andromeda XXV

Before we can perform the kinematic analysis of And XXV we must identify the most probable members of And XXV and remove any contaminants from the MW or M31 halo. It is difficult to differentiate between member and contaminant stars using velocity information alone. This is especially true for foreground MW stars as the two systems have similar systemic velocities. Instead, to determine likely member stars, we use a 'triple–threat' probabilistic approach which was first outlined in Tollerud et al. (2012) and C13, then further developed in Collins et al. (2020, 2021) and Gregory et al. (2019). The method assigns each star a probability of membership using three probability criteria: (1) the star's position on the sky with relation to the centre of And XXV, $P_{\rm dist}$; (2) the star's position on a colour magnitude diagram (CMD) of And XXV, $P_{\rm CMD}$; and (3) the velocity of the star, $P_{\rm vel}$. We discuss each of these criteria in more detail below.

2.3.1 Distance Probability

$\rm P_{dist}$ is determined using radial surface brightness profile modelled as:

$$P_{\rm dist} = \exp\left[-\left(\frac{r^2}{2\eta_{\rm dist} {r_{\rm p}}^2}\right)\right] \tag{2.1}$$

where r is the radial distance of the star from the centre of And XXV (taken to be 0^h 30^m 9.9^s – RA, 46° $51'$ $41"$ – Dec Martin et al. (2016c)) and $\eta_{\rm dist}$ is a free parameter used to scale the exponential profile to the size of And XXV. $\eta_{\rm dist}$ was extensively tested for any potential biases or dependencies and a final value of $\eta_{\rm dist} = 2.5$ was

used. r_p used to modify the half–light radius, $r_{\rm h}$, to account for any ellipticity, described by:

$$r_{\rm p} = \frac{r_{\rm h}(1-\epsilon)}{1+\epsilon\cos(\theta)} \tag{2.2}$$

where $r_{\rm h} = 2.7$ arcmin (Martin et al., 2016c; Savino et al., 2022), ϵ is the ellipticity ($\epsilon = 0.03$) and θ is the stars angular position with respect to the dwarfs major axis ($\theta = -16^{\circ}$) (Martin et al., 2016c).

2.3.2 Colour Magnitude Diagram Probability

$\rm P_{CMD}$ is determined using the colour magnitude diagram of And XXV. A by–eye best–fit isochrone was overlaid onto the CMD to identify the stars most likely to be red giant branch (RGB) stars of And XXV. The isochrone used was an old, metal–poor isochrone ([Fe/H] $= -1.9$ dex, [α/Fe] $= 0.0$ dex, age $= 12$ Gyr) obtained from the `DARTMOUTH` stellar evolutionary models Dotter et al. (2008) shifted to the distance modulus of And XXV, $m - M = 24.38$ (Savino et al., 2022)). The CMD of And XXV and the by–eye best–fit isochrone are shown in the right panel of Figure. 2.1. The minimum distance in colour–magnitude space, $d_{\rm min}$, of each star to the isochrone was converted into a probability of membership using:

$$P_{\rm CMD} = \exp\left[-\left(\frac{{d_{\rm min}}^2}{2{\eta_{\rm CMD}}^2}\right)\right] \tag{2.3}$$

where $\eta_{\rm CMD}$ is another free parameter, this time used to account for the scatter of stars around the best–fit isochrone. Again, this free parameter was tested for any potential biases or dependencies and a final value of $\eta_{\rm CMD} = 0.2$ was chosen.

2.3.3 Velocity Probability

$\rm P_{vel}$ is determined by simultaneously fitting the velocities for all of the stars in the spectroscopic observations by assuming that these stars inhabit a profile of four dynamically distinct peaks. Four Gaussians are used to describe the different peaks which correspond to And XXV stars ($\rm P_{And\ XXV}$), then M31 halo contaminant stars ($\rm P_{M31}$) and two peaks for the MW contaminant stars ($\rm P_{MW1}$, $\rm P_{MW2}$). The MW velocity profile is often assumed to be a single distribution for contaminant removal purposes. However, due to the similarity in systemic velocity for And XXV and the MW, for our study, this assumption is not valid. Instead, we need to include this complexity in our model by modelling the MW as two velocity distributions (e.g. Gilbert et al., 2006). Each Gaussian is defined by a systemic velocity ($\nu_{\rm r}$) and a velocity dispersion (σ_ν), such that the probability of each star belonging to each peak ($\rm P_{And\ XXV}$, $\rm P_{M31}$, $\rm P_{MW1}$ and $\rm P_{MW2}$) is:

$$P_{\rm peak} = \frac{1}{\sqrt{2\pi}\sqrt{\sigma^2_{\nu_{\rm peak}} + {\nu_{\rm err,i}}^2}} \times \exp\left(-\frac{1}{2}\left[\frac{\nu_{\rm peak} - \nu_i}{\sqrt{\sigma_{\nu^2_{\rm peak}} + {\nu_{\rm err,i}}^2}}\right]^2\right) \tag{2.4}$$

Table 2.1: Prior values and results for the variables used in our `emcee` analysis for P_{vel}. [*] *Note: This is not the final systemic velocity and velocity dispersion value for And XXV – it is only used to determine* P_{vel}

Priors:		
Peak	ν_r (kms^{-1})	σ_ν (kms^{-1})
$P_{\text{And XXV}}$	$-130 < \nu_r < -90$	$0 < \sigma_\nu < 50$
P_{M31}	$-400 < \nu_r < -130$	$0 < \sigma_\nu < 200$
P_{MW1}	$-60 < \nu_r < 50$	$0 < \sigma_\nu < 100$
P_{MW2}	$-90 < \nu_r < -50$	$0 < \sigma_\nu < 100$
Results:		
Peak	ν_r (kms^{-1})	σ_ν (kms^{-1})
$P_{\text{And XXV}}$	$-107.6^{+1.5}_{-1.4}$	$5.1^{+2.3}_{-2.0}$ [*]
P_{M31}	$-272.2^{+50.8}_{-46.6}$	$132.1^{+30.7}_{-28.0}$
P_{MW1}	$-45.3^{+14.5}_{-9.2}$	$27.2^{+10.7}_{-9.3}$
P_{MW2}	$-71.1^{+7.8}_{-11.4}$	$38.6^{+15.5}_{-7.9}$

where ν_i and $\nu_{err,i}$ are the velocity and velocity uncertainty of a given star respectively. The overall log–likelihood function is therefore described by:

$$\log(\mathcal{L}) = \sum_{i=1}^{N} \log(\alpha P_{\text{And XXV}} + \beta P_{\text{M31}} + \gamma P_{\text{MW1}} + \delta P_{\text{MW2}}) \tag{2.5}$$

where α, β, γ and δ are constants describing the proportion of stars belonging to And XXV, M31, MW1 and MW2 respectively and are normalised, such that $\alpha + \beta + \gamma + \delta = 1$. The components of this likelihood function were found using `emcee`, a python MCMC package (Foreman-Mackey et al., 2013). The routine used 200 walkers, over 5000 iterations with a burn–in stage of 1550 and uniform flat priors were introduced for each parameter, see Table. 2.1 for a summary of the priors and results for the MCMC analysis.

It is important to note that, while the velocity and velocity dispersion values will likely resemble the final values, this is not the final kinematic result for And XXV. It is only used to determine P_{vel}. This is because it does not consider the impact of any potential M31 or MW contamination in the wings of the And XXV Gaussian, hence why the other two probability filters are important and the combination of all three filters is used to weight the likelihood function in the final kinematic analysis. The probability distribution described by the Gaussian for each peak can then be combined to give P_{vel}, using:

$$P_{vel} = \frac{P_{\text{AndXXV}}}{P_{\text{MW1}} + P_{\text{MW2}} + P_{\text{M31}} + P_{\text{AndXXV}}} \tag{2.6}$$

The final probability of membership to And XXV for each star is the product of

the three probability cuts, such that:

$$P_{\rm member} = P_{\rm dist} \times P_{\rm CMD} \times P_{\rm vel} \tag{2.7}$$

Stars with a probability of $P_{\rm member} > 0.10$ were considered member stars. The probability of membership cut–off is kept intentionally low as we use the velocity dispersion for the kinematic analysis. Hence, we do not want to artificially decrease the velocity dispersion by removing potential candidates with a probability cut that is too strict. Furthermore, all non–members have a probability of membership significantly below this cut–off point. A total of 49 members were identified (as shown in Fig. 2.1). This data contains nearly double the number of members compared to that used in C13.

2.4 Kinematic Analysis of Andromeda XXV

We used another `emcee` routine to determine the velocity (ν) and velocity dispersion (σ_ν) of And XXV. This time, the routine fits a single Gaussian for the 49 member stars, with the likelihood of each star weighted by the star's respective probability, such that the log-likelihood function is:

$$\log(\mathcal{L}) = \sum_{i=1}^{N} \log(P_{\rm member_i} P_{\rm AndXXV_i}) \tag{2.8}$$

The routine used 500 walkers over 5000 iterations with a burn–in stage of 3750. The values of ν and σ_ν for And XXV from the $P_{\rm vel}$ analysis were used as initial guesses and the same flat priors used for $P_{\rm vel}$ were implemented. The resulting posterior distribution can be seen in Fig. 2.2.

2.4.1 Kinematic Results

The velocity and velocity dispersion are well resolved, giving $\nu = -107.7 \pm 1.0$ km s^{-1} and $\sigma_\nu = 3.7^{+1.2}_{-1.1}$ km s^{-1}, the uncertainties are the 1σ uncertainty intervals from the posterior distributions. The properties derived for And XXV are listed in Table 2.2. The velocity and velocity dispersion are consistent with those derived in C13 ($\nu = -107.8 \pm 1.0$ km s^{-1}, $\sigma_\nu = 3.0^{+1.2}_{-1.0}$ km s^{-1}) although our velocity dispersion is slightly higher. This is likely due to the targeting of the C13 study. The first mask preferentially targeted stars close to the centre of And XXV. As seen in Fig. 2.1, the central stars are kinematically colder than those in the outskirts (velocity dispersion of $\sim$2.3 km s^{-1} in the centre vs $\sim$5.7 km s^{-1} on the outskirts). The outermost stars included in the new spectroscopic data set increase the average dispersion measured in this study. It is important to note that at the outskirts of And XXV we are more susceptible to contamination from non–member stars, especially due to the similarity in velocity between And XXV and the foreground MW stars. We extensively tested our membership selection, however, it is possible inclusion of contaminates could potentially contribute to the velocity flaring at larger radii. Furthermore, due to the

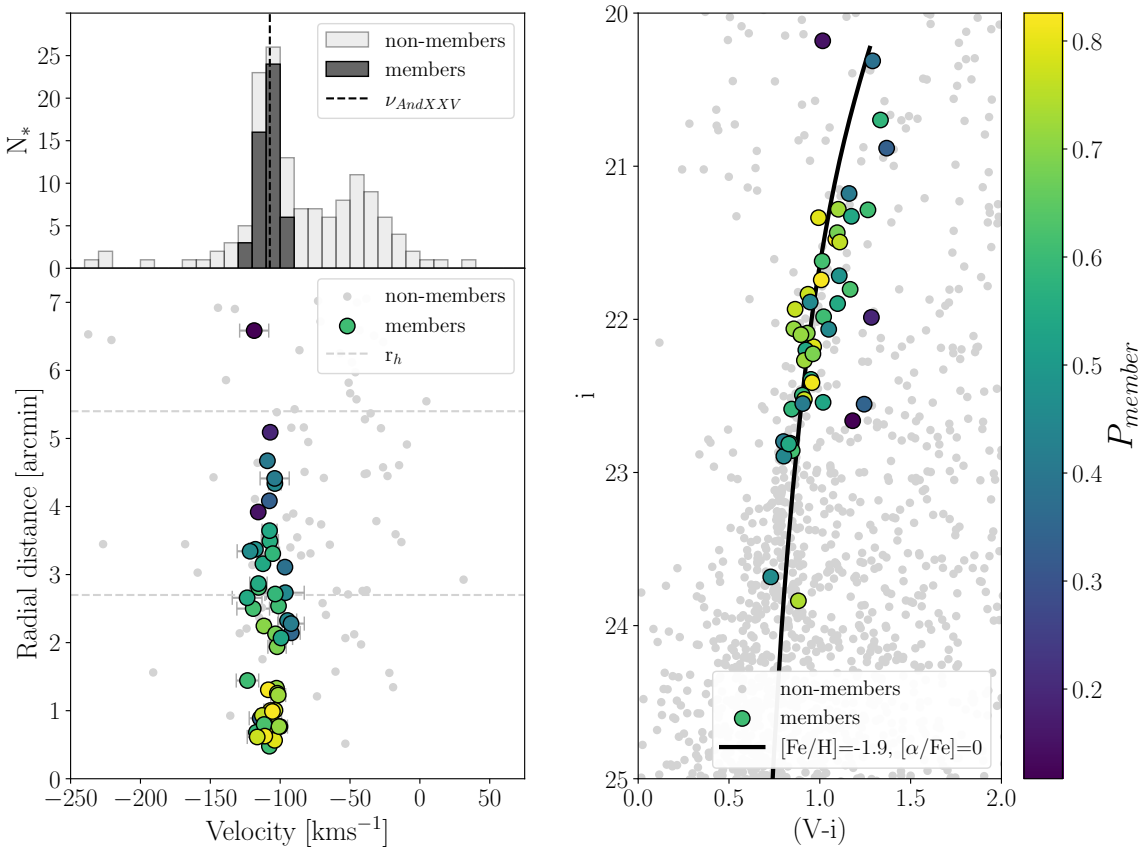

Figure 2.1: Left Top: The velocity histogram from And XXV. Light grey represents non-members likely contamination from foreground MW stars or M31 halo stars. Dark grey represents the 49 identified member stars of And XXV. The black dashed line represents the systemic velocity of And XXV determined in this study. **Left Bottom:** Radial distance from the centre of And XXV as a function of the line of sight velocity. The smaller light grey circles are the non–member stars from the spectroscopic data. The larger coloured circles are the member stars, colour–coded by the probability of membership (see colour bar on the right) and the error bars are the 1σ uncertainties. The horizontal grey dashed lines represent $1\times$ and $2\times$ r_h from the bottom up respectively. **Right:** The colour magnitude diagram for And XXV. Again the smaller light grey circles are non–member stars within $1.5\times$ r_h and the larger coloured circles are the member stars colour–coded by the probability of membership. The black solid line is a by–eye best–fit isochrone ([Fe/H] $= -1.9$ dex, [α/Fe] $= 0.0$ dex, age $= 12$ Gyr) for And XXV taken from the `DARTMOUTH` stellar evolutionary models Dotter et al. (2008) and shifted to the distance modulus of And XXV, $m - M = 24.38$ (Savino et al., 2022)).

size of the uncertainties on the two bins, likely arising from small number statistics, the velocity flaring observed is statistically insignificant within 1σ.

Using the now better constrained velocity dispersion, we can measure the mass, $M(\mathrm{r} < \mathrm{r_h})$, and mass–to–light ratio, $[M/L]_{\mathrm{r_h}}$, contained within the half–light radius of And XXV. Assuming a flat velocity dispersion profile, $M(r < r_\mathrm{h})$ can be calculated using Walker et al. (2009):

$$M(r < r_\mathrm{h}) = 580\, r_\mathrm{h}\, \sigma_\nu^2 \tag{2.9}$$

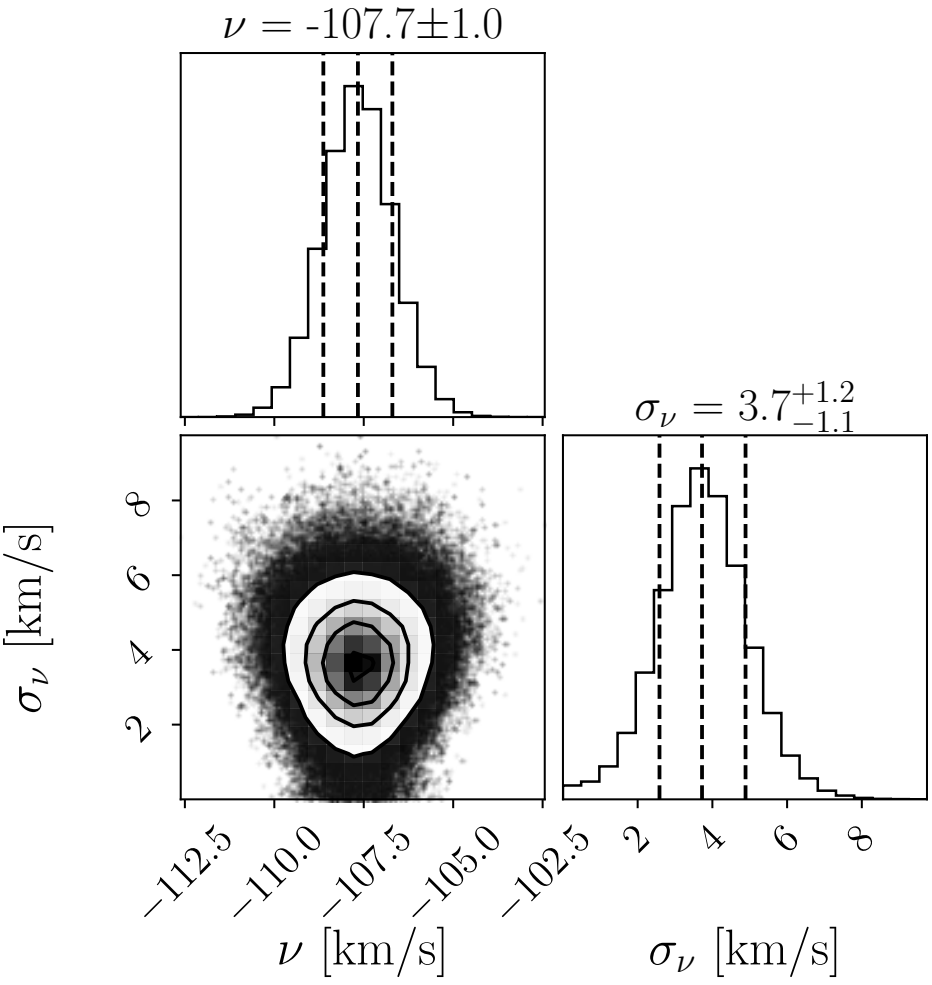

Figure 2.2: A corner plot showing the results of our kinematic analysis using `EMCEE`. The velocity and velocity dispersion are well resolved, giving $\nu_r = -107.7 \pm 1.0$ km s^{-1} and $\sigma_\nu = 3.7^{+1.2}_{-1.1}$ kms^{-1}

The mass of And XXV was determined to be $M(r < r_{\rm h}) = 4.7^{+3.0}_{-2.9} \times 10^6$ M$_\odot$, which is in agreement with the C13 study within the 1σ uncertainties. Using the updated absolute magnitude value of And XXV, $M_{\rm V} = -9.1$ (Savino et al., 2022), which is equal to a luminosity of $L = 3.7^{+1.4}_{-0.5} \times 10^5$ L$_\odot$, the mass–to–light ratio contained within the half–light radius is $[M/L]_{\rm r_h} = 25^{+17}_{-16}$ M$_\odot$/L$_\odot$. The mass–to–light ratio agrees with the value from C13 within the 1σ uncertainties and demonstrates that And XXV is dark matter dominated. Although, assuming Gaussian uncertainties, And XXV is still consistent with a simple stellar system of $[M/L]_{\rm r_h} < 5$ with $\sim 1.25\sigma$. Furthermore, if we instead use the previous luminosity value ($L = 6.8 \times 10^5$ L$_\odot$) with the updated velocity dispersion we derive a mass–to–light ratio of $[M/L]_{\rm r_h} = 15^{+10}_{-9}$ M$_\odot$/L$_\odot$ This demonstrates that the increase in the mass–to–light ratio is due to the combination of the slightly increased velocity dispersion and the updated luminosity value that is almost half the previous value that was used in C13.

Table 2.2: The properties of And XXV. Sources a: Martin et al. (2016c), b: Savino et al. (2022), c: this work.

Property	Value	Source
α,δ (J2000)	00:30:09.9 +46:51:41	a
m_V	$15.3^{+0.3}_{-0.2}$	a
M_V	$-9.1^{+0.3}_{-0.2}$	b
D (kpc)	751.6^{+25}_{-21}	b
r_h (arcmin)	$2.7^{+0.4}_{-0.3}$	a, b
r_h (pc)	590^{+90}_{-47}	a, b
L ($L_\odot$)	$3.7^{+0.4}_{-0.5}\times10^5$	b
ν (kms^{-1})	-107.7±1.0	c
σ_ν (kms^{-1})	$3.7^{+0.4}_{-0.5}$	c
M($r< r_h$) ($M_\odot$)	$4.7^{+3.0}_{-2.9} \times 10^6$	c
$[M/L]_{r_h}$ ($M_\odot/L_\odot$)	25^{+17}_{-16}	c
[Fe/H] (dex)	-1.9±0.1	c
ρ_{DM}(150 pc) ($M_\odot$ kpc^{-3})	$2.3^{+1.4}_{-1.1}\times10^7$	c

2.4.2 Comparison to Kinematics of Local Group dSphs

Dwarf galaxies are typically dark matter dominated systems at all radii and as such we would expect them to have mass–to–light ratios of $[M/L]_{r_h} > 10$ $M_\odot/L_\odot$. The left panel of Fig. 2.3 shows the mass–to–light ratios of LG dSphs, the light grey circles and triangles are M31 and MW dSphs respectively, taken from Tollerud et al. (2012); Collins et al. (2013, 2017, 2020, 2021); Walker et al. (2007, 2009); Simon & Geha (2007); Simon et al. (2011, 2015); Martin et al. (2007, 2013c,b, 2014); Ho et al. (2012); Kirby et al. (2015b, 2017). The pink diamond shows the C13 result. This mass-to light ratio was indicative of a dark matter dominated system, but within the uncertainties did not require the presence of dark matter. The purple star shows the mass–to–light ratio of And XXV derived from this study. We can see that with the combination of the slightly increased velocity dispersion and updated luminosity used in this study, the mass–to–light ratio of And XXV is that of a dark matter dominated system and moves in line with other LG dSphs.

The right panel of Fig. 2.3 shows the mass contained within the half–light radius as a function of the half–light radius for the LG dSphs. Again the light grey circles and triangles are M31 and MW dSphs respectively, taken from the same sources. With the updated velocity dispersion the half–light radius mass moves more in line with what we would expect (compare the pink diamond – C13 to the purple star – this study). Despite this, we can see that the mass of And XXV is still significantly lower when compared to the best–fitting NFW mass profile for the LG population (Collins et al., 2014), illustrated by the solid black line and the light blue shaded region is the 1σ uncertainty. This extended radial behaviour with significantly less mass than expected for its size is also shown by the other four outliers And XXI

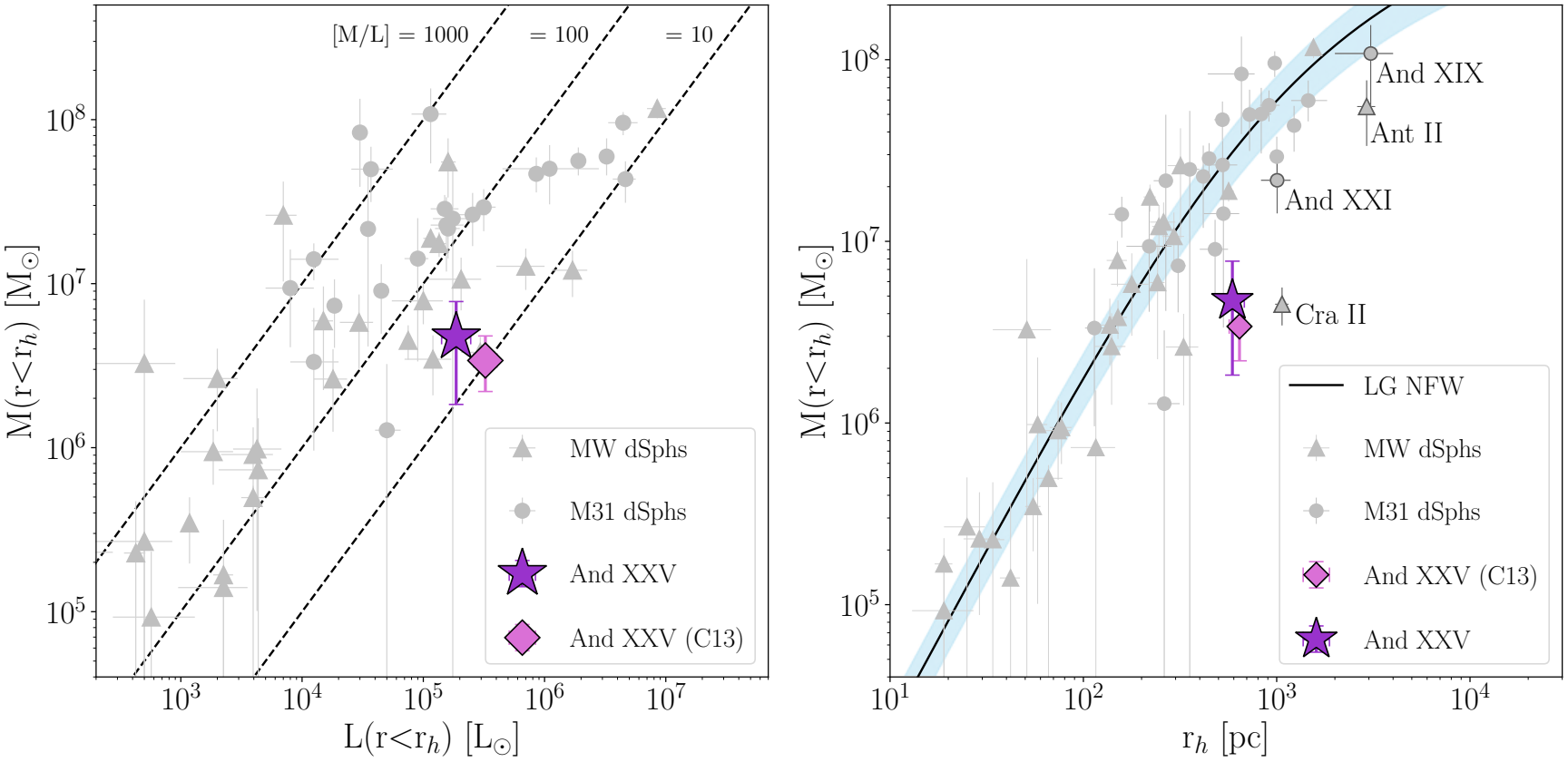

Figure 2.3: Left: Mass–to–light ratios of dSphs in the LG. The diagonal black lines illustrate a mass–to–light ratio of 10, 100 and 1000 from right to left, respectively. **Right:** The mass contained within the half–light radius for the LG dSphs. The solid black line is the best-fitting NFW mass profile for the LG population (Collins et al., 2014), with the 1σ uncertainties for this relationship shown by the blue shaded region. **Both:** The light grey triangles are MW dSphs and the light grey circles are M31 dSphs. The C13 result is illustrated by the pink diamond and the updated value from this study for And XXV is shown by the purple star. For all data points, the error bars show the 1σ uncertainties.

(Collins et al., 2021), And XIX (Collins et al., 2020), Crater II (Torrealba et al., 2016) and Antlia II (Torrealba et al., 2019), as highlighted in Fig. 2.3. For these systems, it is suspected that tides have caused the low masses. Furthermore, C13 noted that tidal interactions could have acted to lower the central density of And XXV, and the increase in velocity dispersion with radius could indicate a tidal influence.

To investigate if we can observe the impact of tides in the kinematics, we altered the Gaussian component of the likelihood function described in Equ. 2.4 to include a velocity gradient component that would indicate the presence of tidal streams, following the methodology outlined in Martin & Jin (2010). No statistically significant velocity gradient was found. It is important to note that this does not mean And XXV has not experienced tidal influences, especially as we potentially run into the same small number statistics issues reported by the C13 as we are trying to fit more parameters than the simple Gaussian outlined in Equ. 2.4. We return to the potential impact of tides on And XXV in § 2.7.

2.5 Metallicity of Andromeda XXV

We determined the metallicity of And XXV by measuring the equivalent widths of the Ca(II) triplet lines from the spectroscopic observations. These absorption lines are a good proxy for iron abundance [Fe/H] (Armandroff & Da Costa, 1991). We focused on the equivalent widths of the Ca(II) triplet feature in the co–added spectra for And XXV. We only include member stars with a good signal–to–noise ratio (S/N), for our data set, this was determined to be $S/N > 2.5$ per pixel, which resulted in a sample that comprised of 32 stars. To calculate the equivalent widths, we followed the methodology outlined in C13. Firstly, we apply a Doppler correction to each star to ensure the spectra are measured in the rest frame. The spectra were then interpolated onto a common framework before co-adding the S/N weighted spectra. Next, the spectra were normalised, such that the mean continuum was equal to one. Finally, we simultaneously fit the continuum and three Gaussian peaks to each of the three Ca(II) triplet lines to obtain the equivalent widths, see Figure (2.4).

The metallicity was determined from the equivalent widths using the approach described by Starkenburg et al. (2010) such that:

$$[\mathrm{Fe/H}] = -2.87 + 0.195\ M + 0.48\ \Sigma Ca - 0.913\ \Sigma Ca^{-1.5} + 0.00155\ \Sigma Ca\ M \quad (2.10)$$

where $\Sigma\mathrm{Ca} = 0.5\mathrm{EW}_{8498} + \mathrm{EW}_{8542} + 0.6\mathrm{EW}_{8662}$ and M is the absolute magnitude of each star given by:

$$M = V - 5 \times \log_{10}(D_{\odot}) + 5 \quad (2.11)$$

where V is the S/N–weighted mean V–band magnitude of the 32 stars and $D_{\odot}$ is the heliocentric distance of the star which, for all stars, was assumed to be the heliocentric distance of And XXV, 751.6 kpc (Savino et al., 2022). This resulted in a metallicity for And XXV of $[\mathrm{Fe/H}] = -1.9 \pm 0.1$ dex. This value is in direct agreement with the result from the C13 study. Furthermore, this result is in agree-

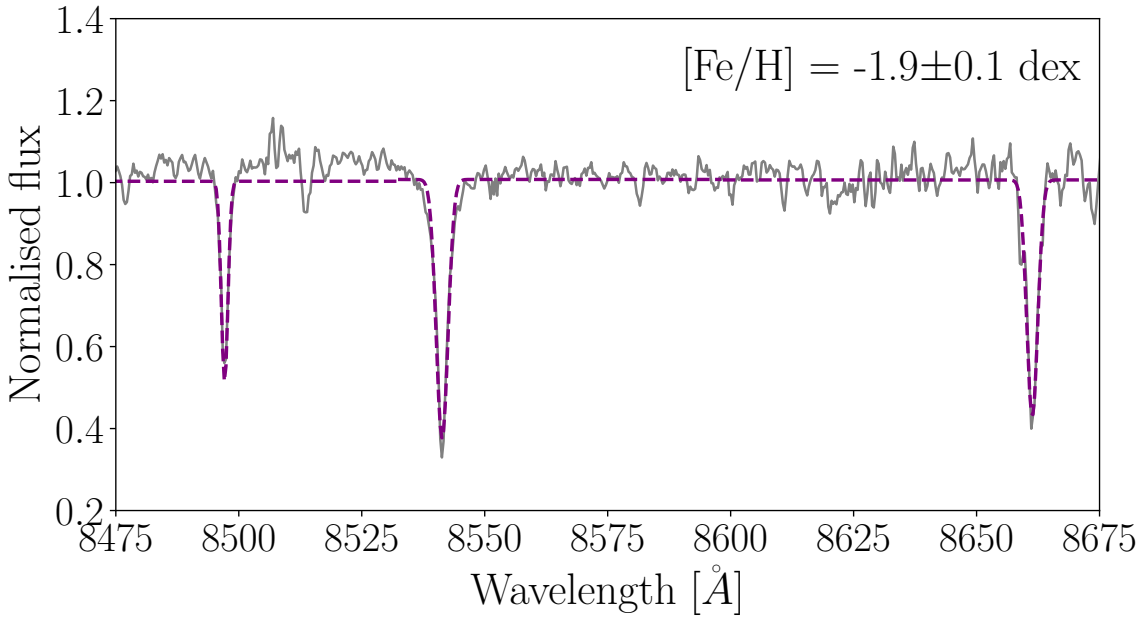

Figure 2.4: The S/N weighted co-added spectra for the Ca(II) triplet region in And XXV. The purple dashed line is the fit to the Ca(II) triplet feature, the final derived metallicity is [Fe/H] $= -1.9 \pm 0.1$ dex.

ment with the luminosity–metallicity relation (Kirby et al., 2013b) for LG dwarfs, as shown in Fig. 2.5 with data taken from the sources mentioned for Fig. 2.3 in addition to Ho et al. (2015) and Wojno et al. (2020). We alo obtained metallicities for individual stars. To do this we performed the same fitting procedure described above but this time for each of the 32 spectra separately. From the individual metallicities, we produced a metallicity distribution function (MDF) from which we determined the mean metallicity of And XXV MCMC with an `EMCEE` routine fitting a Gaussian to the MDF. This analysis produced a metallicity in agreement with the result derived from the co–added spectra, albeit with a slightly larger uncertainty due to the larger systematic errors associated with the individual spectra with low S/N.

2.6 Mass Modelling of Andromeda XXV

2.6.1 `BINULATOR` + `GravSphere` – mass modeling tool

`GravSphere`[1] is the dynamical mass modelling tool we used to measure the dark matter density profile of And XXV and is described described in detail in Read & Steger (2017); Read et al. (2018, 2021); Genina et al. (2020b); Collins et al. (2021). In this section, we briefly review the `GravSphere` methodology and describe its

[1]The updated `GravSphere` code along with the new BINULATOR binning method, described in this paper and Collins et al. (2021), is available to download from `https://github.com/justinread/gravsphere`. `pyGravSphere`, a free form mass version of the `GravSphere` code (Genina et al., 2020b), is available to download from `https://github.com/AnnaGenina/pygravsphere`.

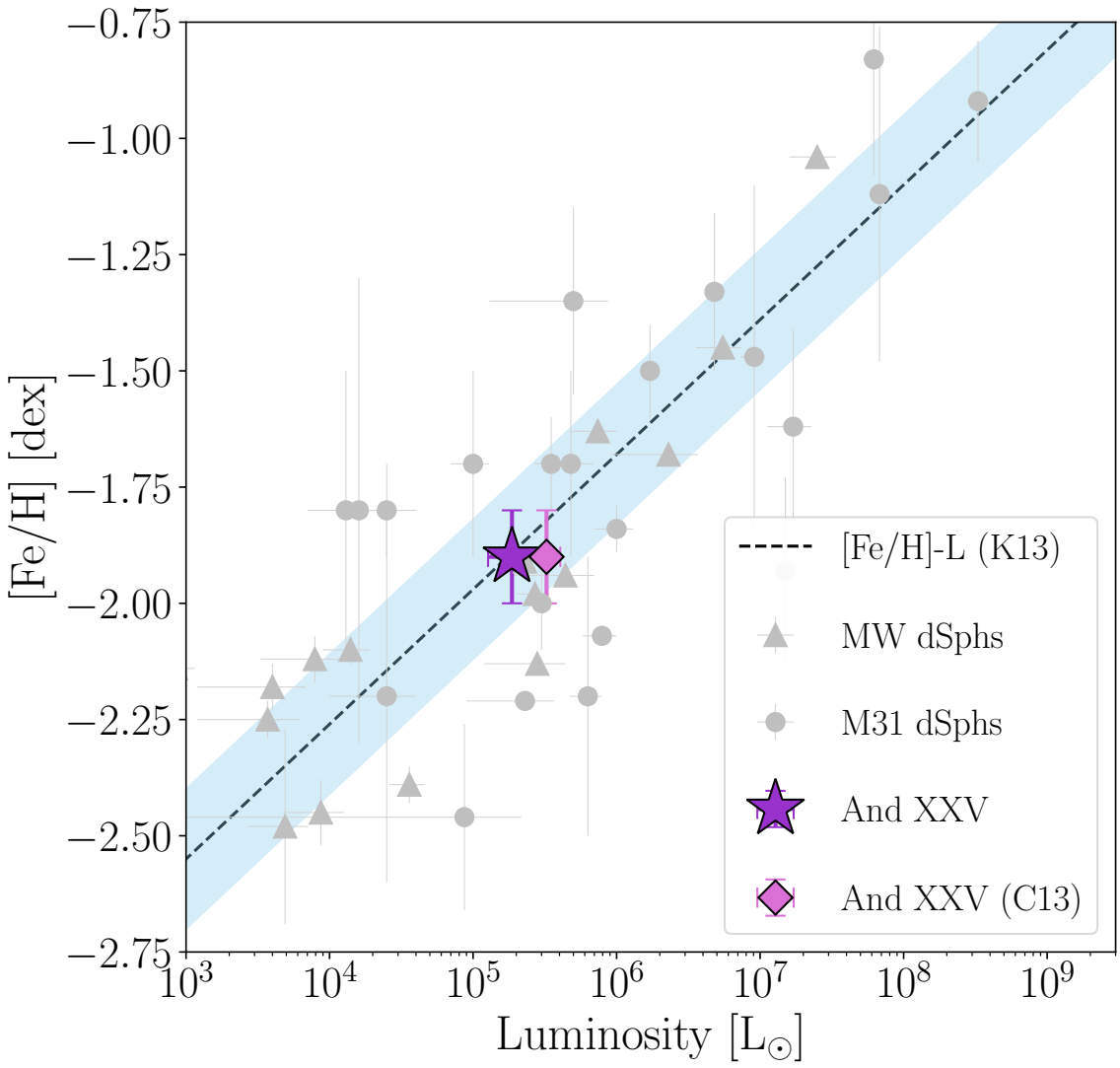

Figure 2.5: The luminosity–metallicity relation for LG dSphs. MW dSphs are represented by light grey triangles whereas the M31 dSphs are the light grey circles. The pink diamond shows the results for And XXV from the C13 study and the purple star shows the result for And XXV from this study derived from the coadd spectra. The black dash line is the best fit luminosity–metallicity relation from Kirby et al. (2013b) with the light blue band illustrating the 1σ scatter. And XXV is in perfect agreement with this relation.

application to And XXV. `GravSphere` solves the projected spherical Jeans equations (Jeans, 1922; Binney & Mamon, 1982) for a set of tracers, in this instance the 49 member stars of And XXV, to determine the dark matter density profile, assuming that it is a spherical, non–rotating system. These equations are known to have a mass–velocity anisotropy degeneracy for which a wide range of solution combinations can satisfy the model (Merrifield & Kent, 1990; Wilkinson et al., 2002; Łokas & Mamon, 2003; de Lorenzi et al., 2009). Several methods have been proposed to break this degeneracy (see e.g. Read & Steger (2017). `GravSphere` addresses it by fitting two higher order "Virial Shape Parameters" (VSPs), first proposed by Merrifield & Kent (1990, see also Richardson & Fairbairn (2014)). The velocity

anisotropy profile is difficult to constrain observationally. However, using VSPs we only need line of sight velocities (easily obtained from spectroscopic observations) to place meaningful constraints on the velocity anisotropy profile, hence breaking the mass–velocity anisotropy degeneracy. `GravSphere` uses a symmetric version of the velocity anisotropy profile, $\tilde{\beta}$, is used to avoid issues with infinite values (Read et al., 2006), where $\tilde{\beta} = 0$ describes an isotropic velocity distribution, $\tilde{\beta} = -1$ a complete tangential and $\tilde{\beta} = 1$ a complete radial distribution. Finally, in line with previous studies (Read et al., 2018; Collins et al., 2021), we adopt the `CORENFWTIDES` model to describe the dark matter distribution. This mass profile includes within its parameterisation the cusped Navarro–Frenk–White profile (NFW; Navarro et al. (1996b)). The NFW profile gives a good fit to dark matter density profiles in pure dark matter simulations and is described by two parameters: a virial mass M_{200} and concentration parameter c_{200}. The `CORENFWTIDES` model adds four new parameters to this: n, r_c, r_t and δ. The first two control how 'cored' or 'cusped' the dark matter profile is inside r_c, where $n = 1$ corresponds to a constant density flat core, $n = 0$ corresponds to an r^{-1} cusp, as in the NFW profile, and $n = -1$ corresponds to an even steeper r^{-2} cusp. The second two parameters model the effect of tidal forces from a larger host galaxy stripping some of the outer mass away, where r_t is the tidal radius beyond which the density falls off as $r^{-\delta}$.

`GravSphere` has been rigorously tested on a wide variety of mock data (Read & Steger, 2017; Read et al., 2018, 2021; Genina et al., 2020b; Collins et al., 2021) and stands up well when compared to other dynamical mass modelling tools (Read et al., 2021). However, for systems with a small number of stars, and/or where the velocity uncertainty is large, the binning routine in the previous version of `GravSphere` can become slightly biased towards cusped profiles (Gregory et al., 2019; Zoutendijk et al., 2021; Collins et al., 2021). To resolve this issue `GravSphere` was updated to include a new separate binning routing, `BINULATOR`, first introduced and outlined in detail in Collins et al. (2021). This update reduces the aforementioned biases by fitting a generalised Gaussian probability distribution to each bin, providing a robust estimate of the mean, variance, kurtosis and corresponding uncertainties for each bin, even for systems with an extremely small sample size – such as And XXV. These estimates are then used as inputs to `GravSphere`. Detailed tests of this updated version of `BINULATOR`+`GravSphere` can be found in Collins et al. (2021) Appendix. A.

2.6.2 Implementing `BINULATOR` + `GravSphere` for Andromeda XXV

The surface brightness profile for And XXV was constructed from photometric data obtained through the LBT imaging described in §2.2.2. We included point sources from the entire data set out to $\sim 5 \times r_h$. For each star the radial distance from the centre of And XXV was measured and a probability of membership was assigned using the $P_{\rm dist}$ and method outlined in Equ. 2.1, albeit with a looser probability constraint ($\mathrm{P_{member}} > 0.01$) and larger η parameters to ensure a representative and complete surface brightness profile. The velocity dispersion profile was constructed from the spectroscopic data for the 49 identified members of And XXV, using the

velocity, velocity uncertainty, radial distance from the centre and the probability of membership determined using Equ. 2.7 for each member star. For both data sets the probability of membership is summed to give the total number of 'effective' tracers:

$$N_{\rm eff} = \sum_{i=0}^{N_{\rm mem}} P_{\rm mem,i} \tag{2.12}$$

giving $N_{\rm eff} = 2450$ for the photometric data and $N_{\rm eff} = 27$ for the velocity data, which were then split into 98 bins of 25 and 3 bins of 9 respectively. `GravSphere` fits the surface brightness profile and radial velocity profile from the kinematic and photometric data input using an `emcee` routine (see Appendix A). For the parameters in the `CORENFWTIDES` profile we implemented the following priors: $7.5 < \log_{10}(M_{200}/{\rm M}_\odot) < 11.5$, $7 < c_{200} < 53$, $-2 < \log_{10}(r_c/{\rm kpc}) < 10$, $1 < \log_{10}(r_t/{\rm kpc}) < 20$, $3 < \delta < 5$ and $-1 < n < 1$. For the symmetric velocity anisotropy, β, the priors were: $-0.1 < \tilde{\beta}_\infty < 1$, $-2 < \log_{10}(r_0/{\rm kpc}) < 0$ and $1 < q < 3$. Finally, for the stellar mass of And XXV we convert the updated luminosity value from Savino et al. (2022) using the assumption of a stellar mass–to–light ratio of 2 for an old stellar population, in line with Simon (2019). This gives a stellar mass of $M_* = 7.5^{+0.6}_{-0.8} \times 10^5$ M$_\odot$.

2.6.3 Dark Matter Density Profile of Andromeda XXV

The resulting dark matter density profile is shown in Fig. 2.6. The dark grey and light grey shaded regions are the 1 and 2 σ uncertainties respectively and the purple dashed line is the half–light radius of And XXV. Within the uncertainties, it is not possible to distinguish between a cusped or cored profile. Instead, we turn our attention to the central dark matter density, $\rho_{\rm DM}(150{\rm pc})$, illustrated by the blue dotted line. This value is used because this is the key region where core formation is expected to reduce dark matter densities, compared to CDM predictions (Read et al., 2018; Genina et al., 2020a). For And XXV, we get a central dark matter density of $\rho_{\rm DM}(150\ {\rm pc}) = 2.3^{+1.4}_{-1.1} \times 10^7$ M$_\odot$ kpc^{-3}, which is in agreement with the mass profiles derived using Walker et al. (2009); Wolf et al. (2010) estimators . The derived central density is low when compared to other LG dSphs, as shown in Fig. 2.7, with data taken from Read et al. (2019). Here dSphs are illustrated as circular data points and dIrrs are triangles. Quiescent (non–star forming) dwarfs are purple, whereas currently star-forming dwarfs are blue. The pre–infall halo masses, M_{200} for the dwarfs in this study and the Read et al. (2019) sample are determined using an abundance matching method described in Read & Erkal (2019), which uses the mean star formation rate averaged over the time when a galaxy was forming stars $\langle {\rm SFR} \rangle$, rather than stellar mass. This method was chosen as it is less susceptible to scatter associated with quenching or tidal interactions which can alter the M_{200} value obtained from traditional stellar mass abundance matching methods. This is particularly pertinent as And XXV may show signs of tidal stripping. The sample of dSph galaxies in Read et al. (2019) was chosen to be tidally isolated in order to measure the impact of dark matter heating on $\rho_{\rm DM}(150$ pc), independently of tidal effects. However, while the dSphs in Read et al. (2019) are known to be

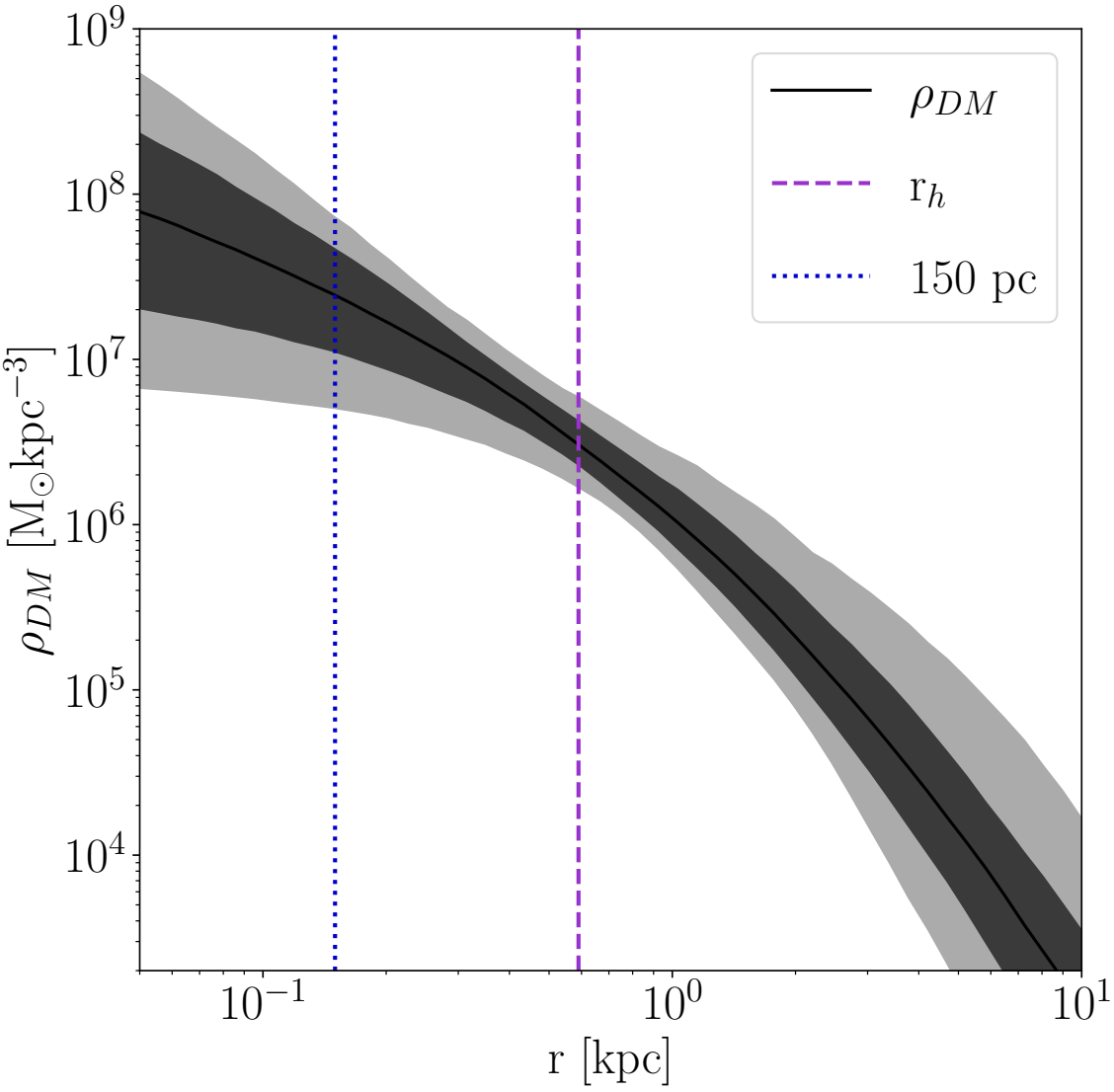

Figure 2.6: The dark matter density profile for And XXV. The dark grey and light grey shaded regions are the 1× and 2× σ uncertainties respectively and the purple dashed line is the literature half–light radius of And XXV (Savino et al., 2022). The blue dotted line corresponds to 150 pc, the radial distance at which we determine the central dark matter density (Read et al., 2018). And XXV has a low central dark matter density of $\rho_{\rm DM}$(150 pc)= $2.3^{+1.4}_{-1.1}\times10^7$ M$_\odot$ kpc^{-3}.

tidally isolated today (based on their orbits, measured using proper motion data from Gaia+HST (Gaia Collaboration et al., 2016, 2018), this does not mean that they have been tidally isolated for their whole history. As shown in Genina et al. (2020b), some dwarfs can have past interactions with one another and/or other infalling structure that lowers their inner densities while leaving them on apparently benign orbits today. While it is not possible to control for this for the dSphs in the Read et al. (2019) sample, like Fornax, such effects cannot explain the similarly low density of the isolated dIrrs in the Read et al. (2019) sample. Fornax is illustrated by the partially filled purple circular data point. Fornax is an interesting case that

has a density and star formation history similar to dIrrs, but is a dSph. As such, its low density could owe to star formation and/or tides (Genina et al., 2022). A star formation (SF) induced dark matter core provides the best fit to the kinematic data for Fornax, but tides could still have had a major influence even though Fornax's orbit looks to be tidally benign today.

When comparing And XXV to the rest of the LG dwarfs we can see just how low And XXV's central dark matter density is, at approximately an order of magnitude smaller than expected for a quiescent dSph, $\rho_{\rm DM}(150{\rm pc}) > 10^8$ M$_\odot$ kpc^{-3}. Instead, And XXV has a central dark matter density more in line with currently star forming dIrrs, $\rho_{\rm DM}(150{\rm pc}) < 10^8$ M$_\odot$ kpc^{-3}, which are expected to have lower central dark matter densities due to the dark matter heating effects of their continued star formation. Even when compared to the unusual Fornax, with even lower central density, And XXV is still a significant outlier. Furthermore, in the top panel in Fig. 2.7, the dark grey band corresponds to a fully cusped profile whereas the light grey band corresponds to a fully cored profile. The width of the bands corresponds to the 1σ scatter in DM halo concentrations (Dutton & Macciò, 2014). Here we can see that And XXV appears to reside in the light grey region which corresponds to a fully cored profile. This behaviour is also reflected in And XXI, another documented M31 outlier for which we have dynamical mass modelling (Collins et al., 2021), as labelled in Fig. 2.7. A recent study by Orkney et al. (2021) showed that gravitational fluctuations due to late minor mergers can also instigate slight core formation, even in dwarfs below this stellar mass–halo mass ratio. Therefore, it is possible that And XXV may have undergone a slight cusp–core transformation, although none of the simulated, isolated, dwarfs reported in Orkney et al. (2021) reach the low density of And XXV.

2.7 Discussion

Dark matter heating is one way in which dwarfs can lower the central dark matter densities. Could the unusually low central density observed in And XXV be due to dark matter heating caused by extended star formation? From the shallow horizontal branch star formation history, we can see that And XXV formed 50 per cent of its total stars 8.7 Gyrs ago and formed 90 per cent of stars (and thus likely finished star forming) 5.8 Gyrs ago (Weisz et al., 2019b). It is possible that And XXV had a very short burst of star formation ∼1–2 Gyrs ago, although within the uncertainties this is not significant and could be an artefact of the method used as many of the dwarfs in their sample display this short burst. Deeper star formation data is required to confirm the nature of this burst. Dark matter heating is more effective in galaxies with extended star formation (Read et al., 2016, 2019), hence the relatively short, isolated bursts of star formation history that And XXV undergoes means it is unlikely that star formation alone could explain the extremely low central density observed in And XXV. The same conclusion was reached for the other outliers with low central densities (Torrealba et al., 2019; Collins et al., 2021). However, in the bottom panel of Fig. 2.7 we can see that And XXV lies below the dashed grey line which indicates the stellar mass–halo mass ratio for which dark matter heating can become viable (Di Cintio et al., 2014).

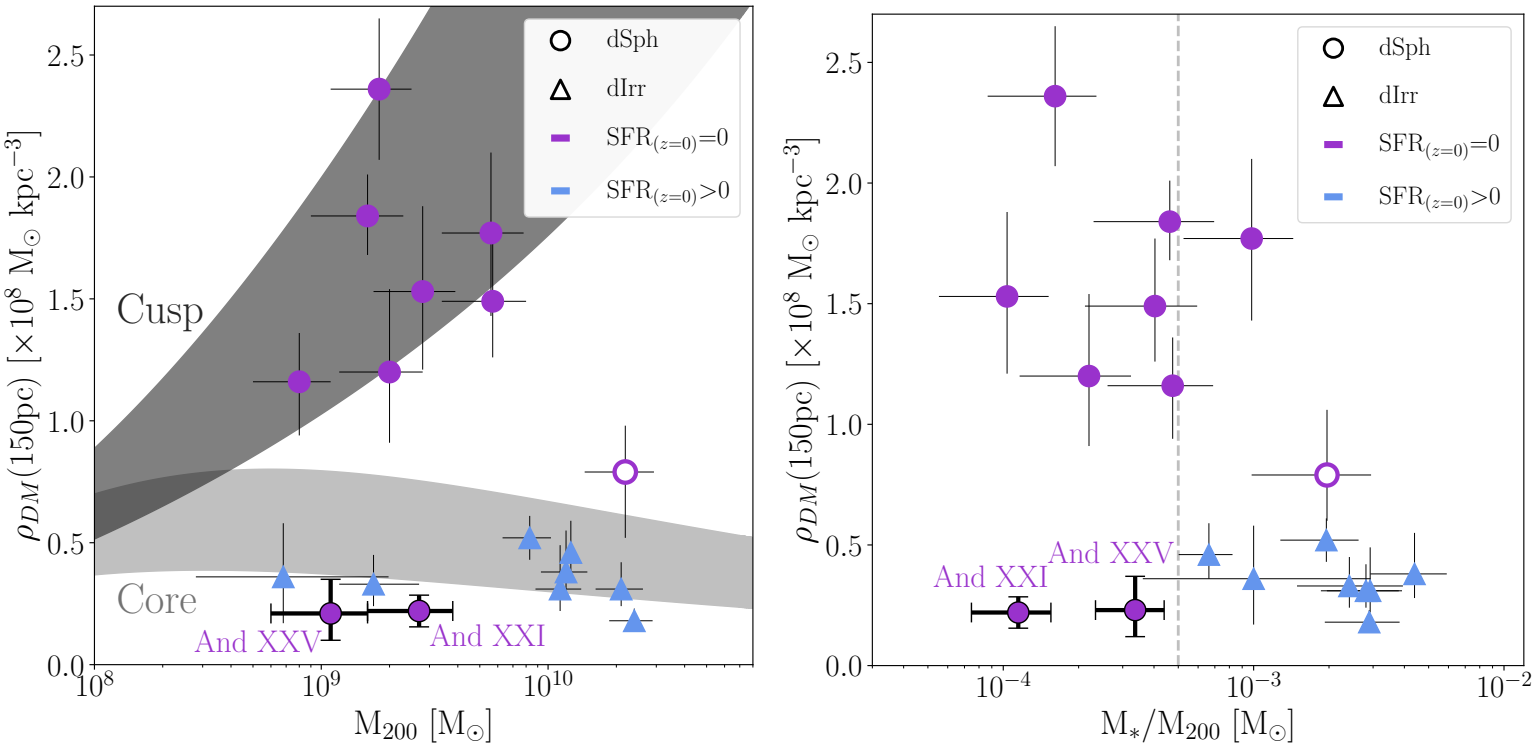

Figure 2.7: Top: The central dark matter density as a function of pre–infall mass, M_{200}. The dark grey band corresponds to the inner DM densities of completely cuspy profiles, whereas the light grey band corresponds to a fully cored coreNFW profile (Read et al., 2016). The width of the bands corresponds to the 1σ scatter in DM halo concentrations (Dutton & Macciò, 2014). **Bottom:** Central dark matter density as a function of the stellar mass to halo mass ratio, M_*/M_{200}. The vertical grey dashed line illustrates the M_*/M_{200} ratio above which cusp–core transformations should become efficient (Di Cintio et al., 2014). **Both:** Circular data points are dSphs, while triangles are dIrrs. Dwarfs that are currently star forming are light blue whereas dwarfs that are quiescent are purple. Fornax is illustrated by the partially filled purple circular data point due to its unusual star formation history atypical of dSphs. The error bars are the 1σ uncertainties. And XXV and And XXI are labelled and have thicker error bars with caps. Data for And XXI were obtained from Collins et al. (2021) and from Read et al. (2019) for the other dwarfs.

Another process that can lower the central density is tidal interactions. Tidal interactions lower densities at all radii, unlike dark matter heating which only lowers the central density. Tidal interactions can be split into two different processes, tidal stripping and tidal shocking. Tidal stripping occurs when the gravitational force from the host galaxy (in this case M31) exceeds the gravitational force from the dwarf allowing matter (dark matter/stars) to become unbound from the dwarf. Tidal stripping preferentially removes matter from the outer radii working inwards. As such the central dark matter density is only noticeably reduced after significant mass loss. For cusped profiles $\gtrsim 99$ per cent of the original mass would need to be lost before the central dark matter density would decrease (Peñarrubia et al., 2008, 2010; Errani et al., 2018; Errani & Peñarrubia, 2020; Errani & Navarro, 2021). However, cored profiles are less efficient at protecting their central densities and require less extreme mass loss for a noticeable effect (Read et al., 2006; Peñarrubia et al., 2010; Brooks & Zolotov, 2014). Tidal shocking is another type of tidal interaction. It occurs for satellites on highly eccentric orbits moving in and out of the gravitational potential of the host. If the resulting gravitational fluctuations occur on shorter time scales than the dynamical time of the interaction, it will dynamically heat the stars and dark matter. The effect of tidal shocking is most pronounced at the pericentre of the orbit, as this is where the gravitational field changes most rapidly. Furthermore, tidal shocking is only effective at lowering central densities for cored systems (Read et al., 2006; Errani et al., 2017, 2018; Errani & Peñarrubia, 2020; van den Bosch & Ogiya, 2018) or for systems that reside in a low concentration dark matter halo (Amorisco, 2019).

At a 3D–projected distance of 85.2 kpc (Savino et al., 2022), And XXV is one of the closest M31 satellites, meaning it may potentially have had a previous encounter with M31 resulting in tidal forces. However, without proper motions, it is difficult to place meaningful constraints on the orbital history to ascertain if And XXV has had any close approaches with M31. Even armed with hypothetical proper motions, it is important to remember that the current orbital properties are not always a robust indicator of possible past close interactions (Lux et al., 2010; Genina et al., 2020a). Without orbital history information, we turn our attention to other potential indicators of tidal interaction. Firstly, we turn to the photometry to see if we can find indications of tidal interactions. No obvious tidal tails or other tidal substructure can be seen in the photometry of And XXV. The photometry used is shallow, as such tidal features, which tend to have low surface brightnesses, could readily be missed. Without dedicated deep imaging out to the very outskirts of And XXV, such tidal substructure would be difficult to detect (e.g. Shipp et al., 2022). Recent studies have shown that dSphs can undergo tidal interactions and show no observable tidal substructure (Read et al., 2006; Peñarrubia et al., 2009; Genina et al., 2020a), this is especially true for dwarfs on highly eccentric orbits, since the episodes of shocking are restricted to only the pericentric passages. As such, the dwarfs can relax back to equilibrium on a dynamical timescale, quickly erasing any signs of the interaction from the main body of the dwarf. Moreover, as the stellar component is strongly embedded in the dark matter halo, dSphs can be excessively stripped by tidal forces preferentially removing dark matter and as such, not demonstrate any observable tidal features in the stars until very extreme mass

loss ($\gtrsim$ 90 per cent Peñarrubia et al., 2008, 2010; Errani et al., 2018). Secondly, in the kinematic analysis, we observed a kinematically colder centre in And XXV with the velocity dispersion increasing with radial distance. This may demonstrate that And XXV is not in dynamical equilibrium which could be due to previous tidal interactions, although it is important to note that within the uncertainties this flaring is not statistically significant. Interestingly a similar kinematic profile is observed in Antlia 2, a system for which tides are the suspected culprit (Torrealba et al., 2019). Moreover, the unusually low mass contained within the half–light radius measured for And XXV could be explained by tidal stripping/shocking, which would reduce the mass of the system over time. This is especially true for cored systems which are able to maintain their original radius while losing mass (Peñarrubia et al., 2010), resulting in the extended radial behaviour observed. Finally, dwarfs undergoing strong tidal interactions, which result in stellar mass loss, are expected to be outliers on the luminosity–metallicity relation (e.g. Tucana III, see Simon et al., 2017). From Fig. 2.5 we can see that And XXV agrees with this relation which suggests it has not lost significant stellar mass through tides; an order of magnitude loss appears unlikely, but stripping $\sim$50 per cent of the stars may be allowed by the data. Furthermore, significant dark matter mass loss can lower the inner density, as can tidal shocking, without any associated stellar mass loss (e.g. Read et al., 2006).

No one piece of evidence is enough to decisively confirm or omit the possibility of either dark matter heating or tidal interactions as the cause of the low central density. However, the above would imply that we may potentially explain And XXV's extremely low central density due to a combination of both factors. Meaning And XXV could have undergone a slight cusp–core transformation from dark matter heating, which made And XXV more susceptible to tidal stripping and shocking which further reduced the central dark matter density, with tidal interactions being the significant contributing factor. This conclusion is in line with the results from studies investigating the other anomalous dwarfs (Torrealba et al., 2019; Collins et al., 2021). Although, detailed analysis in combination with additional data, such as proper motions, is required to consolidate this conclusion. And XXV joins the small but growing list of unusual LG 'puffy' dwarfs with low central densities. Around M31 we now see three such systems (And XXV, And XIX and And XXI). A detailed study (Charles et al, in prep) into potential formation and evolution pathways resulting in the low central densities observed will improve our understanding of the nature of dark matter and potentially place constraints on different cosmological models.

2.8 Conclusions

We present an updated kinematic analysis for And XXV. And XXV was previously identified as a Local Group outlier. Using previous spectroscopic observations in combination with a new data set, providing 49 member stars, nearly double that in the previous study, we were sufficiently able to determine the presence of dark matter within And XXV, for the first time. In addition, we dynamically mass model And XXV using `BINULATOR` + `GravSphere` to constrain its dark matter density profile. Our key findings are as follows:

- We measure the a systemic velocity for And XXV of $\nu = -107.7 \pm 1.0$ km s^{-1} and a velocity dispersion of $\sigma_\nu = 3.7^{+1.2}_{-1.1}$ kms^{-1} These values are consistent with the results derived by C13, which had a much smaller sample size.

- We observe that the most central stars have a low velocity dispersion, which increases with increasing radial distance, potentially indicating And XXV is not in dynamical equilibrium and may have undergone tidal interactions.

- Assuming dynamical equilibrium, we determine the mass contained within the half-light radius to be $M(r < r_{\rm h}) = 4.7^{+3.0}_{-2.9} \times 10^6$ M$_\odot$, which is lower than we would expect for the size of And XXV. This mass value corresponds to a mass–to–light ratio of $[{\rm M/L}]_{\rm r_h} = 25^{+17}_{-16}$ M$_\odot$/L$_\odot$, which, for the first time, indicates And XXV is a dark matter dominated system. Although within the uncertainties And XXV does not require dark–matter to explain the mass–to–light ratio, in agreement with C13.

- For stars with a $S/N > 2.5$ we measure the metallicity of And XXV to be [Fe/H] $= -1.9 \pm 0.1$ dex from the coadded spectra. This is perfect in agreement with C13 and with the luminosity–metallicity relation for low–mass LG dwarfs (Kirby et al., 2013b).

- Using the dynamical mass modelling tool `BINULATOR` + `GravSphere` we measure a low central dark matter density of $\rho_{\rm DM}(150\ {\rm pc}) = 2.3^{+1.4}_{-1.1} \times 10^7$ M$_\odot$ kpc^{-3}. From the dark matter density profile alone we cannot distinguish between a cusped or cored halo. However, when compared to other quiescent star forming dSphs we find the And XXV has a central dark matter density approximately one order of magnitude smaller than we would expect, more similar to the central dark matter density of isolated star forming dIrrs.

- In a companion paper (Charles et al in prep.), we will consider whether dark matter heating, tides, or some combination of these can explain And XXV's low density in the context of LCDM. We will also explore its implications for alternative dark matter models.

Investigating the low central dark matter densities of Andromeda XXI and Andromeda XXV

Manuscripts

The work presented in this chapter is in progress and will shortly be submitted for publication in the Monthly Notices of the Royal Astronomical Society:

- Investigating the unusually low central dark matter densities of Andromeda XXI and Andromeda XXV – (Charles et al., in prep) *First author*

Statement of contribution

I led the analysis of the work presented in this manuscript with significant input from the second author Stacy Kim. Here I detail the coauthor's contributions. Stacy and Annika Peter designed the initial version of the tidal stripping code `dis` (Kim & Peter, 2021). Stacy and I designed and implemented the new density module within `dis`, used within this analysis to calculate the value of the density at different radial distances from the centre instead of the mass enclosed at a radial distance resulting in an average density enclosed within that radius. This allows us to directly compare with the central density values $\rho_{\rm DM}(150\ {\rm pc})$ derived with `GravSphere` in the previous chapter. The observational values for And XXI were obtained from a previous paper written by Michelle Collins (Collins et al., 2021) and also via private communication with Michelle. The star formation histories for And XXI and And XXV were kindly provided by Dan Weisz and is detailed in (Weisz et al., 2019a). Finally, I led the writing of the manuscript, with helpful input from my supervisory team Michelle and Justin Read, as well as Stacy.

Summary

Andromeda (And) XXI and And XXV are dwarf spheroidal galaxies with anomalously low central dark matter densities compared to dwarfs of similar stellar mass. Often the inclusion of baryonic feedback effects can explain the low density of dwarfs. However, we conclusively show that, due to their limited star formation, baryonic feedback from star formation *alone* cannot explain the low densities in these two

systems. In this paper, we use the tidal stripping code `disSat` to investigate a range of possible formation scenarios, cosmologies and combinations thereof that could explain the low central densities observed in And XXI and And XXV. We find for both Cold and Warm Dark Matter cosmologies, And XXI favours a halo that is a -3σ outlier in the mass-concentration relation, whereas And XXV favours significant mass loss due to tides ($\sim$ 99%). For both dwarfs, we cannot reconcile any constant cross-section self-interacting dark matter model with the data. With full population statistics from upcoming dynamical mass-modelling for the remaining M31 satellites, we propose that the combined density profiles of dwarf galaxies will provide crucial tools for placing meaningful constraints on the nature of dark matter.

3.1 Introduction

The nature of dark matter remains an important and outstanding cosmological question. Dark matter is elusive, not interacting with the electromagnetic spectrum through known measurable processes. Instead, we must turn our attention to investigating the effects of its existence on the observable universe (e.g. Tolstoy et al., 2009; Peter, 2012; Buckley & Peter, 2018; Simon, 2019; Sales et al., 2022; Battaglia & Nipoti, 2022). The currently accepted cosmological model of the Universe is the Lambda Cold Dark Matter (ΛCDM) model, in which most of the mass-energy density of the Universe today comprises baryons, dark matter and dark energy (e.g. Peebles, 1982; Bond et al., 1982; Blumenthal et al., 1982, 1984; Planck Collaboration et al., 2016, 2020). This cosmological model has been rigorously tested against a wide range of observations and can explain large-scale structures such as the cosmic microwave background radiation (e.g. Peebles, 1982; Komatsu et al., 2009; Aubourg et al., 2015; Planck Collaboration et al., 2016, 2020), nucleosynthesis (e.g. Walker et al., 1991; Smith et al., 1993; Burles et al., 1999; Cyburt, 2004; Steigman, 2007; Fields, 2011) and structure formation on large scales (e.g. Bond et al., 1996; Springel et al., 2005; Gao et al., 2005a,b; Tegmark et al., 2006; Springel et al., 2006).

On smaller scales, dwarf galaxies provide excellent systems for testing our understanding of dark matter (e.g. Mateo, 1998; Tolstoy et al., 2009; Simon, 2019; Battaglia & Nipoti, 2022). They reside inside dark matter halos, extending well beyond the visible components of the galaxy, making dwarf galaxies some of the most dark matter-dense objects in the Universe (e.g. Mateo, 1998; Simon, 2019; Tolstoy et al., 2009; Battaglia & Nipoti, 2022). Furthermore, they are extremely sensitive to a range of baryonic feedback effects, which makes them good systems to investigate galaxy evolution (e.g. Bullock et al., 2000; Benson et al., 2002; Somerville, 2002; Gatto et al., 2013; Brown et al., 2014; Rey et al., 2020). Furthermore, dwarf galaxies are the most numerous galaxies in the universe (Schechter, 1976; Driver et al., 1994; Blanton et al., 2005; Baldry et al., 2008; McNaught-Roberts et al., 2014). As such, we can find a large sample of dwarfs in our galactic neighbourhood, which can be fully resolved due to their proximity, allowing for detailed investigation. Over the past three decades, numerous dedicated, wide-field observation programs, such as the Sloan Digital Sky Survey (SDSS, Gunn & Knapp, 1993; York et al., 2000), Pan-Andromeda Archaeological Survey (PAndAS, Martin et al., 2006; Ibata et al., 2007; McConnachie et al., 2009), Dark Energy Survey (DES, Bechtol et al., 2015; Abbott et al., 2018) and Panoramic Survey Telescope and Rapid Response System (Pan-STARRS, Chambers et al., 2016), have discovered a plethora of dwarf galaxies within the Local Group, resulting in a consensus of ~ 60 around the Milky Way (e.g. Drlica-Wagner et al., 2020, and references within) and ~ 35 around the Andromeda galaxy (M31) (e.g. McConnachie, 2012; Martin et al., 2016c, and references within).

For nearly thirty years, dwarf galaxies have been a particular focus of the community due to a host of small-scale tensions between their observed number and properties and predictions from dark-matter-only (DMO) structure formation simulations in the LCDM model (e.g. Bullock & Boylan-Kolchin, 2017; Buckley & Peter, 2018; Sales et al., 2022). The earliest of these is the 'cusp-core' problem (Moore, 1994; Flores & Primack, 1994; de Blok, 2010; Navarro et al., 2010; Walker & Peñarrubia,

2011; Read et al., 2017; Genina et al., 2018; Read et al., 2019). ΛCDM predicts that the dark matter density profiles of dwarf galaxies should follow a universal 'cusped' profile defined by a highly dense centre that steeply decreases with radius, such that $\rho_{\rm DM} \propto r^{-1}$ (Dubinski & Carlberg, 1991; Navarro et al., 1996b, 1997; Moore et al., 1999). However, a significant and rapidly growing consensus of dwarfs have been observed with 'cored' dark matter density profiles characterised by a shallow central density slope that remains approximately constant in the centre, such that $\rho_{\rm DM} \sim$ constant (Flores & Primack, 1994; Moore, 1994; de Blok et al., 2001; de Blok, 2010; Marchesini et al., 2002; Simon et al., 2005; Battaglia et al., 2008; Walker et al., 2010; Kuzio de Naray & Kaufmann, 2011; Agnello & Evans, 2012; Amorisco & Evans, 2012; Newman et al., 2013; Read et al., 2017, 2019; Relatores et al., 2019).

Several solutions have been proposed for the cusp-core problem. A solution which has been particularly gaining traction is that stellar feedback processes can cause dark matter cusps to gradually transform to cores via repeated gravitational potential fluctuations, in a process known as dark matter heating (Navarro et al., 1996a; Gnedin & Zhao, 2002; Read & Gilmore, 2005; Mashchenko et al., 2008; Pontzen & Governato, 2012; Zolotov et al., 2012; Brooks & Zolotov, 2014; Oñorbe et al., 2015; Tollet et al., 2016; Read et al., 2016, 2019). Many of these small-scale tensions can be alleviated with the introduction of these baryonic processes, physics which was missing in the first DMO simulations where the tensions were first identified. However, dark matter heating is only expected to be effective in galaxies that have a stellar-mass-to-halo-mass ratio of $\rm M_*/M_{200} \gtrsim 5 \times 10^{-4}$ (Di Cintio et al., 2014, but see Orkney et al., 2021) and have experienced extended star formation (Read et al., 2016, 2019). As such, while dark matter heating can explain the diversity of central densities found in most dwarfs, a handful of recent dwarf discoveries have challenged this picture.

Recently, two such anomalously low density dwarfs have been found around the Andromeda galaxy (M31): Andromeda (And) XXI (Collins et al., 2013, 2021) and And XXV (Collins et al., 2013; Charles et al., 2023). Both dwarfs were discovered as part of the PAndAS survey (Martin et al., 2009, And XXI; Richardson et al., 2011, And XXV). With the inclusion of spectroscopic data allowing for a detailed kinematic study (Collins et al., 2013), the dwarfs began to reveal their unusual properties. Both dwarfs display radially extended morphologies, with significantly less mass than expected for their size. Furthermore, they both have low velocity dispersions ($\sigma_\nu < 5.0$ kms^{-1}). Even more intriguingly, dynamical mass modelling analysis demonstrates that they both have low central dark matter densities of $\rho_{\rm DM}(150\text{ pc}) = 2.6^{+2.4}_{-1.5} \times 10^7$ M$_\odot$ kpc^{-3} and $\rho_{\rm DM}(150\text{ pc}) = 2.3^{+1.4}_{-1.1} \times 10^7$ M$_\odot$ kpc^{-3}, for And XXI and And XXV respectively, significantly lower than dwarfs of a similar stellar mass (Collins et al., 2021, And XXI; Charles et al., 2023, And XXV). Around the MW, two similar dwarfs have been found, Crater II (Torrealba et al., 2016) and Antlia II (Torrealba et al., 2019). All four dwarfs have had relatively short star formation times (Walker et al., 2019; Weisz et al., 2019a); as such, it is expected that baryonic feedback processes have played little-to-no effect (Collins et al., 2021; Charles et al., 2023). Dark matter heating *alone* cannot explain the low central densities of these dwarfs.

Instead, we turn to other density-lowering mechanisms. For example, tidal inter-

actions are unavoidable, at some level, for all satellite galaxies and will act to lower their densities. This can happen through two main methods, tidal stripping and tidal shocking (e.g. Mayer et al., 2001; Johnston et al., 2002; Hayashi et al., 2003; Kravtsov et al., 2004; Read et al., 2006; D'Onghia et al., 2009; Peñarrubia et al., 2008, 2009, 2010; Kazantzidis et al., 2011; Tomozeiu et al., 2016; Frings et al., 2017; Garrison-Kimmel et al., 2017; Fattahi et al., 2018; van den Bosch & Ogiya, 2018; Errani et al., 2018; Errani & Peñarrubia, 2020; Errani & Navarro, 2021). Tidal stripping occurs when a subhalo (dwarf galaxy) encroaches on a more massive host halo. The gravitational force of the host causes the matter within the dwarf to become unbound and is gravitationally removed. Although tidal stripping is present across all radii, it is most effective from at extreme edges of the subhalo working inwards (Peñarrubia et al., 2010). For dwarfs with cusped dark matter profiles, extreme tidal mass loss ($\gtrsim$ 99 per cent of the original mass) is required before the central dark matter density is noticeably reduced (Peñarrubia et al., 2008, 2010; Errani et al., 2018; Errani & Peñarrubia, 2020; Errani & Navarro, 2021). Cored profiles are less dense in the centre and hence less efficient at protecting the centre of the subhalo from tidal stripping, requiring less extreme mass loss for a noticeable decrease of the central density (Read et al., 2006; Peñarrubia et al., 2010; Brooks & Zolotov, 2014). Furthermore, tidal shocking can accelerate the effects of tidal stripping, especially for dwarfs which reside in a low concentration halo (Amorisco, 2019). Tidal shocking is also most effective at lowering central densities for cored systems (Read et al., 2006; Errani et al., 2017, 2018; Errani & Peñarrubia, 2020; van den Bosch & Ogiya, 2018).

Alternatively, halos can be born with lower concentrations. This presents another possible explanation for the central dark matter densities while remaining within a ΛCDM cosmology. The concentration parameter, c_{200}, is representative of the halo's central density and is described by the ratio of halos virial radius, r_{200}, and its scale radius, $r_{\rm s}$, such that $c_{200} = r_{200}/r_{\rm s}$. The dark matter distribution for halos in a ΛCDM paradigm can be described by a Navarro–Frenk–White (NFW) profile (Navarro et al., 1996b, 1997). A common parameterisation of this profile uses c_{200} and the halo mass, M_{200}. These halo properties are correlated via known mass-concentration relations, for example Dutton & Macciò (2014). The mass-concentration relation has been measured to have an intrinsic lognormal scatter of $\sigma \log_{10}(c_{200}) \sim 0.1$. This scatter in the mass-concentration relation means that individual dwarfs may live in less (or more) concentrated halos than the average. This has been argued as another possible explanation for the low central densities of Antlia II and Crater II (Amorisco, 2019). If And XXI and And XXV reside inside lower-than-average concentrated halos, it would result in a lower central density and would make tidal processes more efficient at further lowering the central densities.

Moving beyond the canonical ΛCDM, alternative dark matter cosmologies can also present possible solutions for lower-density centres. Firstly, we look at warm dark matter (WDM) (e.g. Bond et al., 1982; Bardeen et al., 1986; Bode et al., 2001). On large scales, CDM and WDM are virtually indistinguishable. However, WDM differs from CDM on small scales due to the lack of small-scale density fluctuations. When WDM particles decoupled from normal matter, they were still relativistic, so when they eventually became non-relativistic, they still had comparatively high

velocities (compared to CDM). This allows the WDM particles to escape out of overdense regions smaller than the 'free-streaming' length, suppressing the mass transfer function below a certain cutoff that washes out small-scale overdensities. Dwarfs in a WDM cosmology reside inside halos with predominantly cuspy profiles, albeit with small cores of $\sim 10-20$ pc (Macciò et al., 2012), but significantly lower central densities than CDM (e.g. Schneider et al., 2012). The severity of the density decrease depends on the velocity of the WDM particles, characterised by the thermal relic mass of the particle.

Another alternative cosmology that could result in a lower central dark matter density is self-interacting dark matter (SIDM) (e.g. Spergel & Steinhardt, 2000 and see Tulin & Yu, 2018; Adhikari et al., 2022, for a review). Unlike CDM, described by the collisionless Boltzmann equation and where the only relevant dark matter interaction is gravitational, DM particles in SIDM obey an additional force that allows the particles to interact with one another. The simplest form of SIDM interaction is an elastic scattering scenario governed by a cross-section, $\sigma_{\rm SI}/m_\chi$, in which an energy exchange between dark matter particles occurs. There is a negligible difference in halo densities at early formation times between CDM and SIDM since the densities are such that the collision probability is low, the central cores will be small (e.g. Buckley & Peter, 2018; Tulin & Yu, 2018; Adhikari et al., 2022, and references therein). However, the collisions become more frequent over time as the halos form highly dense central regions, and the central core will grow in size. Eventually, the dark matter particles can scatter from the centre as quickly as they are gravitationally accreted. Density growth is halted, and the resulting dark matter density profile can form a large cored centre compared to the cuspy high-density CDM profiles (e.g. Spergel & Steinhardt, 2000; Rocha et al., 2013; Peter et al., 2013; Buckley et al., 2014; Vogelsberger et al., 2014; Lin & Loeb, 2016; Tulin & Yu, 2018).

Full cosmological hydrodynamic simulations of dwarf galaxies that correctly resolve the combined physics of dark matter heating and tides are not yet possible due to the extreme dynamic range and resolution requirements required to capture both (e.g. Kazantzidis et al., 2004; Pontzen & Governato, 2012; van den Bosch & Ogiya, 2018). As such, for the time being, we must study how such heating and tides impact dwarfs using controlled follow-up simulations or semi-analytic models (e.g. van den Bosch & Ogiya, 2018; Errani & Navarro, 2021). Here, we do this using the `dis` semi-analytic code that has been calibrated on high resolution simulations (Kim & Peter, 2021). This paper investigates the possible formation mechanisms, cosmologies, and combinations thereof described above that could explain the low central densities observed in And XXI and And XXV. The structure of this chapter is as follows: in § 3.2, we detail our methodology. The results, focusing on each potential formation mechanism and cosmology in turn, are presented in § 3.3. We discuss the ramifications of our results, possible cosmological constraints and future prospects in § 3.4, and, finally, we conclude in § 3.5.

3.2 Methods

To compute the effect of the different central density lowering mechanisms discussed above, we first calculate the halo mass, M_{200}, using an abundance matching method

using the mean star formation rate of the dwarf $\langle \mathrm{SFR} \rangle$, described in §3.2.1. In §3.2.2 we outline how to calculate the theoretical coring due to star formation, which will be used to parameterise the coreNFW profile, using M_{200} in combination with the star formation history of the dwarf. Next, we define the dark matter density profiles and mass-concentration relations we assume for CDM (both NFW and coreNFW), WDM and SIDM in §3.2.3. Finally, we outline the tidal stripping methodology, using the tidal stripping prescriptions from Peñarrubia et al. (2010), for each of these dark matter density profiles in §3.2.3

3.2.1 Determining Halo Mass

To determine the halo masses, M_{200}, of And XXI and And XXV, we use the novel abundance matching technique described in Read & Erkal (2019). This uses the mean star formation rate $\langle \mathrm{SFR} \rangle$, averaged over the time when a galaxy is forming stars as an indicator of M_{200}, rather than the stellar mass, M_*. We implemented this abundance matching method as it is less susceptible to induced scatter due to quenching. To obtain $\langle \mathrm{SFR} \rangle$ for And XXV, we used the star formation history derived in Weisz et al. (2019a). We implemented the same assumption outlined in Read & Erkal (2019) where SFR(t) $>$ max[SFR]/3 to avoid the $\langle \mathrm{SFR} \rangle$ being biased low by periods where the star formation rate is slowly declining due to quenching. Like Read & Erkal (2019), we find our results are insensitive to this assumption. For And XXV, we obtain $\langle \mathrm{SFR} \rangle = 1.6 \pm 0.5 \times 10^4$ $\mathrm{M}_\odot$/yr which corresponds to $M_{200} = 2.1 \pm 0.6 \times 10^9$ $\mathrm{M}_\odot$. Collins et al. (2021) used the same method for And XXI, giving $\langle \mathrm{SFR} \rangle = 2.1 \pm 0.5 \times 10^4$ $\mathrm{M}_\odot$/yr and $M_{200} = 2.7 \pm 1.1 \times 10^9$ $\mathrm{M}_\odot$.

3.2.2 Determining Coring Due to Star Formation

To determine the amount of coring due to star formation, we used the `coreNFW` profile from Read et al. (2016). This profile modifies the standard NFW profile by introducing a suppression factor to the inner slope of the density profile due to star formation:

$$M_{\mathrm{cNFW}}(< r) = M_{\mathrm{NFW}} f^n, \tag{3.1}$$

where M_{NFW} is the enclosed mass profile at a given radius,r, for an NFW described by:

$$
\begin{aligned}
M_{\rm NFW}(r) &= M_{200} g_c \left[\ln\left(1+\frac{r}{r_{\rm s}}\right) - \frac{r}{r_{\rm s}}\left(1+\frac{r}{r_{\rm s}}\right)^{-1} \right] \\
g_c &= \frac{1}{\log(1+c) - \frac{c}{1+c}} \\
r_s &= r_{200}/c \\
r_{200} &= \left[\frac{3}{4} M_{200} \frac{1}{\pi \Delta \rho_{\rm crit}} \right] \\
&,
\end{aligned}
\tag{3.2}
$$

where c is the halo 'concentration parameter', $\Delta = 200$, $\rho_{\rm crit}$ is the critical density of the Universe at redshift z = 0 ($\rho_{\rm crit} = 135.05$ M$_\odot$kpc^{-3}) and M_{200} is the virial mass (calculated in § 3.2.1). The suppression factor caused by star formation, f^n, lowers the dark matter profile below a core radius r_c, such that:

$$
\begin{aligned}
f^n &= \left[\tanh\left(\frac{r}{r_{\rm c}}\right) \right]^n \\
r_{\rm c} &= 1.75\ r_h,
\end{aligned}
\tag{3.3}
$$

where $r_{\rm h}$ is the half light radius. The parameter n controls the gradient of the core ($0 < n \leq 1$), where $n = 0$ represents no coring and $n = 1$ represents a full cusp-core transformation. n is determined using the total star formation time, t_{SF}, such that:

$$
n = \tanh\left(0.04 \frac{t_{\rm SF}}{t_{\rm dyn}}\right), \tag{3.4}
$$

where $t_{\rm dyn}$ is the dynamical time which describes the circular orbit time at $r_{\rm s}$.

$$
t_{\rm dyn} = 2\pi \sqrt{\frac{{r_{\rm s}}^3}{G M_{\rm NFW}(r_{\rm s})}}, \tag{3.5}
$$

For both dwarfs, we obtained very small amounts of coring due to star formation ($n = 0.37$ And XXI; $n = 0.18$; And XXV) as expected from their relatively short star formation times ($t_{\rm SF} = 4.75$ Gyrs And XXI; $t_{\rm SF} = 2.3$ Gyrs And XXV). Although the coring due to star formation does lower the central density and begins to move the density more in line with cosmological predictions, it is still significantly lower than expected. For And XXI and And XXV, dark matter heating alone cannot explain the unusually low central densities.

3.2.3 Dark Matter Profiles

For the dark matter profiles, we assume the functional form of an $\alpha\beta\gamma$ broken power law (Hernquist, 1990; Zhao, 1996; Kravtsov et al., 1998):

$$\rho(r) = \frac{\rho_0}{(r/r_s)^\gamma \left[1 + (r/r_s)^\alpha\right]^{(\beta-\gamma)/\alpha}}, \tag{3.6}$$

For the usual cuspy NFW the profile (Navarro et al., 1996b) is such that $(\alpha, \beta, \gamma) = (1, 3, 1)$, which gives the typical NFW profile:

$$\rho_{\rm NFW}(r) = \frac{\rho_0}{(r/R_s)\left[1 + (r/R_s)\right]^2}, \tag{3.7}$$

For fully-cored NFW profiles $(\alpha, \beta, \gamma) = (1, 3, 0)$. However, these fully-cored profiles produce infeasibly larger cores than those formed from baryonic feedback. Furthermore, we have shown in § 3.2.2 that for both And XXI and And XXV we expect the dwarfs to have undergone very little of a cusp-core transformation due to their limited star formation times. Instead, for more realistic cored profiles, we use the `coreNFW` profile described in equation (3.1). By taking the radial derivative of $M_{\rm cNFW}$, we get the density profile for our cored dwarfs:

$$\rho_{\rm cNFW}(r) = f^n \rho_{\rm NFW} + \frac{n f^{n-1}(1 - f^2)}{4\pi r^2 r_{\rm c}} M_{\rm NFW}, \tag{3.8}$$

To investigate dwarfs residing in halos with unusual concentration parameters, we determine the distribution of concentration parameters for each dwarf via a bootstrap method. For each dwarf, we drew 100,000 random samples from the Dutton & Macciò (2014) mass-concentration relation:

$$\log_{10}(c_{200}) = 0.905 - 0.101 \log_{10}(M_{200}h - 12), \tag{3.9}$$

allowing for the natural scatter of $\sigma \log_{10}(c_{200}) = 0.1$. From this, we found that for both dwarfs, the concentration parameter can vary from ~ 14 to ~ 3 for c_μ to $c_{-3\sigma}$ respectively.

For WDM cosmologies, the structure of the halos have been shown to be essentially identical in functional form to the CDM profiles described in equations (3.7 and 3.8), but are normalised to have lower central densities than CDM, as a result of their later formation (Schneider et al., 2012). The mass-concentration relation will be suppressed due to the later formation times. We implement the relation outlined in Schneider et al. (2012) to account for this:

$$\frac{c_{\rm WDM}(M)}{c_{\rm CDM}(M)} = \left(1 + 1.5 \times \frac{M_{\rm hm}}{M}\right)^{-0.3} \tag{3.10}$$

When determining the unusual concentration parameters for WDM profiles, we shift the mean of the distribution using this conversion and assume that the distribution has the same intrinsic scatter as the Dutton & Macciò (2014) relation of $\Delta \log_{10}(c_{200}) = 0.1$. We investigated a range of WDM particles, with thermal relic masses varying from 10 keV to 1 keV.

Finally, for the SIDM dark matter profile, we use the model for the SIDM halo

density profile derived from Rocha et al. (2013), which assumes a constant, velocity-independent self-interaction cross-section, σ/m. We define a radius, r_1, where, for a given age of halo, the scattering rate per particle is equal to one. At radial distances of $r > r_1$, the halo follows an NFW profile, however, inside r_1, the density instead follows a Burkert profile:

$$\rho_B(r) = \frac{\rho_0}{(1 + r/r_B)(1 + r^2/r_B^2)}, \tag{3.11}$$

where r_B is the Burkert core radius. For dwarf-scale halos, $r_B \approx 1.3r_1$ based of fits to the Merry and Pippin halos from Elbert et al. (2015, $M_{200} \sim 10^{10} M_\odot$) as well as the low-mass halos range of Rocha et al. (2013, $M_{200} \sim 10^{12} M_\odot$). We do not include baryonic feedback effects in the production of the coring for our SIDM profiles. For And XXI and And XXV, this is a valid assumption as the coring due to star formation will be negligible compared to the coring due to self-interactions. This assumption should be a good approximation for all but the most massive satellites (e.g. the Large and Small Magellanic Clouds, Sagittarius, and Fornax; Robles et al., 2017).

3.2.4 Tidal Stripping

While tidal stripping largely removes mass outside-in, it removes mass at all radii, and can significantly lower central densities. Thus to model how tidal stripping lowers the densities of And XXI and XXV, we follow the procedure outlined in Peñarrubia et al. (2010), which is based on fitting functions to high-resolution N-body simulations. We use the implementation in the open-source code `dis`[1], which has been described in Kim & Peter (2021). We summarise the key details here.

Peñarrubia et al. (2010) found that when satellites with $\alpha\beta\gamma$ profiles (Hernquist, 1990; Zhao, 1996; Kravtsov et al., 1998) are stripped, their density profiles rapidly converge to r^{-5} at large radius. We adopt their fits for how the structure and normalization of density profiles change with increasing stripping. As noted in Appendix A of Kim & Peter (2021), their prescription can cause an artificial rise in density at small radii $\lesssim r_{200}/100$ when the halos are first stripped, contrary to expectations that densities monotonically fall with stripping at all radii. This could potentially affect our calculations at 150 pc. However, it was only found to be an issue for small tidal mass loss ($m_{\rm left} > 0.9$). As we only consider profiles with moderate tidal stripping ($m_{\rm left} \leq 0.1$) or no tidal stripping ($m_{\rm left} = 1$), we do not expect this phenomenon to be an issue. Fits were not provided for non-$\alpha\beta\gamma$ profiles in Peñarrubia et al. (2010). Thus for coreNFW and SIDM profiles, which are both modified NFW profiles, we conservatively use the tidal stripping formulae for stripped NFW profiles. The resultant densities are thus upper limits, as cored halos are more severely affected by stripping than cuspy NFW halos.

Using `dis`, we investigate three stages of tidal stripping (1) no tidal stripping ($m_{\rm left} = 1$), (2) moderate tidal stripping ($m_{\rm left} = 0.1$, i.e 90% tidal mass loss) and (3) extreme tidal stripping ($m_{\rm left} = 0.01$, i.e 99% tidal mass loss). These values of tidal stripping were chosen because a noticeable reduction in the central densities

[1] https://github.com/stacykim/disSat/tree/main

of dwarf galaxies is expected at $\sim 90\%$ for dwarfs in a cored halo and $\sim 99\%$ for dwarfs in a cuspy halo (Peñarrubia et al., 2010).

For a scenario to be considered a viable solution, it needs to be able to explain the density across the radial density profile, not just the centre. For example, a potential density lowering mechanism may be able to eventually reduce the central density but result in a density that is far too low at the outskirts. As such, we require a scenario to be able to reconcile the density at both the centre ($r = 150$ pc) and the half-light radius ($r = r_{\rm h}$). These values are derived from the density profiles presented in Collins et al. (2021); Charles et al. (2023): $\rho_{r_{\rm h}} = 2.8^{+0.9}_{-0.7} \times 10^6$ M$\odot$ kpc^{-3} - And XXI and $\rho_{r_{\rm h}} = 3.0^{+1.0}_{-0.7} \times 10^6$ M$\odot$ kpc^{-3} - And XXV, $\rho(150\text{pc}) = 2.6^{+2.4}_{-1.5} \times 10^7$ M$\odot$ kpc^{-3} - And XXI and $\rho(150\text{pc}) = 2.3^{+1.4}_{-1.1} \times 10^7$ M$\odot$ kpc^{-3} - And XXV.

3.3 Results

3.3.1 Cold Dark Matter (CDM)

Firstly we consider And XXI and And XXV in the standard ΛCDM cosmology, the results for which are shown in Figure 3.1. And XXI is shown in the left panels, and And XXV in the right panels. Furthermore, the top panels show the density results at $r = 150$ pc and the bottom panels at $r = r_{\rm h}$ (AndXXI: $r_{\rm h} = 922$ pc, And XXV: $r_{\rm h} = 590$ pc Savino et al., 2022). The grey line and shaded region show the observed densities and corresponding 1σ uncertainty for both dwarfs. The values were obtained from the radial profile measured from the dynamical mass modelling of both dwarfs (Collins et al., 2021; Charles et al., 2023). The dark blue lines show the results assuming an NFW density profile, whereas the light blue lines assume a coreNFW profile. The line series illustrate different tidal stripping prescriptions. The corresponding shaded region for each line illustrates the 1σ uncertainty, which is comprised of the observational uncertainties mostly dominated by the uncertainty in M_{200} arising from the abundance matching. Moving from left to right across each panel highlights the effect of reducing the halo concentration. Starting with a median concentration halo, c_μ, to an extremely low-density halo, $c_{-3\sigma}$. For a tidal stripping or halo concentration scenario to work, the theoretical density we derive must match the observed at both points of the radial profile.

For both dwarfs, we find that the NFW profile cannot explain both the low central and half-light radius densities of And XXI or And XXV. Furthermore, we find that for And XXV, the NFW profile with no tidal stripping (dark blue solid line) we cannot recover the half-light radius density at all, producing results that are too dense for all of the scenarios we investigated. Even when accounting for slight coring due to star formation (light blue solid line), we still cannot recover the density at both parts of the radial profile, thus, other density-lowering mechanisms are required, which we investigate below. Moreover, when comparing the two profiles, we can see that for both dwarfs at the outskirts, there is very little difference. This is because the NFW and coreNFW profiles are similar at large r since the coring only affects the centre. Therefore, when we move into the centre, we see the two profiles diverge more noticeably; this is especially true for And XXI as it has slightly higher coring than And XXV, so the difference between NFW and coreNFW will

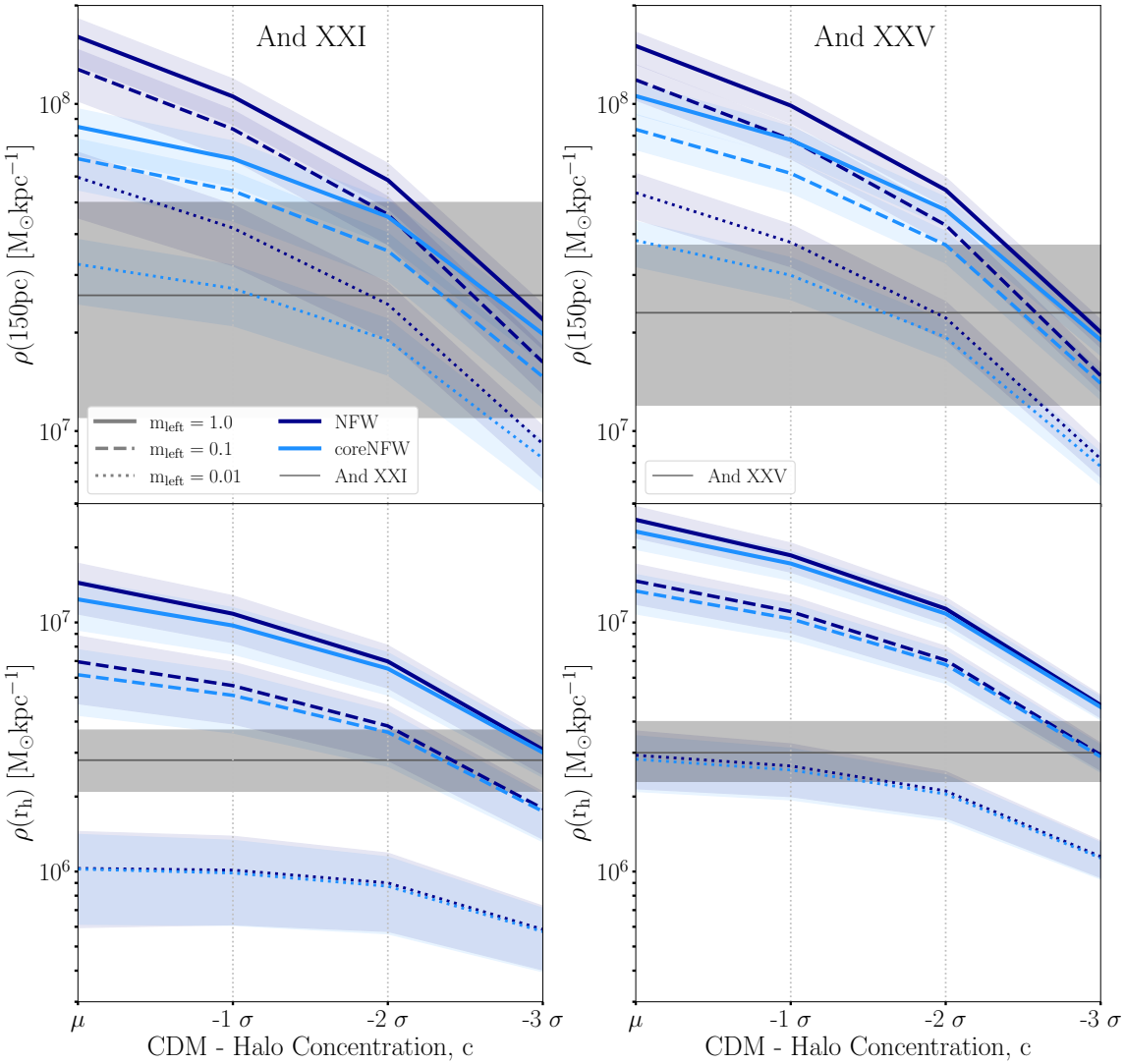

Figure 3.1: Left Top: The density measured at 150 parsecs from the centre of And XXI against the concentration of the dark matter halo. The dark blue line series describes a standard NFW profile, whereas the light blue line series describes the coreNFW that accounts for coring due to star formation. The shaded regions show the 1σ uncertainty due to M_{200}. The line shows the density for an unstripped And XXI, the dashed line for a tidal mass loss of 90% and the dotted line for 99%. The grey line and shaded region show the density at 150pc measure for And XXI and the corresponding 1σ uncertainty. **Left Bottom**: The same as above, but now for the density at the half–light radius. **Right:** The same as before, but for And XXV

be more pronounced. This shows that even a small amount of coring due to star formation ($n \sim 0.18 - 0.37$) is enough to reduce the dwarf's central density to a noticeable difference.

CDM: Tidal Stripping

Firstly, we turn our attention to the effects of tidal stripping on And XXI and And XXV. For both dwarfs, we ask, how likely is tidal stripping? And XXV is one

of the closest M31 satellites at a 3D-projected distance of only 85.2 kpc (Savino et al., 2023). And XXI is further away at 124.4 kpc (Savino et al., 2023). Orbital histories would allow us to determine if either dwarf had a previous close approach with M31 and how likely a tidal stripping scenario is. For the Milky Way dwarfs armed with proper motions, it is possible to determine the orbital histories of the dwarfs. For example, proper motions are available for Antlia II and Crater II, which show that both are on plunging orbits, with a pericentres only 10s of kpc from the galactic centre (Fritz et al., 2018; Fu et al., 2019; Torrealba et al., 2019). It has, therefore, been suggested that tides are a potential culprit for the low central densities of Antlia II and Crater II (Torrealba et al., 2016; Caldwell et al., 2017; Sanders et al., 2018; Fu et al., 2019; Torrealba et al., 2019; Ji et al., 2021 but for Crater II see a detailed study by Borukhovetskaya et al., 2022, refuting tides in CDM). Unfortunately, proper motions are currently unavailable for And XXI and And XXV; as such, it is impossible to concretely conclude the tidal impact experienced by the dwarfs. Although, it is also important to remember that even if we had access to hypothetical proper motions for the M31 dwarfs, caution still needs to be applied as it has been shown that the current orbital properties of dwarfs are not always a robust indicator of possible past close interactions (Lux et al., 2010; Genina et al., 2022).

Without proper motions, we must instead turn to any possible fingerprints that may allude to And XXI or And XXV having undergone tidal interactions. Both dwarfs do not exhibit any tidal substructure, such as tidal tails, in their photometry. However, it is important to note that dark matter is preferentially stripped over the stars as the stellar component is strongly embedded in the halo. A dwarf can, therefore, be excessively stripped by tidal forces and not demonstrate any observable tidal features in the stars until extreme mass loss has occurred ($\gtrsim$ 90 per cent for an NFW profile, Peñarrubia et al., 2008, 2010; Errani et al., 2018). Furthermore, the photometry was gathered as part of a wide field survey designed for large-scale, whole-population dwarf discovery. As such, the instrumental setup is not dedicated to detecting low surface brightness features such as tidal substructures, which requires very deep photometry across a wide field of view that covers many half-light radii (e.g. Shipp et al., 2022). It is plausible that And XXI and And XXV may have some tidal substructure that could be revealed by deeper photometry.

Kinematically, both dwarfs display some unusual features in their velocity dispersion profiles. And XXV displays a potential radially increasing velocity dispersion profile, which may indicate that the dwarf is not in dynamical equilibrium due to a tidal interaction (Charles et al., 2023). A similar bump in the radial profile is observed for And XXI (Collins et al., 2021). However, this kinematic flaring is not considered statistically significant, likely due to small-number statistics issues arising from the relatively small sample sizes, and no concrete evidence of tidally induced velocity gradients can be garnered (Collins et al., 2021; Charles et al., 2023). Although interestingly, a similar kinematic trait can also be observed in Antlia 2. Armed with a larger kinematic sample, the authors concluded this was likely an indication of tidal interaction (Torrealba et al., 2019). Furthermore, when comparing both And XXI and And XXV to dwarfs of similar stellar mass, it can be seen that they are both outliers on the stellar-mass-half-light radius relation. The dwarfs

display a 'puffy' or radially extended morphology, with significantly less mass compared to objects of similar size or luminosity (Collins et al., 2021; Charles et al., 2023)

Finally, we look at the luminosity-metallicity relation. Dwarfs that have undergone extreme tidal interactions resulting in stellar mass loss are expected to be outliers of this relation (e.g. Tucana III, see Simon et al., 2017). Both dwarfs lie perfectly on luminosity-metallicity relation (Collins et al., 2021; Charles et al., 2023), which suggests they have not lost significant *stellar* mass through tides, although stripping ∼50 per cent of the stars may be allowed within the scatter of the relation. Moreover, through tidal shocking it is possible for dwarfs to lose significant amounts of dark matter without any associated stellar mass loss (e.g. Read et al., 2006).

Even if irrefutable evidence of a tidal interaction is not observed in a dwarf, it is important to note that does not mean a tidal interaction has not occurred, as dwarfs can undergo tidal interactions but show no observable tidal substructure (Read et al., 2006; Peñarrubia et al., 2009; Genina et al., 2022). This is especially true for dwarfs with highly eccentric orbits. The tidal shocking is restricted to the extreme pericentric phase of the orbit; as such, the dwarfs can return to equilibrium on a dynamical timescale, quickly erasing any signs of the interaction. The current observational data shows some hints that And XXI and And XXV may have undergone tidal stripping. However, it is not possible to definitively confirm (nor discount) a tidal stripping scenario.

In Figure 3.1 we demonstrate the effects of tidal stripping. Due to the uncertainty surrounding And XXI and And XXV's tidal history, we investigate a variety of tidal stripping scenarios, ranging from $m_{\rm left} = 1$ (no tidal stripping, solid line), $m_{\rm left} = 0.1$ (moderate tidal stripping - 90%, dashed line) and $m_{\rm left} = 0.01$ (extreme tidal stripping - 99%, dotted line). For And XXV, the density at both points of the radial profile can be explained if the dwarf has experienced 99% tidal mass loss. However, we do note that this would be on the extreme end allowed by the current observational data. Whereas, for And XXI, we find that 99% tidal mass loss can reproduce the density at the centre but strips too much mass at large radii and results in too low of a density at the outskirts. We do not find a tidal stripping scenario that alone can explain the density profile of And XXI.

CDM: Unusual Halo Concentrations

Next, we investigate the effects of the concentration of the dark matter subhalo that the dwarf resides in. How probable is a low-concentration halo for And XXI and And XXV? Due to the known scatter in the mass-concentration relation, there will be a variety of permissible halo concentrations. Indeed, around the Milky Way, it has been proposed that Antlia II and Crater II could reside inside low-concentration halos (Amorisco, 2019). Furthermore, dwarfs that reside in low-concentration halos are artificially puffed up by tidal heating, which could explain the unusual radial behaviour shown by both dwarfs. We also find evidence of halos that appear to be outliers in the opposite direction with overly dense centres (e.g. Draco, Read et al., 2018).

We consider a range of halo concentrations accounting for the scatter in the

Table 3.1: The lowest amount of tidal stripping required to reconcile the density of And XXI and And XXV at $r = 150$ pc and $r = r_{\rm h}$ in a CDM paradigm, for different halo concentrations and dark matter profiles.

halo concentration	NFW (CDM)		coreNFW (CDM)	
	And XXI	And XXV	And XXI	And XXV
c_{μ}	-	-	-	0.01
$c_{-1\sigma}$	-	0.01	0.1	0.01
$c_{-2\sigma}$	0.1	0.01	0.1	0.01
$c_{-3\sigma}$	1.0	0.1	1.0	0.1

concentration-mass relation, ranging from an average halo (c_{μ}) to halos 3σ below the median ($c_{-3\sigma}$), moving from left to right in Figure 3.1. This translates to a range of concentration parameters of ∼14 to ∼3 for both dwarfs. We find that And XXV cannot be explained by a low-concentration halo alone. However, the low density of And XXI can be explained if it resides inside a $c_{-3\sigma}$ outlier with no requirement for tidal stripping.

The key question is, how many satellites of M31 do we expect to reside inside these extreme concentration halos? Recent work by Doliva-Dolinsky et al. (2023) predicts that M31 hosts 92^{+19}_{-26} satellites within the magnitude range of $-17 < M_{\rm V} < -5.5$ and the projected distance range from M31 of $30 < r_{\rm M31} < 300$ kpc. Even accounting for the upper limit on the number of satellites at 111, we would expect only one (∼0.17) subhalo with a concentration of $< c_{-3\sigma}$. Currently, out of the two dwarfs we have investigated, we only require And XXI to reside inside a $< c_{-3\sigma}$ concentration halo, which is in agreement with this expectation. It is also important to remember that both dwarfs were purposely chosen for investigation as they are known to reside in unusually low-density halos. However, if other M31 satellites were also found to require a $< c_{-3\sigma}$ concentration halo, this would bring the number of low-concentration halos into serious tension. For example, an M31 subhalo population of $600 - 960$ would be required such that the existence of two subhalos around M31 with a concentration of $< c_{-3\sigma}$ does not provide a tension. This would, at first glance, appear to be in contrast to the results presented in Doliva-Dolinsky et al. (2023), but it is possible that the predicted satellite population from Doliva-Dolinsky et al. (2023) does not encompass the true subhalo population of M31 when accounting for subhalo destruction and occupancy. Not all of the $600 - 960$ subhalos would necessarily host a luminous component. However, for this to be the case, it would require a halo occupancy fraction of $\sim 10 - 15\%$, which is in stark contradiction with predictions for halos with mass $\sim 10^9$ (e.g. Benson et al., 2002; Okamoto et al., 2008; Benitez-Llambay & Frenk, 2020; Nadler et al., 2020c)

If, instead, we also allow for the inclusion of tides, we find that with 90% tidal mass loss, And XXV can be described by a halo concentration of $\sim c_{-2.5\sigma}$ and And XXI can be explained with only the need for a $\sim c_{-2\sigma}$ halo. Around M31, we would expect between $\sim 2 - 3$ subhalos with a $< c_{-2\sigma}$ concentration, meaning that both And XXI and And XXV are within the expected number of satellites requiring $< c_{-2\sigma}$.

CDM: Summary

Overall we find very little difference between the scenarios permitted by an NFW and coreNFW. With the two profiles sharing the same viable scenarios and the core NFW profile only permitting two additional scenarios (And XXI: $c = c_{-1\sigma} + m_{\rm left} = 0.1$, And XXV: $c = c_{\mu} + m_{\rm left} = 0.01$). This demonstrates that while dark matter heating does begin to lower the central density, this process alone is unable to explain the low central densities of And XXI and And XXV in a CDM cosmology, in part due to the limited coring undergone by these two dwarfs. However, we are able to find a range of possible scenarios involving extreme tidal stripping and unusually low halo concentrations. It is possible to reduce the severity of the required scenario by introducing a combination of both factors. We summarise all of the viable CDM scenarios in Table 3.1.

For And XXI, the simplest solution requires the dwarf to reside inside a halo with a concentration that is a -3σ outlier on the mass-concentration relation. For And XXV simplest solution that invokes the least number of variables is that the dwarf has undergone tidal stripping resulting in $\sim 99\%$ mass loss. Both solutions are on the extreme end of their respective scales, which are potentially difficult to reconcile with observation data (tidal stripping) or cosmological predictions (low concentration). Furthermore, even when combining tidal stripping with low halo concentrations, And XXV requires tidal stripping of $> 90\%$.

3.3.2 Warm Dark Matter (WDM)

Next, we consider And XXI and And XXV in the context of a WDM cosmology as subhalos in WDM have been shown to have densities than CDM (e.g. Schneider et al., 2012). The results are shown in Figures 3.2 and 3.3. We found that similar to CDM, there was little difference between the NFW and coreNFW profiles; therefore, for this analysis, we only show the coreNFW profile (the NFW profiles can be found in Appendix B for completeness).

First, looking at the dwarfs in a simple WDM cosmology, with no mass loss and a median concentration halo, we find that the density of And XXI at both $r = 150$ pc and $r = r_{\rm h}$ can be explained by a WDM particle with a thermal relic mass of $m_{\rm WDM} \sim 1$ keV, whereas, And XXV requires a thermal relic mass of $m_{\rm WDM} < 1$ keV. While the consensus on WDM particle constraints is still widely debated, only a handful of studies have found a lower bound for the WDM thermal relic mass of < 1 keV (e.g. Vegetti et al., 2018; Ritondale et al., 2019 - gravitational lensing; Alvey et al., 2021 - dwarf galaxies).

Instead, many previous studies investigating a range of astronomical systems have ruled out a WDM particle this extreme, instead favouring a range of lower bounds as low as $m_{\rm WDM} \sim 2$ keV up to $m_{\rm WDM} \sim 7$ keV (e.g. Viel et al., 2006; Seljak et al., 2006; Iršič et al., 2017; Murgia et al., 2018 - Lyman-α emission lines; Polisensky & Ricotti, 2011; Kennedy et al., 2014; Jethwa et al., 2018; Nadler et al., 2019, 2020c,b; Newton et al., 2021 - MW satellites; Gilman et al., 2019, 2020; Hsueh et al., 2020 - flux ratios of gravitational lensing images; Erkal & Belokurov, 2015; Banik et al., 2018; Banik & Bovy, 2019 - stellar streams). Furthermore, recent works combining the results from multiple different dark matter probes have pro-

vided even tighter constraints, resulting in higher lower bounds for WDM thermal relic mass. For example, a study by Banik et al. (2021) combining constraints from stellar streams and dwarf galaxy satellite counts found $m_{\rm WDM} > 6.2$ keV. A similar study probing dark matter substructure through a combination of strong gravitational lensing and MW satellite counts found an even more stringent constraint of $m_{\rm WDM} > 9.7$ keV (Nadler et al., 2021). Whereas, Enzi et al. (2021) combined three probes, strong gravitational lensing of extended sources, the Lyman-α forest, and MW satellite counts found a more lenient constraint of $m_{\rm WDM} > 6$ keV. Most recent studies favour $m_{\rm WDM} > 3$ keV (potentially up to $m_{\rm WDM} > 5$ keV) predominantly from Lyman-α analysis, with multiprobe studies potentially hinting at the need for a higher constraint of $m_{\rm WDM} \gtrsim 6$ keV.

We conclude that the thermal relic masses required to explain the low central densities of And XXI and And XXV with WDM alone are ruled out by current constraints. Instead, we find we need to either invoke tides, an unusual halo concentration or a combination of both to recover the low central densities of And XXI and And XXV. We investigate the effect of each in turn below.

WDM: Tidal Stripping

Here we consider And XXI and And XXV in a WDM cosmology allowing for tidal stripping (note these profiles consider a halo of median concentration, c_μ). The results are shown in Figure 3.2. Even in WDM, significant tidal stripping is required to explain the low central densities of each dwarf. We find that the central density of And XXI can be explained with only 90% tidal mass loss for thermal relic masses of $m_{\rm WDM} < 3$ keV. However, 3 keV is on the extreme lower end of literature constraints (and potentially ruled out by recent multiprobe work). Although, if we allow for 99% tidal mass loss instead, we find that while the central density is reconciled, the density at the outskirts is too low - similar to the behaviour observed for CDM. Moving now to And XXV, again similar to the results for CDM, we find that for WDM with thermal relic masses of $m_{\rm WDM} \sim 2 - 10$ keV the density at both parts of the radial profile can be reconciled if And XXV has experienced 99% tidal mass loss.

WDM: Unusual Halo Concentrations

Next, we consider And XXI and And XXV in a WDM cosmology allowing for unusually low halo concentrations (note these profiles do not include tidal stripping, $m_{\rm left} = 1.0$). The results are shown in Figure 3.3. For thermal relic masses of $m_{\rm WDM} < 4$ keV And XXI only requires a halo of $c_{-2\sigma}$ concentration. However, if we move to higher thermal relic masses, we find that And XXI must instead reside inside a $c_{-3\sigma}$ halo, the same as for CDM. For And XXV, the density profile can only be replicated if it resides inside a $c_{-3\sigma}$ concentration halo and, interestingly, only for a thermal relic mass range of $\sim 2.5 - 6.5$ keV within the 68% confidence interval. As discussed in § 3.3.1, we would only expect ∼0.17 halos to have a concentration this low. Therefore, WDM requiring both And XXI and And XXV to be a -3σ outlier already presents a moderate tension, which will only worsen if more dwarfs are found to need such extreme halo concentrations. However, this can be alleviated

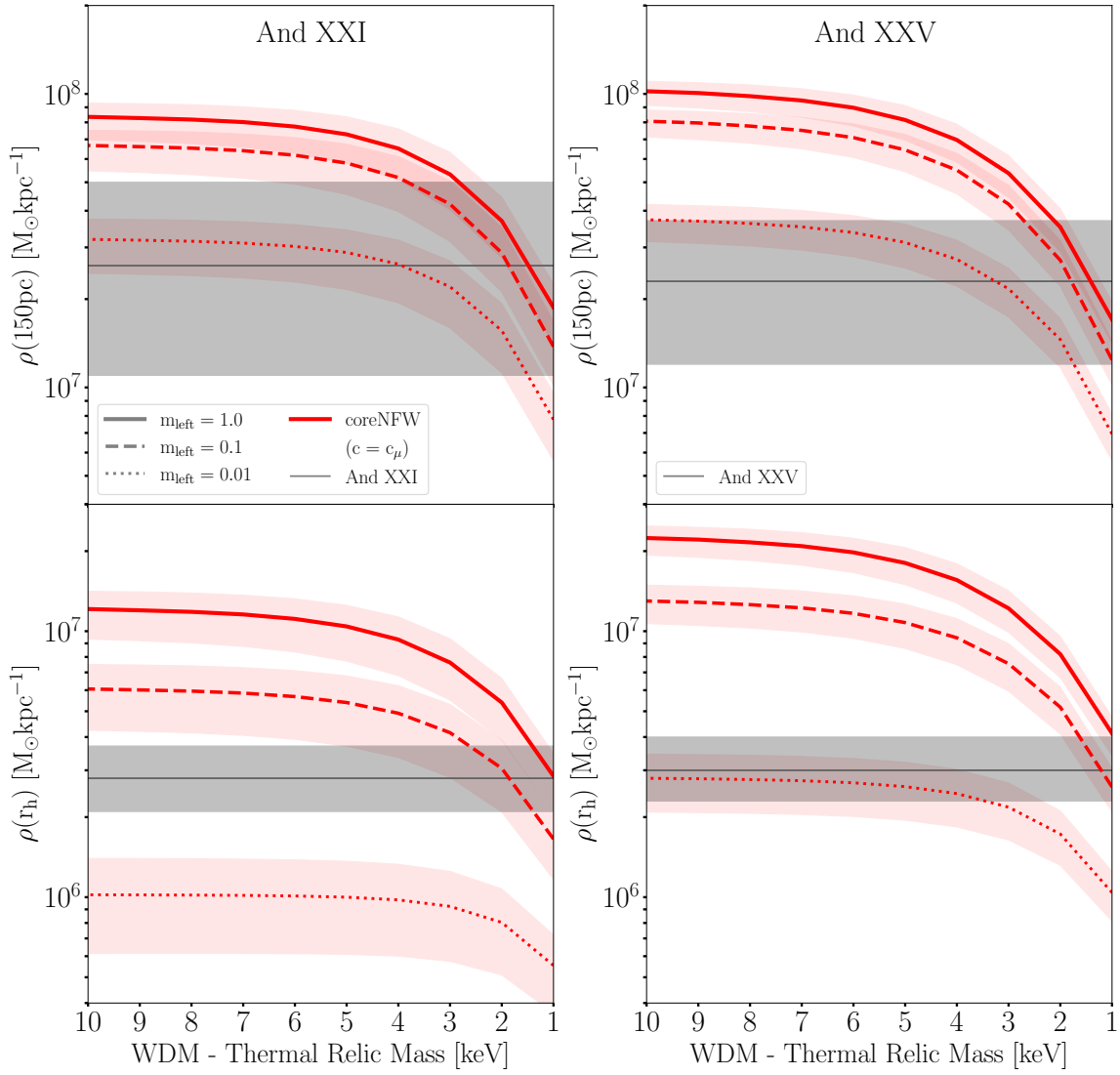

Figure 3.2: Left Top: The density measured at 150 parsecs from the centre of And XXI against the thermal relic mass of the WDM particle. The red line series describes the coreNFW that accounts for coring due to star formation. The shaded regions show the 1σ uncertainty due to M_{200}. The line shows the density for an unstripped And XXI, the dashed line for a tidal mass loss of 90% and the dotted line for 99%. Note here we consider the effect of only tidal stripping in a WDM cosmology; as such, the concentration of the halo is held at a constant c_μ. The grey line and shaded region show the density at 150pc measure for And XXI and the corresponding 1σ uncertainty. **Left Bottom**: The same as above, but now for the density at the half-light radius. **Right:** The same as before, but for And XXV

somewhat if And XXV is instead a result of tidal interactions as outlined above in §3.3.2.

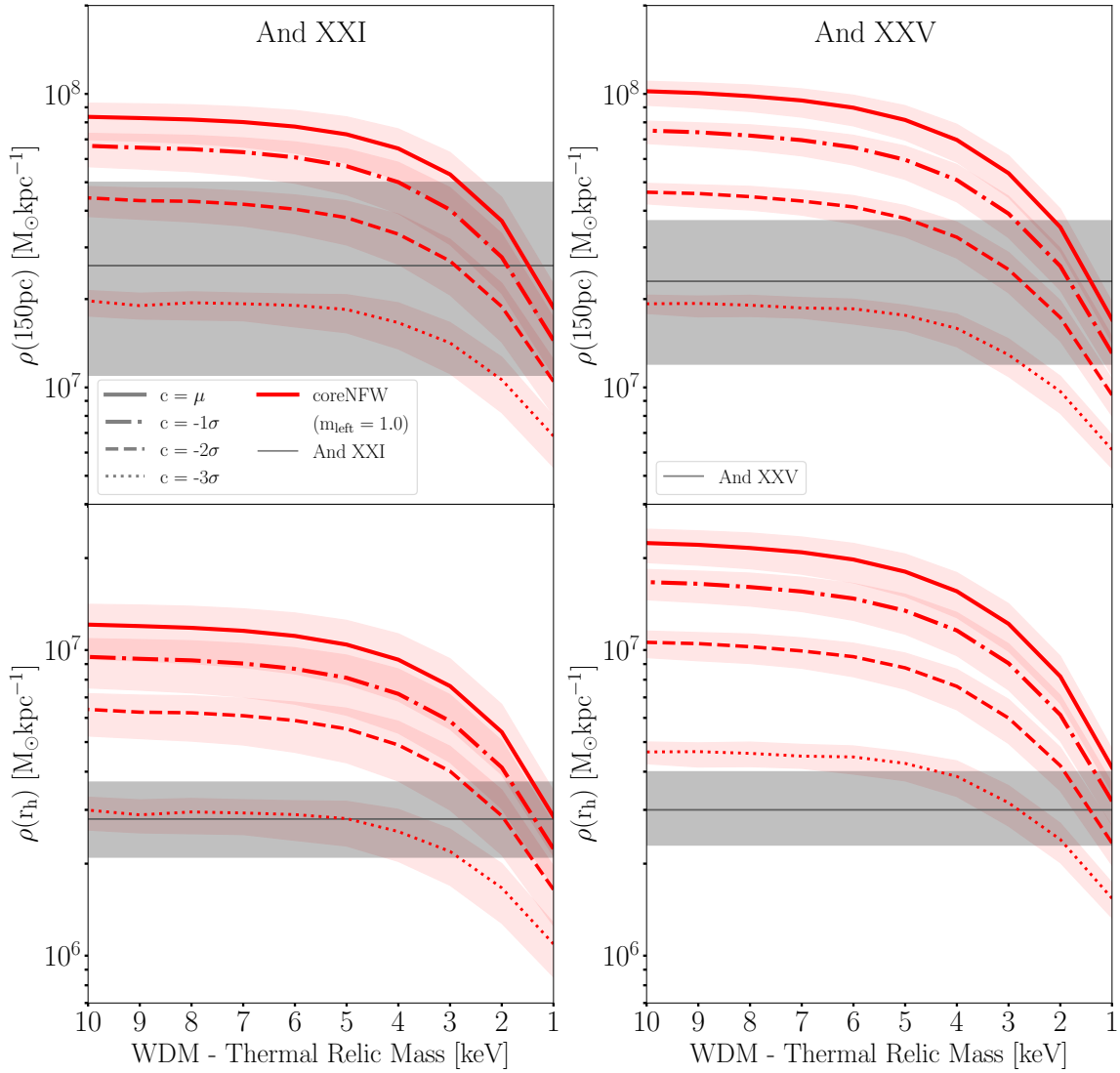

Figure 3.3: Left Top: Again, showing the density measured at 150 parsecs from the centre of And XXI against the thermal relic mass of the WDM particle where the red line series describes the coreNFW that accounts for coring due to star formation and the shaded regions show the 1σ uncertainty due to M_{200}. However, this figure shows only the effects of halo concentration; as such, these profiles are not tidally stripped ($m_{\rm left} = 1.0$). The solid line shows the density for an average concentration halo (c_μ) And XXI, then dot-dashed, dashed, and dotted lines illustrate a $c_{-1\sigma}$, $c_{-2\sigma}$ and $c_{-3\sigma}$ halo concentration, respectively. The grey line and shaded region show the density at 150pc measure for And XXI and the corresponding 1σ uncertainty. **Left Bottom**: The same as above, but now for the density at the half-light radius. **Right:** The same as before, but for And XXV

3.3.3 WDM - Combining Tides and Unusual Halo Concentrations

Here we present the results combining both low halo concentration and tidal stripping in a WDM cosmology for a coreNFW profile. Figure 3.4 and Figure 3.5 show

a snapshot of different halo concentrations accounting for tidal stripping mass loss regime of $m_{\rm left} = 0.1$ and $m_{\rm left} = 0.01$, respectively.

By combining density lowering mechanisms it is possible to reduce the severity of the required scenario. For example, for And XXI accounting for tidal stripping resulting in $m_{\rm left} = 0.1$ we find that the halo concentration requirement is relaxed to $c_{-2\sigma}$. Furthermore, for And XXV we can reconcile the density profile if it resides in a $c_{-3\sigma}$ concentration halo.

For a tidal stripping scenario of $m_{\rm left} = 0.01$ we are unable to reconcile the density at the outskirts ($r = r_{\rm h}$) for And XXI as the resulting density is too low. It is possible that And XXI instead resides inside an overly dense halo (i.e. $c_{+n\sigma}$), and as such a tidal stripping scenario of $m_{\rm left} = 0.01$ cannot be ruled out. However, the puffy, radially extended nature of And XXI would be an intriguing characteristic of an overly dense halo. On the other hand, for And XXV we can explain the density profile with a combination of tidal stripping such that $m_{\rm left} = 0.01$ and a $c_{-1\sigma}$ or c_{μ} halo concentration.

WDM:Summary

We find the simplest solution for And XXV for sensible WDM masses is to allow for 99% tidal mass loss. However, we do not find a tidal stripping scenario that works for And XXI. Instead, And XXI, for sensible WDM masses, requires a $c_{-3\sigma}$ concentration halo. These results mimic those for CDM. Furthermore, similar to CDM, the tidal stripping and halo concentrations required are on the extreme end. Although it is again possible to reduce the rarity of both dwarfs by allowing for a combination of both factors. For example, And XXI can be explained with a $c_{-2\sigma}$ halo if it has undergone 90% tidal stripping and And XXV can be reconciled with a halo concentration of only $c_{-1\sigma}$ but needs 99% tidal mass loss.

3.3.4 Self-Interacting Dark Matter (SIDM)

Finally, in Figure 3.6, we investigate And XXI and And XXV in the context of a SIDM cosmology. We investigate a range of constant cross-sections from 0.5 to 50 cm^2/g. For a halo with no stripping ($m_{\rm left} = 1.0$) and a median concentration (c_{μ}) in a SIDM cosmology, we do not find a constant cross-section scenario that can explain either And XXI or And XXV. We find that the constant-cross-section models are too effective at forming large and extended cores in the centre. As such, the level of tidal stripping required to reconcile the density at the half-light radius results in a central density that is too low. If we allow for 90% tidal stripping, then we can tentatively reconcile the density within the 1σ uncertainties for a cross-section of $\sigma_{\rm m} = 4 - 5$ cm^2/g for And XXI. Furthermore, for And XXV, we can only recover a cross-section $\sigma_{\rm m} \sim 5$ cm^2/g within the 2σ uncertainties allowing for 90% tidal stripping. This result is in agreement with other recent work that has been shown to discount constant cross sections for SIDM cosmologies (e.g. Zavala et al., 2019; Kim & Peter, 2021; Slone et al., 2021; Silverman et al., 2022). SIDM was first introduced as a potential solution to some of the small-scale challenges for CDM, and these solutions required a cross-section in the order of $\sigma_{\rm SI}/m_{\chi} \sim 1 - 5$ cm^{2}g^{-1} (Zavala et al., 2013; Rocha et al., 2013; Kamada et al., 2017; Ren et al., 2019).

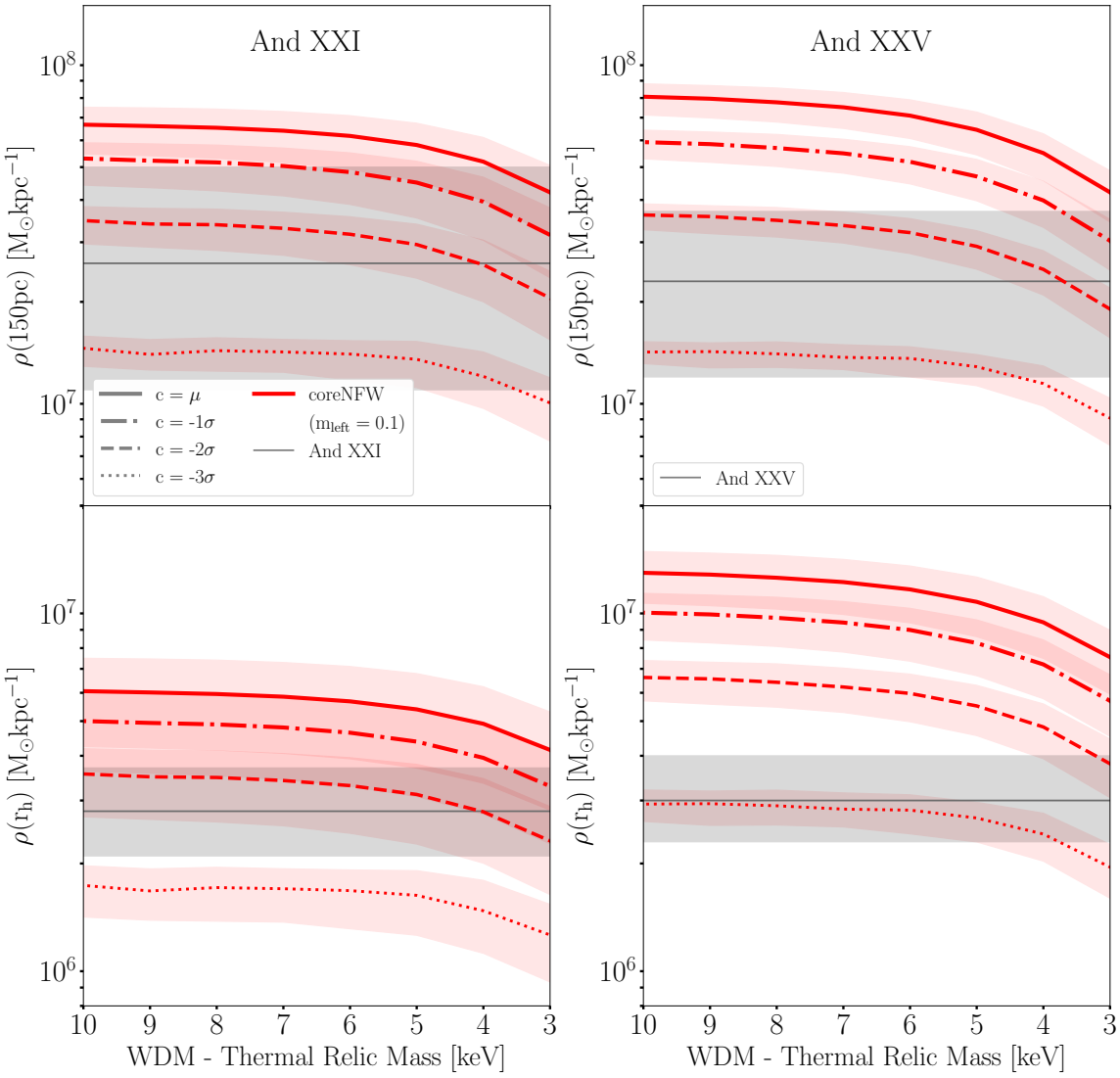

Figure 3.4: Left Top: Again, showing the density measured at 150 parsecs from the centre of And XXI against the thermal relic mass of the WDM particle where the red line series describes an coreNFW profile that accounts for coring due to star formation and the shaded regions show the 1σ uncertainty due to M_{200}. However, this figure shows only the effects of halo concentration; as such, these profiles are not tidally stripped ($m_{\rm left} = 1.0$). The solid line shows the density for an average concentration halo (c_μ) And XXI, then dot-dashed, dashed, and dotted lines illustrate a $c_{-1\sigma}$, $c_{-2\sigma}$ and $c_{-3\sigma}$ halo concentration, respectively. The grey line and shaded region show the density at 150pc measure for And XXI and the corresponding 1σ uncertainty. **Left Bottom**: The same as above, but now for the density at the half-light radius. **Right:** The same as before, but for And XXV

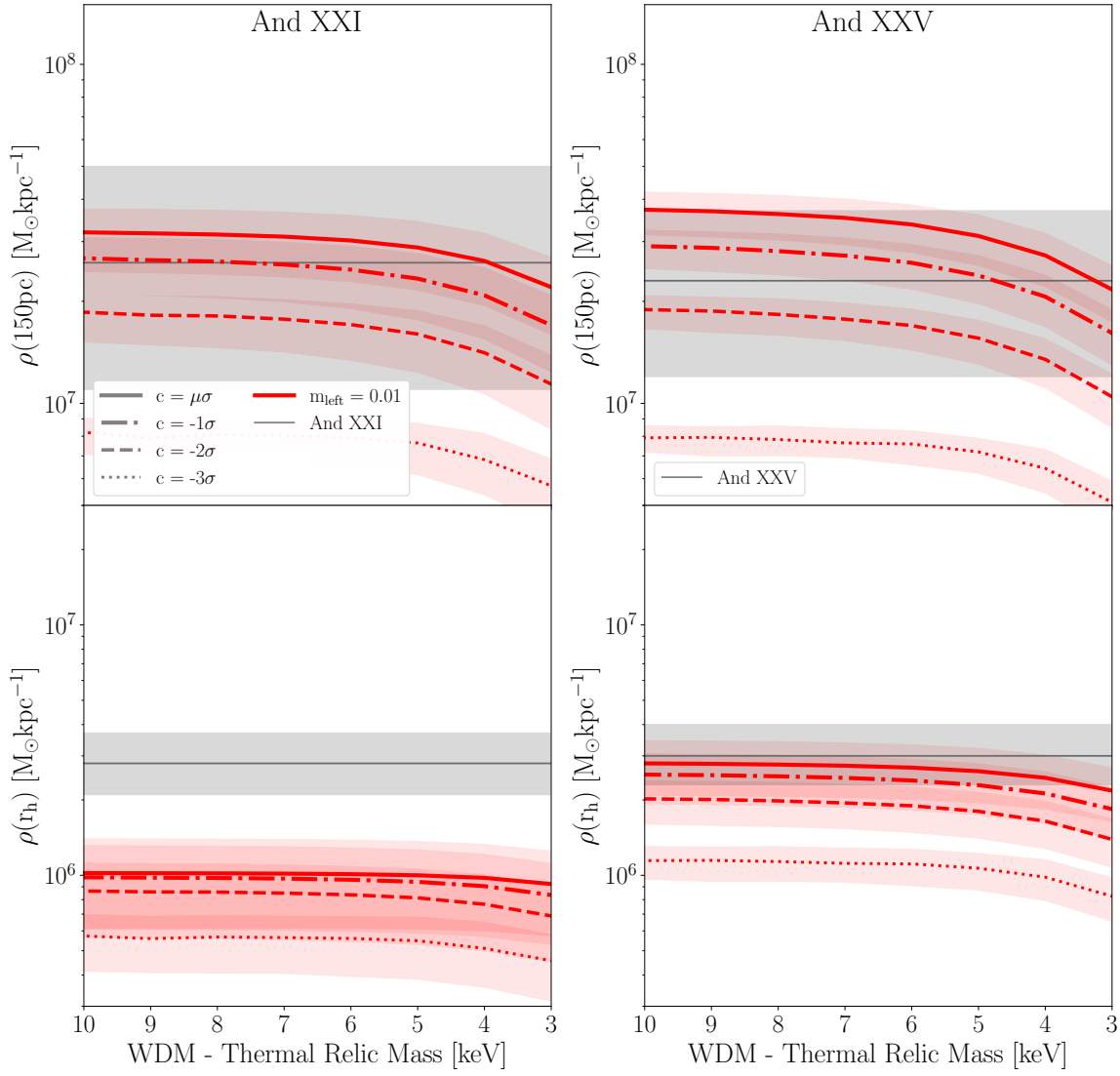

Figure 3.5: Left Top: Again, showing the density measured at 150 parsecs from the centre of And XXI against the thermal relic mass of the WDM particle where the red line series describes an coreNFW profile that accounts for coring due to star formation and the shaded regions show the 1σ uncertainty due to M_{200}. However, this figure shows only the effects of halo concentration; as such, these profiles are not tidally stripped ($m_{\rm left} = 1.0$). The solid line shows the density for an average concentration halo (c_μ) And XXI, then dot-dashed, dashed, and dotted lines illustrate a $c_{-1\sigma}$, $c_{-2\sigma}$ and $c_{-3\sigma}$ halo concentration, respectively. The grey line and shaded region show the density at 150pc measure for And XXI and the corresponding 1σ uncertainty. **Left Bottom**: The same as above, but now for the density at the half-light radius. **Right:** The same as before, but for And XXV

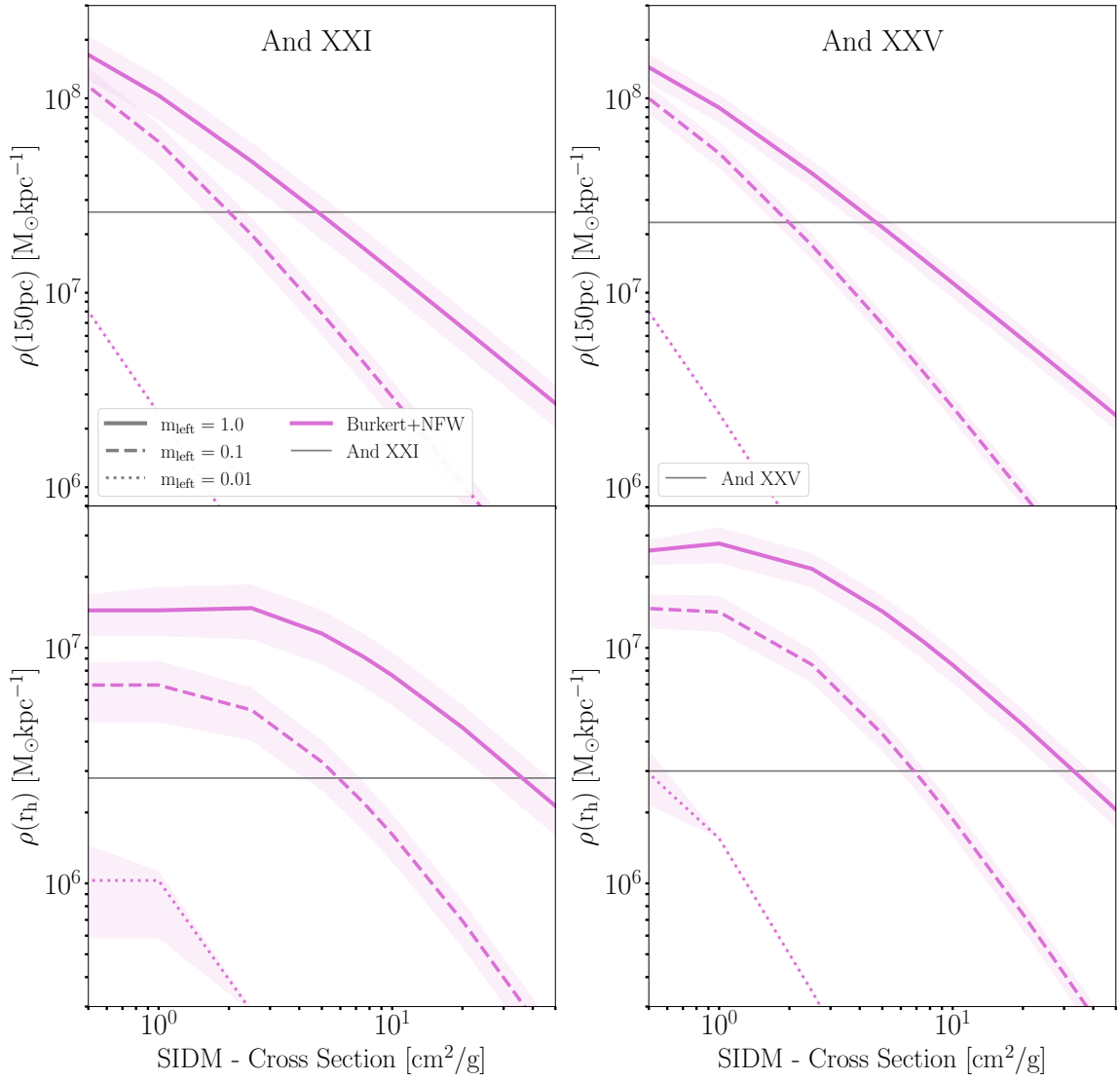

Figure 3.6: **Left**: The density measured at 150 parsecs from the centre of And XXI against the interaction cross-section of the SIDM particle. The purple line series describes the Burkert+NFW profile. The shaded regions show the 1σ uncertainty due to M_{200}. The solid line shows the density for an unstripped And XXI, the dashed line for a tidal mass loss of 90% and the dotted line for 99%. Note here we consider the effect of only tidal stripping in a SIDM cosmology; as such, the concentration of the halo is held at a constant μc. The grey line and shaded region show the density at 150pc measure for And XXI and the corresponding 1σ uncertainty. **Left Bottom**: The same as above, but now for the density at the half-light radius. **Right:** The same as before, but for And XXV

An upper limit on the cross-section of $\sigma_{\rm SI}/m_\chi < 1$ cm^{2}g^{-1} was further reinforced by additional observational sources (e.g. Miralda-Escudé, 2002; Randall et al., 2008; Peter et al., 2013; Harvey et al., 2015; Kim et al., 2017; Wittman et al., 2018; Harvey et al., 2019). Furthermore, constraints from dwarf galaxy observations brought this lower limit down to $\sigma_{\rm SI}/m_\chi < 0.5$ cm^{2}g^{-1} (e.g. Read et al., 2018; Valli & Yu, 2018).

Instead, a velocity-dependent cross-section has been proposed as a solution to the shortcomings of a constant cross-section models (e.g. Kaplinghat et al., 2016;

Vogelsberger et al., 2016; Nadler et al., 2020a; Correa, 2021). In popular velocity-dependant SIDM models, the cross-section is dictated by the relative velocity of the dark matter particles, such that it behaves like a collisional fluid on small scales transitioning to approximately collisionless at large scales. The cross section is roughly constrained to be in the order of 0.1 cm^2g^{-1}, 1 cm^2g^{-1}, and 10 cm^2g^{-1} for galaxy cluster, galactic, and dwarf-galaxy halos, respectively, where the velocity dispersion of DM particles ranges from ~ 1000 to ~ 1 kms^{-1} (e.g. Kaplinghat et al., 2016; Elbert et al., 2018; Sagunski et al., 2021; Andrade et al., 2022). This model type is supported by theoretical work invoking a 'hidden sector' particle physics governed by dark analogues of the fundamental forces (e.g. Feng et al., 2009; Tulin et al., 2013a,b; Boddy et al., 2014; Cline et al., 2014; Cyr-Racine et al., 2016). Interestingly at the characteristic velocities of And XXI and And XXV, the allowed velocity-dependent cross-sections vary a lot, but tend to be of $\mathcal{O}(10-100)cm^2/g$, at which point core-collapse scenarios become important.

Core-collapse scenarios within SIDM are another mechanism which can can alter the central densities (e.g. Lynden-Bell & Wood, 1968; Kochanek & White, 2000; Colín et al., 2002; Balberg et al., 2002; Koda & Shapiro, 2011; Elbert et al., 2015; Zavala et al., 2019; Essig et al., 2019; Turner et al., 2021). This process occurs significantly after the core has formed and reached its maximum size. At this stage, self-interactions can lead to energy outflows from the centre of the dwarf to the outer regions (opposite to the outwards-in energy flow that causes core formation), resulting in energy transfer away from the centre. This redistribution of energy causes the dark matter particles to infall, and this process continues to accelerate in a run-away fashion reestablishing dense centers, denser than that predicted by CDM. Core-collapse was initially discounted as a viable method for producing dwarf with high central densities within SIDM as the process was expected to occur on timescales greater than the age of the Universe (Balberg et al., 2002; Koda & Shapiro, 2011; Elbert et al., 2015; Essig et al., 2019). However, recent work has shown the process can be accelerated by tidal stripping (Nishikawa et al., 2020; Correa, 2021).

From the constant cross-section SIDM results presented in Figure 3.6, all of the scenarios that are able to reconcile the density at the half-light radius produced significantly under-dense central densities. Core-collapse will increase the central density of a dwarf while leaving the density on the outskirts unchanged. It is possible that And XXV and And XXI may be in a transitional period of SIDM core-collapse scenario accelerated by tidal stripping. Although, a detailed study is required to conclusively confirm or omit core-collapse as a possibility for these dwarfs. Furthermore, it is possible that ram pressure stripping and dark matter heating may alter the timescales for which core-collapse scenarios become viable (e.g. Zeng et al., 2022). However, the effects of these processes are still widely unknown. As such, we are currently unable to parameterise their effects to be able to implement into `dis`. Significant further research is required, which is beyond the scope of this thesis. It is also important to consider that `dis` currently implements tidal stripping prescriptions assumed from cusped tidal tracks instead of cored tidal tracks more suited to SIDM models. We aim to implement a feature that allows for a range of inner slope parameterisation and, hence, a range of tidal tracks before the publication of the

manuscript detailed in this chapter.

3.4 Discussion

We have shown that the usually low central dark matter density of And XXI and And XXV cannot be explained simply by the inclusion of stellar feedback. Furthermore, we found that the low central densities could not be explained by *just* tidal stripping, *just* a low halo concentration, or *just* an alternative dark matter model; focusing on a single density-lowering mechanism alone was not sufficient. Instead, we needed a combination of mechanisms (e.g. dark matter heating *and* tides, dark matter heating *and* low halo concentration, tides *and* low halo concentration) to be able to explain these unusual dwarfs. Both And XXI and And XXV can only be understood in CDM if they have experienced stellar feedback *and* reside in extremely low concentration halo ($c_{-3\sigma}$) or have undergone severe tidal stripping ($m_{\rm left} < 0.01$). And XXV favours an extreme tidal stripping scenario ($m_{\rm left} < 0.01$), whereas And XXI favours residing in a halo with very low concentration ($c_{-3\sigma}$). These results demonstrate the importance of considering density lowering effects beyond only the (now standard) stellar feedback when investigating dwarf galaxy evolution. It is possible to slightly lower the severity of the required scenario for both dwarfs by combining the effects of all three density-lowering mechanisms, but the required scenarios were still moderately extreme ($\sim c_{-2\sigma}$, $\sim m_{\rm left} < 0.1$). This highlights the importance of considering effects in combination rather than focusing solely on a single mechanism when considering the diversity of satellite dwarf densities.

This is not an issue specific to CDM, and cannot be simply explained away by considering the two dwarfs in a WDM cosmology. Thermal relic masses of $\lesssim 1$ keV are required to reconcile the density of the two dwarfs. While there is still debate surrounding WDM constraints, WDM thermal relic masses this low have been ruled out by other observations. Moreover, at higher thermal relic masses, the intrinsic halo concentrations (while lower) were comparable to CDM, such that the degree of tidal stripping or concentration outlier required to explain them were similar. SIDM alone also could not explain the densities of And XXI and And XXV, as we were unable to recover any constant cross-section model that could explain the density profile of both dwarfs. We found that a constant cross-section model was too efficient at forming large extended central cores. Alternative SIDM models, such as velocity-dependant or core-collapse models, may be able to reconcile the dark density profile of the two dwarfs; however, further detailed study is required to investigate the viability of the models for And XXI and And XXV.

While the halo concentrations and tidal stripping scenarios required to explain And XXI and And XXV are on the extreme end, it is important to remember that these two dwarfs were chosen because they were known to have unusually low central densities. Furthermore, the results are still in agreement with the number of expected low density halos from CDM expectations. However, if more M31 dwarf galaxies are found to require halos with $c_{-3\sigma}$ concentrations, this would begin to present a serious tension. It is, therefore, important that we continue to probe anomalous dwarfs. Around M31, a potentially interesting candidate is And XIX.

And XIX is an ultra-diffuse galaxy characterised by its large half-light radius and low surface brightness. While this dwarf is yet to undergo dynamical mass modelling to determine its dark matter density profile, features in its kinematics indicate that it may have undergone tidal processes that caused the dwarf to 'puff up', resulting in its extreme size and low surface brightness (Collins et al., 2020), making And XIX an interesting dwarf to study using the methodology presented here. Furthermore, around the Milky Way Antlia II and Crater II have already been identified with low central dark matter densities, similar to And XXI and And XXV, with tides and low concentration halos being put forward as a possible explanation (Torrealba et al., 2016; Caldwell et al., 2017; Sanders et al., 2018; Fu et al., 2019; Torrealba et al., 2019; Amorisco, 2019; Ji et al., 2021. It is also important to consider dwarfs that are outliers in the opposite direction, dwarfs that appear to be over-dense compared to CDM predictions. A valid dark matter model will need to be able to explain a full population of satellite galaxies. For example, Draco and Leo II are Milky Way satellites with high central dark densities (e.g. Read et al., 2018, 2019), as well as the isolated Tucana (e.g. Gregory et al., 2019), which would all make for interesting systems to study in complement to the low-density dwarfs.

The methodology presented here has merit beyond simply studying outlying systems in an attempt to explain their anomalous dark matter profiles. In this study, with only two data points, it is not possible to place significant constraints on different dark matter models. However, it serves as a useful proof of concept. Armed with dark matter profiles for a large population of dwarf satellites, this methodology provides a framework to place meaningful constraints on dark matter models as well as test different mechanisms for galaxy formation and evolution. A substantial handful of Milky Way dwarfs have already been mass-modelled (e.g. Łokas, 2002; Walker & Peñarrubia, 2011; Charbonnier et al., 2011; Jardel & Gebhardt, 2012; Amorisco et al., 2013; Bonnivard et al., 2015; Read et al., 2018; Pascale et al., 2018; Strigari et al., 2018; Read et al., 2019; Zoutendijk et al., 2021; Evans et al., 2022). Conversely, around M31, we currently only have the dark matter density profiles for And XXI (Collins et al., 2021) and And XXV (Charles et al., 2023), although with upcoming work mass-modelling the entirety of the PAndAS M31 dwarfs (Pickett et al., in prep), we will soon have another system population to study.

Along with the dark matter profiles, we need to narrow down the observational sources of uncertainties surrounding the evolution of these dwarfs. The most significant unknown is the orbital histories of the dwarfs from which the degree of tidal stripping can be inferred. For the Milky Way, we are able to garner information surrounding the likelihood of past tidal interactions from proper motions obtained with Gaia (e.g. Fritz et al., 2018; Simon, 2018; Casetti-Dinescu et al., 2018, 2022; Fu et al., 2019; Torrealba et al., 2019; Li et al., 2021). However, due to the distance to the M31 dwarfs, Gaia is unable to provide sufficiently precise proper motions to determine the orbits for the M31 dwarfs. However, recent work by Sohn et al. (2020) has shown that obtaining proper motions for M31 satellites is possible using multi-epoch Hubble Space Telescope (HST) observations across a timeframe of ~ 8 years. The HST-informed proper motions can be complemented with dedicated, deep photometry designed to search for low surface brightness tidal features. We can also place moderate constraints on the amount of coring due to star formation with detailed

star formation histories. Due to their relative distance, the star formation histories of the Milky Way dwarfs are often well-constrained, with deep colour-magnitude diagrams reaching down to the main sequence turn off. However, for the M31 dwarfs, it is not possible to obtain such photometry from ground-based observations. Instead, for the M31 dwarfs, we have to turn to the horizontal branch to derive star formation history. Fortuitously, from Weisz et al. (2014, 2019a), we have access to a wealth of star formation histories for the M31 dwarfs from space-based horizontal branch imaging. Furthermore, recent studies have shown with multi-orbit space-based observations, it is possible to reach the main sequence turn-off for the M31 (Skillman et al., 2017; Collins et al., 2022a; Savino et al., 2023).

We propose with upcoming dynamical mass-modelling for the M31 dwarfs, in combination with improvements to observations to narrow down uncertainties, the dark matter density profiles of dwarf galaxies will make powerful probes to place meaningful constraints on dark matter physics and dwarf galaxy formation and evolution.

3.5 Conclusions

And XXI and And XXV are two dwarf galaxy satellites of M31 with usually low central densities. In this chapter, we investigated a range of central-density lowering mechanisms and dark matter models to identify possible formation and/or cosmological scenarios which could explain the low central densities of these dwarfs. Our key findings are as follows:

- We show that stellar feedback alone cannot explain the low central densities of And XXI and And XXV. Instead, other density-lowering mechanisms are required in combination with stellar feedback. This highlights the importance of considering other baryonic feedback processes other than just the (now standard) stellar feedback.
- In both CDM and WDM, an NFW profile cannot explain the density of And XXV, even when accounting for extreme tidal stripping or low halo concentrations, indicating the need for some initial coring due to stellar feedback.
- The density profile of And XXV can be reconciled if the dwarf has experienced an extreme tidal stripping regime of $> 99\%$ tidal mass loss in both CDM and WDM cosmologies.
- The density profile of And XXI can be recovered if the dwarf resides inside a halo that is a -3σ outlier on the mass-concentration relation. Again, the result was the same in both CDM and WDM cosmologies.
- Only one (~ 0.17) halo around M31 is predicted to have a concentration of $c_{-3\sigma}$. Therefore, while this current requirement for And XXI is in agreement with this prediction, it will present a significant tension if more M31 dwarfs are found to require halos that are -3σ outliers.

- For both CDM and WDM, the rarity of the solution can be slightly reduced by combining the effects of both tidal stripping and low-concentration halos, but the resulting scenarios still require moderate stripping and low halo concentrations ($> 90\%$ tidal mass loss and halos that are a $\gtrsim -2\sigma$ outlier).
- WDM alone cannot reconcile the low densities of And XXI and And XXV as the thermal relic masses required were in the region of ~ 1 keV, which have been ruled out by other observations.
- We were unable to recover a constant cross-section SIDM model that could explain the density of either dwarf. It is possible that other SIDM models (such as velocity-dependent models or core-collapse scenarios) may be viable, although this was out of the scope of this study.
- We propose the methodology presented in this study, in combination with the dark matter density profiles from upcoming dynamical mass-modelling of the M31 PAndAS dwarfs, will provide a crucial tool for placing meaningful constraints on dark matter models and galaxy evolution processes.

Discovering New Andromeda/Triangulum Satellites

Manuscripts

The work presented in this chapter is based on the following two manuscripts published in Monthly Notices of the Royal Astronomical Society:

- Pisces VII: discovery of a possible satellite of Messier 33 in the DESI legacy imaging surveys – Martínez-Delgado et al. (2022) *(third author)*
- Pegasus V/Andromeda XXXIV – a newly discovered ultrafaint dwarf galaxy on the outskirts of Andromeda – Collins et al. (2022a) *(second author)*

Statement of contribution

My main contribution to these two studies was designing and implementing the member stars identification, structural parameters and luminosity analysis outlined in § 4.1.3 for Pisces VII and § 4.2.3 for Pegasus V. I also helped validate the `DRAGONS` reduction of the Gemini observations for Pegasus V. Finally, I supported with writing both manuscripts.

The overall and ongoing project is led by David Martínez–Delgado. Both objects were first identified as interesting candidates in the DESI Legacy Imaging Survey by Giuseppe Donatiello and David Martínez–Delgado. Walter Boschin was the PI for the Telescopio Nazionale Galileo observations for Pisces VII. Michelle Collins was the PI for Pegasus V directors discretionary time observations with Gemini. The reduction of both dwarfs was performed by Matteo Monelli. Michelle Collins designed and implemented the distance analysis for both dwarfs.

Summary

In the previous two chapters, we focused on the dark matter distribution inside two anomalous M31 dwarfs. This analysis provided a framework to apply to the remaining M31 population (Pickett et al., in prep). Excitingly, there are many upcoming surveys which promise to discover an abundance of new dwarf galaxies within the Local Group (e.g. Ivezić et al., 2019; Spergel et al., 2015), hopefully providing more interesting anomalous dwarfs to challenge and improve our understanding of dark matter. However, in the meantime, it is also important to remember that there is still a wealth of untapped data within previous legacy survey data.

Alongside my PhD work, I had the pleasure of partaking in an ongoing collaboration searching for dwarf galaxy candidates within the Andromeda/Triangulum System. In this chapter, I present two studies detailing our discovery of two ultra faint dwarfs, Pisces VII and Pegasus V. The dwarfs were discovered as partially resolved sources by visual inspection of the DESI Legacy Imaging Surveys. Both dwarfs have tantalising features which could help push our understanding of ultra faint dwarfs and present interesting systems to study using the methodology detailed in Chapters 2 and 3.

4.1 Pisces VII: Discovery of a possible satellite of Messier 33 in the DESI Legacy Imaging Surveys

Abstract

We report deep imaging observations with DOLoRes@TNG of an ultra–faint dwarf satellite candidate of the Triangulum galaxy (M33) found by visual inspection of the public imaging data release of the DESI Legacy Imaging Surveys. Pisces VII/Triangulum (Tri) III is found at a projected distance of 72 kpc from M33, and using the tip of the red giant branch method we estimate a distance of $D = 1.0^{+0.3}_{-0.2}$ Mpc, meaning the galaxy could either be an isolated ultra–faint or the second known satellite of M33. We estimate an absolute magnitude of $M_V = -6.1 \pm 0.2$ if Pisces VII/Tri III is at the distance of M33, or as bright as $M_V = -6.8 \pm 0.2$ if the galaxy is isolated. At the isolated distance, it has a physical half–light radius of $r_h = 131 \pm 61$ pc consistent with similarly faint galaxies around the Milky Way. As the tip of the red giant branch is sparsely populated, constraining a precision distance is not possible, but if Pisces VII/Tri III can be confirmed as a true satellite of M33 it is a significant finding. With only one potential satellite detected around M33 previously (Andromeda XXII/Tri I), it lacks a significant satellite population in stark contrast to the similarly massive Large Magellanic Cloud. The detection of more satellites in the outskirts of M33 could help to better illuminate if this discrepancy between expectation and observations is due to a poor understanding of the galaxy formation process, or if it is due to the low luminosity and surface brightness of the M33 satellite population which has thus far fallen below the detection limits of previous surveys. If it is truly isolated, it would be the faintest known field dwarf detected to date.

4.1.1 Introduction

With a stellar mass of $M_* = 3 \times 10^9 M_\odot$ (McConnachie, 2012), and a halo mass of $\sim 10^{11} M_\odot$ (Corbelli et al., 2014), the Triangulum spiral galaxy (M33) is the most massive satellite of the Andromeda galaxy (M31) and one of the most massive galaxies of the Local Group. With this mass, the ΛCDM cosmological paradigm predicts that M33 should host a number of its own satellites. Cosmological simulations find it should have between 9–25 companions with stellar mass $> 10^3 M_\odot$ (e.g. Dooley et al. 2017; Patel et al. 2018b; Bose et al. 2018), and at least 1 with $M_* > 10^6 M_\odot$ (Deason et al., 2013). However, to date, only one potential satellite has been uncovered: Andromeda (And) XXII/Triangulum (Tri) I, which has a stellar mass of $2{\times}10^4 M_\odot$ (Martin et al., 2009, 2016c). This was found in the framework of the Pan–Andromeda Archaeological Survey (PAndAS; McConnachie et al. 2009), an observing program which has conducted a deep survey of the M33 halo out to ∼1/3 of its virial radius.

To date, no brighter satellites have been found outside this radius in shallower surveys such as the SDSS. There is also a notable dearth of globular clusters around

M33 compared to other spiral galaxies (Cockcroft et al., 2011). This negligible satellite population is in stark contrast to that of the similarly massive Large Magellanic Cloud (LMC), which has upwards of 7 known satellite galaxies (e.g. Jethwa et al. 2016; Fritz et al. 2019; Erkal & Belokurov 2020). Part of this is due to the difference in limiting magnitude that can be probed in M33 versus the far nearer LMC. But even so, the lack of bright companions ($M_* > 10^4 M_\odot$) is surprising.

Previously, this lack of satellite galaxies and far flung globular clusters of M33 was attributed to its dynamical evolution. Warps to its outer stellar and HI disks were thought to originate from a prior interaction with M31 occurring ∼2 Gyr ago, which would have stripped much of M33's stellar halo and satellites (McConnachie et al., 2009; Cockcroft et al., 2011). Nevertheless, newer studies which include up–to–date proper motions for M31 and M33 suggest that the latter is more likely on its first infall to the M31 system (e.g. Patel et al. 2017; van der Marel et al. 2019). If this scenario is correct, M33's satellite system should extend beyond a single, low mass satellite.

This dramatic gap between theoretical expectations and observations could imply our understanding of the formation of low mass galaxies is flawed. Perhaps the feedback recipes used in hydro–dynamical surveys are incorrect, or we are wrong about the nature of dark matter itself. Or, it could be that the majority of M33 satellites have luminosities and surface brightnesses that lie just below the detection limits of previous surveys. In any event, given the paucity of known M33 satellites, even a single new detection or exclusion of a companion has the potential to completely change our understanding of the M33 system, and galaxy formation more widely.

In the last decades, the discoveries of Andromeda satellites have been made by means of visual inspection or automatic algorithm searches in stellar density maps of resolved red giant branch (RGB) stars, counted in selected areas of the colour magnitude diagrams (CMDs) from large scale photometric survey data, such as the Sloan Digital Sky Survey (SDSS, Abazajian et al. 2009) and the Panoramic Survey Telescope and Rapid Response System (Pan–STARRs; Chambers et al. 2016; Martin et al. 2013c,b). However, the main contribution to the dwarf census of M31 satellites came from PAndAS with the wide–field imager on the Canada French Hawaii Telescope (CFHT) (McConnachie et al., 2009; Martin et al., 2009; Richardson et al., 2011).

Although the M31 stellar halo photometry from the PAndAS is significantly deeper than those from the SDSS or Pan–STARRs, this ground–based data can only reach the red clump locus in the CMDs at the distance of Andromeda. Thus, low–mass systems with absolute magnitude fainter than $M_V \sim -6$ are very hard to detect because of the lack of enough RGB star tracers in their CMDs, yielding a cut–off in the luminosity function of satellites of M31 (see Brasseur et al. 2011; their Figure 1). An alternative approach is to search for partially resolved stellar over–densities in the public deep images recently available from the DESI Legacy Imaging Surveys (DESI LIS; Dey et al. 2019). These data were obtained with the *Dark Energy Camera* (DECam) mounted on the Blanco 4–m telescope, located at the Cerro Torrolo Inter–American Observatory (Flaugher et al., 2015), which reach surface brightness as faint as ∼ 29 mag arcsec^{-2}. This low surface regime allows us

to detect the underlying, unresolved population of these systems as a diffuse light round over-density overlapping a small ($\sim$ 1–2 arcmin) clump of faint stars.

Using this approach, we have very recently identified a partially resolved dwarf galaxy candidate outside the PAndAS survey footprint. Placed at the distance of M33, it would be located at a projected distance of $\gtrsim$70 kpc from the Triangulum galaxy. Unfortunately, the DESI LIS photometry is too shallow to allow the measurement of an accurate distance, making it impossible to reject it as a background isolated dwarf situated a few Mpcs behind Andromeda (as e.g. the Do I dwarf; Martínez-Delgado et al. 2018). In this paper, we present follow–up photometric observations, a distance estimate and structural analysis of this stellar system that suggests its likely association to M33.

4.1.2 Observations and Data Reduction

Pisces VII/Tri III[1] was discovered in the Pisces constellation by the amateur astronomer Giuseppe Donatiello as a partially resolved over–density in the Pisces constellation. It was found by visual inspection of the available DESI LIS images of an extensive area of 20° × 30° in the surroundings of the Triangulum galaxy (M33), outside the PAndAs footprint (see Figure 4.1 left panel)[2]. The detection was subsequently confirmed by a visual inspection of the SDSS DR9 images and follow–up observations using the Italian Telescopio Nazionale Galileo (TNG) described in § 4.1.2. The position of the centre of this new dwarf galaxy is given in Table 4.1.

TNG Imaging Observations

We used deep images of a 8.6'x8.6' field around the candidate galaxy obtained with the focal reducer instrument DOLoRes (see http://www.tng.iac.es/instruments/lrs/) of the 3.58–m TNG taken on November 17 2020 (program A42DDT2; P.I.: W. Boschin). These observations include 41x180 sec unbinned (scale 0.252″/pixel) exposures in the g'–band and 20x180 sec unbinned exposures in the r'–band, with a median seeing of 1.15" and 0.85", respectively. The raw data were preprocessed in a routine way using standard IRAF tasks, i.e. dividing the trimmed and bias–subtracted images by a master flat field produced from multiple twilight sky–flat exposures.

Images were reduced using the DAOPHOT/ALLFRAME suite of programmes (Stetson, 1987, 1994), largely following the method outlined by Monelli et al. (2010b). For each individual image, we performed the initial steps: i) search for stellar sources, ii) aperture photometry, iii) PSF derivation, iv) PSF photometry with ALLSTAR. Then images were registered with DAOMASTER and stacked on a median image. This was used to extract a deeper list of stars, which was fed to ALLFRAME. This provides individual catalogues with better determined position and instrumental

[1] Following the naming convention suggested in the Appendix of Martin et al. (2009), we suggest for this galaxy the dual naming introduced with the discovery of Pegasus/And VI, Cassiopeia/And VII or Pisces VI/And XXII.

[2] Our search for dwarf satellite candidates around M33 was performed using the *Legacy Survey Sky Viewer* web site available in legacysurvey.org/viewer.

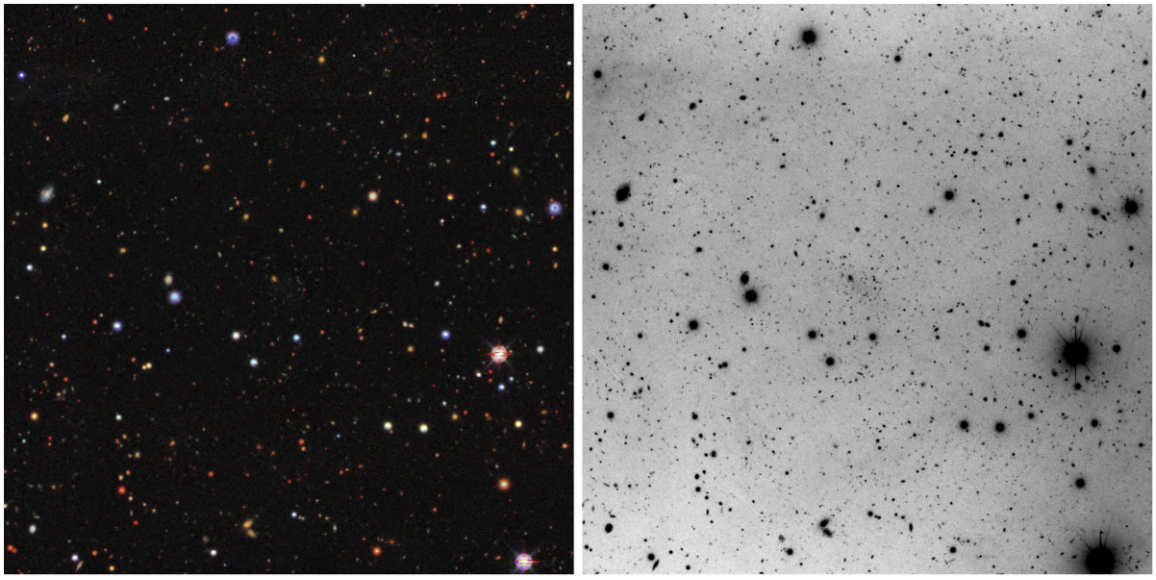

Figure 4.1: *Left panel*: Image of the dwarf galaxy Pisces VII/Tri III from the DESI LIS. *Right panel*: TNG r–band image of the galaxy obtained from TNG follow-up observations (see 4.1.2). The total field of view of both images is $8.6' \times 8.6'$. North is up, East is left.

magnitude of the input sources. The updated photometry allowed us to refine the PSF (using improved list of stars) and the geometric transformations (leading to a better coadded image and cleaner input list). A final run of ALLFRAME provided the final photometry. The list of sources was cleaned using the *sharpness* parameter, and further polished by removing object after a visual inspection on the stacked image.

The photometric calibration was performed using local standard from the Pan STARRs 1 survey (Chambers et al., 2016), using 121 stars in common. The mean magnitudes were calibrated with a linear relation for the g–band, and a zero point for the r–band. The calibrated local standard agree well below 0.01 mag with the tabulated ones, with standard deviation of the order of 0.03 mag. All data are then extinction corrected using the reddening maps from Schlafly & Finkbeiner (2011).

4.1.3 Methods

Identifying Probable Members

To determine the structural properties of the dwarf candidate, we identify stars that are most likely to be associated with the dwarf from the CMD. We select stars that lie on or near the RGB of the system. Three selection criteria were used to filter the foreground and background contaminants out of the data. First, the morphology of each datum was assessed and only stellar (point–like) sources were included. Second, a CMD selection box consisting of a colour cut ($0.4 < r < 1.1$), and limiting magnitude ($r < 24.0$) was introduced. Finally, we use an old, metal–poor isochrone to trace the RGB (12 Gyrs, [α/Fe]=0.4 dex, [Fe/H]=-2.0 dex) taken from the Dartmouth isochrones, Dotter et al. 2008), and measure the minimum distance, d_{min}, of each datum to the isochrone to calculate a probability

of membership defined by:

$$P_{iso} = \exp\left[-\left(\frac{d_{min}^2}{2\eta^2}\right)\right] \tag{4.1}$$

where η is a free parameter used to account for scatter about the isochrone. We set $\eta = 0.01$ and use a low probability cut of $P_{iso} > 0.05$ to isolate the most likely RGB candidates. This allows a broad selection of stars, without including too many obvious foreground contaminants by constraining the wider CMD selection box to the region around the isochrone. If a datum satisfied these criteria it is considered a probable member of the dwarf galaxy. A total of 52 probable member stars were identified within $\sim 1'$ of the centre of the overdensity, as illustrated in Figure 4.2.

Structural Properties

The structural properties were determined using the iterative Bayesian approach of Markov Chain Monte Carlo (MCMC) analysis and we use the `emcee` code developed by Foreman-Mackey et al. (2013) to implement this. Our methodology followed the procedure outlined in Martin et al. (2016c), summarised below.

The radial density profile of the dwarf galaxy, $\rho_{\rm dwarf}(r)$, can be described by:

$$\rho_{\rm dwarf}(r) = \frac{1.68^2}{2\pi r_{\rm h}^2(1-\epsilon)} N^* \exp\left(\frac{-1.68r}{r_{\rm h}}\right) \tag{4.2}$$

where ϵ is the ellipticity, defined by the minor–to–major axis ratio, $\epsilon = 1-(b/a)$ and $r_{\rm h}$ is the half–light radius. N* is the number of likely member stars inside the CMD selection box associated to the dwarf, r is the elliptical radius such that:

$$\begin{aligned} r = \Bigg(\Big(\frac{1}{1-\epsilon} ((x-x_0)\cos\theta - (y-y_0)\sin\theta) \Big)^2 \\ + \Big((x-x_0)\sin\theta - (y-y_0)\cos\theta \Big)^2 \Bigg)^{\frac{1}{2}} \end{aligned} \tag{4.3}$$

where θ is the position angle of the major axis, x_0 and y_0 are co–ordinates for the centre of the candidate dwarf galaxy and x and y are the coordinates on the plane tangent to the sky at the center of the DOLoRes field. The background contamination is considered constant and is determined by subtracting the contribution of the dwarf, which is calculated by performing a normalized integration of the radial density profile from the total number of potential members identified, n. Hence, the background, Σ_b, can be described by:

$$\Sigma_b = \frac{\left(n - \int_A \rho_{\rm dwarf}\, dA\right)}{\int_A dA}. \tag{4.4}$$

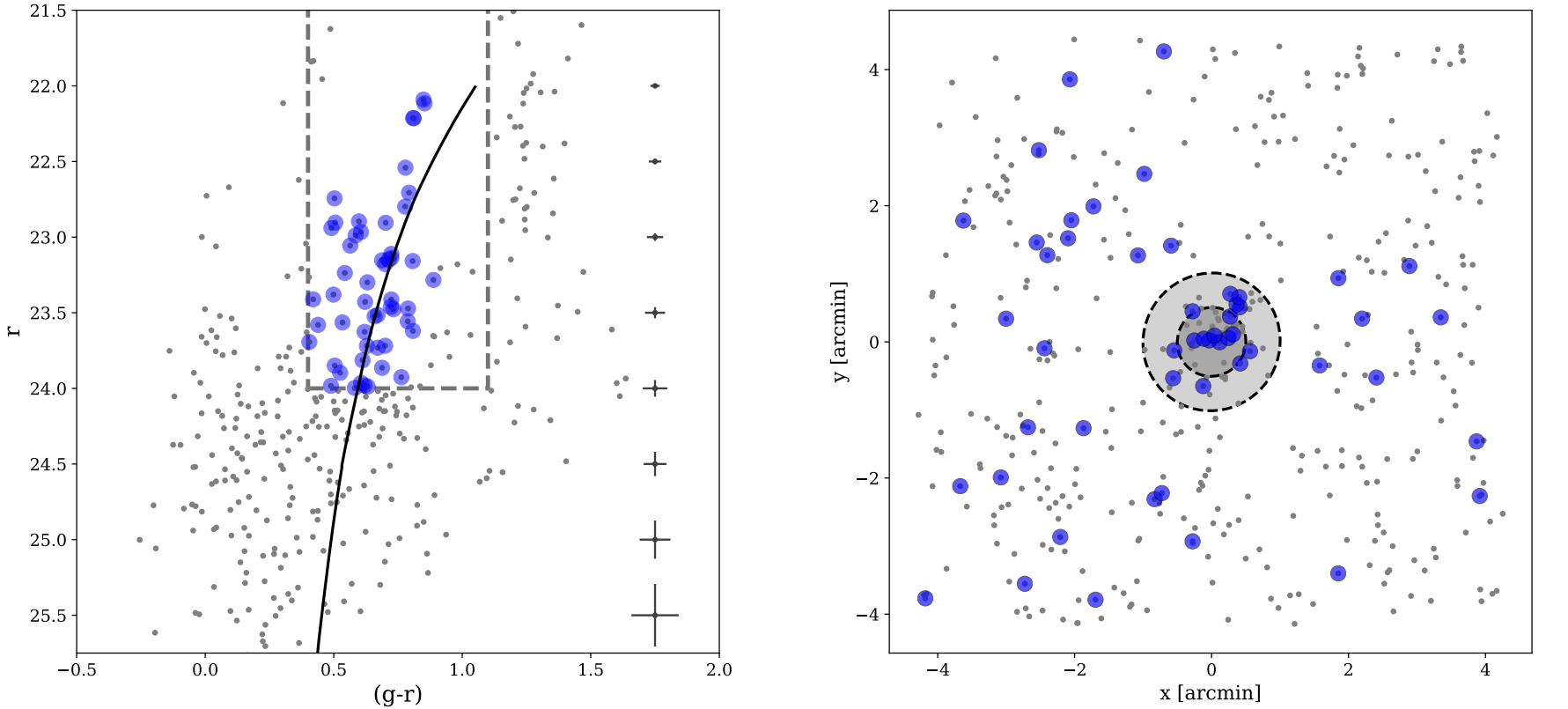

Figure 4.2: Left: Colour magnitude diagram within 1' of the centre of Pisces VII/Tri III. The grey data points indicate the complete data set observed. The blue data points are the sources deemed likely members of the candidate dwarf galaxy. The solid black line is an isochrone from the Dartmouth isochrone database with [Fe/H] = -2.0, dex [α/Fe] = 0.4 dex and age = 12 Gyr. The grey dashed lines indicate the CMD selection box used. **Right:** Spatial density plot of the observed data, with blue points showing the likely members of the dwarf galaxy which pass the criteria described in § 4.1.3. The dashed circles shaded grey show 1× and 2 × $r_{\rm h}$.

Equations 4.2, 4.3 and 4.4 combine together to give the following likelihood function, used in the MCMC analysis:

$$\rho_{\rm model}(r) = \rho_{\rm dwarf}(r) + \Sigma_b. \tag{4.5}$$

Uniform flat priors were used to constrain the parameter space to physical solutions but were kept broad to ensure the analysis wasn't over–constrained, see Table 4.2. The `emcee` routine used 100 walkers, over a total of 10,000 iterations with a burn in stage of 8,500. Figure 4.3 is the resulting corner plot from the MCMC analysis and the derived structural parameters are summarised in Table 4.1.

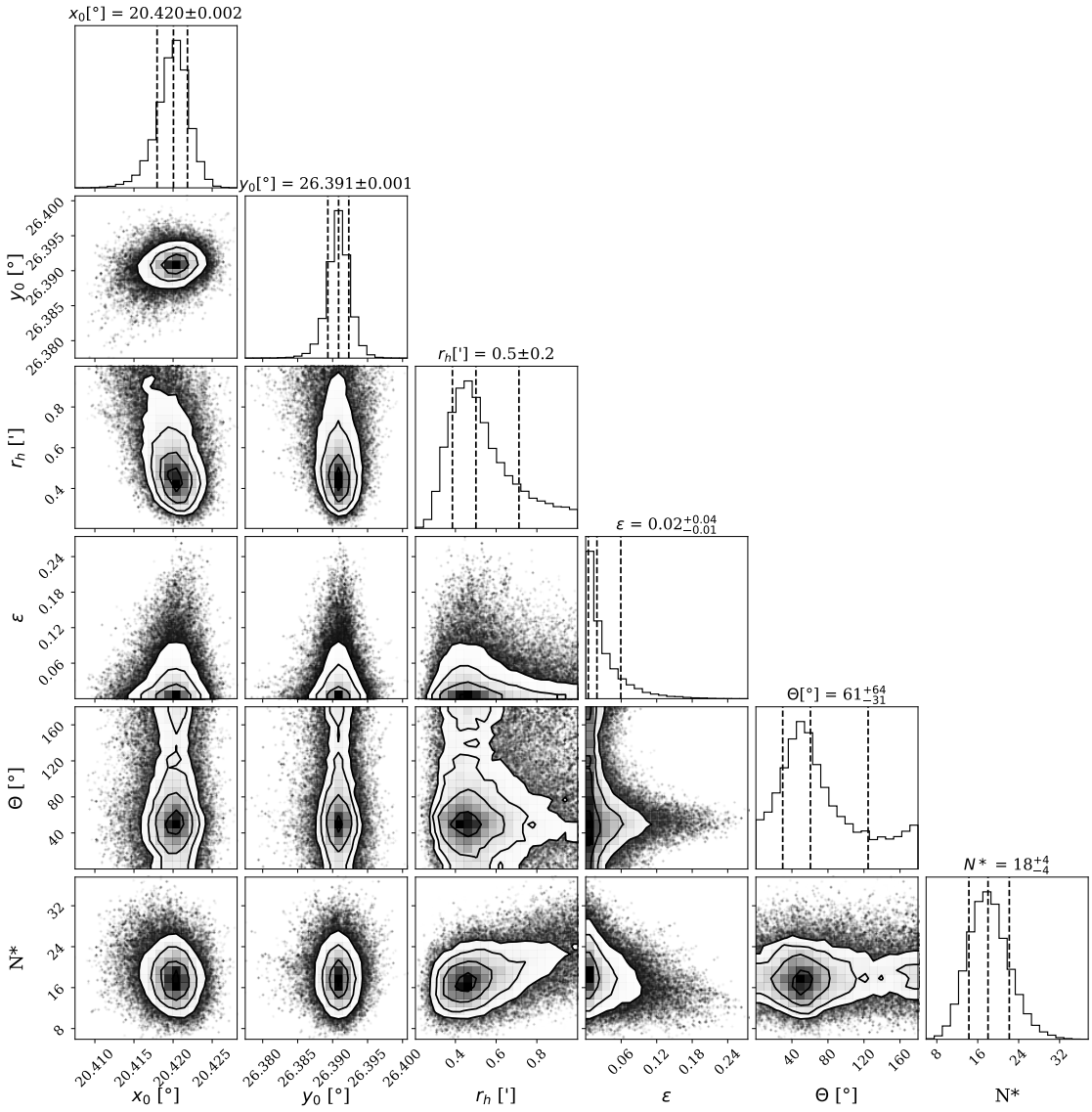

Figure 4.3: 2D and marginalized PDFs for the central coordinates of the system, x_0 and y_0, the half–light radius, r_h, the ellipticity, ϵ, the position angle of the major axis, θ and the number of stars belonging to the system from the CMD selection criteria, N^* . The dashed lines represent the mean value and 1σ uncertainties.

Table 4.1: The final structural and photometric properties for the dwarf.

Property	Value
RA	$1^h\ 21^m\ 40.5^s \pm 0.8^s$
Dec	$26°23'\ 24" \pm 4"$
$r_{\rm h}$ (arcmin)	0.5 ± 0.2
D (kpc)	1000^{+300}_{-200}
$r_{\rm h}$ (pc)	131 ± 61
M_V	-6.8 ± 0.2
μ_0 (mag arcsec^{-2})	27.7 ± 0.3
L ($L_\odot$)	$3.7^{+0.8}_{-0.6} \times 10^4$
ϵ	$0.02\ ^{+0.04}_{-0.02}$
θ (°)	$61\ ^{+62}_{-30}$
N*	$18\ ^{+4}_{-4}$

Table 4.2: The priors used in the `emcee` routine.

MCMC Parameter	Value
x_0 (radians)	$0.3 \leqslant x_0 \leqslant 0.4$
y_0 (radians)	$0.45 \leqslant y_0 \leqslant 0.5$
$r_{\rm h}$ (arcmin)	$0 \leqslant r_h < 1$
ϵ	$0 \leqslant \epsilon \leqslant 1$
θ (radians)	$0 \leqslant \theta \leqslant \pi$
N^*	$0 < N^* \leqslant n$

Next we plot a stellar radial density profile using the parameters that were deduced from the MCMC analysis, which we show in Figure 4.4. The error bars on the data points represent the Poisson uncertainties for each point. We overplot the exponential profile deduced using MCMC, which agrees very well with the observed profile. In addition we perform a basic chi–squared fit of the exponential profile shown in Equation 4.2 to this binned data. We recover a very similar value for $r_{\rm h} = 0.48'$, completely consistent with the MCMC approach.

The Distance to the Dwarf

To determine the distance to Pisces VII/Tri III, we use the Tip of the Red Giant Branch (TRGB) method. We construct a luminosity function for our dwarf galaxy (see Figure 4.5), using all sources within $2 \times r_{\rm h}$ of the galaxy's centroid and colours of $0.3 < g - r < 1.1$. This produces a reasonably tight selection of RGB stars, and minimises foreground contamination. From this, we subtract an area–normalised background luminosity function constructed from sources with the same colour cut, between 2.5–3.5 arcmin from our source. The grey shaded area in Figure 4.5 shows the region below which our photometry is $< 90\%$ complete.

The TRGB in the r–band should have an absolute magnitude of $M_{r,\rm TRGB} = -3.01 \pm 0.1$ (Sand et al., 2014). To begin with, we apply a Sobel edge detection filter to the luminosity function (Lee et al., 1993). This has been a historically popular way of finding the sharp edge of the TRGB, but it doesn't consider any

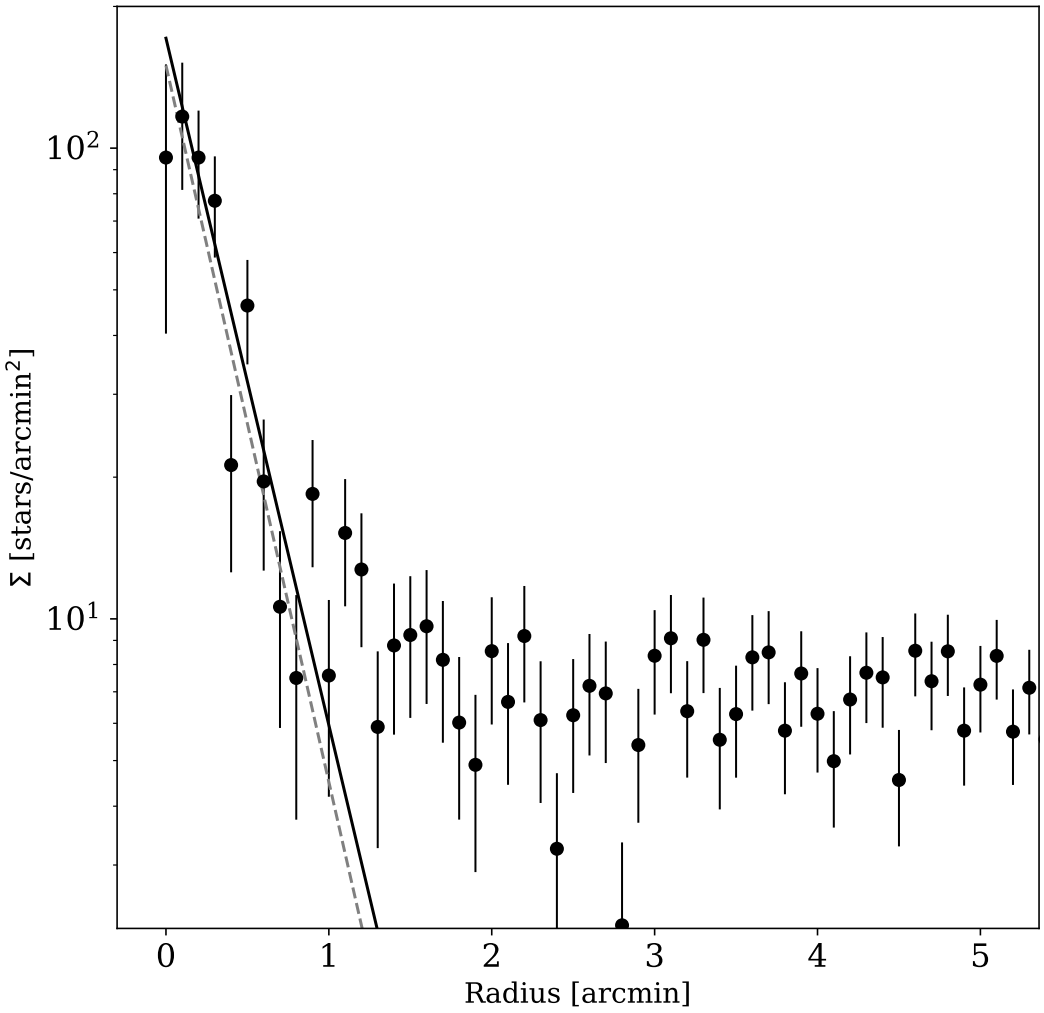

Figure 4.4: Stellar radial density profile with the observed data binned in elliptical annuli with the favoured structural properties of ellipticity, the position angle, the structural centre and the number of stars. The solid black fit uses the MCMC values and the dashed grey line is the chi-squared fit, which yields a value for $r_{\rm h} = 0.48'$.

uncertainties in the data. From this, we find a possible value for the TRGB at $r = 22.1$, which is marked as the black dashed line in Figure 4.5. This corresponds to physical distance estimate of 1.05 Mpc. Owing to the paucity of stars within our dataset, this method has merely located the 3 brightest stars in the dataset. The dot–dashed line represents the TRGB location for an object at the distance of M33 (820 kpc, Conn et al. 2012). In Figure 4.6, we show the CMD for all stars witin $2 \times r_{\rm h}$ of the dwarf galaxy with isochrones of varying metallicity overlaid at each of these proposed distances (Dotter et al., 2008). For a distance of 820 kpc, the dwarf appears metal poor, with [Fe/H]~ -2.0.

As a second step, we could also look for a peak in the luminosity function at

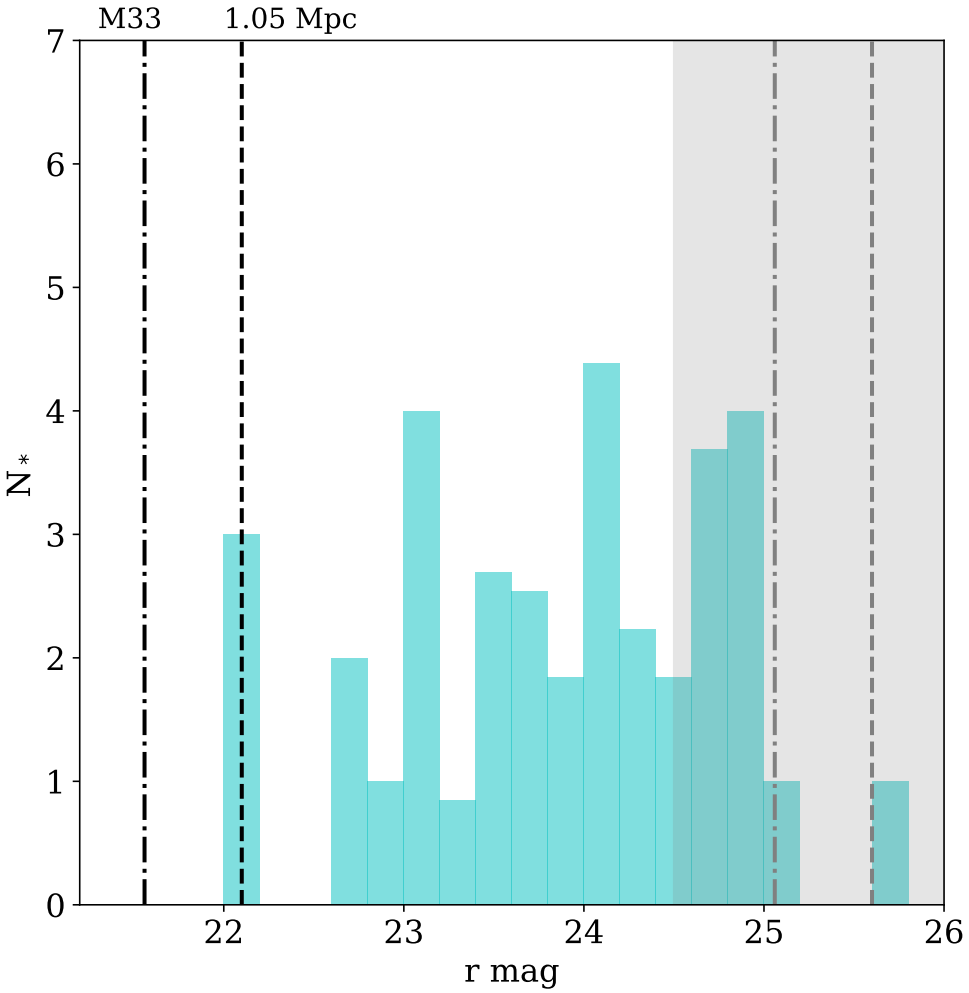

Figure 4.5: A background corrected luminosity function for all stars within $2 \times r_{\rm h}$ of the galaxy centre. The grey shaded region shows the point at which our completeness drops below 90%. Using a Sobel edge detection filter, we find a peak in the luminosity function at $r = 22.1$, which is indicated as the dashed black line. The location of the TRGB of M33 is shown as a dot–dashed line. The grey lines show the predicted locations for the HB in the LF for these three distances.

the location of the horizontal branch (HB). The HB is a secure distance estimator and it is typically better populated than the RGB, allowing a better constraint. In Figure 4.5, we also show the predicted location of the HB assuming the Sobel distance estimate, as well as the HB for an object at the distance of M33. However, as our photometry is incomplete at these magnitudes, we cannot locate this feature.

A more rigorous way of searching for the TRGB is to use Bayesian inference (e.g. Conn et al. 2012). Here, we follow the method outlined by Tollerud et al. (2016), who model the RGB and background population simultaneously as a broken power law in luminosity, with the break located at the TRGB. The luminosity function is

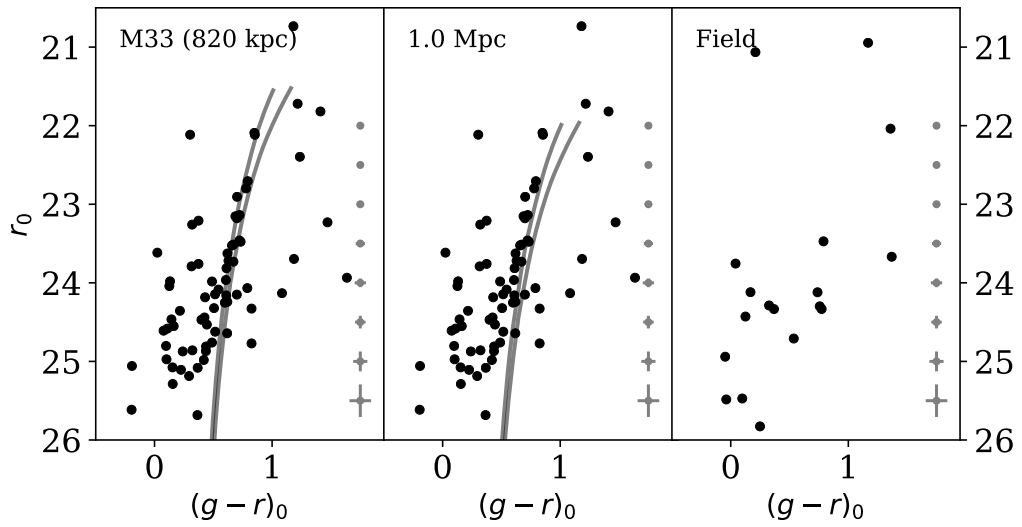

Figure 4.6: The first 2 panels show the CMD for all sources within $2 \times r_{\rm h}$ of the centre of the dwarf. In each panel, Dotter et al. (2008) isochrones with an age of 12 Gyr, $[\alpha/\mathrm{Fe}] = +0.4$ and metallicities of $[\mathrm{Fe/H}] = -2.0$ and -2.5 are overlaid for two different distances: The distance to M33 (820 kpc), and that from our TRGB analysis (1.0 Mpc). The final panel shows a control field located away from the centre of the dwarf of equal area. Using the TRGB estimate, the isochrones imply the system is very metal poor, whereas the M33 distance gives a good match to the colours of the RGB stars.

also convolved with the photometric uncertainties, providing an advantage over the Sobel method above. We adapt their public TRGB fitting code (see Tollerud 2016) for our dataset, and summarise their method briefly below. The assumed luminosity function, $\phi_{\rm RGB}$ is defined as

$$\begin{aligned} &\phi_{\rm TRGB}(m, m_{\rm trgb}, \alpha, \beta, f) \\ &= \begin{cases} \frac{\alpha e^{\alpha(m-m_{\rm trgb})}}{e^{\alpha(m_2-m_{\rm trgb}}-e^{\alpha(m_1-m_{\rm trgb}}} & \text{if } m > m_{\rm trgb} \\ f\frac{\beta e^{\beta(m-m_{\rm trgb})}}{e^{\beta(m_2-m_{\rm trgb}}-e^{\beta(m_1-m_{\rm trgb}}} & \text{if } m \leq m_{\rm trgb} \end{cases} \end{aligned} \tag{4.6}$$

where m is the stellar magnitude, $m_{\rm trgb}$ is the TRGB magnitude, α and β describe the power law slopes of the RGB and background respectively, and f gives the fraction of stars in the background population (such that the fraction on the RGB is $1 - f$). We then write the per star likelihood as

$$\begin{aligned} &\mathcal{L}(m_i \mid m_{\rm trgb}, \alpha, \beta, f) \\ &= N \int_{m_1}^{m_2} \phi_{\rm RGB}(m_{\rm trgb}, \alpha, \beta, f) \\ &\quad \times \mathcal{N}\left[m_i - m, \sigma(m)\right] \mathrm{d}m \end{aligned} \tag{4.7}$$

where m_i are the extinction–corrected magnitudes for each star, m_1 and m_2 are the

bright and faint limits of the data, N is a normalization constant (determined by numerical integration), $\mathcal{N}$ is the standard Gaussian distribution and $\sigma(m)$ are the per–star uncertainties.

Our primary interest is the value of $m_{\rm trgb}$, so we use Bayesian inference with this model to determine posterior probabilities for this using Equation 4.7 as our likelihood function. We implement uniform priors on f of U(0, 1), and for α and β we use the same priors as Conn et al. (2012) of U(0, 2). For $m_{\rm trgb}$ we adopt a more informative prior based on the results of our Sobel filter method above, setting this to U(20, 23.1). For m_i, we use our r–band magnitudes and use the same colour selection function as for the luminosity function above ($0.5 < g - r < 1.1$), and only include stars with $r < 24$ to ensure we are using a complete sample. We then numerically integrate Equation 4.6 over a grid of m using the trapezoid rule for a given set of parameters, and take the total likelihood as the sum of the logarithm of this over all stars.

We again use EMCEE to sample the posterior distribution for the model parameters for this broken power–law distribution. The results of this are shown in the left panel Figure 4.7. The results are inconclusive, and highly dependent on both the priors and the colour and distance selection. Using purely the colour cut, and the whole field of view, we find a triple–peaked distribution, with higher posterior values for $m_{\rm trgb} \sim 21.8, 22.1$ and 22.7 (corresponding to distances of $\sim 0.9 - 1.4$ Mpc). If we narrow the colour cut slightly to exclude the bluer stars which may or may not be members ($0.5 < g - r < 1.1$), we instead recover the Sobel value for the TRGB of $m_{\rm trgb} = 22.0^{+0.6}_{-0.5}$ (right panel Figure 4.7), corresponding to a distance of $D = 1.0^{+0.3}_{-0.2}$ Mpc. If we only include stars within the central two half–light radii (to exclude background contaminants), we measure $m_{\rm trgb} = 21.9 \pm 0.5$ ($D = 960^{+200}_{-190}$ kpc).

This sensitivity to our selection criteria is driven by the scant number of stars both within the dwarf galaxy itself, and in the surrounding field. The model is highly sensitive to individual stars, and the uncertainties in all cases are likely underestimated. The stellar populations are scarce, making it difficult to distinguish between foreground and dwarf stars (as shown by the f parameter in both corner plots). Overall, this approach appears to favour an isolated distance for Pisces VII/Tri III. To confirm this, we require deeper data which would allow us to resolve the better populated horizontal branch or main sequence turn–off. For the rest of the paper, we assume a distance for the dwarf of $D = 1.0^{+0.3}_{-0.2}$ Mpc, and use these to calculate a physical size and luminosity range for this candidate.

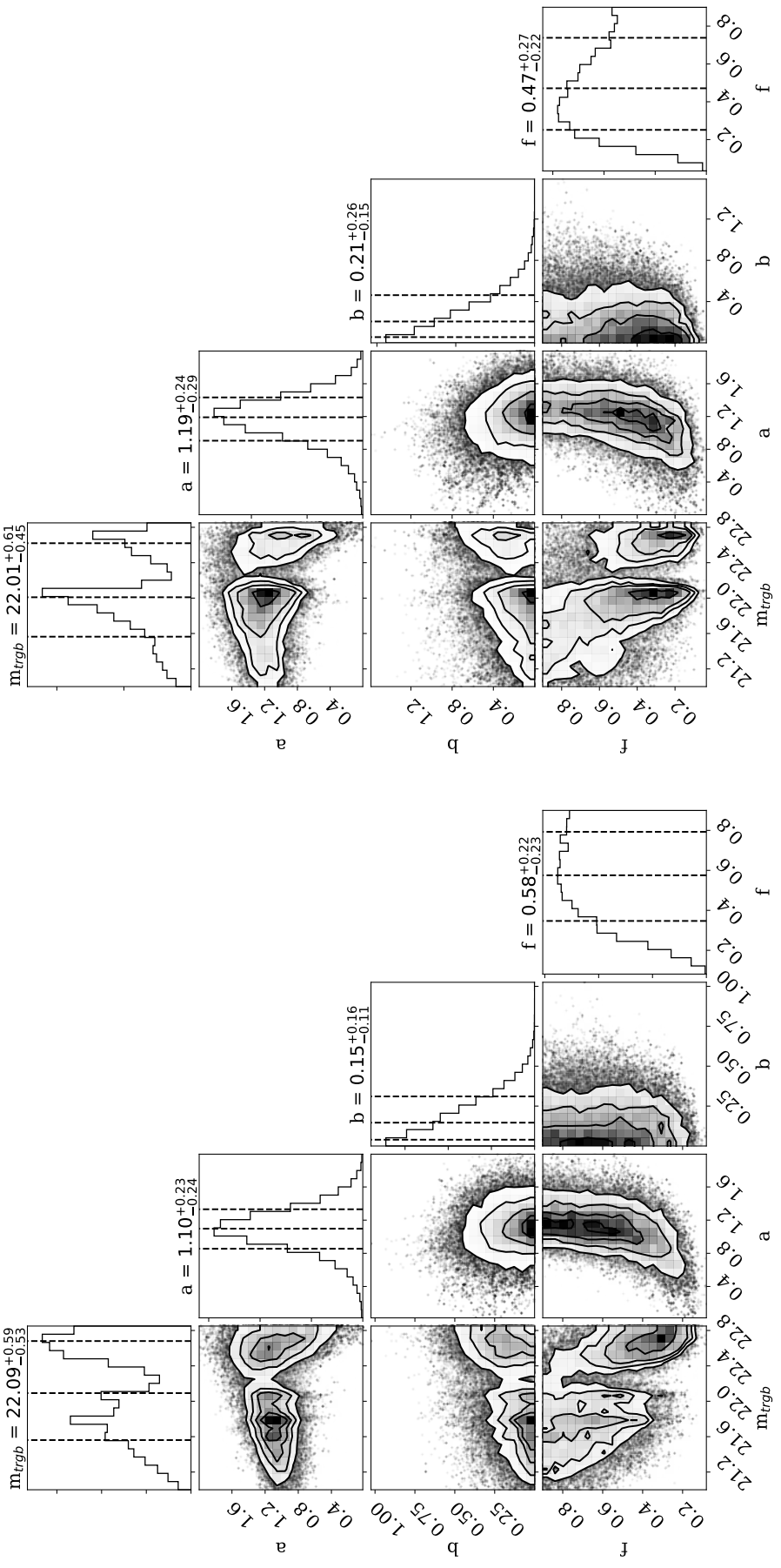

Figure 4.7: Left: Posterior distribution for the MCMC TRGB finding algorithm using our standard colour cut. The key parameter of interest is $m_{\rm trgb}$. For this colour cut, the distribution shows 3 peaks, and is poorly constrained, resulting in a distant estimate between 0.9–1.4 Mpc. **Right:** The same, but for a marginally tighter colour cut ($0.5 < g - r < 1.1$). Here, $m_{\rm trgb} = 22.0^{+0.6}_{-0.5}$, favouring an isolated distance of $D = 1.0^{+0.3}_{-0.2}$ Mpc. The posterior results are very sensitive to assumptions of priors and colour cuts, owing to the paucity of stars (dwarf and background model) in the region.

Luminosity

The luminosity of Pisces VII/Tri III was calculated using a methodology similar to the approach outlined in Martin et al. (2016c). A probability density function (PDF) was made using a theoretical luminosity function, describing the number of expected star counts per narrow magnitude bin for a stellar population with an age of 12 Gyr, $[\alpha/\mathrm{Fe}] = +0.4$ dex and metallicity of $[\mathrm{Fe/H}] = -2.0$ dex. This PDF was then used to weight random sampling in magnitude space. Stars which are selected from the isochrone which have a magnitude above the magnitude limit on the CMD used in our analysis ($r < 24.0$) are flagged. The magnitude is then converted into the corresponding luminosity. When converting into a luminosity the uncertainty in the distance was considered by sampling the distance from a Gaussian distribution centered around the results from the distance modulus with a σ corresponding to the uncertainty of the distance modulus. The process of random sampling was repeated until a total of N^* flagged stars was obtained, matching our dataset. Once this limit was reached the luminosity of all sampled stars was summed, including those not flagged, to give a final luminosity value. The whole process was repeated 1000 times and an average luminosity was obtained. Assuming the isolated distance, the resulting magnitudes were $M_r = -6.5 \pm 0.3$ and $M_g = -6.8 \pm 0.2$. The uncertainty comes from the standard deviation of the 1000 iterations, wherein uncertainty is introduced in the random sampling of the distance Gaussian indicative of the distance error. We then convert this into an absolute magnitude in the V–band using the colour transforms of Jordi et al. (2006), giving $M_V = -6.8 \pm 0.2$. Assuming Pisces VII/Tri III is instead an M33 satellite, the resulting g and r band magnitudes are $M_r = -6.1 \pm 0.2$ and $M_g = -6.3 \pm 0.3$, giving $M_V = -6.1 \pm 0.2$.

From these values, we find the total luminosity of the dwarf galaxy to be $L = 2.1 \pm 0.4 \times 10^4\,\mathrm{L}_\odot$ and $L = 3.7^{+0.8}_{-0.6} \times 10^4\,\mathrm{L}_\odot$ for the M33 and isolated distances respectively. We also calculate the distance independent central surface brightness of the dwarf galaxy μ_0, and find a value of $\mu_0 = 27.6 \pm 0.2$.

4.1.4 Discussion and Conclusions

We report the discovery of Pisces VII/Tri III, a new dwarf galaxy in the surroundings of M33 by visual inspection of the publicly available image of the DESI LIS outside the PAndAs survey footprint. Using deeper follow–up imaging from DOLoRes@TNG we attempt to constrain a distance for this dwarf. The paucity of stars makes this extremely challenging, but based on both a Sobel and MCMC approach, the likely distance $D = 1.0^{+0.3}_{-0.2}$ Mpc, making it either a satellite of M33, or an isolated ultra–faint dwarf (UFD) in the field. It is faint and compact with $M_V = -6.1 \pm 0.2$ for the M33 distance or $M_V = -6.8 \pm 0.2$ for the isolated case. It would then have a half–light radius of $r_\mathrm{h} = 119 \pm 48$ pc for an M33 distance or $r_\mathrm{h} = 131 \pm 61$ pc for the isolated case, comparable to UFDs of the Milky Way (see Figure 4.8). This luminosity would make it one of the faintest dwarf galaxies detected beyond the Milky Way, and potentially the faintest detected field galaxy to–date.

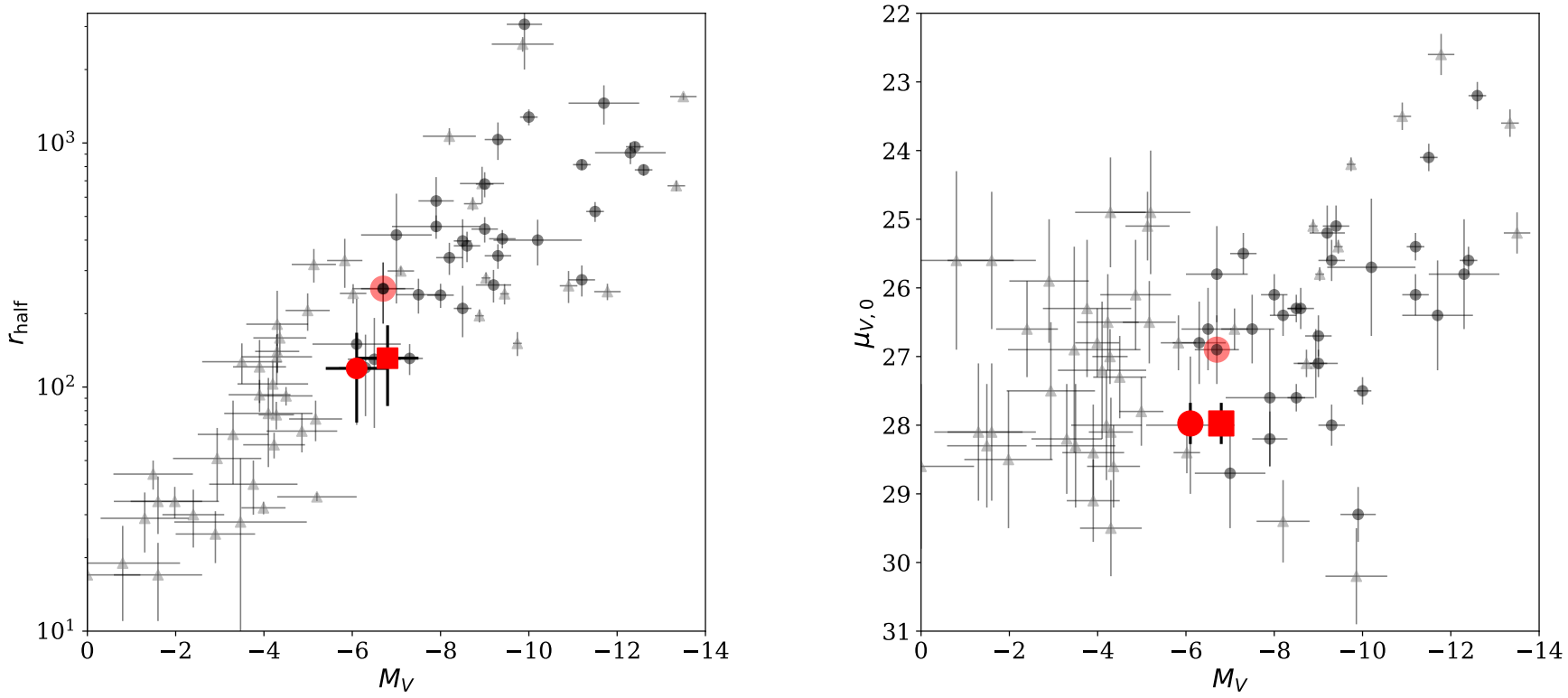

Figure 4.8: Left: M_V vs $r_{\rm h}$ for dwarf spheroidal galaxies of the Milky Way (light grey triangles) and M31 (dark grey circles). Our new candidate is highlighted as a large red circle (for an M33 distance) and a red square (for the isolated distance), and fits comfortably within the size–luminosity relation for Local Group dwarfs. The point with the red shading is the only other likely satellite of M33, Andromeda XXII/Triangulum I. **Right:** M_V vs central surface brightness, $\mu_{V,0}$, for Local Group dwarfs.

Armed with the structural and photometric properties of our dwarf, we can place it in context with the other dwarf galaxies of the Local Group. In Figure 4.8, we show the relationship between luminosity and half–light radius (left) and surface brightness (right). The light grey triangles show Milky Way satellites, while dark grey circles show M31 satellites. These values are compiled from a number of sources (McConnachie, 2012; Koposov et al., 2015; Bechtol et al., 2015; Drlica-Wagner et al., 2015; Martin et al., 2016c; Weisz et al., 2019a). Our candidate is highlighted as a large red circle and square for the M33 and isolated distances respectively. It is only the second potential satellite galaxy of M33 discovered. The other, Andromeda XXII, is highlighted with red shading[3].

Our derived properties for the new dwarf are perfectly consistent with other ultra–faint dwarf galaxies. If this galaxy was confirmed as a satellite of M33, it would alleviate the current tension between the observed and predicted number of satellites around M33 (Patel et al., 2018b). Given its low luminosity, it also suggests it may be the tip of the iceberg in terms of finding more ultra–faint dwarfs in the M31–M33 system.

The new census of dwarf galaxies and the homogeneous distance measurements for all the known M31 satellites from the PAndAS survey suggest the possible existence of a coherent flattened galaxy plane of 15 satellite galaxies in that survey volume (Ibata et al., 2013). This Great Plane of Andromeda (GPoA, see Fig 4.9) is almost edge–on orientated and extends more than 400 kpc from the center of M31. Interestingly, this plane seems to be aligned with the Giant Stellar Stream in the M31 halo and, in contrast with a similar satellite plane found in the Milky Way (Pawlowski et al., 2012), it is not perpendicular to its galactic disk but inclined ∼50 degrees. The existence of these kinematically correlated satellite planes in the Local Group spirals are very rare in cosmological simulations based on the ΛCDM paradigm (e.g. Pawlowski 2018). Some solutions proposed for this possible small–scale problem for the ΛCDM theory are the accretion of dwarf galaxies along filaments of the cosmic web (e.g. Buck et al. 2015), infall of satellites in groups (e.g. Samuel et al. 2020) or a possible tidal dwarf galaxy origin for some of the satellites of Andromeda (Hammer et al., 2018).

The available DESI LIS imaging data outside the PAndAs footprint also allows us to explore the existence of additional members of this possible GPoA at larger projected distances from M31. Figure 4.9 shows the position of the Pisces VII/Tri III with respect to M33 and the GPoA (Pawlowski, 2018). It clearly lies off the plane, and in projection seems likely associated to the outer M33 halo.

The discovery of Pisces VII/Tri III by visual inspection of a limited area around M33 using the DESI LIS deep imaging suggests that there is still room for discovery of low surface brightness dwarf galaxies lurking in the outskirts of Andromeda, beyond the bounds of the PAndAS survey. To confirm whether it is a bona–fide satellite of M33, a precision distance should be measured using deep imaging. Follow–up studies using the Hubble Space Telescope would allow the HB and main sequence of the dwarf to be resolved, allowing us to distinguish between the distances measured from the scarce RGB stars. In addition, spectroscopy of its brightest member stars

[3]Laevens 2/Tri II is a Milky Way dwarf galaxy situated at 30 kpc (Laevens et al. 2015; Kirby et al. 2015a; Martin et al. 2016b; Kirby et al. 2017).

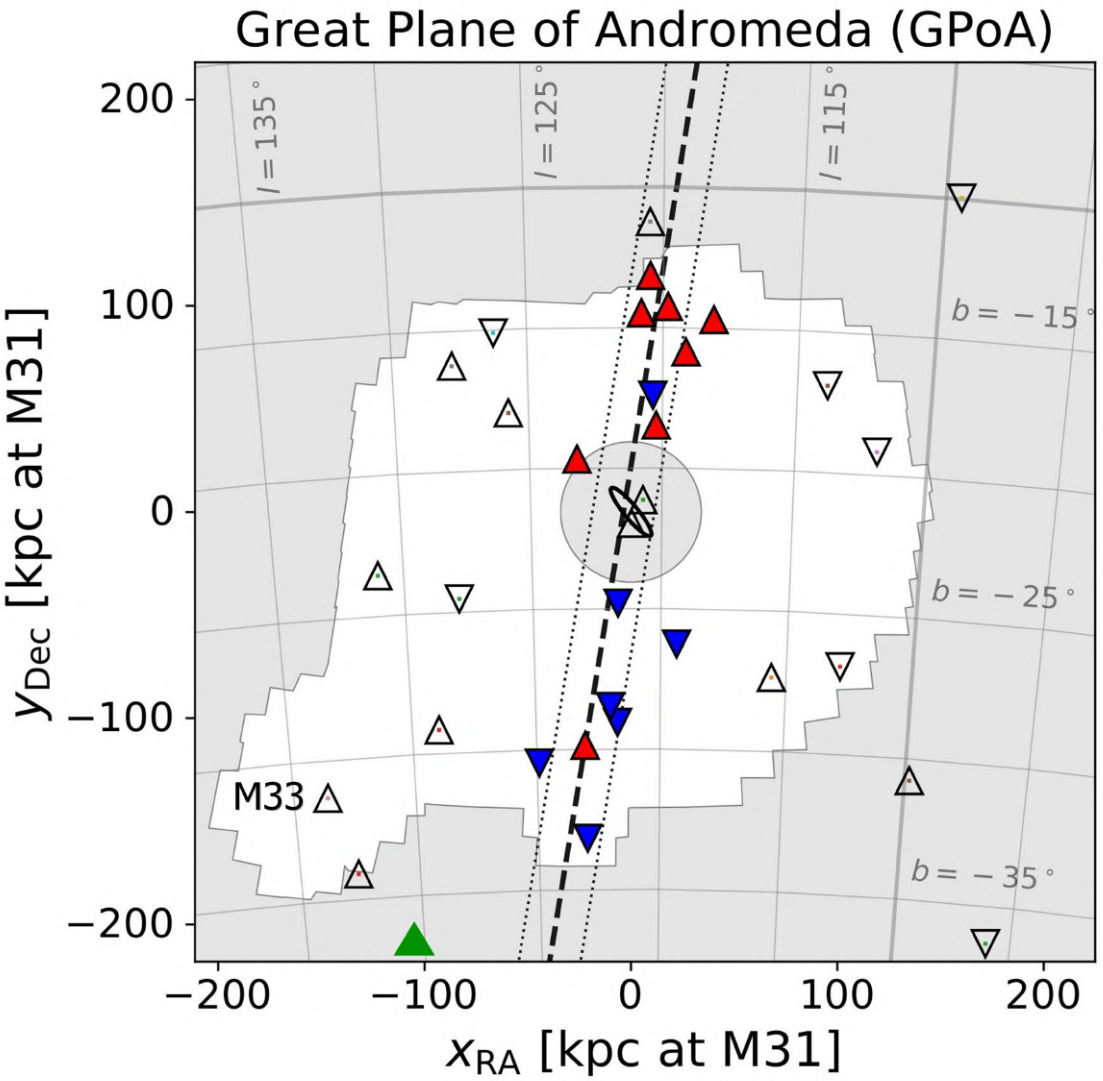

Figure 4.9: Position of Pisces VII/Tri III (*green triangle*) with respect to M31 (black ellipse) and M33 and the GPoS. The dashed and dotted lines indicate the orientation and width of the best–fit GPoS respectively. The white footprint corresponds to the region explored by the PAndAS survey. Satellites with measured radial velocities are showed as color–coded triangles, according to whether they are approaching (blue) or receding (red) relative to M31. Adapted from Figure 1 in Pawlowski (2018).

would allow us to determine whether it is dynamically bound to M33. Given the faint nature of the stars, an 8–10 m class telescope, such as Keck, would be required.

4.2 Pegasus V/Andromeda XXXIV – a newly discovered ultra–faint dwarf galaxy on the outskirts of Andromeda

Abstract

We report the discovery of an ultra–faint dwarf in the constellation of Pegasus. Pegasus V/Andromeda XXXIV (Peg V) was initially identified in the public imaging data release of the DESI Legacy Imaging Surveys and confirmed with deep imaging from Gemini/GMOS-N. The colour magnitude diagram shows a sparse red giant branch (RGB) population and a strong over–density of blue horizontal branch stars. We measure a distance to Peg V of $D = 692^{+33}_{-31}$ kpc, making it a distant satellite of Andromeda with $M_V = -6.3 \pm 0.2$ and a half–light radius of $r_{\rm half} = 89 \pm 41$ pc. It is located ~ 260 kpc from Andromeda in the outskirts of its halo. The RGB is well–fit by a metal–poor isochrone with [Fe/H]$= -3.2$, suggesting it is very metal poor. This, combined with its blue horizontal branch could imply that it is a reionisation fossil. This is the first detection of an ultra–faint dwarf outside the deep Pan–Andromeda Archaeological Survey area, and points to a rich, faint satellite population in the outskirts of our nearest neighbour.

4.2.1 Introduction

The last two decades have seen an explosion in the detection of faint dwarf galaxies in the Local Group (e.g. Willman et al., 2005a,b; Belokurov et al., 2006, 2007, 2008; McConnachie et al., 2008; Martin et al., 2009; Bechtol et al., 2015; Koposov et al., 2015; Torrealba et al., 2016, 2018, 2019; Mau et al., 2020; Cerny et al., 2021a,b). Wide–field imaging surveys such as the Sloan Digital Sky Survey (Abazajian et al., 2009), Pan–STARRS (Chambers et al., 2016), the Pan–Andromeda Archaeological Survey (PAndAS, McConnachie et al. 2009), the Dark Energy Survey (DES, Abbott et al. 2018) and the DECam Local Volume Exploration Survey (DELVE, Drlica-Wagner et al. 2021) have uncovered a wealth of substructures orbiting the Milky Way (MW) and Andromeda (M31) galaxies. Despite the discovery of dozens of new dwarf satellites, it is complex to reconcile their numbers with theoretical predictions (e.g. Tollerud et al., 2008; Koposov et al., 2009; Walsh et al., 2009; Bovill & Ricotti, 2011b; Bullock & Boylan-Kolchin, 2017; Kim et al., 2018).

At the bright end ($L \gtrsim 10^5\,{\rm L}_\odot$), predictions and observations are in good agreement (e.g. Sawala et al., 2016; Read et al., 2019; Kim et al., 2018; Engler et al., 2021). As such, it is likely that the remaining gap will be resolved as we push to ever–lower luminosities with new surveys, such as the Vera C. Rubin Legacy Survey of Space and Time (Tollerud et al., 2008; Bovill & Ricotti, 2011a). In M31, detection of the faintest galaxies has been limited to the central 150 kpc probed by PAndAS, which has discovered dwarf galaxies down to $L \sim 2 \times 10^4\,{\rm L}_\odot$ ($M_V \sim -6$, e.g. McConnachie et al. 2009; Richardson et al. 2011; Martin et al. 2013a). Work by Martin et al. (2016c) demonstrated that there are likely many more faint dwarfs lurking just below the detection limit of the survey, and discoveries of brighter dwarfs at much

greater distances ($\gtrsim$ 200 kpc) in shallower surveys (Martin et al., 2013c,b) suggest that there is a wealth of galaxies to be found out to the virial radius of the system.

These faintest dwarfs provide tight constraints on reionisation and stellar feedback physics as their gas reservoirs can more easily escape their low mass potentials. Deep imaging studies with the Hubble Space Telescope have shown that UFDs tend to have their star formation quenched early (e.g. Brown et al., 2014; Sacchi et al., 2021), representing the relics of the very first galaxies (Bovill & Ricotti, 2009). They are also extremely dark matter dominated (e.g. Simon & Geha, 2007; Martin et al., 2007; Geha et al., 2009; Simon, 2019) and so their detection and further study may allow us insight into the nature of the dark matter particle.

With the value of finding new dwarfs to address these problems in mind, we have been conducting a visual inspection of imaging data from the DESI Legacy Imaging Survey (Dey et al., 2019) in the vicinity of M31 and Triangulum (M33) to search for ultra–faint companions to both systems. We have already identified a potential UFD satellite of M33 – Pisces VII/Triangulum III (Martínez-Delgado et al., 2022). In this paper, we report on a newly discovered UFD satellite of M31 in the constellation of Pegasus – Pegasus (Peg) V/Andromeda (And) XXXIV. In § 4.2.2 we discuss the DESI Legacy Survey imaging, plus our deep follow–up observations with Gemini/GMOS–N, then in § 4.2.3 we present the properties of, and distance to, Peg V. Finally we discuss the significance of our findings in § 4.2.4.

4.2.2 Identification and Gemini Observations

Peg V was identified as a partially resolved over–density in the DESI Legacy Imaging Survey (see left panel of Figure 4.10) by amateur astronomer Giuseppe Donatiello. Given its position on–sky, it was a good candidate for an ultra–faint M31 satellite (projected distance of $\sim$ 240 kpc). We were awarded directors discretionary time (proposal ID GN–2021B–DD–106) to perform deep imaging with Gemini/GMOS–N to resolve its stellar populations. Our observations were carried out on the nights of 2021–11–01 and 2021–11–25 and employed the g– and r–band filters. The total imaging time was 2250 s in g– band (split into 5×450 s exposures) and 1500 s in r– band (split into 5×300 s exposures). The images were pre–processed using the Gemini DRAGONS pipeline which performs standard bias, flat field and cosmic ray corrections to the images before producing a final stacked image (which can be seen in the right hand panel of Figure 4.10). The stacked images were then reduced using DAOPHOT/ALLFRAME (Stetson, 1987, 1994) in largely the same manner as Monelli et al. (2010b) and Martínez-Delgado et al. (2022). Briefly, we search for stellar sources on each stacked image and then perform aperture photometry, PSF derivation and PSF photometry with ALLSTAR. The resulting list of stars is then passed to ALLFRAME to construct individual catalogues with better determined position and instrumental magnitude of the input sources and provides the final photometry. We perform the photometric calibration using local standard stars from the Pan–STARRS1 3π survey (Chambers et al., 2016). The mean magnitudes were calibrated with a linear relation for the g–band, and a zero point for the r–band. We extinction correct the data using the reddening maps from Schlegel et al. (1998), re–calibrated by Schlafly & Finkbeiner (2011).

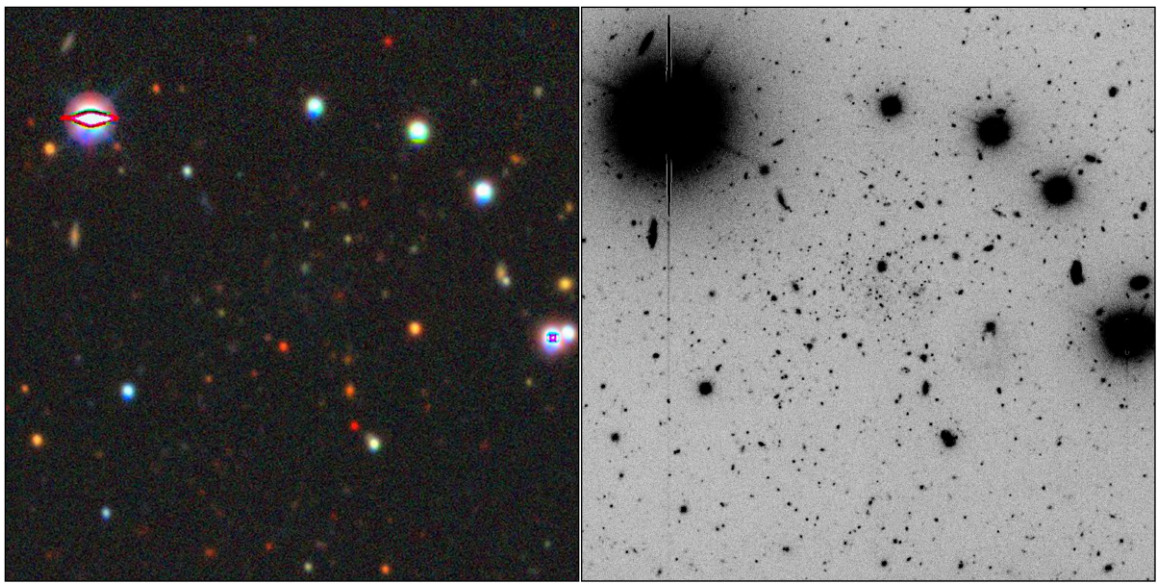

Figure 4.10: *Left panel*: Image of the dwarf galaxy Peg V from the DESI Legacy Imaging Survey. *Right panel*: Gemini/GMOS–N combined g– and r–band image of the galaxy obtained from Gemini follow–up observations (see § 4.2.2). North is up, East is left. In both images, the field of view is $150'' \times 150''$.

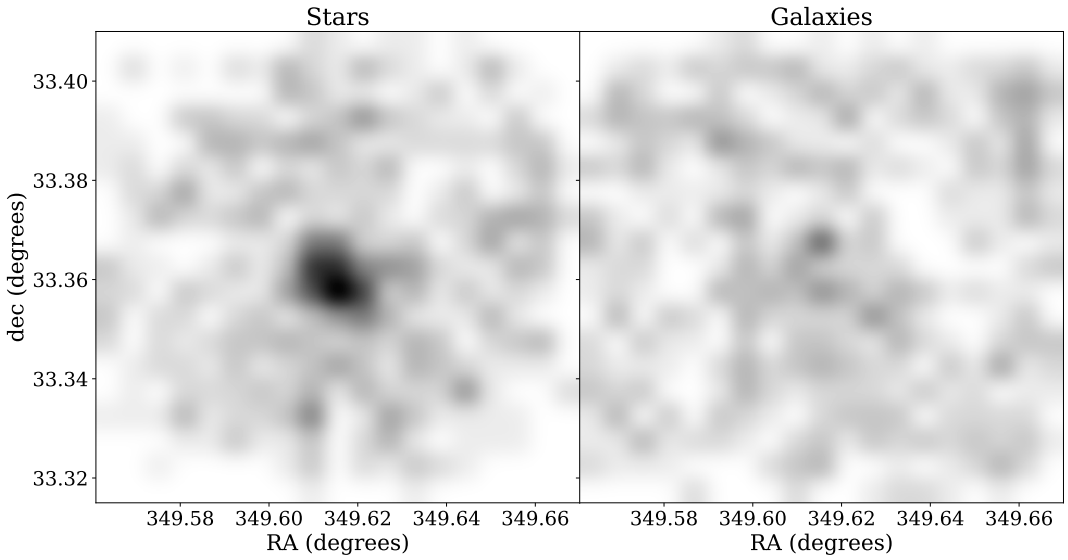

Figure 4.11: Filtered maps of all sources considered stars (*left*) vs galaxies (*right*) within our GMOS–N field of view. A clear over–density is seen in the stellar map which is not reproduced in the galaxies panel.

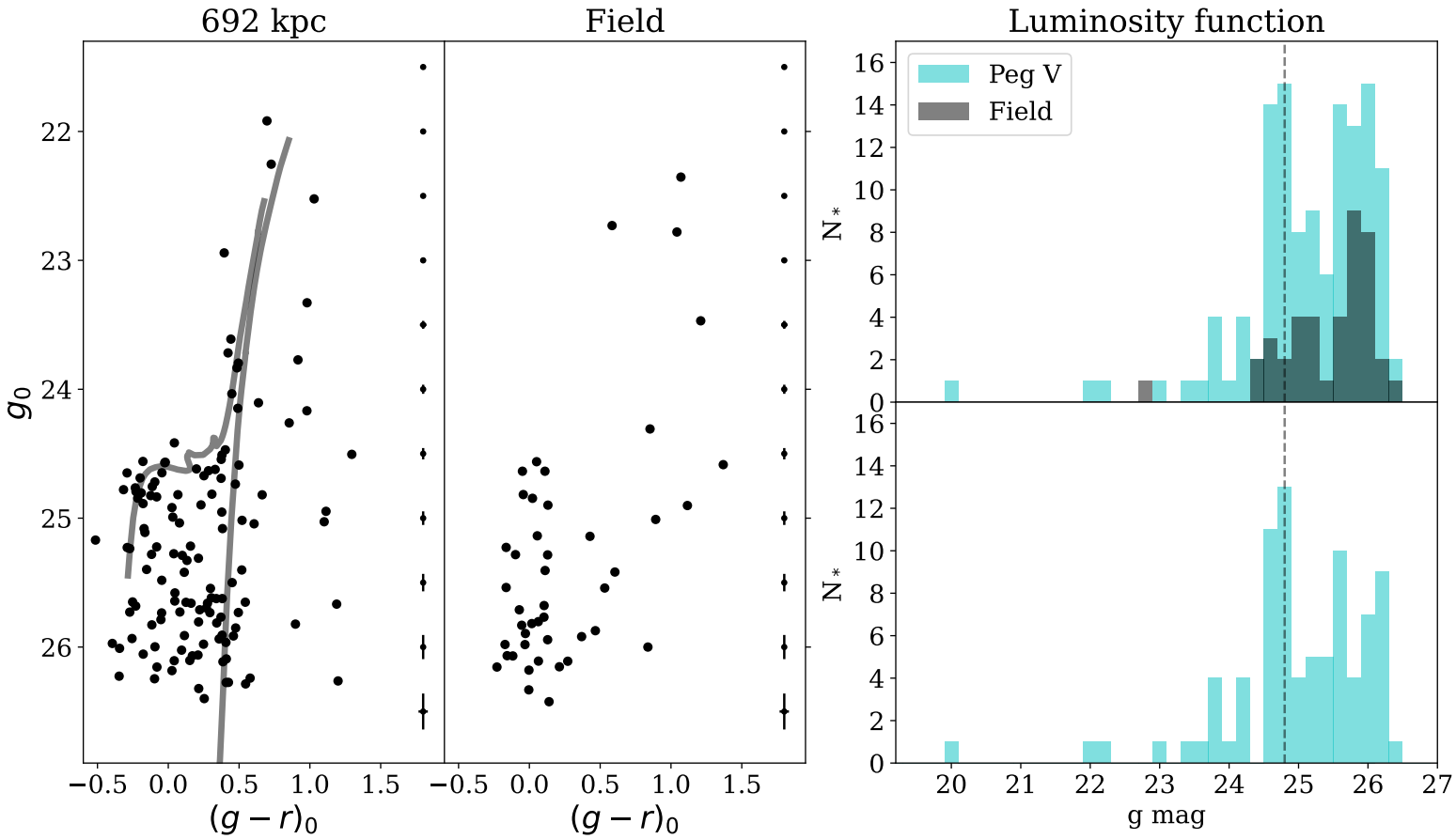

Figure 4.12: In the first two panels, we show the CMD for all stars within $2r_{\rm half}$ of Peg V (left) compared to the stellar populations in an equal area annulus beyond the dwarf to demonstrate the field contamination (right). We overlay a metal poor ([Fe/H]$= -3.2$) isochrone with age 12.5 Gyr shifted to 692 kpc (centre), representing the distance measured from the HB. Finally, we show the luminosity function in the right most panels. The top shows all stars within $2r_{\rm half}$ (cyan) and the field population (grey), and the lower panel shows the background corrected case. The dashed grey line shows the position of the blue HB feature.

Star–galaxy separation was performed using the sharpness parameter. In the left panel of Figure 4.11 we show the distribution of stars across the GMOS field of view, with the right panel showing the galaxy distribution. There is a clear over–density in the centre of the stellar map. In in the left panel of Figure 4.12 we show a colour magnitude diagram (CMD) for all stars within 0.8 arcmin of this over–density compared to an equal area annulus beyond 1.6 arcmin in the centre panel. An old (12.5 Gyr), metal–poor ([Fe/H]= −3.2) BaSTI isochrone (Hidalgo et al., 2018)[4] is overlaid, shifted to a distance of ∼ 700 kpc to highlight the red-giant branch (RGB) and horizontal branch (HB) feature.

4.2.3 Properties of Pegasus V

We determine the structural parameters for Peg V using the same Markov–Chain Monte Carlo (MCMC) inference technique as presented in Martínez-Delgado et al. (2022). We defer to that work for a detailed discussion, and briefly outline this process below. The method is based on that of Martin et al. (2016c) and uses EMCEE (Foreman-Mackey et al., 2013) to sample the posterior. We include all stars which fall within a broad colour magnitude cut of $r_0 < 25.5$ and $-0.5 < (g-r)_0 < 0.9$, giving 79 stars total. We then assume these stars comprise both members of the dwarf galaxy, and a foreground/background population. We assume the radial density profile, $\rho_{\rm dwarf}$ of the dwarf can be modelled as an exponential profile, with an ellipticity of $\epsilon = 1-(b/a)$ and $r_{\rm half}$ is the half–light radius. N^* is the number of likely member stars inside the CMD selection box associated to the dwarf.

We assume the fore/background contamination, Σ_b, is constant across the field and determine this by subtracting the dwarf galaxy stars (which we calculate by integrating the radial density profile) from the total number of potential members identified. We combine these assumptions into a likelihood function which is then used in the MCMC analysis:

$$\rho_{\rm model}(r) = \rho_{\rm dwarf}(r) + \Sigma_b. \tag{4.8}$$

We use broad, flat uniform priors for all parameters. The EMCEE routine used 100 walkers, over a total of 10,000 iterations with a burn in of 9,250. These numbers were determined based on a visual inspection of the traces. We show the results in Figure 4.13 and summarise them in Table 4.3. We find a position for Peg V of α =23:18:27.8±0.1, δ =33:21:32±3, a half–light radius of $r_{\rm half} = 0.44^{+0.2}_{-0.1}$ arcmin, and do not resolve an ellipticity.

The CMD for Peg V presents us with a sparse RGB and a well–populated HB feature. Given its projected distance from Andromeda of $D_{\rm proj} \sim 245$ kpc, the most likely scenario is that Peg V is an M31 satellite.

To determine its distance, we use two techniques that focus on the RGB and HB populations. For the RGB, we employ the same Bayesian tip of the red giant branch (TRGB) approach as in Tollerud et al. (2016) and Martínez-Delgado et al. (2022), which we briefly summarise below. We model the RGB and background population simultaneously as a broken power law with slopes of α and β in luminosity

[4] http://basti-iac.oa-abruzzo.inaf.it/isocs.html

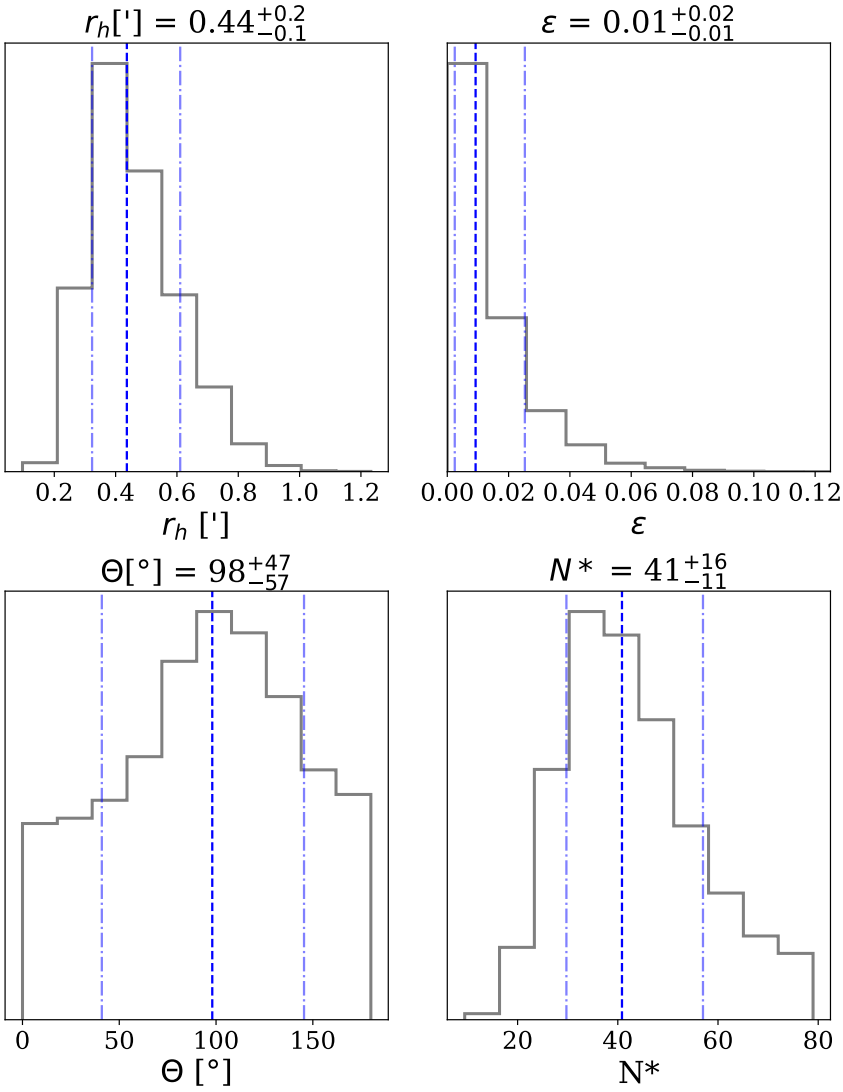

Figure 4.13: Marginalised posteriors for the structural parameters of Peg V. We show the the half–light radius, $r_{\rm half}$, ellipticity, ϵ, position angle, θ and the number of stars belonging to Peg V, N_* . The dashed lines represent the median value and 1σ uncertainties.

respectively. We assume a fraction f of stars in the background population (such that the fraction on the RGB is $1-f$) with the break located at the TRGB, $m_{\rm TRGB}$.

We use Bayesian inference to determine posterior probabilities for $m_{\rm TRGB}$, using uniform priors for all parameters, with U(0, 1) for f and U(0, 2) for α and β. For $m_{\rm TRGB}$ we use a broad prior of U(17, 22.5). We use the same colour selection as for the structural parameters of $(-0.5 < g - r < 0.9)$, but only include stars with $r_0 < 24$ to isolate the RGB. We use only stars within $2r_{\rm half}$, as if we include stars beyond this, the model has trouble distinguishing between background and dwarf (given the sparsity of RGB stars). We numerically integrate this luminosity function over a grid of m using the trapezoid rule for each set of parameters, and take the total likelihood as the sum of the logarithm of this over all stars.

We use EMCEE to sample the posterior distribution for the model parameters and find a solution of $m_{\rm TRGB} = 21.2^{+1.0}_{-1.8}$, corresponding to a distance of $D = 682^{+391}_{-355}$ kpc.

Table 4.3: The final structural and photometric properties for Peg V.

Property	Value
RA	$23^h\ 18^m\ 27.8^s \pm 0.1^s$
Dec	$33°21'\ 32'' \pm 3''$
$r_{\rm half}$ (arcmin)	$0.4^{+0.2}_{-0.1}$
D (kpc)	692^{+33}_{-31}
$D_{\rm M31}$ (kpc)	242^{+12}_{-11}
$r_{\rm half}$ (pc)	87^{+40}_{-54}
M_V	-6.3 ± 0.2
μ_0 (mag arcsec^{-2})	26.3 ± 0.3
L ($L_\odot$)	$2.8^{+0.6}_{-0.4} \times 10^4$
ϵ	0.01 ± 0.01
θ (°)	$96\ ^{+47}_{-57}$
N*	$41\ ^{+16}_{-11}$
$E(B-V)$ (mag)	0.06

This fit is poorly constrained owing to the small number of sources on the RGB.

A more precise distance can be determined by assuming the stars at $g_0 \sim 24.5$ constitute the HB. In the right–hand panels of Figure 4.12 we show the luminosity function in the g–band for Peg V. There is a pronounced bump at $g_0 \sim 24.8 \pm 0.1$ which we assume is the HB. With $M_{g,\rm HB} = 0.6$ (Irwin et al., 2007), we measure a distance of $D = 692^{+33}_{-31}$ kpc, entirely consistent with the RGB approach but with far smaller uncertainties.

In panel 1 of Figure 4.12 we show our isochrones shifted to this distance. We see that the HB and RGB features for the 12.5 Gyr isochrone perfectly overlap with the stellar populations of Peg V, suggesting that our candidate is an extremely metal poor M31 satellite.

Armed with a distance, we follow the approach of Martin et al. (2016c) and Martínez-Delgado et al. (2022) to measure the luminosity of Peg V. Using theoretical luminosity functions generated the PARSEC stellar models (Marigo et al., 2008; Girardi et al., 2010b), we define a probability distribution function (PDF) which describes the expected number of RGB stars per magnitude bin. We use an old (12 Gyr), metal–poor ([Fe/H]$= -2.5$), α enhanced ([α/Fe] $= +0.4$) isochrone with a Kroupa IMF. We randomly sample from this luminosity function to reproduce our observed dwarf which is simplified as having N_* stars (where N_* is taken from our MCMC analysis) above our magnitude cut of $r_0 < 25.5$. We record the sampled magnitude for all stars above and below this cut. Once N_* is reached, we sum all stars that were randomly sampled to get the total luminosity of Peg V. We repeat this procedure 1000 times to measure the average luminosity plus a statistical uncertainty for each observed magnitude band. We then convert these to the V band to obtain $M_V = -6.3 \pm 0.2$ for a distance of $D = 692^{+33}_{-31}$ kpc where both distance and luminosity uncertainties are included.

4.2.4 Discussion & Conclusions

We have discovered a new Local Group ultra–faint dwarf in the constellation of Pegasus and characterised it using deep Gemini/GMOS-N imaging. Peg V/And XXXIV is a far–flung M31 satellite with $M_V = -6.3 \pm 0.2$, located 242 kpc from the centre of the system. This places it close to the virial radius of M31 (estimated to be between $\sim 250 - 300$ kpc, e.g. Patel et al. 2018a; Kafle et al. 2018; Blaña Díaz et al. 2018). It is also the faintest M31 satellite detected outside of the PAndAS Survey. Given its size and luminosity, it is most likely a dwarf galaxy. However, at the lower 1σ bound on the radius, it could be consistent with the extended globular cluster population in M31's halo (e.g. Mackey et al. 2013).

The strong blue HB of Peg V makes it somewhat unique in Andromeda. M31 dwarf satellites typically possess far redder HBs (e.g. Da Costa et al. 1996, 2000, 2002) with only a handful showing a significant blue component. Martin et al. (2017) present homogeneous single orbit HST observations for 20 M31 satellite galaxies which well–resolve their HBs. They assess the colour of their HB features by computing the ratio, η, of the number of blue HB stars ($n_{\rm BHB}$) to the total number of HB stars ($n_{\rm BHB} + n_{\rm RHB}$). They find only two examples of dwarfs with relatively high fractions of blue HB stars, giving $\eta \sim 0.4$ (Andromeda XI and XVII). Repeating their analysis for Peg V, we find $\eta = 0.5 \pm 0.2$, setting it apart from the rest of the system. As blue HB stars are typically considered to trace ancient stellar populations, this could imply Peg V was quenched very early, making it a good candidate for a reionisation fossil (Bovill & Ricotti, 2009). It is also more similar to the UFDs of the MW, all of which appear to have been quenched $\gtrsim 10$ Gyr ago (Brown et al., 2014; Weisz et al., 2014; Sacchi et al., 2021) and possess blue HB features. The RGB stars of Peg V are also extremely blue, and are well described by the most metal–poor BaSTI isochrone (see Figure 4.12). This further supports that it was rapidly quenched by reionisation. If true, further study of its chemical properties may allow us to place constraints on the earliest epochs of star formation.

The RGB of Peg V also looks sparser than one may expect given its strong HB population. This may be partially explained by field contamination. Additionally, when comparing the CMD of Peg V to those of similarly bright dSphs in the MW, its RGB seems under–dense, which may mean we have overestimated its luminosity. Our method is susceptible to shot–noise given the sensitivity to a few individual bright stars. However, its CMD is similar to that of And XX ($M_V = -6.4$, Martin et al. 2016c). It may be that space–based imaging can allow more sophisticated modelling of the luminosity function and a robust determination of Peg V's intrinsic brightness.

With deep space–based imaging we could further probe the star formation history of Peg V, and learn if it is a candidate for a fossil galaxy quenched by reionisation. It also has a few bright RGB stars which can be targeted with 8–10m telescopes to measure their velocities and chemistry. Given its remote position in the halo, kinematics may also allow constraints of its orbit around M31 and the likelihood of previous interactions with its host that may also have quenched its star formation.

The discovery of Peg V in the DESI Legacy Imaging Survey bodes well for future discoveries of ultra–faint dwarfs in M31 and the wider Local Group with current and future surveys. It paints a rosy picture for simultaneously solving both the

missing satellite and field galaxy problems in our cosmic backyard. Our systematic visual inspection of the DESI images successfully detects partially resolved ultra–faint dwarf satellites in the M31/M33 system, which might be overlooked in the automatic detection of over–densities in stellar density maps (e.g. DELVE). Thus, both approaches are extremely complementary.

Conclusions

Chapters 2/3: And XXI & And XXV – The M31 Dwarfs with Low Central Densities

In Chapter 2, using new spectroscopic observations, I presented new kinematic analysis for And XXV. With the larger data set, I found that the velocity dispersion and, therefore, mass and mass–to–light ratio slightly increased. However, the results still showed that And XXV is radially extended and has significantly less mass contained within the half–light radius than dwarfs of comparable size. I then extended this analysis to include dynamical mass modelling of And XXV to investigate its dark matter density profile. This analysis is the first of its kind for And XXV, and only the second time this has been applied to an M31 satellite, the other being And XXI (Collins et al., 2021). From the dark matter density profile, it was not possible to constrain the shape of the inner slope to discern between a cusp or a cored profile due to the size of the uncertainties. Instead, I focused on the central density, measured at 150 pc. I found that And XXV has an unusually low central dark matter density compared to other dwarfs of a comparable halo mass. This was similar to the result found by Collins et al. (2021) for And XXI.

The central densities of these two dwarfs are approximately an order of magnitude less dense than we would expect for their halo mass, in an LCDM cosmology and in the absence of tides and/or significant dark matter heating. Their density puts them in line with a cored NFW profile and comparable to currently star forming dIrrs in the Local Group, an unexpected result for two quiescent dSphs. Coring is expected in star forming dwarfs due to the feedback effects of star formation (dark matter heating). However, And XXV and And XXI have undergone short bursty episodes of star formation. As such, dark matter heating is not expected to have significantly lowered their central densities. This posed an interesting question, can we reconcile the unusually low central densities of And XXV and AndXXI in CDM, or do we need to invoke another type of dark matter?

I looked to answer this question in Chapter 3. I confirmed that both dwarfs had undergone minimal coring due to star formation, and dark matter heating alone cannot explain the low central densities. Instead, I investigated the effects of tidal stripping and/or low halo concentrations in CDM, WDM and SIDM cosmologies. I found the low central density of And XXV and And XXI can be reconciled within a CDM cosmology, albeit by invoking extremes of tidal stripping and halo concentration. And XXV appears to favour a tidal stripping scenario resulting in $\sim 99\%$ tidal mass loss. Whereas And XXI favours an extremely low concentration halo that is 3σ below the median halo concentration. Introducing a WDM cosmology did not significantly reduce the severity of tidal stripping or halo concentration required. While WDM lowers the halo concentration of dwarf galaxies, the difference between

CDM and WDM halo concentrations is minimal for higher thermal relic masses. As such, low thermal relic masses ($\lesssim$ 1 keV), which have already been ruled out by other observations, were required to explain And XXV and And XXI. Instead, I found that WDM required similar levels of tidal stripping and/or low halo concentrations to those for CDM. For both CDM and WDM, it was possible to slightly reduce the severity of the scenario required by introducing a combination of both tidal stripping and low halo concentration. However, the required scenarios were still in the regime of moderate tidal stripping ($> 90\%$ mass loss) and outlying halo concentrations ($< -\sim 2\sigma$). Proper motion data from multi–epoch would allow us to better constrain the orbital histories of And XXV and And XXI and, thus, the expected tidal mass loss, reducing one of the current factors of uncertainty. For SIDM, we did not find a constant cross–section model that could reconcile the central density of either dwarf. We found that the models were too effective at forming extended cores in the centre. As such, by the time the density at the half–light radius was in agreement with the density of the dwarf, the centre was significantly under–dense.

Before the manuscript presented in Chapter 3 is submitted for publication, I aim to extend the SIDM section to investigate the viability of both core collapse and velocity–dependent SIDM models. I currently tentatively rule out these possibilities from the preliminary analysis. However, I would like to investigate them in more detail, potentially implementing the parameterisation presented in Gilman et al. (2021), before concretely commenting feasibility of these SIDM models for And XXV and And XXI. Furthermore, I currently implement the tidal stripping prescriptions from (Peñarrubia et al., 2008, 2010). Errani & Navarro (2021) presented an updated version of these prescriptions, made possible by the higher numerical resolution of their simulations. While this new relation is very similar, it deviates slightly from the Peñarrubia et al. (2008, 2010) relation at the high mass loss regime. As this is the realm of mass loss required for And XXI and And XXV, I would like to implement these new tidal stripping prescriptions. However, the relations in Errani & Navarro (2021) are given in terms of characteristic mass, velocity and crossing time. These values are specific to the simulations used to derive them. The paper does not appear to present a method to convert the unphysical 'characteristic' properties from the simulations to physical properties I can obtain from observations. It might be possible to obtain the conversion parameters via a numerical root–finding algorithm. Else, I hope to communicate directly with the authors of Errani & Navarro (2021) to discuss this conversion.

The methodology outlined in these two chapters presents a framework for the analysis of the remaining M31 dwarf galaxy satellites. The kinematic and dynamical mass modelling for the remaining dwarfs with spectroscopic data presented in Collins et al. (2013) is already underway (Pickett et al., in prep), using the methods outlined in Chapter 2. This analysis may potentially be extended to also include the M31 dwarfs with spectroscopic observations from the Spectroscopic and Photometric Landscape of Andromeda's Stellar Halo (SPLASH) survey (Kalirai et al., 2010; Tollerud et al., 2012). This research will provide an additional population sample within the Local Group, providing more data points and another system

to compare against the Milky Way. The analysis outlined in Chapter 3 not only presented possible solutions to the low central density in And XXV and And XXI, but it is also an important proof of concept for dark matter constraints. However, with only two dwarfs, it is not possible to make substantial dark matter constraints. When combined with this new full population of M31, it offers the potential to place constraints on dark matter in different cosmologies as well as dwarf galaxy formation and evolution mechanisms.

Chapter 4: New Dwarf Discoveries Around M31/M33

In Chapter 4, I detailed the discovery of two UFD dwarf galaxies within the M31/M33 system, Pisces VII and Pegasus V. Both of the dwarfs were partially resolved over densities discovered by-eye in publically available DESI Legacy Imaging Survey data. From follow–up photometry, we were able to derive the distance, structural parameters, and luminosity of both dwarfs. Pegasus V was found to be a far–flung satellite of M31, located at the very outskirts of the virial radius of M31 and outside of the PAndAS footprint. It was found to be extremely metal–poor with a blue horizontal branch, indicating it could be a reionisation fossil. For Pisces VII, it was difficult to measure a precise distance from the TNG photometry. This meant that the dwarf could be a satellite of either M31 or M33. With deeper photometry, we were later able to constrain the distance and confirm Pisces VII is a satellite of M33 in a later paper by Collins et al. (2023). In contrast to Pegasus V, Pisces VII showed hints exciting hints of a young blue stellar sub–population, which I will discuss below. The collaboration is continuing to investigate other potential candidates around the M31/M33 system with the hopes of discovering more interesting dwarfs. These potential dwarfs, in combination with the dwarfs from upcoming surveys, will make for exciting new systems to push our understanding of dark matter and galaxy formation.

In the last year since these two studies were published, exciting developments have occurred within our group and the wider community. Firstly, a different group reported the discovery of Pegasus W, another ultra–faint dwarf found in the DESI Legacy Imaging Survey data that lies beyond the virial halo of M31 (McQuinn et al., 2023). With follow–up HST imaging, they could target stars with magnitudes just below the horizontal branch, where they find Pegasus W may have a young ($<$ 500 Myr) stellar component. As mentioned, we had previously observed a strikingly similar feature in the CMD of Pisces VII. However, due to the magnitude limit of our TNG imaging, we ran into star–galaxy separation issues at the magnitude we saw these potentially young blue stars.

We have also been attempting to obtain HST imaging of Pisces VII and Pegasus V. Deeper spaced–based imaging would allow us to reach the MSTO, which would be undetectable from ground–based telescopes. By reaching the MSTO we can break the age–metallicity degeneracy and hence derive precise star formation histories. Furthermore, we would be able to concretely identify the nature of the intriguing plume of young blue stars in Pisces VII. I have been PI for two proposals focusing on Pisces VII and co–PI on two focusing on Pegasus V. Due to the extremely competitive nature of HST proposals, we have yet to be successful, but

we hold out hope for future cycles. We were successfully awarded Directors Discretionary Time from Gemini to observe both Pegasus V (as discussed in § 4.2) and also Pisces VII (Collins et al., 2023). The reduction of this follow–up data was done by Michelle Collins and Mahdieh Navabi, and the analysis was led by Michelle Collins and Noushin Karim. With the deeper data from Gemini, we were able to tentatively identify the presence of blue stars consistent with ages of ~ 1.5 Gyr in the CMD of Pisces VII.

The blue stars identified in both Pisces VII and Pegasus W may turn out to be simply contamination, such as background galaxies masquerading as stars due to poor star–galaxy separation. However, a recent study by Savino et al. (2023), using deep HST imaging to decipher the star formation histories of six UFD M31 satellites, conclusively observed a young blue stellar component in And XIII. They found that And XIII only formed 10% of its stars before $z = 5$, with 75% of its stellar mass forming in a rapid burst between $z \sim 2-3$, showing that And XIII is a 'young' UFD that was not quenched by reionisation, unlike the Milky Way UFDs. Furthermore, they found that the six M31 UFDs presented with more extended star formation histories than the Milky Way UFDs, hinting at the importance of environmental effects. These observational results are supported by a number of recent simulations that have shown reionisation does not have to quench star formation UFDs (e.g. Oñorbe et al., 2015; Fitts et al., 2017; Munshi et al., 2019; Rey et al., 2020; Gutcke et al., 2022). If the potential young stellar components of Pisces VII and Pegasus W are found to be genuine, these dwarfs will add two more 'young' UFD systems to the census, a number that will undoubtedly grow with the wealth of UFDs predicted to be discovered by the Vera C. Rubin Observatory (Ivezić et al., 2019) and the Nancy Grace Roman Space Telescope (Spergel et al., 2015).

Final Thoughts

I feel extremely privileged to have contributed a small slice of research to the wider field, helping to develop our understanding of dark matter. I am excited to see what interesting secrets the remaining M31 dwarfs hold, as well as the new dark matter constraints that we can place with another population of dwarf galaxies to sample. Furthermore, we are on the precipice of a new epoch of rapid dwarf discovery with upcoming surveys. These surveys promise to extend the limits of dwarf discovery and will undoubtedly uncover systems that push the parameter space describing dwarf galaxies to new extremes. These upcoming dwarf discoveries will likely provide new challenges and raise many more questions surrounding the nature of dark matter. The observational analysis of these dwarfs, using the methods outlined in this thesis, in combination with state–of–the–art simulations, will help improve our understanding of dark matter. With the eventual hope that we can sufficiently constrain the nature of dark matter, resulting in its detection.

Appendix

A Chapter 2: Radial Profiles from `GravSphere`

Here we include the radial profile fits from `GravSphere`, see Fig. 1. First, the top panel shows the well defined surface brightness profile, Σ_*. The blue data points are the binned photometry from the LBT imaging data out to four effective half light radii. Second, in the bottom panel is the radial velocity dispersion, $\sigma_{\rm LOS}$. The blue data points are the binned velocity dispersion data taken from our probability weighted member stars. For both panels, the black line shows the fit from `GravSphere` with the dark and light gray shaded regions showing the 1 and 2σ uncertainty intervals respectively. The vertical purple dashed line is the half-light radius of And XXV. We see that the observed surface brightness profile is well reproduced by `GravSphere`. We note that the same velocity dispersion increasing with increasing radius behaviour is observed in the binned kinematic data that is explained in § 2.4.2 and § 2.7. We reiterate that this behaviour may indicate that And XXV is not in dynamical equilibrium and could be indicative of And XXV having undergone tidal interactions. The velocity dispersion profile inferred by GravSphere within the 1σ uncertainties for all bins. However, from visual inspection it seems possible that `GravSphere` has artificially biased the velocity dispersion to higher values at small radii in an attempt to fit this flaring feature. Although, this potential bias would not affect the conclusion that And XXV has an unusually low central dark matter density. A lower velocity dispersion profile would result in a lower density. As such, the value from this study can be considered an upper bound of the density.

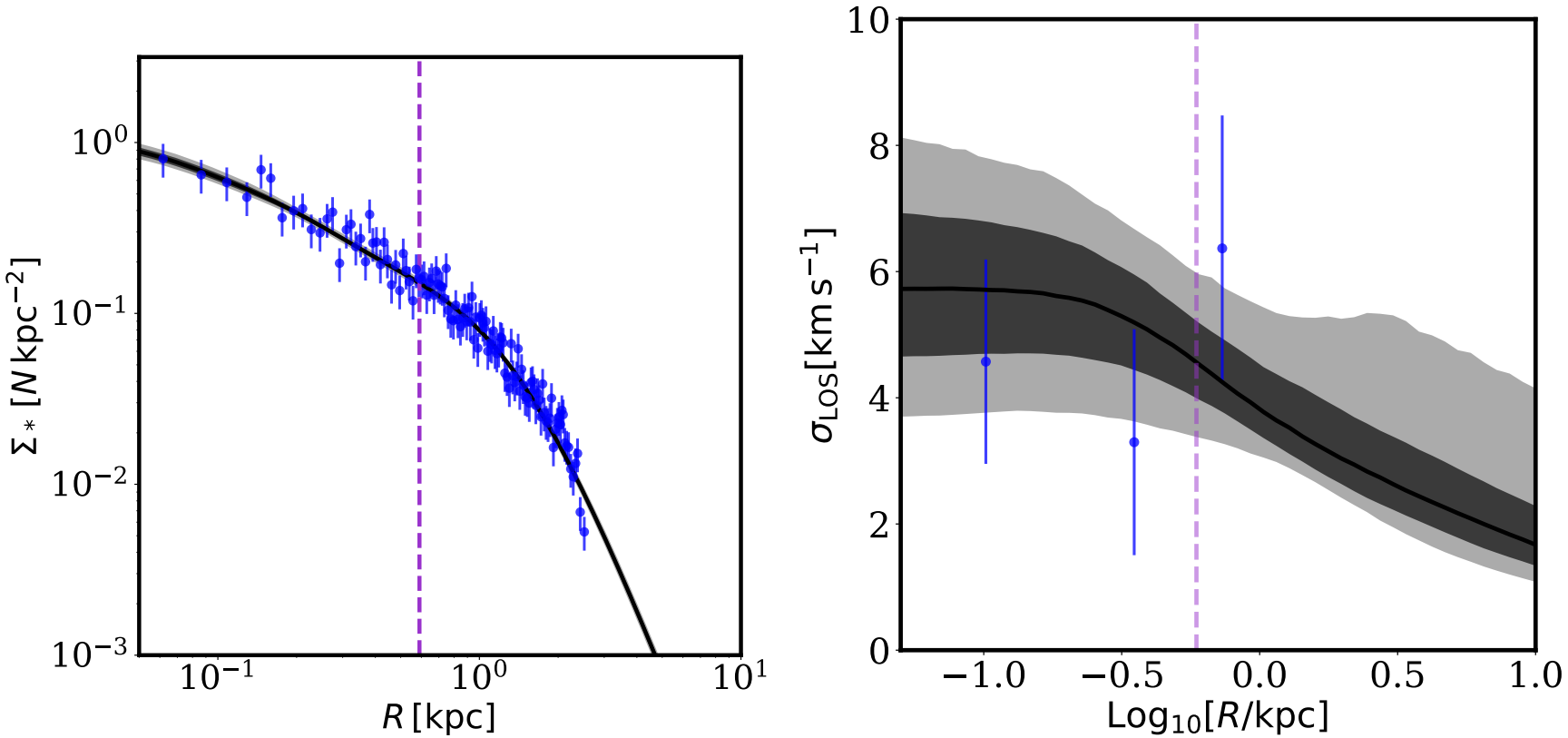

Figure 1: Top: The surface brightness profile, Σ_*. The blue data points are the binned photometry from the LBT imaging data. **Bottom:** The radial velocity dispersion, $\sigma_{\rm LOS}$. The blue data points are the binned velocity dispersions from our probability weighted member stars. **Both:** The black line shows the fit from `GravSphere`. The 1 and 2σ uncertainty intervals are shown by the dark grey and light grey shaded regions, respectively. The vertical purple dashed line is the half-light radius of And XXV.

B Chapter 3: WDM - NFW Profiles

Here we present the WDM plus tidal stripping and WDM plus halo concentration plots for an NFW profile (note the coreNFW profiles are shown in the main body of the chapter). Figure 2 shows the effects of tidal stripping in a WDM cosmology for an NFW profile and Figure 3.

We find very little difference between the coreNFW and NFW profiles. The central densities ($r = 150$ pc) are lower for the coreNFW profiles, as the slight coring makes the dwarfs more susceptible to tidal stripping. However, the density at the outskirts ($r = r_{\rm h}$) is similar for both profiles. A successful tidal stripping prescription needs to be able to explain the entire radial profile. As such, due to the similarity between the profiles at the outskirts, the scenarios able to reconcile the low central densities of And XXI and And XXV are the same regardless of the effects of dark matter heating.

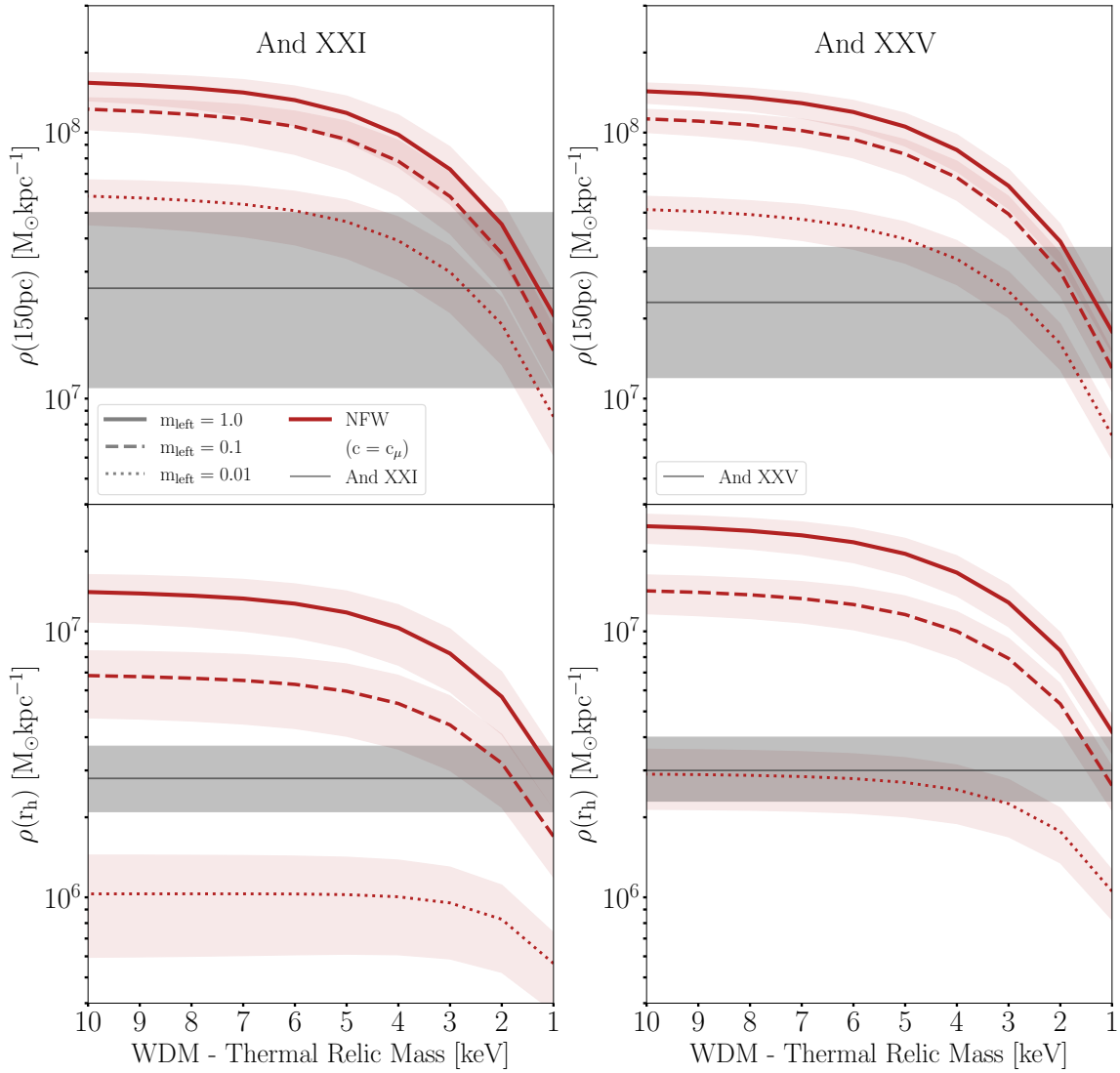

Figure 2: Left Top: The density measured at 150 parsecs from the centre of And XXI against the thermal relic mass of the WDM particle. The dark red line series describes an NFW profile. The shaded regions show the 1σ uncertainty due to M_{200}. The line shows the density for an unstripped And XXI, the dashed line for a tidal mass loss of 90% and the dotted line for 99%. Note here we consider the effect of only tidal stripping in a WDM cosmology; as such, the concentration of the halo is held at the median concentration c_μ. The grey line and shaded region show the density at 150pc measure for And XXI and the corresponding 1σ uncertainty. **Left Bottom**: The same as above, but now for the density at the half-light radius. **Right:** The same as before, but for And XXV

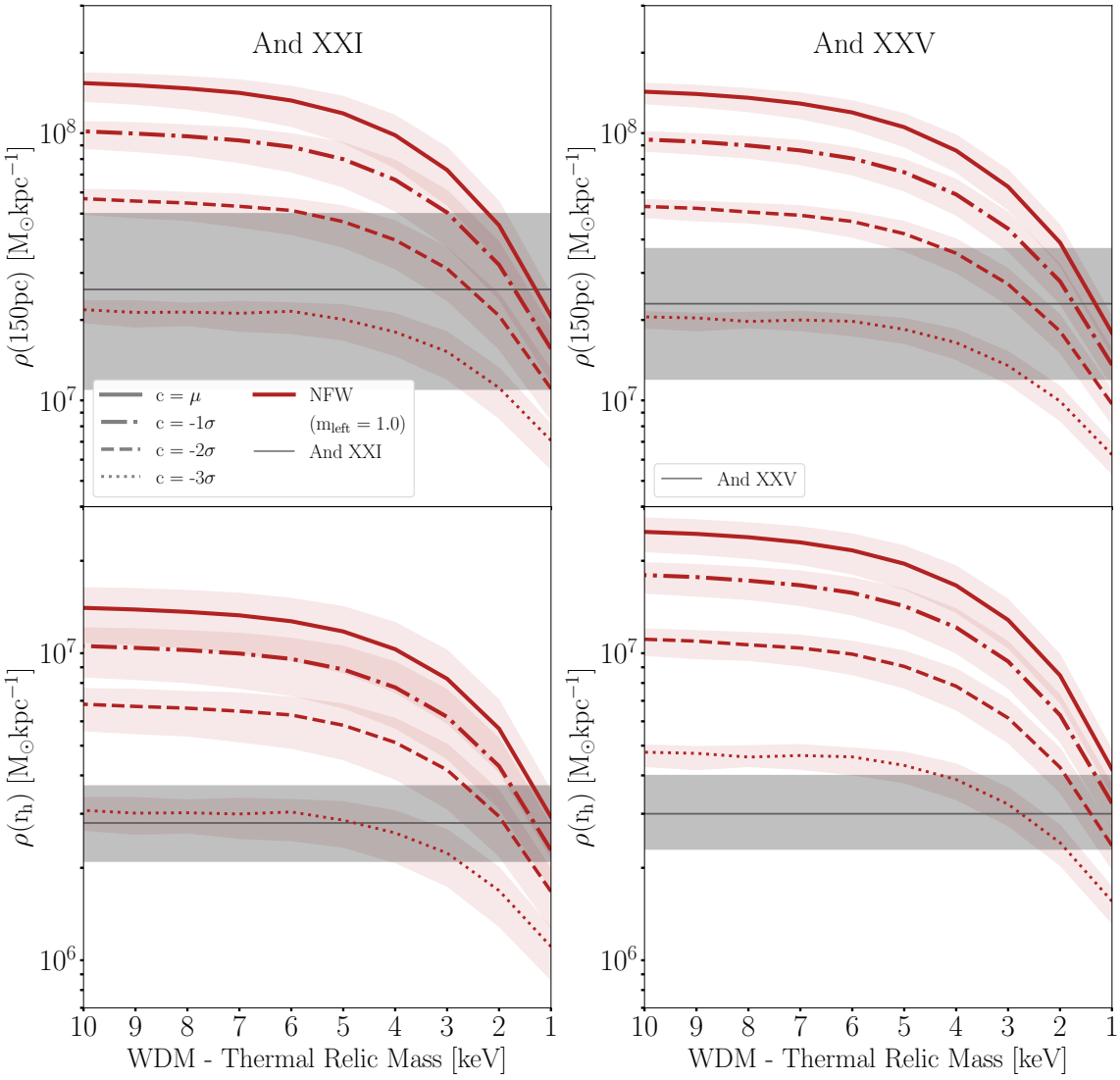

Figure 3: Left Top: Again, showing the density measured at 150 parsecs from the centre of And XXI against the thermal relic mass of the WDM particle where the dark red line series describes an NFW profile and the shaded regions show the 1σ uncertainty due to M_{200}. However, this figure shows only the effects of halo concentration; as such, these profiles are not tidally stripped ($m_{\rm left} = 1.0$). The solid line shows the density for an average concentration halo (c_μ) And XXI, then dot-dashed, dashed, and dotted lines illustrate a $c_{-1\sigma}$, $c_{-2\sigma}$ and $c_{-3\sigma}$ halo concentration, respectively. The grey line and shaded region show the density at 150pc measure for And XXI and the corresponding 1σ uncertainty. **Left Bottom**: The same as above, but now for the density at the half-light radius. **Right:** The same as before, but for And XXV

Bibliography

Aalseth C. E. et al., 2011, Phys. Rev. Lett., 106, 131301
Abazajian K. N. et al., 2009, ApJS, 182, 543
Abbott T. M. C. et al., 2018, ApJS, 239, 18
Adhikari S. et al., 2022, arXiv e-prints, arXiv:2207.10638
Agnello A., Evans N. W., 2012, ApJ, 754, L39
Aguirre A., Schaye J., Quataert E., 2001, ApJ, 561, 550
Akerib D. S. et al., 2017, Phys. Rev. Lett., 118, 021303
Alvey J. et al., 2021, MNRAS, 501, 1188
Amorisco N. C., 2019, MNRAS, 489, L22
Amorisco N. C., Agnello A., Evans N. W., 2013, MNRAS, 429, L89
Amorisco N. C., Evans N. W., 2012, ApJ, 756, L2
Andernach H., Zwicky F., 2017, arXiv e-prints, arXiv:1711.01693
Andrade K. E., Fuson J., Gad-Nasr S., Kong D., Minor Q., Roberts M. G., Kaplinghat M., 2022, MNRAS, 510, 54
Angloher G. et al., 2012, European Physical Journal C, 72, 1971
Aprile E. et al., 2011, Phys. Rev. Lett., 107, 131302
Arbey A., Mahmoudi F., 2021, Progress in Particle and Nuclear Physics, 119, 103865
Arcadi G., Dutra M., Ghosh P., Lindner M., Mambrini Y., Pierre M., Profumo S., Queiroz F. S., 2018, European Physical Journal C, 78, 203
Armandroff T. E., Da Costa G. S., 1991, AJ, 101, 1329
Armandroff T. E., Davies J. E., Jacoby G. H., 1998, AJ, 116, 2287
Armandroff T. E., Jacoby G. H., Davies J. E., 1999, AJ, 118, 1220
Astropy Collaboration et al., 2022, apj, 935, 167
Astropy Collaboration et al., 2018, AJ, 156, 123
Astropy Collaboration et al., 2013, A&A, 558, A33
Aubourg É. et al., 2015, Phys. Rev. D, 92, 123516
Avila-Reese V., Colín P., Valenzuela O., D'Onghia E., Firmani C., 2001, ApJ, 559, 516
Balberg S., Shapiro S. L., Inagaki S., 2002, ApJ, 568, 475
Baldry I. K., Glazebrook K., Driver S. P., 2008, MNRAS, 388, 945
Banik N., Bertone G., Bovy J., Bozorgnia N., 2018, , 2018, 061
Banik N., Bovy J., 2019, MNRAS, 484, 2009
Banik N., Bovy J., Bertone G., Erkal D., de Boer T. J. L., 2021, , 2021, 043
Bardeen J. M., Bond J. R., Kaiser N., Szalay A. S., 1986, ApJ, 304, 15
Barnard E. E., Ranyard A. C., 1894, Knowledge: An Illustrated Magazine of Science, 17, 253
Barrena R., Biviano A., Ramella M., Falco E. E., Seitz S., 2002, A&A, 386, 816
Battaglia G., Helmi A., Tolstoy E., Irwin M., Hill V., Jablonka P., 2008, ApJ, 681, L13
Battaglia G., Nipoti C., 2022, Nature Astronomy, 6, 659

Bechtol K. et al., 2015, ApJ, 807, 50
Begeman K. G., Broeils A. H., Sanders R. H., 1991, MNRAS, 249, 523
Behnke E. et al., 2011, Phys. Rev. Lett., 106, 021303
Bell E. F., Slater C. T., Martin N. F., 2011, ApJ, 742, L15
Belokurov V., 2013, New Astronomy Reviews, 57, 100
Belokurov V. et al., 2008, ApJ, 686, L83
Belokurov V. et al., 2007, ApJ, 654, 897
Belokurov V. et al., 2006, ApJ, 647, L111
Benitez-Llambay A., Frenk C., 2020, MNRAS, 498, 4887
Bennett C. L. et al., 2003, ApJS, 148, 97
Benson A. J., Bower R. G., Frenk C. S., Lacey C. G., Baugh C. M., Cole S., 2003, ApJ, 599, 38
Benson A. J., Frenk C. S., Lacey C. G., Baugh C. M., Cole S., 2002, MNRAS, 333, 177
Bernabei R. et al., 2010, European Physical Journal C, 67, 39
Bertone G., Hooper D., Silk J., 2005, Phys. Rep., 405, 279
Bertone G., Tait T. M. P., 2018, Nature, 562, 51
Binney J., 1980, MNRAS, 190, 873
Binney J., Mamon G. A., 1982, MNRAS, 200, 361
Binney J., Tremaine S., 2008, Galactic Dynamics: Second Edition
Blaña Díaz M. et al., 2018, MNRAS, 481, 3210
Blanton M. R., Lupton R. H., Schlegel D. J., Strauss M. A., Brinkmann J., Fukugita M., Loveday J., 2005, ApJ, 631, 208
Blumenthal G. R., Faber S. M., Primack J. R., Rees M. J., 1984, Nature, 311, 517
Blumenthal G. R., Pagels H., Primack J. R., 1982, Nature, 299, 37
Boddy K. K., Feng J. L., Kaplinghat M., Tait T. M. P., 2014, Phys. Rev. D, 89, 115017
Bode P., Ostriker J. P., Turok N., 2001, ApJ, 556, 93
Bond J. R., Kofman L., Pogosyan D., 1996, Nature, 380, 603
Bond J. R., Szalay A. S., Turner M. S., 1982, Phys. Rev. Lett., 48, 1636
Bonnivard V. et al., 2015, ApJ, 808, L36
Borukhovetskaya A., Navarro J. F., Errani R., Fattahi A., 2022, MNRAS, 512, 5247
Bose S., Deason A. J., Frenk C. S., 2018, ApJ, 863, 123
Bosma A., 1978, PhD thesis, University of Groningen, Netherlands
Bovill M. S., Ricotti M., 2009, ApJ, 693, 1859
Bovill M. S., Ricotti M., 2011a, ApJ, 741, 17
Bovill M. S., Ricotti M., 2011b, ApJ, 741, 18
Bradač M., Allen S. W., Treu T., Ebeling H., Massey R., Morris R. G., von der Linden A., Applegate D., 2008, ApJ, 687, 959
Brasseur C. M., Martin N. F., Macciò A. V., Rix H.-W., Kang X., 2011, ApJ, 743, 179
Bressan A., Marigo P., Girardi L., Salasnich B., Dal Cero C., Rubele S., Nanni A., 2012, MNRAS, 427, 127
Brooks A. M., Zolotov A., 2014, ApJ, 786, 87
Brown T. M. et al., 2012, ApJ, 753, L21
Brown T. M. et al., 2014, ApJ, 796, 91

Buck T., Macciò A. V., Dutton A. A., 2015, ApJ, 809, 49
Buck T., Macciò A. V., Dutton A. A., Obreja A., Frings J., 2019, MNRAS, 483, 1314
Buckley M. R., Peter A. H. G., 2018, Phys. Rep., 761, 1
Buckley M. R., Zavala J., Cyr-Racine F.-Y., Sigurdson K., Vogelsberger M., 2014, Phys. Rev. D, 90, 043524
Bullock J. S., Boylan-Kolchin M., 2017, ARA&A, 55, 343
Bullock J. S., Kravtsov A. V., Weinberg D. H., 2000, ApJ, 539, 517
Burles S., Nollett K. M., Truran J. W., Turner M. S., 1999, Phys. Rev. Lett., 82, 4176
Caldwell N. et al., 2017, ApJ, 839, 20
Cannon R. D., Hawarden T. G., Tritton S. B., 1977, MNRAS, 180, 81P
Canterna R., Flower P. J., 1977, ApJ, 212, L57
Carretta E., Gratton R. G., Clementini G., Fusi Pecci F., 2000, ApJ, 533, 215
Casetti-Dinescu D. I., Girard T. M., Schriefer M., 2018, MNRAS, 473, 4064
Casetti-Dinescu D. I., Hansen C. K., Girard T. M., Kozhurina-Platais V., Platais I., Horch E. P., 2022, AJ, 163, 1
Cerny W. et al., 2023, arXiv e-prints, arXiv:2306.04690
Cerny W. et al., 2021a, ApJ, 910, 18
Cerny W. et al., 2021b, ApJ, 920, L44
Chambers K. C. et al., 2016, arXiv e-prints, arXiv:1612.05560
Chan T. K., Kereš D., Oñorbe J., Hopkins P. F., Muratov A. L., Faucher-Giguère C. A., Quataert E., 2015, MNRAS, 454, 2981
Chapman S. C. et al., 2013, MNRAS, 430, 37
Charbonnier A. et al., 2011, MNRAS, 418, 1526
Charles E. J. E. et al., 2023, MNRAS, 521, 3527
Cherwinka J. et al., 2012, Astroparticle Physics, 35, 749
Choi J., Dotter A., Conroy C., Cantiello M., Paxton B., Johnson B. D., 2016, ApJ, 823, 102
Cline J. M., Liu Z., Moore G. D., Xue W., 2014, Phys. Rev. D, 90, 015023
Clowe D., Bradač M., Gonzalez A. H., Markevitch M., Randall S. W., Jones C., Zaritsky D., 2006, ApJ, 648, L109
Clowe D., Gonzalez A., Markevitch M., 2004, ApJ, 604, 596
Cockcroft R. et al., 2011, ApJ, 730, 112
Colín P., Avila-Reese V., Valenzuela O., Firmani C., 2002, ApJ, 581, 777
Collins M. L. M. et al., 2013, ApJ, 768, 172
Collins M. L. M. et al., 2014, ApJ, 783, 7
Collins M. L. M., Charles E. J. E., Martínez-Delgado D., Monelli M., Karim N., Donatiello G., Tollerud E. J., Boschin W., 2022a, MNRAS, 515, L72
Collins M. L. M. et al., 2023, arXiv e-prints, arXiv:2305.13966
Collins M. L. M. et al., 2021, MNRAS, 505, 5686
Collins M. L. M., Tollerud E. J., Rich R. M., Ibata R. A., Martin N. F., Chapman S. C., Gilbert K. M., Preston J., 2020, MNRAS, 491, 3496
Collins M. L. M., Tollerud E. J., Sand D. J., Bonaca A., Willman B., Strader J., 2017, MNRAS, 467, 573

Collins M. L. M., Williams B. F., Tollerud E. J., Balbinot E., Gilbert K. M., Dolphin A., 2022b, MNRAS, 517, 4382
Conn A. R. et al., 2012, ApJ, 758, 11
Cooper M. C., Newman J. A., Davis M., Finkbeiner D. P., Gerke B. F., 2012, spec2d: DEEP2 DEIMOS Spectral Pipeline
Corbelli E., Thilker D., Zibetti S., Giovanardi C., Salucci P., 2014, A&A, 572, A23
Correa C. A., 2021, MNRAS, 503, 920
Côté P., West M. J., Marzke R. O., 2002, ApJ, 567, 853
Cyburt R. H., 2004, Phys. Rev. D, 70, 023505
Cyr-Racine F.-Y., Sigurdson K., Zavala J., Bringmann T., Vogelsberger M., Pfrommer C., 2016, Phys. Rev. D, 93, 123527
Da Costa G. S., Armandroff T. E., Caldwell N., 2002, AJ, 124, 332
Da Costa G. S., Armandroff T. E., Caldwell N., Seitzer P., 1996, AJ, 112, 2576
Da Costa G. S., Armandroff T. E., Caldwell N., Seitzer P., 2000, AJ, 119, 705
Da Costa G. S., Ortolani S., Mould J., 1982, ApJ, 257, 633
Davis M., Efstathiou G., Frenk C. S., White S. D. M., 1985, ApJ, 292, 371
de Blok W. J. G., 2010, Advances in Astronomy, 2010, 789293
de Blok W. J. G., McGaugh S. S., Bosma A., Rubin V. C., 2001, ApJ, 552, L23
de Blok W. J. G., Walter F., Brinks E., Trachternach C., Oh S. H., Kennicutt, R. C. J., 2008, AJ, 136, 2648
de Jong J. T. A., Rix H. W., Martin N. F., Zucker D. B., Dolphin A. E., Bell E. F., Belokurov V., Evans N. W., 2008, AJ, 135, 1361
de Lorenzi F. et al., 2009, MNRAS, 395, 76
Deason A. J., Conroy C., Wetzel A. R., Tinker J. L., 2013, ApJ, 777, 154
Dey A. et al., 2019, AJ, 157, 168
Di Cintio A., Brook C. B., Macciò A. V., Stinson G. S., Knebe A., Dutton A. A., Wadsley J., 2014, MNRAS, 437, 415
Dicke R. H., 1946, Review of Scientific Instruments, 17, 268
Diemer B., 2018, ApJS, 239, 35
Dodelson S., 2011, International Journal of Modern Physics D, 20, 2749
Doliva-Dolinsky A. et al., 2022, ApJ, 933, 135
Doliva-Dolinsky A. et al., 2023, arXiv e-prints, arXiv:2303.01528
Dolphin A. E., 2002, MNRAS, 332, 91
D'Onghia E., Besla G., Cox T. J., Hernquist L., 2009, Nature, 460, 605
Dooley G. A., Peter A. H. G., Yang T., Willman B., Griffen B. F., Frebel A., 2017, MNRAS, 471, 4894
Doppler C., 1846, Annalen der Physik, 144, 1
Dotter A., Chaboyer B., Jevremović D., Kostov V., Baron E., Ferguson J. W., 2008, ApJS, 178, 89
Driver S. P., Phillipps S., Davies J. I., Morgan I., Disney M. J., 1994, MNRAS, 266, 155
Drlica-Wagner A. et al., 2020, ApJ, 893, 47
Drlica-Wagner A. et al., 2015, ApJ, 813, 109
Drlica-Wagner A. et al., 2021, ApJS, 256, 2
Dubinski J., Carlberg R. G., 1991, ApJ, 378, 496
Dutton A. A., Macciò A. V., 2014, MNRAS, 441, 3359

Eddington A. S., 1915a, MNRAS, 75, 366
Eddington A. S., 1915b, MNRAS, 76, 37
Eddington A. S., 1923, The mathematical theory of relativity
Efstathiou G., Bond J. R., White S. D. M., 1992, MNRAS, 258, 1P
Einasto J., 1965, Trudy Astrofizicheskogo Instituta Alma-Ata, 5, 87
Einstein A., 1917, Sitzungsberichte der Königlich Preussischen Akademie der Wissenschaften, 142
Einstein A., 1936, Science, 84, 506
Elbert O. D., Bullock J. S., Garrison-Kimmel S., Rocha M., Oñorbe J., Peter A. H. G., 2015, MNRAS, 453, 29
Elbert O. D., Bullock J. S., Kaplinghat M., Garrison-Kimmel S., Graus A. S., Rocha M., 2018, ApJ, 853, 109
Engler C. et al., 2021, MNRAS, 507, 4211
Enzi W. et al., 2021, MNRAS, 506, 5848
Erkal D., Belokurov V., 2015, MNRAS, 454, 3542
Erkal D., Belokurov V. A., 2020, MNRAS, 495, 2554
Errani R., Navarro J. F., 2021, MNRAS, 505, 18
Errani R., Peñarrubia J., 2020, MNRAS, 491, 4591
Errani R., Peñarrubia J., Laporte C. F. P., Gómez F. A., 2017, MNRAS, 465, L59
Errani R., Peñarrubia J., Walker M. G., 2018, MNRAS, 481, 5073
Essig R., McDermott S. D., Yu H.-B., Zhong Y.-M., 2019, Phys. Rev. Lett., 123, 121102
Evans A. J., Strigari L. E., Zivick P., 2022, MNRAS, 511, 4251
Faber S. M. et al., 2003, in Society of Photo-Optical Instrumentation Engineers (SPIE) Conference Series, Vol. 4841, Instrument Design and Performance for Optical/Infrared Ground-based Telescopes, Iye M., Moorwood A. F. M., eds., pp. 1657–1669
Fall S. M., Efstathiou G., 1980, MNRAS, 193, 189
Famaey B., McGaugh S. S., 2012, Living Reviews in Relativity, 15, 10
Fattahi A., Navarro J. F., Frenk C. S., Oman K. A., Sawala T., Schaller M., 2018, MNRAS, 476, 3816
Feng J. L., 2010, ARA&A, 48, 495
Feng J. L., Kaplinghat M., Tu H., Yu H.-B., 2009, , 2009, 004
Feng J. L., Kumar J., 2008, Phys. Rev. Lett., 101, 231301
Ferreras I., Charlot S., Silk J., 1999, ApJ, 521, 81
Fields B. D., 2011, Annual Review of Nuclear and Particle Science, 61, 47
Fisher J. R., Tully R. B., 1975, A&A, 44, 151
Fisher J. R., Tully R. B., 1981, ApJS, 47, 139
Fitts A. et al., 2017, MNRAS, 471, 3547
Flaugher B. et al., 2015, AJ, 150, 150
Flores R. A., Primack J. R., 1994, ApJ, 427, L1
Flynn C., Gould A., Bahcall J. N., 1996, ApJ, 466, L55
Foreman-Mackey D., 2016, The Journal of Open Source Software, 1, 24
Foreman-Mackey D., Hogg D. W., Lang D., Goodman J., 2013, PASP, 125, 306
Freeman K. C., 1970, ApJ, 160, 811

Frings J., Macciò A., Buck T., Penzo C., Dutton A., Blank M., Obreja A., 2017, MNRAS, 472, 3378
Fritz T. K., Battaglia G., Pawlowski M. S., Kallivayalil N., van der Marel R., Sohn S. T., Brook C., Besla G., 2018, A&A, 619, A103
Fritz T. K., Carrera R., Battaglia G., Taibi S., 2019, A&A, 623, A129
Fry A. B. et al., 2015, MNRAS, 452, 1468
Fu S. W., Simon J. D., Alarcón Jara A. G., 2019, ApJ, 883, 11
Gaia Collaboration et al., 2018, A&A, 616, A1
Gaia Collaboration et al., 2016, A&A, 595, A2
Gallart C. et al., 2015, ApJ, 811, L18
Gao L., Springel V., White S. D. M., 2005a, MNRAS, 363, L66
Gao L., White S. D. M., Jenkins A., Frenk C. S., Springel V., 2005b, MNRAS, 363, 379
Garrison-Kimmel S. et al., 2019, MNRAS, 487, 1380
Garrison-Kimmel S. et al., 2017, MNRAS, 471, 1709
Gatto A., Fraternali F., Read J. I., Marinacci F., Lux H., Walch S., 2013, MNRAS, 433, 2749
Geha M., Willman B., Simon J. D., Strigari L. E., Kirby E. N., Law D. R., Strader J., 2009, ApJ, 692, 1464
Genina A. et al., 2018, MNRAS, 474, 1398
Genina A., Read J. I., Fattahi A., Frenk C. S., 2020a, arXiv e-prints, arXiv:2011.09482
Genina A., Read J. I., Fattahi A., Frenk C. S., 2022, MNRAS, 510, 2186
Genina A. et al., 2020b, MNRAS, 498, 144
Gilbert K. M. et al., 2006, ApJ, 652, 1188
Gilman D., Birrer S., Nierenberg A., Treu T., Du X., Benson A., 2020, MNRAS, 491, 6077
Gilman D., Birrer S., Treu T., Nierenberg A., Benson A., 2019, MNRAS, 487, 5721
Gilman D., Bovy J., Treu T., Nierenberg A., Birrer S., Benson A., Sameie O., 2021, MNRAS, 507, 2432
Gilmore G., Wilkinson M. I., Wyse R. F. G., Kleyna J. T., Koch A., Evans N. W., Grebel E. K., 2007, ApJ, 663, 948
Girardi L. et al., 2010a, ApJ, 724, 1030
Girardi L. et al., 2010b, ApJ, 724, 1030
Gnedin O. Y., Zhao H., 2002, MNRAS, 333, 299
Gregory A. L. et al., 2020, MNRAS, 496, 1092
Gregory A. L., Collins M. L. M., Read J. I., Irwin M. J., Ibata R. A., Martin N. F., McConnachie A. W., Weisz D. R., 2019, MNRAS, 485, 2010
Gunn J. E., Knapp G. R., 1993, in Astronomical Society of the Pacific Conference Series, Vol. 43, Sky Surveys. Protostars to Protogalaxies, Soifer B. T., ed., p. 267
Guo Q. et al., 2020, Nature Astronomy, 4, 246
Gutcke T. A., Pfrommer C., Bryan G. L., Pakmor R., Springel V., Naab T., 2022, ApJ, 941, 120
Hammer F., Yang Y. B., Wang J. L., Ibata R., Flores H., Puech M., 2018, MNRAS, 475, 2754
Hargis J. R., Willman B., Peter A. H. G., 2014, ApJ, 795, L13

Harrington R. G., Wilson A. G., 1950, PASP, 62, 118
Harris C. R. et al., 2020, Nature, 585, 357
Harvey D., Massey R., Kitching T., Taylor A., Tittley E., 2015, Science, 347, 1462
Harvey D., Robertson A., Massey R., McCarthy I. G., 2019, MNRAS, 488, 1572
Hayashi E., Navarro J. F., Taylor J. E., Stadel J., Quinn T., 2003, ApJ, 584, 541
Hernquist L., 1990, ApJ, 356, 359
Herschel J. F. W., 1833, Philosophical Transactions of the Royal Society of London Series I, 123, 359
Herschel J. F. W., 1864, Philosophical Transactions of the Royal Society of London Series I, 154, 1
Herschel W., 1786, Philosophical Transactions of the Royal Society of London Series I, 76, 457
Hidalgo S. L. et al., 2018, ApJ, 856, 125
Higgs C. R., McConnachie A. W., 2021, MNRAS, 506, 2766
Higgs C. R. et al., 2016, MNRAS, 458, 1678
Ho N. et al., 2012, ApJ, 758, 124
Ho N., Geha M., Tollerud E. J., Zinn R., Guhathakurta P., Vargas L. C., 2015, ApJ, 798, 77
Hodge P. W., 1971, ARA&A, 9, 35
Hoffman G. L., Helou G., Salpeter E. E., Glosson J., Sandage A., 1987, ApJS, 63, 247
Hogan C. J., Dalcanton J. J., 2000, Phys. Rev. D, 62, 063511
Hooper D., Profumo S., 2007, Phys. Rep., 453, 29
Hsueh J. W., Enzi W., Vegetti S., Auger M. W., Fassnacht C. D., Despali G., Koopmans L. V. E., McKean J. P., 2020, MNRAS, 492, 3047
Hubble E., 1929, Proceedings of the National Academy of Science, 15, 168
Hubble E. P., 1926, ApJ, 64, 321
Huggins W., 1868, Philosophical Transactions of the Royal Society of London Series I, 158, 529
Hunter J. D., 2007, Computing in Science & Engineering, 9, 90
Ibata R., Martin N. F., Irwin M., Chapman S., Ferguson A. M. N., Lewis G. F., McConnachie A. W., 2007, ApJ, 671, 1591
Ibata R., Sollima A., Nipoti C., Bellazzini M., Chapman S. C., Dalessandro E., 2011, ApJ, 738, 186
Ibata R. A., Gilmore G., Irwin M. J., 1994, Nature, 370, 194
Ibata R. A. et al., 2013, Nature, 493, 62
Iorio G., Fraternali F., Nipoti C., Di Teodoro E., Read J. I., Battaglia G., 2017, MNRAS, 466, 4159
Iršič V. et al., 2017, Phys. Rev. D, 96, 023522
Irwin M., Lewis J., 2001, New Astronomy Reviews, 45, 105
Irwin M. J. et al., 2007, ApJ, 656, L13
Irwin M. J., Bunclark P. S., Bridgeland M. T., McMahon R. G., 1990, MNRAS, 244, 16P
Irwin M. J., Ferguson A. M. N., Huxor A. P., Tanvir N. R., Ibata R. A., Lewis G. F., 2008, ApJ, 676, L17
Israel F. P., Koornneef J., 1988, A&A, 190, 21

Ivezić Ž. et al., 2019, ApJ, 873, 111
Jardel J. R., Gebhardt K., 2012, ApJ, 746, 89
Jeans J. H., 1922, MNRAS, 82, 122
Jethwa P., Erkal D., Belokurov V., 2016, MNRAS, 461, 2212
Jethwa P., Erkal D., Belokurov V., 2018, MNRAS, 473, 2060
Ji A. P. et al., 2021, ApJ, 921, 32
Johnston K. V., Choi P. I., Guhathakurta P., 2002, AJ, 124, 127
Jordi K., Grebel E. K., Ammon K., 2006, A&A, 460, 339
Jungman G., Kamionkowski M., Griest K., 1996, Phys. Rep., 267, 195
Kafle P. R., Sharma S., Lewis G. F., Robotham A. S. G., Driver S. P., 2018, MNRAS, 475, 4043
Kalberla P. M. W., Shchekinov Y. A., Dettmar R. J., 1999, A&A, 350, L9
Kalirai J. S. et al., 2010, ApJ, 711, 671
Kamada A., Kaplinghat M., Pace A. B., Yu H.-B., 2017, Phys. Rev. Lett., 119, 111102
Kaplinghat M., Tulin S., Yu H.-B., 2016, Phys. Rev. Lett., 116, 041302
Kapteyn J. C., 1922, ApJ, 55, 302
Kazantzidis S., Kravtsov A. V., Zentner A. R., Allgood B., Nagai D., Moore B., 2004, ApJ, 611, L73
Kazantzidis S., Łokas E. L., Callegari S., Mayer L., Moustakas L. A., 2011, ApJ, 726, 98
Kennedy R., Frenk C., Cole S., Benson A., 2014, MNRAS, 442, 2487
Kim S. Y., Peter A. H. G., 2021, arXiv e-prints, arXiv:2106.09050
Kim S. Y., Peter A. H. G., Hargis J. R., 2018, Phys. Rev. Lett., 121, 211302
Kim S. Y., Peter A. H. G., Wittman D., 2017, MNRAS, 469, 1414
Kirby E. N., Boylan-Kolchin M., Cohen J. G., Geha M., Bullock J. S., Kaplinghat M., 2013a, ApJ, 770, 16
Kirby E. N., Cohen J. G., Guhathakurta P., Cheng L., Bullock J. S., Gallazzi A., 2013b, ApJ, 779, 102
Kirby E. N., Cohen J. G., Simon J. D., Guhathakurta P., 2015a, ApJ, 814, L7
Kirby E. N., Cohen J. G., Simon J. D., Guhathakurta P., Thygesen A. O., Duggan G. E., 2017, ApJ, 838, 83
Kirby E. N., Simon J. D., Cohen J. G., 2015b, ApJ, 810, 56
Kleyna J. T., Wilkinson M. I., Evans N. W., Gilmore G., 2001, ApJ, 563, L115
Klypin A., Kravtsov A. V., Valenzuela O., Prada F., 1999, ApJ, 522, 82
Kochanek C. S., White M., 2000, ApJ, 543, 514
Koda J., Shapiro P. R., 2011, MNRAS, 415, 1125
Kolb E. W., Turner M. S., 1990, The early universe, Vol. 69
Komatsu E. et al., 2009, ApJS, 180, 330
Koposov S. E., Belokurov V., Torrealba G., Evans N. W., 2015, ApJ, 805, 130
Koposov S. E., Yoo J., Rix H.-W., Weinberg D. H., Macciò A. V., Escudé J. M., 2009, ApJ, 696, 2179
Kravtsov A. V., 2013, ApJ, 764, L31
Kravtsov A. V., Gnedin O. Y., Klypin A. A., 2004, ApJ, 609, 482
Kravtsov A. V., Klypin A. A., Bullock J. S., Primack J. R., 1998, ApJ, 502, 48

Kroupa P., Pawlowski M., Milgrom M., 2012, International Journal of Modern Physics D, 21, 1230003
Kuzio de Naray R., Kaufmann T., 2011, MNRAS, 414, 3617
Kuzio de Naray R., McGaugh S. S., de Blok W. J. G., 2008, ApJ, 676, 920
Labrie K., Anderson K., Cárdenes R., Simpson C., Turner J. E. H., 2019, in Astronomical Society of the Pacific Conference Series, Vol. 523, Astronomical Data Analysis Software and Systems XXVII, Teuben P. J., Pound M. W., Thomas B. A., Warner E. M., eds., p. 321
Laevens B. P. M. et al., 2015, ApJ, 802, L18
Leavitt H. S., Pickering E. C., 1912, Harvard College Observatory Circular, 173, 1
Lee B. W., Weinberg S., 1977, Phys. Rev. Lett., 39, 165
Lee M. G., Freedman W. L., Madore B. F., 1993, ApJ, 417, 553
Li H., Hammer F., Babusiaux C., Pawlowski M. S., Yang Y., Arenou F., Du C., Wang J., 2021, ApJ, 916, 8
Lin H. W., Loeb A., 2016, , 2016, 009
Łokas E. L., 2002, MNRAS, 333, 697
Łokas E. L., Mamon G. A., 2003, MNRAS, 343, 401
Longeard N. et al., 2021, MNRAS, 503, 2754
Longeard N. et al., 2018, MNRAS, 480, 2609
Lovell M. R., Frenk C. S., Eke V. R., Jenkins A., Gao L., Theuns T., 2014, MNRAS, 439, 300
Lovell M. R., Gonzalez-Perez V., Bose S., Boyarsky A., Cole S., Frenk C. S., Ruchayskiy O., 2017, MNRAS, 468, 2836
Ludlow A. D., Navarro J. F., Angulo R. E., Boylan-Kolchin M., Springel V., Frenk C., White S. D. M., 2014, MNRAS, 441, 378
Lux H., Read J. I., Lake G., 2010, MNRAS, 406, 2312
Lynden-Bell D., Wood R., 1968, MNRAS, 138, 495
Macciò A. V., Paduroiu S., Anderhalden D., Schneider A., Moore B., 2012, MNRAS, 424, 1105
Mackey A. D. et al., 2013, ApJ, 770, L17
Madau P., Shen S., Governato F., 2014, ApJ, 789, L17
Majewski S. R. et al., 2007, ApJ, 670, L9
Marchesini D., D'Onghia E., Chincarini G., Firmani C., Conconi P., Molinari E., Zacchei A., 2002, ApJ, 575, 801
Marigo P., Girardi L., Bressan A., Groenewegen M. A. T., Silva L., Granato G. L., 2008, A&A, 482, 883
Markevitch M., Gonzalez A. H., David L., Vikhlinin A., Murray S., Forman W., Jones C., Tucker W., 2002, ApJ, 567, L27
Martin N. F. et al., 2014, ApJ, 793, L14
Martin N. F. et al., 2016a, MNRAS, 458, L59
Martin N. F., Ibata R. A., Bellazzini M., Irwin M. J., Lewis G. F., Dehnen W., 2004, MNRAS, 348, 12
Martin N. F., Ibata R. A., Chapman S. C., Irwin M., Lewis G. F., 2007, MNRAS, 380, 281
Martin N. F. et al., 2016b, ApJ, 818, 40

Martin N. F., Ibata R. A., Irwin M. J., Chapman S., Lewis G. F., Ferguson A. M. N., Tanvir N., McConnachie A. W., 2006, MNRAS, 371, 1983
Martin N. F. et al., 2016c, ApJ, 833, 167
Martin N. F., Ibata R. A., McConnachie A. W., Mackey A. D., Ferguson A. M. N., Irwin M. J., Lewis G. F., Fardal M. A., 2013a, ApJ, 776, 80
Martin N. F., Jin S., 2010, ApJ, 721, 1333
Martin N. F. et al., 2009, ApJ, 705, 758
Martin N. F. et al., 2013b, ApJ, 779, L10
Martin N. F. et al., 2013c, ApJ, 772, 15
Martin N. F. et al., 2017, ApJ, 850, 16
Martínez-Delgado D. et al., 2018, A&A, 620, A126
Martínez-Delgado D., Karim N., Charles E. J. E., Boschin W., Monelli M., Collins M. L. M., Donatiello G., Alfaro E. J., 2022, MNRAS, 509, 16
Mashchenko S., Wadsley J., Couchman H. M. P., 2008, Science, 319, 174
Mateo M. L., 1998, ARA&A, 36, 435
Mather J. C. et al., 1990, ApJ, 354, L37
Mau S. et al., 2020, ApJ, 890, 136
Mayer L., Governato F., Colpi M., Moore B., Quinn T., Wadsley J., Stadel J., Lake G., 2001, ApJ, 559, 754
McConnachie A. W., 2012, AJ, 144, 4
McConnachie A. W. et al., 2008, ApJ, 688, 1009
McConnachie A. W. et al., 2009, Nature, 461, 66
McGaugh S. S., 2012, AJ, 143, 40
McGaugh S. S., Lelli F., Schombert J. M., 2016, Phys. Rev. Lett., 117, 201101
McGaugh S. S., Rubin V. C., de Blok W. J. G., 2001, AJ, 122, 2381
McNaught-Roberts T. et al., 2014, MNRAS, 445, 2125
McQuinn K. B. W., Mao Y.-Y., Buckley M. R., Shih D., Cohen R. E., Dolphin A. E., 2023, ApJ, 944, 14
Merrifield M. R., Kent S. M., 1990, AJ, 99, 1548
Merritt D., Graham A. W., Moore B., Diemand J., Terzić B., 2006, AJ, 132, 2685
Messier C., 1774, Mémoires de l'Academie, 1771, 435
Messier C., 1781, Catalogue des Nébuleuses et des Amas d'Étoiles (Catalog of Nebulae and Star Clusters). Connoissance des Temps ou des Mouvements Célestes
Meylan G., 1987, A&A, 184, 144
Milgrom M., 1983a, ApJ, 270, 371
Milgrom M., 1983b, ApJ, 270, 384
Milgrom M., 1983c, ApJ, 270, 365
Miralda-Escudé J., 2002, ApJ, 564, 60
Mo H., van den Bosch F. C., White S., 2010, Galaxy Formation and Evolution
Monelli M. et al., 2010a, ApJ, 722, 1864
Monelli M. et al., 2010b, ApJ, 720, 1225
Moore B., 1994, arXiv e-prints, astro
Moore B., Ghigna S., Governato F., Lake G., Quinn T., Stadel J., Tozzi P., 1999, ApJ, 524, L19
Morrison H. L., Harding P., Hurley-Keller D., Jacoby G., 2003, ApJ, 596, L183

Munshi F., Brooks A. M., Applebaum E., Christensen C. R., Quinn T., Sligh S., 2021, ApJ, 923, 35
Munshi F., Brooks A. M., Christensen C., Applebaum E., Holley-Bockelmann K., Quinn T. R., Wadsley J., 2019, ApJ, 874, 40
Murgia R., Iršič V., Viel M., 2018, Phys. Rev. D, 98, 083540
Nadler E. O., Banerjee A., Adhikari S., Mao Y.-Y., Wechsler R. H., 2020a, ApJ, 896, 112
Nadler E. O., Birrer S., Gilman D., Wechsler R. H., Du X., Benson A., Nierenberg A. M., Treu T., 2021, ApJ, 917, 7
Nadler E. O., Gluscevic V., Boddy K. K., Wechsler R. H., 2019, ApJ, 878, L32
Nadler E. O., Gluscevic V., Boddy K. K., Wechsler R. H., 2020b, ApJ, 897, L46
Nadler E. O. et al., 2020c, ApJ, 893, 48
Natarajan P., Zhao H., 2008, MNRAS, 389, 250
Navarro J. F., Eke V. R., Frenk C. S., 1996a, MNRAS, 283, L72
Navarro J. F., Frenk C. S., White S. D. M., 1996b, ApJ, 462, 563
Navarro J. F., Frenk C. S., White S. D. M., 1997, ApJ, 490, 493
Navarro J. F. et al., 2010, MNRAS, 402, 21
Neto A. F. et al., 2007, MNRAS, 381, 1450
Newman A. B., Treu T., Ellis R. S., Sand D. J., 2013, ApJ, 765, 25
Newton O., Cautun M., Jenkins A., Frenk C. S., Helly J. C., 2018, MNRAS, 479, 2853
Newton O. et al., 2021, , 2021, 062
Nishikawa H., Boddy K. K., Kaplinghat M., 2020, Phys. Rev. D, 101, 063009
Oñorbe J., Boylan-Kolchin M., Bullock J. S., Hopkins P. F., Kereš D., Faucher-Giguère C.-A., Quataert E., Murray N., 2015, MNRAS, 454, 2092
Okamoto T., Gao L., Theuns T., 2008, MNRAS, 390, 920
Olszewski E. W., Schommer R. A., Suntzeff N. B., Harris H. C., 1991, AJ, 101, 515
Oman K. A. et al., 2015, MNRAS, 452, 3650
Oort J. H., 1932, Bull. Astron. Inst. Netherlands, 6, 249
Öpik E., 1915, Bull. de la Soc. Astr. de Russie, 21, 150
Orkney M. D. A. et al., 2021, MNRAS, 504, 3509
Pascale R., Posti L., Nipoti C., Binney J., 2018, MNRAS, 480, 927
Patel E., Besla G., Mandel K., Sohn S. T., 2018a, ApJ, 857, 78
Patel E., Besla G., Sohn S. T., 2017, MNRAS, 464, 3825
Patel E., Carlin J. L., Tollerud E. J., Collins M. L. M., Dooley G. A., 2018b, MNRAS, 480, 1883
Pawlowski M. S., 2018, Modern Physics Letters A, 33, 1830004
Pawlowski M. S., Pflamm-Altenburg J., Kroupa P., 2012, MNRAS, 423, 1109
Peñarrubia J., Benson A. J., Walker M. G., Gilmore G., McConnachie A. W., Mayer L., 2010, MNRAS, 406, 1290
Peñarrubia J., Navarro J. F., McConnachie A. W., 2008, ApJ, 673, 226
Peñarrubia J., Navarro J. F., McConnachie A. W., Martin N. F., 2009, ApJ, 698, 222
Peccei R. D., Quinn H. R., 1977, Phys. Rev. Lett., 38, 1440
Peebles P. J. E., 1982, ApJ, 263, L1
Penzias A. A., Wilson R. W., 1965, ApJ, 142, 419

Percival W. J., Cole S., Eisenstein D. J., Nichol R. C., Peacock J. A., Pope A. C., Szalay A. S., 2007, MNRAS, 381, 1053
Peter A. H. G., 2012, arXiv e-prints, arXiv:1201.3942
Peter A. H. G., Rocha M., Bullock J. S., Kaplinghat M., 2013, MNRAS, 430, 105
Planck Collaboration et al., 2016, A&A, 594, A13
Planck Collaboration et al., 2020, A&A, 641, A6
Poincare H., 1906, Popular Astronomy, 14, 475
Polisensky E., Ricotti M., 2011, Phys. Rev. D, 83, 043506
Pontzen A., Governato F., 2012, MNRAS, 421, 3464
Pontzen A., Governato F., 2014, Nature, 506, 171
Preskill J., Wise M. B., Wilczek F., 1983, Physics Letters B, 120, 127
Preston J. et al., 2019, MNRAS, 490, 2905
Raby S. et al., 2008
Randall S. W., Markevitch M., Clowe D., Gonzalez A. H., Bradač M., 2008, ApJ, 679, 1173
Read J. I., Agertz O., Collins M. L. M., 2016, MNRAS, 459, 2573
Read J. I., Erkal D., 2019, MNRAS, 487, 5799
Read J. I., Gilmore G., 2005, MNRAS, 356, 107
Read J. I., Iorio G., Agertz O., Fraternali F., 2017, MNRAS, 467, 2019
Read J. I. et al., 2021, MNRAS, 501, 978
Read J. I., Steger P., 2017, MNRAS, 471, 4541
Read J. I., Trentham N., 2005, Philosophical Transactions of the Royal Society of London Series A, 363, 2693
Read J. I., Walker M. G., Steger P., 2018, MNRAS, 481, 860
Read J. I., Walker M. G., Steger P., 2019, MNRAS, 484, 1401
Read J. I., Wilkinson M. I., Evans N. W., Gilmore G., Kleyna J. T., 2006, MNRAS, 367, 387
Relatores N. C. et al., 2019, ApJ, 887, 94
Ren T., Kwa A., Kaplinghat M., Yu H.-B., 2019, Physical Review X, 9, 031020
Rey M. P., Pontzen A., Agertz O., Orkney M. D. A., Read J. I., Rosdahl J., 2020, MNRAS, 497, 1508
Richardson J. C. et al., 2011, ApJ, 732, 76
Richardson T., Fairbairn M., 2014, MNRAS, 441, 1584
Ritondale E., Vegetti S., Despali G., Auger M. W., Koopmans L. V. E., McKean J. P., 2019, MNRAS, 485, 2179
Roberts M. S., Rots A. H., 1973, A&A, 26, 483
Robles V. H. et al., 2017, MNRAS, 472, 2945
Rocha M., Peter A. H. G., Bullock J. S., Kaplinghat M., Garrison-Kimmel S., Oñorbe J., Moustakas L. A., 2013, MNRAS, 430, 81
Rogstad D. H., Shostak G. S., 1972, ApJ, 176, 315
Rubin V. C., 1983, Science, 220, 1339
Rubin V. C., Ford, W. K. J., Thonnard N., 1978, ApJ, 225, L107
Rubin V. C., Ford, W. K. J., Thonnard N., 1980, ApJ, 238, 471
Rubin V. C., Ford, W. K. J., Thonnard N., Burstein D., 1982, ApJ, 261, 439
Rubin V. C., Ford, W. Kent J., 1970, ApJ, 159, 379
Rutledge G. A., Hesser J. E., Stetson P. B., 1997a, PASP, 109, 907

Rutledge G. A., Hesser J. E., Stetson P. B., Mateo M., Simard L., Bolte M., Friel E. D., Copin Y., 1997b, PASP, 109, 883
Sacchi E. et al., 2021, ApJ, 920, L19
Safarzadeh M., Loeb A., 2021, ApJ, 914, L37
Sagunski L., Gad-Nasr S., Colquhoun B., Robertson A., Tulin S., 2021, , 2021, 024
Sales L. V., Wetzel A., Fattahi A., 2022, Nature Astronomy, 6, 897
Salvadori S., Ferrara A., 2009, MNRAS, 395, L6
Sameie O. et al., 2021, MNRAS, 507, 720
Samuel J., Wetzel A., Chapman S., Tollerud E., Hopkins P. F., Boylan-Kolchin M., Bailin J., Faucher-Giguère C.-A., 2020, arXiv e-prints, arXiv:2010.08571
Sand D. J. et al., 2014, ApJ, 793, L7
Sand D. J. et al., 2022, ApJ, 935, L17
Sanders J. L., Evans N. W., Dehnen W., 2018, MNRAS, 478, 3879
Sanders R. H., 1996, ApJ, 473, 117
Sanders R. H., Noordermeer E., 2007, MNRAS, 379, 702
Sanders R. H., Verheijen M. A. W., 1998, ApJ, 503, 97
Savino A. et al., 2023, arXiv e-prints, arXiv:2305.13360
Savino A. et al., 2022, arXiv e-prints, arXiv:2206.02801
Sawala T. et al., 2016, MNRAS, 457, 1931
Schechter P., 1976, ApJ, 203, 297
Schlafly E. F., Finkbeiner D. P., 2011, ApJ, 737, 103
Schlegel D. J., Finkbeiner D. P., Davis M., 1998, ApJ, 500, 525
Schneider A., Smith R. E., Macciò A. V., Moore B., 2012, MNRAS, 424, 684
Schneider A., Trujillo-Gomez S., Papastergis E., Reed D. S., Lake G., 2017, MNRAS, 470, 1542
Seljak U., Makarov A., McDonald P., Trac H., 2006, Phys. Rev. Lett., 97, 191303
Shapley H., 1938, Nature, 142, 715
Shen S., Madau P., Conroy C., Governato F., Mayer L., 2014, The Astrophysical Journal, 792, 99
Shipp N. et al., 2022, arXiv e-prints, arXiv:2208.02255
Silverman M., Bullock J. S., Kaplinghat M., Robles V. H., Valli M., 2022, arXiv e-prints, arXiv:2203.10104
Simon J. D., 2018, ApJ, 863, 89
Simon J. D., 2019, ARA&A, 57, 375
Simon J. D., Bolatto A. D., Leroy A., Blitz L., Gates E. L., 2005, ApJ, 621, 757
Simon J. D. et al., 2015, ApJ, 808, 95
Simon J. D., Geha M., 2007, ApJ, 670, 313
Simon J. D. et al., 2011, ApJ, 733, 46
Simon J. D. et al., 2017, ApJ, 838, 11
Simpson C. M., Grand R. J. J., Gómez F. A., Marinacci F., Pakmor R., Springel V., Campbell D. J. R., Frenk C. S., 2018, MNRAS, 478, 548
Skillman E. D. et al., 2017, ApJ, 837, 102
Slater C. T., Bell E. F., Martin N. F., 2011, ApJ, 742, L14
Slone O., Jiang F., Lisanti M., Kaplinghat M., 2021, arXiv e-prints, arXiv:2108.03243
Smith M. S., Kawano L. H., Malaney R. A., 1993, ApJS, 85, 219

Smith S., 1936, ApJ, 83, 23
Smoot G. F. et al., 1992, ApJ, 396, L1
Sohn S. T., Patel E., Fardal M. A., Besla G., van der Marel R. P., Geha M., Guhathakurta P., 2020, ApJ, 901, 43
Somerville R. S., 2002, ApJ, 572, L23
Spergel D. et al., 2015, arXiv e-prints, arXiv:1503.03757
Spergel D. N., Steinhardt P. J., 2000, Phys. Rev. Lett., 84, 3760
Springel V., Frenk C. S., White S. D. M., 2006, Nature, 440, 1137
Springel V. et al., 2008, MNRAS, 391, 1685
Springel V. et al., 2005, Nature, 435, 629
Stadel J., Potter D., Moore B., Diemand J., Madau P., Zemp M., Kuhlen M., Quilis V., 2009, MNRAS, 398, L21
Starkenburg E. et al., 2010, A&A, 513, A34
Steigman G., 2007, Annual Review of Nuclear and Particle Science, 57, 463
Steigman G., Turner M. S., 1985, Nuclear Physics B, 253, 375
Stetson P. B., 1987, PASP, 99, 191
Stetson P. B., 1994, PASP, 106, 250
Strigari L. E., Bullock J. S., Kaplinghat M., 2007, ApJ, 657, L1
Strigari L. E., Frenk C. S., White S. D. M., 2018, ApJ, 860, 56
Tegmark M. et al., 2006, Phys. Rev. D, 74, 123507
Thuan T. X., Martin G. E., 1981, ApJ, 247, 823
Thuan T. X., Seitzer P. O., 1979a, ApJ, 231, 327
Thuan T. X., Seitzer P. O., 1979b, ApJ, 231, 680
Tielens A. G. G. M., Hollenbach D., 1985, ApJ, 291, 722
Tisserand P. et al., 2007, A&A, 469, 387
Tollerud E., 2016, Rgbmcmr: V0.1
Tollerud E. J. et al., 2012, ApJ, 752, 45
Tollerud E. J., Bullock J. S., Strigari L. E., Willman B., 2008, ApJ, 688, 277
Tollerud E. J., Geha M. C., Grcevich J., Putman M. E., Weisz D. R., Dolphin A. E., 2016, ApJ, 827, 89
Tollet E. et al., 2016, MNRAS, 456, 3542
Tolstoy E., Hill V., Tosi M., 2009, ARA&A, 47, 371
Tomozeiu M., Mayer L., Quinn T., 2016, ApJ, 827, L15
Torrealba G. et al., 2018, MNRAS, 475, 5085
Torrealba G. et al., 2019, MNRAS, 488, 2743
Torrealba G., Koposov S. E., Belokurov V., Irwin M., 2016, MNRAS, 459, 2370
Tulin S., Yu H.-B., 2018, Phys. Rep., 730, 1
Tulin S., Yu H.-B., Zurek K. M., 2013a, Phys. Rev. D, 87, 115007
Tulin S., Yu H.-B., Zurek K. M., 2013b, Phys. Rev. Lett., 110, 111301
Tully R. B., Boesgaard A. M., Dyck H. M., Schempp W. V., 1981, ApJ, 246, 38
Turner H. C., Lovell M. R., Zavala J., Vogelsberger M., 2021, MNRAS, 505, 5327
Valli M., Yu H.-B., 2018, Nature Astronomy, 2, 907
van Albada T. S., Bahcall J. N., Begeman K., Sancisi R., 1985, ApJ, 295, 305
van den Bergh S., 1972, ApJ, 171, L31
van den Bosch F. C., Ogiya G., 2018, MNRAS, 475, 4066
van der Marel R. P., Anderson J., 2010, ApJ, 710, 1063

van der Marel R. P., Fardal M. A., Sohn S. T., Patel E., Besla G., del Pino A., Sahlmann J., Watkins L. L., 2019, ApJ, 872, 24
van Dokkum P., Danieli S., Abraham R., Conroy C., Romanowsky A. J., 2019, ApJ, 874, L5
van Dokkum P. et al., 2018, Nature, 555, 629
van Zee L., Salzer J. J., Haynes M. P., O'Donoghue A. A., Balonek T. J., 1998, AJ, 116, 2805
Vandenberg D. A., Bolte M., Stetson P. B., 1990, AJ, 100, 445
Vegetti S., Despali G., Lovell M. R., Enzi W., 2018, MNRAS, 481, 3661
Viel M., Lesgourgues J., Haehnelt M. G., Matarrese S., Riotto A., 2006, Phys. Rev. Lett., 97, 071301
Virtanen P. et al., 2020, Nature Methods, 17, 261
Vogelsberger M., Zavala J., Cyr-Racine F.-Y., Pfrommer C., Bringmann T., Sigurdson K., 2016, MNRAS, 460, 1399
Vogelsberger M., Zavala J., Loeb A., 2012, MNRAS, 423, 3740
Vogelsberger M., Zavala J., Simpson C., Jenkins A., 2014, MNRAS, 444, 3684
Walker A. R. et al., 2019, MNRAS, 490, 4121
Walker M. G., Mateo M., Olszewski E. W., Gnedin O. Y., Wang X., Sen B., Woodroofe M., 2007, ApJ, 667, L53
Walker M. G., Mateo M., Olszewski E. W., Peñarrubia J., Evans N. W., Gilmore G., 2009, ApJ, 704, 1274
Walker M. G., McGaugh S. S., Mateo M., Olszewski E. W., Kuzio de Naray R., 2010, ApJ, 717, L87
Walker M. G., Peñarrubia J., 2011, ApJ, 742, 20
Walker T. P., Steigman G., Schramm D. N., Olive K. A., Kang H.-S., 1991, ApJ, 376, 51
Walsh S. M., Willman B., Jerjen H., 2009, AJ, 137, 450
Wang J., White S. D. M., 2007, MNRAS, 380, 93
Watkins L. L., Evans N. W., van de Ven G., 2013, MNRAS, 430, 971
Weinberg D. H., Bullock J. S., Governato F., Kuzio de Naray R., Peter A. H. G., 2015, Proceedings of the National Academy of Science, 112, 12249
Weisz D. R. et al., 2011, ApJ, 739, 5
Weisz D. R. et al., 2019a, MNRAS, 489, 763
Weisz D. R., Dolphin A. E., Skillman E. D., Holtzman J., Gilbert K. M., Dalcanton J. J., Williams B. F., 2014, ApJ, 789, 147
Weisz D. R. et al., 2019b, ApJ, 885, L8
Wetzel A. R., Hopkins P. F., Kim J.-h., Faucher-Giguère C.-A., Kereš D., Quataert E., 2016, ApJ, 827, L23
Wheeler C., Phillips J. I., Cooper M. C., Boylan-Kolchin M., Bullock J. S., 2014, MNRAS, 442, 1396
White S. D. M., 1976, MNRAS, 177, 717
White S. D. M., Rees M. J., 1978, MNRAS, 183, 341
Whiting A. B., Hau G. K. T., Irwin M., 1999, AJ, 118, 2767
Wilkinson M. I., Kleyna J., Evans N. W., Gilmore G., 2002, MNRAS, 330, 778
Willman B. et al., 2005a, AJ, 129, 2692
Willman B. et al., 2005b, ApJ, 626, L85

Wilson A. G., 1955, PASP, 67, 27
Wittman D., Golovich N., Dawson W. A., 2018, ApJ, 869, 104
Wojno J., Gilbert K. M., Kirby E. N., Escala I., Beaton R. L., Tollerud E. J., Majewski S. R., Guhathakurta P., 2020, ApJ, 895, 78
Wolf J., Martinez G. D., Bullock J. S., Kaplinghat M., Geha M., Muñoz R. R., Simon J. D., Avedo F. F., 2010, MNRAS, 406, 1220
Worthey G., 1994, ApJS, 95, 107
Worthey G., 1999, in Astronomical Society of the Pacific Conference Series, Vol. 192, Spectrophotometric Dating of Stars and Galaxies, Hubeny I., Heap S., Cornett R., eds., p. 283
York D. G. et al., 2000, AJ, 120, 1579
Zavala J., Lovell M. R., Vogelsberger M., Burger J. D., 2019, Phys. Rev. D, 100, 063007
Zavala J., Vogelsberger M., Walker M. G., 2013, MNRAS, 431, L20
Zeng Z. C., Peter A. H. G., Du X., Benson A., Kim S., Jiang F., Cyr-Racine F.-Y., Vogelsberger M., 2022, MNRAS, 513, 4845
Zhao H., 1996, MNRAS, 278, 488
Zolotov A. et al., 2012, ApJ, 761, 71
Zoutendijk S. L., Brinchmann J., Bouché N. F., den Brok M., Krajnović D., Kuijken K., Maseda M. V., Schaye J., 2021, A&A, 651, A80
Zucker D. B. et al., 2006, ApJ, 650, L41
Zucker D. B. et al., 2004, ApJ, 612, L121
Zucker D. B. et al., 2007, ApJ, 659, L21
Zwicky F., 1933, Helvetica Physica Acta, 6, 110
Zwicky F., 1937, ApJ, 86, 217